UNIVERSITY OF SOUTHAMPTON

FABRICATION AND CHARACTERISATION OF YTTERBIUM : ERBIUM CODOPED PHOSPHOSILICATE FIBRES FOR OPTICAL AMPLIFIERS AND LASERS

By Guillaume Vienne

A thesis submitted for the degree of Doctor of Philosophy

FACULTY OF ENGINEERING AND APPLIED SCIENCE

DEPARTMENT OF ELECTRONICS & COMPUTER SCIENCE

OPTOELECTRONICS RESEARCH CENTRE

September 1996

UNIVERSITY OF SOUTHAMPTON

ABSTRACT

FACULTY OF ENGINEERING AND APPLIED SCIENCE

DEPARTMENT OF ELECTRONICS & COMPUTER SCIENCE
OPTOELECTRONICS RESEARCH CENTRE

Doctor of Philosophy

FABRICATION AND CHARACTERISATION OF YTTERBIUM : ERBIUM CODOPED PHOSPHOSILICATE FIBRES FOR OPTICAL AMPLIFIERS AND LASERS

by Guillaume Vienne

This thesis deals with the fabrication, characterisation, and applications of ytterbium : erbium codoped fibres. The fibres are fabricated by modified chemical vapour deposition (MCVD) combined with the solution doping technique. The properties of phosphate glasses are reviewed and we show that the fabrication process must be adapted to cope with the low viscosity of the phosphate glass. We identify the three major pitfalls which initially plagued the fabrication process and show how they can be avoided. We also describe how all glass double-clad fibres can be fabricated.

The composition of the core glass is measured by energy dispersive X-ray spectrometry and inductively coupled plasma mass spectrometry. The latter technique offers sufficient accuracy to evaluate erbium and ytterbium absorption cross-sections. Raman and infrared spectroscopy are also used to gain insight into the structure of the glass. Techniques to evaluate the suitability of our fibres for efficient devices are presented and some loss mechanisms are investigated.

Addition of aluminium to Er/Yb codoped phosphosilicate fibres in the region [Al]<[P] is studied for the first time to our knowledge. We show that the ternary Al/P/Si system is not a simple juxtaposition of the binary Al/Si and P/Si systems. Nevertheless, we find evidence that the rare-earths remain essentially coupled to phosphate sites for the region [Al] < [P], although addition of aluminium still appears to reduce rare-earth clustering.

Finally, we present a model of Er/Yb devices based on the formalism of the rate equations, and give examples of how it can be useful to predict the effect of modifications in fibre design. To conclude we present the devices which have benefited from this work, particularly single frequency grating feedback lasers and cladding pumped lasers.

To my parents

La transmission d'images : une utopie du XIX^e^ siècle.

Transmission of pictures, a 19th century utopia, imagined for the year 2000.

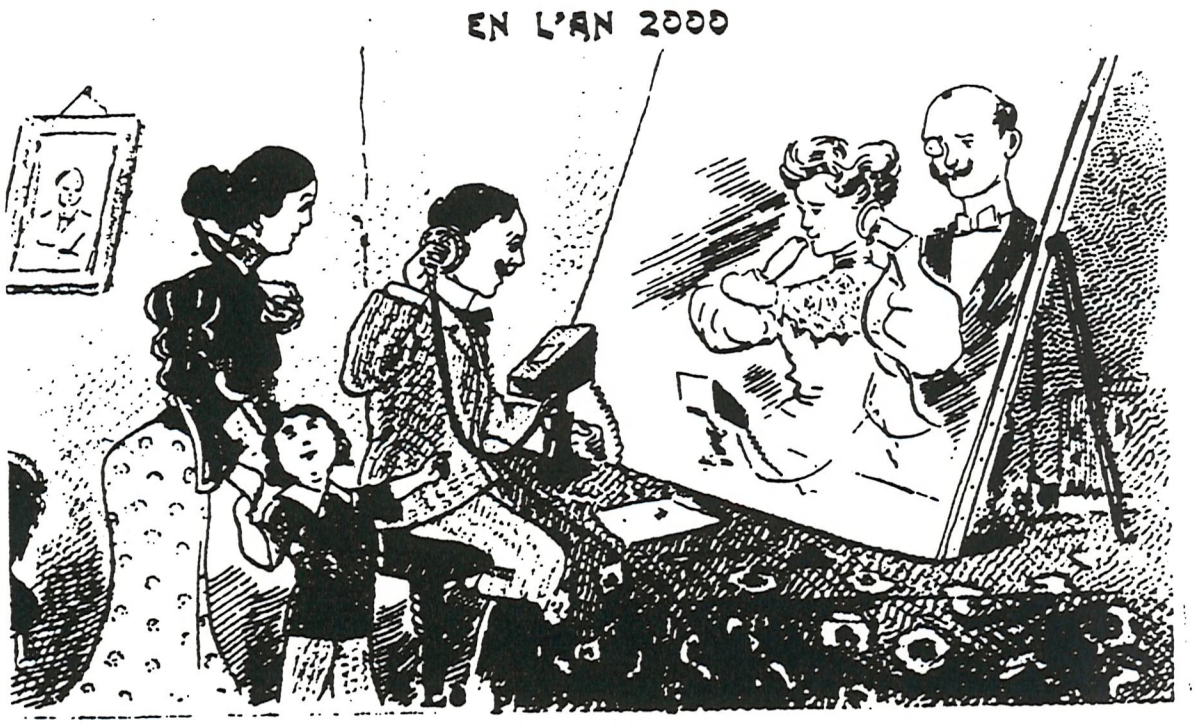

Contents

List of Figures

List of abbreviations

ASE	Amplified Spontaneous Emission
CW	Continuous Wave
DBR	Distributed Bragg Reflector
DFB	Distributed FeedBack
EDFA	Erbium Doped Fibre Amplifier
EDS	Energy Dispersive X-ray Spectrometry
ESA	Excited State Absorption
ESR	Electron Spin Resonance
EXAFS	Extended X-ray Absorption Fine Structure
FWHM	Full Width Half Maximum
ICP-MS	Inductively Coupled Plasma - Mass Spectrometry
MAS-NMR	Magic Angle Spinning - Nuclear Magnetic Resonance
MCVD	Modified Chemical Vapor Deposition
MOPA	Master Oscillator Power Amplifier
MVE	Maximal Vibrational Energy
NA	Numerical Aperture
NBO	Non-Bridging Oxygen
ppm	part per million
RIP	Refractive Index Profile
SEM	Scanning Electron Microscope
TAT	Trans-Atlantic Telecommunication
WDM	Wavelength Division Multiplexing
YAG	Yttrium Aluminium Garnet
YLF	Yttrium Lithium Fluoride

List of symbols

Symbol	Value or [Unit]	Description
A	$[m^2]$	Area of fibre core
c	$2.998.10^8$ m s^{-1}	Speed of light in vacuum
C_{up}	$[m^3\ s^{-1}]$	Upconversion constant
d	[m]	Fibre core diameter
$d(RE^{3+})$	[ion cm^{-3}]	Density of trivalent rare-earth cation
D_{SiO2}	2.2 g cm^{-3}	Density of silica
E	[J]	Energy
g_i	[1]	Degeneracy of level i
h	$6.626\ 10^{-34}$ J s	Planck constant
$I(r)$	[W cm^{-2}]	Fundamental mode intensity distribution
k	$1.381\ 10^{-23}$ J K^{-1}	Boltzmann constant
k_f	[ion $cm^{-3}\ s^{-1}$]	Initial decay of the mechanism feeding the green fluorescence
k_{tr}	$[m^3\ s^{-1}]$	Transfer parameter
loss	[1]	Round-trip cavity loss (in a laser)
L_{min}	[m]	Minimum fibre length required for lasing
M	[g]	Molar mass
n	[1]	Index of refraction
$n(r)$	[ion cm^{-3}]	Dopant density distribution
N	[ion cm^{-3}]	Concentration or population
N_A	$6.02.10^{23}$	Avogadro number
N^{Er}	[ion cm^{-3}]	Total erbium population
N_1^{Er}	[ion cm^{-3}]	Population of the $^4I_{15/2}$ level of erbium
N_2^{Er}	[ion cm^{-3}]	Population of the $^4I_{13/2}$ level of erbium
N_3^{Er}	[ion cm^{-3}]	Population of the $^4I_{11/2}$ level of erbium
N_g	[ion cm^{-3}]	Population of the $^4S_{3/2}$ level of erbium
N^{Yb}	[ion cm^{-3}]	Total ytterbium population
N_1^{Yb}	[ion cm^{-3}]	Population of the $^4F_{5/2}$ level of ytterbium
N_2^{Yb}	[ion cm^{-3}]	Population of the $^4F_{7/2}$ level of ytterbium
P_{ase}^{+}	[mW]	Amplified stimulated emission power copropagating with the pump
P_{ase}^{-}	[mW]	Amplified stimulated emission power counterpropagating with the pump

P_{launch}	[mW]	Launched pump power
P_p	[mW]	Pump power
P_s	[mW]	Total signal power
P_s^+	[mW]	Signal power copropagating with the pump
P_s^-	[mW]	Signal power counterpropagating with the pump
P_{th}	[mW]	Lasing threshold power
r	[1]	ratio of $[Yb^{3+}]$ to $[Er^{3+}]$
R_1	[1]	input mirror reflectivity for the signal
R_2	[1]	output mirror reflectivity for the signal
$[RE^{3+}]$	[ppm]	Rare-earth concentration
S	[%]	Laser slope efficiency
t_f	[s]	Decay time of the mechanism feeding the green fluorescence
t_g	[s]	Decay time of the green fluorescence
T	[°C]	Temperature
V	[1]	V value
w	[μm]	Beam spot size
W_e	[s^{-1}]	Stimulated emission rate of erbium
W_{NR}	[s^{-1}]	Non-radiative decay rate
W_p	[s^{-1}]	Pump rate of ytterbium
W_{tr}	[s^{-1}]	Transfer rate
α	[1]	Ratio of erbium absorption cross-section to erbium emission cross-section
$\alpha_{b,p}$	[dB m^{-1}]	Background losses at the pump wavelength
$\alpha_{b,s}$	[dB m^{-1}]	Background losses at the signal wavelength
α_p	[dB m^{-1}]	Pump absorption
β	[1]	Ratio of ytterbium absorption cross-section to erbium emission cross-section
γ	[dB m^{-1}]	Local amplifier gain
Γ	[1]	Beam-core overlap factor
Γ_p	[1]	Pump beam-core overlap factor
Γ_s	[1]	Signal beam-core overlap factor
η_{abs}	[1]	Fraction of pump power absorbed
λ	[μm]	Wavelength
λ_{cutoff}	[μm]	Cutoff wavelength of the LP_{11} mode
λ_p	[μm]	Pump wavelength
λ_s	[μm]	Signal wavelength

μ	[1]	Inversion coefficient
ν	[s^{-1}]	Frequency
σ_a	[m^2]	Absorption cross-section
σ_e	[m^2]	Emission cross-section
τ_f^{Er}	[s]	Fluorescence lifetime of the erbium $^4I_{13/2}$ level
τ_f^{Yb}	[s]	Fluorescence lifetime of the ytterbium $^4F_{7/2}$ level
τ_{tr}	[s]	Small signal transfer time

Acknowledgements

I would like to extend my gratitude to the members of the Optoelectronics Research Centre, for their support and guidance during the time I have spent thus far in Southampton. In particular I would like to thank Dr J. D. Minelly for his friendly supervision in the framework of the HIRAFS project, and Dr L. Dong for his leading role in the silica fabrication group. I am also very grateful to Miss J. E. Caplen for introducing me to fibre fabrication techniques, and for nicely pulling some of my preforms and my leg. I would also like to thank our clean-room-mates from Fibrecore Limited, who shared their expertise many times. Dr B. Samson has always been generous of his time and taught me many measurement skills. Dr W. S. Brocklesby made his lab an attractive place, and preformed Raman and fluorescence measurements on some Er/Yb fibres. Dr Z. Harutjunian and Z. J. Chen performed many laser measurements presented in this thesis. I feel very grateful to Dr J. T. Kringlebotn for his constant supply of ideas, and for demonstrating and modelling Er/Yb single frequency lasers. I am deeply indebted to Dr R. Paschotta for his very useful simulation programs, and Dr J. Nilsson for many helpful and motivating discussions. Dr E. Tarbox has kindly accepted to correct this thesis. I have greatly appreciated the support of my friend Kharren during the educating but not always easy time of the writing up. Finally, I would like to thank my supervisor, Prof. D. N. Payne, for giving me this opportunity to start a research career on materials.

Chapter 1

INTRODUCTION

1.1 Development of optical communications

Optical communication is a concept which had long been contemplated because light at hundreds of terahertz frequency provides almost limitless bandwidth. But it took the invention of the laser in 1960 for photonics to knock at the door of telecommunications. For almost a decade, no one answered. Actually, in its earlier years, laser technology searched in many quarters for a suitable home. But the door opened in 1966 when Kao and Hockman, at STC in England, theorised that silica-based optical fibre could exhibit sufficiently low loss to make long-distance optical transmission feasible [Kao_66]. When transmission through glass fibre was first proposed, no glass existed with sufficiently low optical absorption, and no means existed for fabricating the composite refractive index structure needed to guide light. At the time, optical quality glass exhibited loss of 1000 dB / km, but loss less than 20 dB / km was required if this new transmission mode were to compete with existing coaxial systems. It was quickly realised that the need to reduce both transition-metal and hydroxyl impurities was a major obstacle. In 1970, Corning Glass Works in the United States broke the 20 dB / km barrier [Kapron_70], and, with a maturing technology in semiconductor lasers, there was no question that the fibre optics revolution had begun.

As for coaxial cables, the two main constraints on system length were (and still are) power budget and dispersion. The first of these is a simple function of transmitter power, receiver sensitivity and fibre attenuation, whereas the second is a more complicated function of the fibre dispersion and optical source characteristics. The development of semiconductor lasers was crucial to operating wavelength of the telecom systems, and resulted in 3 transmission windows. The early commercial systems operated in the first transmission window, around 850 nm, with typical fibre attenuation of 3 - 5 dB / km with repeater spacing in the range 5 - 10 km. By 1980, 1300 nm semiconductor lasers significantly advanced to allow for initial transmission demonstration. Long span transmission in the 2nd transmission window, around 1300 nm, was possible with minimal chromatic dispersion and losses around 0.4 dB / km. The third transmission window was opened in the mid-1980s with the development of 1550 nm laser transmitters which enhanced the transmission span with minimal losses of around 0.15

dB / km. The material dispersion is higher at 1550 nm than at 1300 nm, but fibres can be designed so that the waveguide dispersion compensates for the material dispersion and dispersion compensation techniques are now practical. Beside offering lower attenuation, the 3rd transmission window has the added attraction of enabling the use of the Erbium Doped Fibre Amplifier (the EDFA is described in §1.2.1), making 1.55 μm the preferred wavelength of operation in practical systems.

In the 1980s, fibres began to be extensively deployed in the world's transmission systems. The impact of the technology since then has been spectacular. In 1988 we witnessed the first generation of undersea lightwave systems, TAT-8, going into service. Starting with heavy traffic links between telephone central offices, fibre spread through our metropolitan areas and into our office buildings. By 1996, more than 70 million km [Rausch_96] had been deployed. Today, only the "last mile" to the residence and small business is left. Completing the fibre telecommunications network to all its endpoints is critical to the broadband services envisioned in the future.

Photonics will naturally migrate onto customer premises as it displaces electronic communications functions down to the 200 μm boundary[1] [Ross_92]. Already we have campus and building fibre wiring systems, fibre local area networks, and optical data links in backplanes; eventually we will have intraboard networks, interchip, and even intrachip photonics interconnections. Thus a substantial part of communications technology stands for photonics.

1.2 Rare-earth doped fibres

In the initial development of the optical fibre technology, success was measured by how little the glass medium interacted with the transmitted light or the surroundings. Now interest has moved beyond transparency, and glasses are being sought to amplify and otherwise process optical signals. It is possible intentionally to induce interactions for specific purposes. If the core of a fibre is doped with optically active elements such as rare-earth ions and pumped with light of an appropriate wavelength, it may act as an amplifying medium.

[1] This value was estimated considering only the energy required for transmission and thus is only approximate. However, it makes it clear that photonics is the method-of-choice for transmission over a very large domain.

The small core size (several microns in diameter) of single mode optical fibre allows high pump intensities for modest (mW) pump powers. Moreover, the intensity can be maintained over long lengths and this leads to ultra-low lasing thresholds. In fact the first glass laser ever demonstrated [Snitzer_61] was flash-pumped in the form of an optical fibre, a configuration which was used to overcome the difficulties of obtaining high-quality glass in bulk form. The idea of guided-wave glass lasers attracted little attention for the next 24 years. The idea resurfaced in 1985 because both optical fibre and laser diode technologies had advanced to a stage where low-loss, rare-earth-doped, single-mode fibres could be fabricated and high-power semiconductor sources were available to pump them. In addition low cost fibre components were available. Even so, it was only after the demonstration in 1987 of a high gain, erbium-doped fibre amplifier (EDFA) operating in the third telecommunication window at 1.54 μm that widespread interest in rare-earth doped fibres was shown by the optical telecom community [Mears_87].

1.2.1 The erbium doped fibre amplifier

It is a most fortuitous coincidence that erbium ions can easily store and emit energy around 1.54 μm, the wavelength of lowest loss in silica fibres. This rare earth can be incorporated in a silica fibre by different methods, described in chapter 2, to form the active region of the erbium doped fibre amplifier (EDFA). In Fig. 1.1, it can be seen that the amplifier in its simplest form comprises only 3 basic components : fibre, coupler, and diode laser so that it is highly reliable, small, highly efficient and potentially cheap.

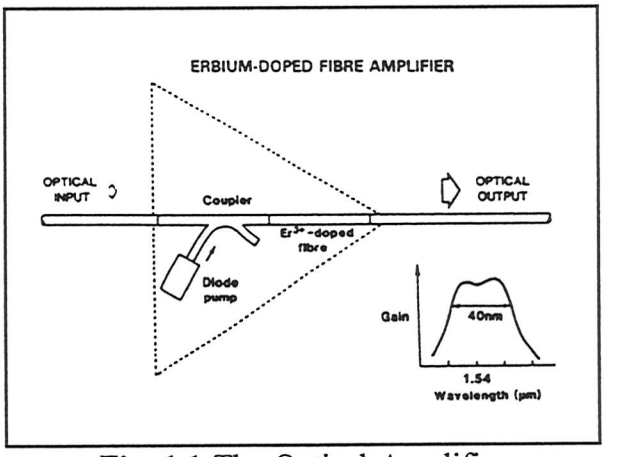

Fig. 1.1 The Optical Amplifier

Compared with the alternative of a transmission link using electronic repeaters, an all-optical link has the merit that it is transparent to the transmission code format and bit-rate. It can be upgraded by changing only the transmitter and receiver and not the repeaters. A decade ago much work was carried out in telecommunication laboratories to study the five different types of optical amplifiers available to replace electronic repeaters : Raman, Brillouin, parametric,

semiconductor, and rare-earth doped amplifiers. The EDFA outperformed its rivals because of its most impressive combination of attractive properties for operation in a lightwave telecommunication system :

- compatibility with fibre systems - It may be directly spliced into a network with very low insertion loss;
- insensitivity to signal polarisation - It is due to the random orientation of the active ions dipoles in the glass matrix. This property is very important because standard optical fibres do not preserve polarisation;
- low noise - It allows hundreds of EDFAs to be incorporated along a fibre telecommunication link, which can span more than 10.000 km, whilst still preserving low distortion / error rates;
- large bandwidth & immunity to interference between channels - These two properties are essential to the deployment of future Wavelength Division Multiplexing systems (WDM);
- high saturation power & no distortion in saturation - Unlike a diode amplifier, the EDFA has a saturation output power which increases with pump power, as well as the ability to operate deep in saturation without signal distortion;
- high efficiency & diode pumpable - It can be pumped at 1480 nm and 980 nm with very high pump efficiency (5.1 dB / mW and 11 dB / mW respectively have been demonstrated) and gain in excess of 50 dB can be obtained.

1.2.2 Fibre lasers

A fibre laser is an optically pumped laser and as such acts as a photon converter. Rare-earth doped fibre lasers use the 'raw' photons emitted by diode lasers to excite rare-earth ions contained within the fibre core which subsequently emit a stable, well controlled laser beam. They also convert the pump photon wavelength, usually to longer wavelength, but also to shorter wavelength by upconversion. This allows rare-earth doped fibre lasers to cover most of the silica glass transparency range and new transitions at longer wavelengths are sought after in new glasses

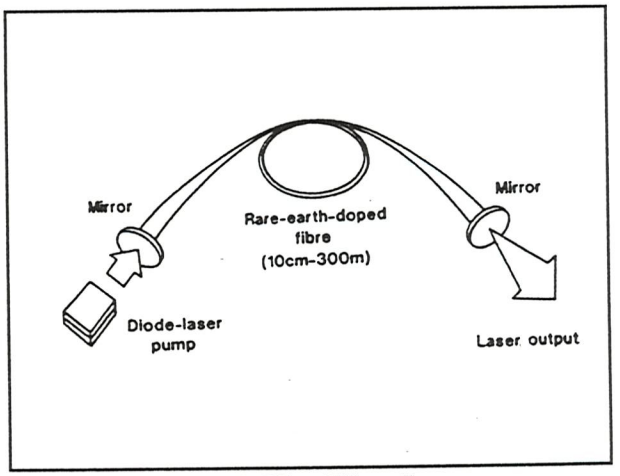

Fig. 1.2 The Fibre Laser

transparent in the near to mid infrared. Fibre lasers, and particularly cladding pumped fibre lasers, are also excellent brightness enhancers for diode arrays.

Fig. 1.2 shows a basic fibre laser design. In practice fibre gratings often replace the dielectric mirrors to form the cavity. The waveguide nature of the fibre resonator makes mirror alignment simple, eliminates thermal focusing and ensures perfect transverse mode selection. In addition, the geometry of the fibre, ie high surface to volume ratio, also means that the thermal problems that plague bulk lasers are largely eliminated. A further advantage over bulk crystal lasers is the broad absorption offered by the rare-earths in glass, which obviates the need for selection and temperature stabilisation of the pump-diode wavelength. The high gain provided by the rare-earths allows many items to be introduced in the cavity without undue attention to be paid for the associated losses. In particular, modulators and saturable absorbers can be introduced to operate the laser in pulsed regime by the well known Q-switching and modelocking techniques. The pulsed regime is particularly interesting for sensors, rangefinding and material processing (surgery, marking) applications. An advantage of the fibre configuration is that the peak power handling capability (set by the material damage) is tens of kW, a figure which considerably exceeds that obtainable from diode lasers. Mode locking, where the fibre laser generates a regular train of soliton pulses, is an exciting mode of operation for use as a telecommunication source.

Fibre lasers have many advantages over diode lasers, and might well exceed them in performance in all but one aspect. Diode lasers can be directly modulated by an electrical signal whereas the fibre laser requires an external modulator. On the other hand this situation is changing as the move to higher modulation rates is taking place, and diode lasers also require an external modulator in high speed telecom systems. In telecommunications or spectroscopy, 'single frequency' operation, where only one of the possible resonator modes is allowed, is also important to inhibit intensity noise generated by both intermode competition and mode-hopping. As a consequence of the broad fluorescence linewidth of rare-earths in glass, the output emission of fibre lasers is in general broadband, containing many thousands of cavity modes. However, by inserting wavelength selective elements in the cavity or by using a ring cavity 'single frequency' operation can be obtained. The spectral linewidth for single-frequency operation is given by the Schawlow-Townes limit which indicates that the linewidth is inversely proportional to the resonator length. Since typical fibre lasers are meters in length, whereas diode-lasers are submillimeter, fibre lasers can exhibit single-frequency operation with linewidths in the kilohertz region, whereas diode lasers have megahertz linewidths. This is a very attractive attribute of fibre lasers.

1.3 Why codoping?

Codoping can be employed in active optical devices for :

- widening the choice of pumping schemes by offering an extended absorption spectrum;

- increasing the pump absorption by possible incorporation of a high concentration of donors, which eventually offer a higher absorption cross-section than the acceptors;

- allowing a degree of freedom in the absorption to gain ratio by choosing the donor to acceptor concentration ratio;

- building up population inversion more easily and avoiding self termination by quenching a transition from the donor.

These four possibilities were recognised early on, particularly the first two. Numerous codoping schemes have been studied to increase the optical conversion efficiency of flashlamp pumped glass rod lasers, such as Nd:Yb:Er in Li-Mg-SiO_2 glass [Edwards_74] or Yb:Tm in silicate glass [Gandy_67]. Double-pumped phosphors, investigated to convert the IR light to the visible, were also sensitised with Yb^{3+} to allow pumping from the only available compact sources at the time : the GaAs diodes [Auzel_73]. The possibility of choosing gain and absorption with a degree of freedom is exploited in codoping schemes involving ytterbium as a donor. The fact that ytterbium is a two level system means that concentration quenching is marginal and that no Excited State Absorption (ESA) is present. More recently the fourth possibility has attracted attention, for instance in 1480 nm lasers based on Tm-doped fluorozirconate glass, where Ho^{3+} has been shown to shorten the $^3H_4$ lifetime of Tm^{3+} without affecting the lifetime of the $^3F_4$ upper state [Pafcheck_90]. It would take much too long to list all of the codoping schemes attempted to date.

One of the earliest and most widely studied schemes is the Er/Yb codoping of crystals and glasses. It received renewed interest when the erbium doped fibre amplifier emerged as a key component in future optical telecommunications networks, and led to the many new devices discussed later in this chapter.

Fig. 1.3 demonstrates the role of Yb^{3+} sensitisation: It offers a broader absorption with a particularly high peak at 976 nm. This is reinforced by the fact that high absorption can be

maintained even when the erbium concentration is low if the ytterbium to erbium concentration ratio is high. This is particularly advantageous because concentration quenching is much less pronounced in ytterbium than in erbium.

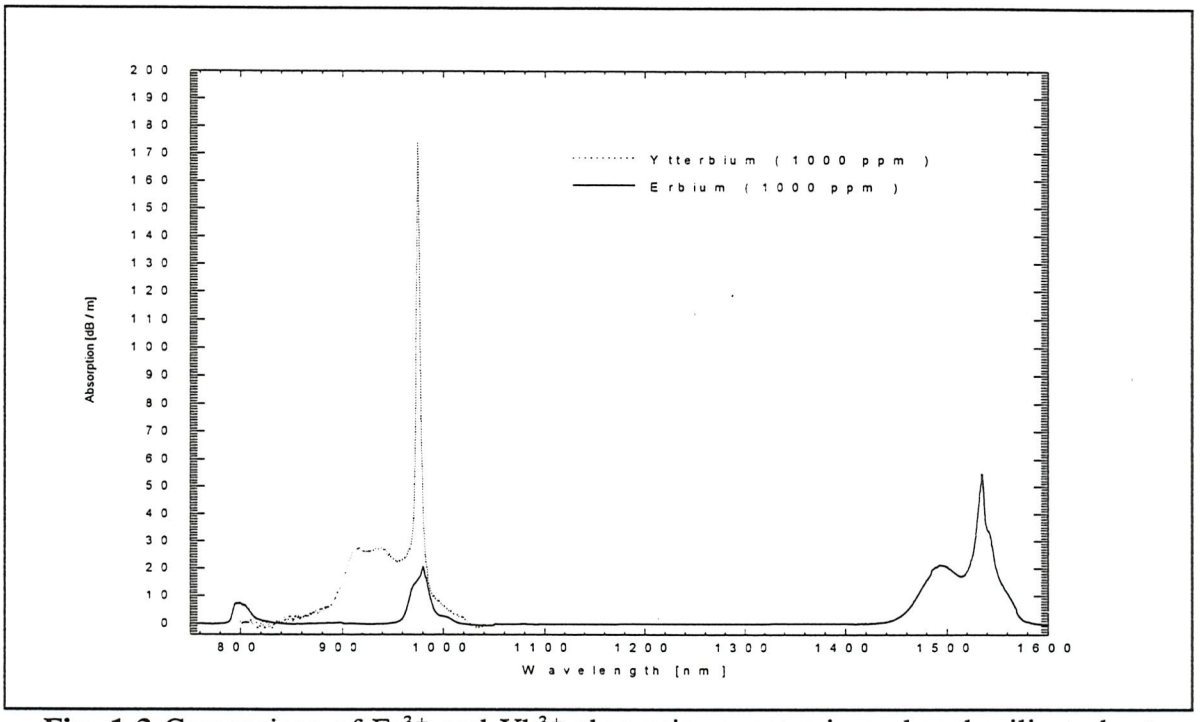

Fig. 1.3 Comparison of Er^{3+} and Yb^{3+} absorption spectra in a phosphosilicate host $[Er^{3+}] = [Yb^{3+}] = 1000$ ppm

1.4 Previous work at Southampton:

The first codoped fibre fabricated in Southampton, ND385, was an Er/Yb fibre with a germanosilicate core. It was fabricated in 1986, still in the early days of the solution doping technique.

All of the ND4xx series of Er/Yb fibres were based on a germanosilicate core. In the latest fibres of this series a small amount of phosphorus was added during the deposition. For the ND5xx fibres the core composition was modified. Germanium was partially replaced by aluminium incorporated from the solution, to allow higher rare-earth concentrations.

Fermann characterised the ND4xx and ND5xx series of Er/Yb fibres [Fermann_88]. He measured the donor fluorescence decay with no acceptor excitation and fitted it to curves predicted by energy transfer models accounting for slow or fast donor diffusion. He also measured the gain as a function of pump power in ND385 and deduced that in this

germanosilicate fibre only a maximum of 30% erbium inversion could be obtained. No germanosilicate fibre could be made to lase. However a slope of 5% (absorbed) was measured in ND545 when pumping with a miniature Nd: YAG laser. This measurement clearly showed the onset of saturation at a pump power of circa 50 mW. Barnes obtained a slope of 12% (absorbed) in another aluminosilicate Er/Yb fibre, ND536, and demonstrated the possibility of Q-switching [Barnes_89]. Sensitising with Yb was mainly considered for avoiding the ESA problem associated with the 800 nm pumping of Er.

After a one-year-gap, at the end of 1989, fabrication of the ND6xx series started. This time the aluminium concentration was reduced and the phosphorus concentration was greatly increased. Time was spent adjusting the process, particularly the deposition parameters. This approach led to the highly efficient ND715, and the subsequent fibres were fabricated from the same host to reproduce its performances. At the same time, Taylor fabricated phosphate core fibres, based on commercially available bulk glasses Schott SEP4 (core) / APC7 (clad), by the rod-in-tube technique. The two types of fibres were compared and from absorption & fluorescence spectra and lasing performances the phosphosilicate fibres made by MCVD were seen to mimic the phosphate core fibres [Townsend_91].

The availability of an highly efficient Er/Yb fibre motivated a lot of device work. The new pumping schemes offered by Yb sensitisation were attractive for power amplification. The first Er/Yb fibre amplifier was demonstrated in 1991 [Grubb_91]. Grubb used a miniature Nd:YAG rod pumped by AlGaAs diode arrays, emitting at 800 nm, as a brightness converter. Minelly demonstrated another tandem pumping scheme based on a double-cladding Nd fibre, pumped by a multi-stripe diode emitting at 800 nm [Minelly_92]. Later, the development of high power diode arrays emitting at 962 nm allowed direct pumping into the cladding of an Er/Yb fibre coated with low index silicone [Minelly_92']. Direct pumping of the fibre, as opposed to tandem pumping, increased optical efficiency and device compactness.

Lincoln carried out spectroscopic measurements in the ND5xx and ND7xx series. Results are summarised in [Lincoln_93]. One of the measurements was aimed at comparing the rate of multiphonon decay from the $^4I_{11/2}$ level of Er. This parameter is known to be crucial for the net energy transfer, as explained in the next chapter, but could not be measured directly, because the fluorescence from the $^4I_{11/2}$ level of Er could not be distinguished from the fluorescence of the $^4F_{5/2}$ level of Yb. It was proposed instead to measure the decay from the $^4S_{3/2}$ level, using an argon laser to excite the Er. This decay is also dominated by phonon emission. Two sets of results emerged from this measurement: the ND5xx fibres had a $^4S_{3/2}$

lifetime of around 1.2μs , whereas the ND7xx fibres had a lifetime of around 0.4μs. Lincoln also showed that the decay from the ND5xx fibres was noticeably less single-exponential than the decay from the ND7xx fibres. Lincoln interpreted the results in terms of preferred and available sites for the rare-earths in the two different hosts. He also measured the Raman peak ratio $R_{P=O}$, defined in §5.2, which increases with the number of high phonon energy P=O bonds, and saw no correlation with the P_2O_5 content. However, he observed that $R_{P=O}$ increased with decreasing fluorescence linewidth, i.e., with decreasing aluminium content. From this study of the ND5xx and ND7xx fibres, it was concluded that although incorporation of aluminium offers several advantages, it reduces the coupling of the rare-earths to the high phonon energy P=O bonds.

1.5 Motivations

In this section, I wish to give a short overview of the technological interest of the devices based on Er - Yb codoped fibres, and to stress the relevance of each project. The details of the most recent devices will be described in chapter 6.

Low power EDFAs are now well established in long haul telecommunication. Following long-haul telecommunications the second key application will be in video and data distribution in local-area networks. EDFAs capable of high output powers (>20 dBm) will be needed to compensate for splitting losses incurred in emerging large-scale subscriber distribution networks and in analogue transmission of multiple TV channels. The search for EDFAs with high output power depends largely upon the availability of a sufficiently powerful and practical pump source. The approach adopted by our sponsor, Amoco Inc., was to pump Er/Yb fibres at the long edge of the Yb absorption around 1.05 μm, with their miniature Nd:YAG or Nd:YLF lasers. These lasers utilised high reliability, low-brightness AlGaAs pump sources, and were readily scalable to powers in excess of 1 W. Although this approach proved very successful and output powers approaching 30 dBm were demonstrated, the pump source dominated the price of the amplifier.

Direct pumping from laser diodes is a much cheaper approach. Newly available high power diode arrays at 980 nm are now considered the way forward for high power amplifiers. This approach requires the development of an all glass cladding pumped fibre, presented in this thesis, to efficiently launch the pump light. In this waveguide geometry ytterbium sensitisation is essential to maintain a high enough pump rate.

With the advent of low-cost, high power diode arrays, new applications are also possible for fibre lasers. The low power end of the material processing market now appears within reach. To seize this opportunity the Department of Trade and Industry (DTI) decided to launch HIRAFS (HIgh RAdiance FIbre Sources), a new two years project starting in January 1996. This project links the University of Southampton, in charge of the fibre fabrication and laser design, with GMMT Caswell (GEC Marconi Material Technology), in charge of developing high power diode arrays at 975 nm, and DIOMED, a company established in the medical laser market with expertise in beam stacking techniques for broadstripe diodes. We aim for a practical fibre laser emitting around 1550 nm capable of delivering 10 W CW or 10 mJ in pulsed mode. Meeting these target specifications should allow fibre lasers to enter the medical laser and the laser marking markets.

Ytterbium codoping of erbium fibres is not only useful to scale up the power of devices operating at 1.5 μm. It is also a way to obtain narrow linewidth, stable sources for applications in sensing, spectroscopy and telecommunications. The required single frequency operation is best achieved in fibre Distributed FeedBack (DFB) lasers. For the linewidth of the gratings achieved so far, it is necessary to use only a few centimetres of gain medium to maintain the single frequency operation. Ytterbium codoping comes into play to allow a large absorption of the pump power in these short fibre length.

Chapter 2

BACKGROUND

2.1 The rare-earth elements

The rare-earths are divided into two groups of 14 elements each. The lanthanides, listed in table 2.1, are characterised by the filling of the 4f shell, whereas the actinides are characterised by the filling of the 5f shell. Only the lanthanides are considered here as all of the actinides are radioactive. Among the lanthanides only promethium is unstable (its half-life is less than 20 years). In condensed matter the trivalent (3+) level of ionization is the most stable for lanthanide ions. Ionisation preferentially removes the 6s and 5d electrons, and the electronic configuration for these ions is that of the xenon structure plus a number of 4f electrons shown in table 2.1.

Name	Lanthanum	Cerium	Praseodymium	Neodymium	Promethium	Samarium	Europium	Gadolinium	Terbium	Dysprosium	Holmium	Erbium	Thulium	Ytterbium	Lutetium
Atomic mass	138.9	140.1	140.9	144.2	146.9	150.4	152.0	157.2	158.9	162.5	164.9	167.3	168.9	173.0	175
Symbol	La	Ce	Pr	Nd	Pm	Sm	Eu	Gd	Tb	Dy	Ho	Er	Tm	Yb	Lu
Atomic #	57	58	59	60	61	62	63	64	65	66	67	68	69	70	71
RE:[Xe] $6s^2$ ...	5d	4f 5d	$4f^3$	$4f^4$	$4f^5$	$4f^6$	$4f^7$	$4f^7$ 5d	$4f^9$	$4f^{10}$	$4f^{11}$	$4f^{12}$	$4f^{13}$	$4f^{14}$	$4f^{14}$ 5d
RE^{3+}: [Xe] ...	-	$4f^1$	$4f^2$	$4f^3$	$4f^4$	$4f^5$	$4f^6$	$4f^7$	$4f^8$	$4f^9$	$4f^{10}$	$4f^{11}$	$4f^{12}$	$4f^{13}$	$4f^{14}$

Table 2.1 The Lanthanides

One of the basic results of the theory of quantum mechanics is that each physical system can be found, upon measurement, in only one of a predetermined set of energetic states - the so-called eigenstates of the system. With each of these states we associate an energy that corresponds to the total energy of the system when occupying that state. The energy diagrams

can be found in [Macfarlane_87]. The observed infrared and visible optical spectra of the trivalent rare-earth ions are a consequence of transitions between the 4f states.

From the perspective of optical and electronic properties, the most important feature of the rare-earths is the lanthanide contraction. This is a consequence of imperfect screening by the 4f electrons, which leads to an increase in effective nuclear charge as the atomic number increases in the lanthanide series. As a result, the 4f electrons become increasingly more tightly bound with increasing Z. The rare-earth ion size consequently decreases from about 1.20 Å to 0.85 Å from lanthanum to lutetium. The 4f wave functions for La (Z=57) lie outside the xenon shell, but by neodymium (Z=60) they have contracted so much that the maximum lies within the $5s^2 5p^6$ closed shells of the xenon structure. The resulting shielding makes the transitions only weakly sensitive to the type of host and causes the 4f → 4f transitions of rare-earth solid state material to exhibit relatively sharp lines, as compared to transition metals, for instance. Another consequence is that the excited states are only weakly coupled to lattice phonons and experience weak nonradiative relaxation so that radiative transitions can be highly efficient.

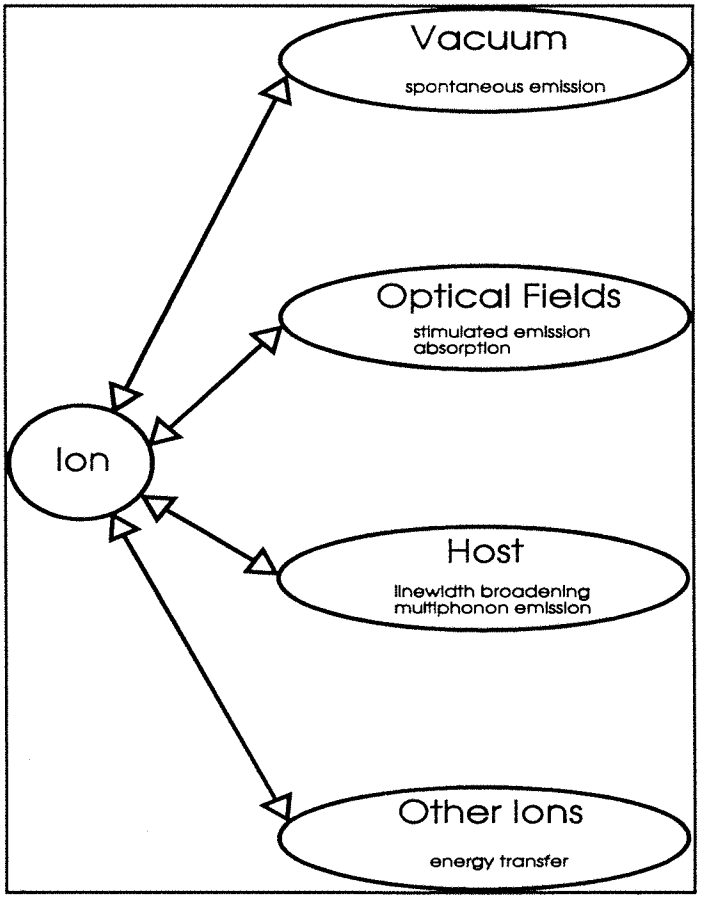

Fig. 2.1 Interactions between a rare-earth ion and its environment

Fig. 2.1 shows the different interactions of a rare-earth ion with its environment. The rare-earth in vacuum can spontaneously deexcite by emitting a photon. The probability of this event is given by the Einstein A coefficient [Loudon_83].

In the presence of an electromagnetic field, interaction between the electron charge and the electric field or between the electron spin and the magnetic field can cause transitions by multipolar interactions, the so called absorption and stimulated emission. The probabilities of these events are equal and are given by the Einstein B coefficient. The photon emitted by stimulated emission is coherent with the incident photon. Stimulated emission can lead to amplification if population inversion of the levels of a transition is achieved.

In addition to changing their electronic state through interaction with the electromagnetic field, rare-earth ions can undergo transitions as the result of their interaction with vibrations of the host material. The resulting multiphonon decay is important in the Yb : Er system as is explained in §2.4. The host is an important factor, affecting not only the multiphonon decay but also the shape of the absorption and emission spectra. The crystal field lifts the J degeneracy of a level and determines the position of the Stark components of a multiplet. The host also affects the free ion by the mechanism of covalent bonding, the sharing of electrons between the rare-earth ion and its ligands, which partially screens the 4f electrons and reduces the effective nuclear charge. This mechanism is referred to as the nephelauxetic effect. It manifests itself as a rescaling of the entire energy level diagram. For glasses this translates into host-to-host shifts up to a few percent in the separation between the levels. More covalent glasses emit and absorb at longer wavelengths than the predominantly ionic glasses.

The energy transfer mechanism is the basis of the work presented in this thesis and it will be introduced in the following section.

2.2 Energy transfer

We saw that the rare-earth ions are unique spectroscopically because the optically active transitions within the $4f^n$ core are well shielded from outside influences. There is, however, possibility of energy transfer which relies upon the small interactions between rare-earth ions (essentially electron exchange or Coulomb interactions). Energy from a donor ion - also called sensitiser - is transferred to a nearby acceptor ion - also called activator - which can be of the

same species as the donor, as for instance in the detrimental concentration quenching of Er^{3+} amplifiers (discussed in §4.5), or of another species, as is the case in codoped systems.

2.2.1 Principles of energy transfer

The mathematics of energy transfer can be complicated and is extensively exposed in the references of this section. In the following we wish to present only the underlying physics.

Nonradiative energy transfers affect the excited state of the donor, changing the lifetime and the intensity of the emission. The transfer probability depends strongly on the distance R between donor and acceptor and is given by :

$W_{DA} = x / R^s$ s = 6 for dipole-dipole interaction (2-1)

s = 8 for dipole-quadrupole interaction

s = 10 for quadrupole-quadrupole interaction

$= y\, e^{-R/L}$ for exchange interaction (L is the effective average Bohr radius)

$$\textit{where } x \textit{ and } y \textit{ are proportional to } \int_0^\infty f_d(\nu)\, F_a(\nu)\, d\nu$$

$f_d(\nu)$ is the donor emission spectrum

$F_a(\nu)$ is the acceptor absorption spectrum

If we consider two ions with excited states of different energies, the rate of energy transfer should drop to zero when the overlap integral vanishes. However, it is found experimentally that energy transfer takes place without overlap provided that the overall energy conservation is maintained by production or annihilation of phonons. The energy transfer rate shows an inverse exponential dependence on the energy mismatch.

Up to this point we have been dealing with the microscopic case of two ions interacting with one another. Experiments in energy transfer generally do not measure the transfer between isolated pairs of ions. To discuss the case of macroscopic samples with many ions and to obtain link with experimental facts, a statistical analysis of the energy transfers is necessary. If there are N_a acceptor ions in a volume V around the donor, the observed decay of donor fluorescence will be multi-exponential because of contributions from all donor-acceptor pairs

with different values of R. If ρ(R) expresses the probability distribution of different radial separations, one can write the ensemble averaged time dependence resulting from pulsed excitation as :

$$\phi(t) = e^{-t/\tau_0} \lim_{\substack{N_a \to \infty \\ V \to \infty}} \left[\int_V e^{-W_{DA}(R)\, t} \rho(R)\, dV \right]^{N_a} \qquad (2\text{-}2)$$

where the limits are taken in such a way that the ratio N_a / V becomes the acceptor concentration. τ_0 is the intrinsic lifetime of the donor fluorescence which competes with the energy transfer. Much work has been devoted to determining the expression of $\phi(t)$ for different interaction mechanisms and acceptor spatial distributions [Inokuti_65], [Wright_76], [Tonooka_91], [Rotman_96].

The donor fluorescence time dependence described by any model of the interaction is controlled by the more rapid depletion of the closely-spaced pairs. If the donor concentration is low, the excitations will fade out in the same site where they appeared. Increasing the donor concentration results in a more active transfer of excitation between the donors and when excitation diffusion occurs, the transfer is accelerated. This is the so called migration-accelerated quenching regime described in detail in [Gapontsev_89]. The long transfer time donor-acceptor pairs lose excitation due to migration towards the most effective trapping sites. In the limit of rapid excitation diffusion the kinetic of the decay is governed by the fastest donor-acceptor pair transfer and becomes exponential [Yokota_67].

2.2.2 The Erbium : Ytterbium system

Fig. 2.2 illustrates schematically the mechanism leading to emission at 1.54μm in an Er/Yb doped fibre: Absorption of a pump photon (800-1070nm) by an Yb^{3+} ion promotes an electron from the $^2F_{7/2}$ ground state level to the $^2F_{5/2}$ manifold, nonradiative energy transfer from this level to the $^4I_{11/2}$ level of Er^{3+}occurs, nonradiative decay to the upper lasing level $I^4_{13/2}$ follows, and fluorescence to the ground state, centered at 1.54μm, is observed.

The mechanism described above is ideal. In fact, there are many possible loss mechanisms that we will investagate in chapter 4. One of them, which dictates the choice of the host, is presented in the following section.

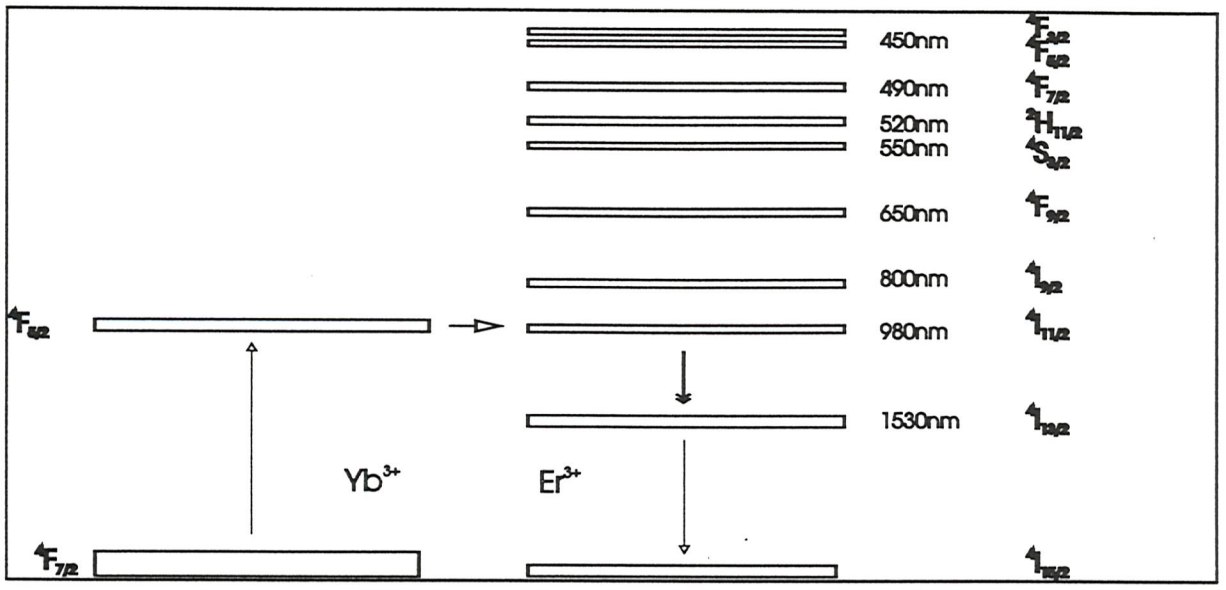

Fig. 2.2 Er/Yb Energy diagrams (after [Miniscalco_91]) & transfer mechanism

2.3 The importance of the host' s Maximum Vibrational Energy (MVE)

If energy can be tranferred forwards (from ytterbium to erbium) it can equally be transferred backwards, i.e. $[(Er^{3+},{}^4I_{11/2});(Yb^{3+},{}^2F_{7/2})] \rightarrow [(Er^{3+},{}^4I_{15/2});(Yb^{3+},{}^2F_{5/2})]$. We will see that if the MVE of the host is chosen adequately the effect of the back transfer can be minimised. We will first describe how the nonradiative decay rate depends on the MVE in different glasses.

2.3.1 The nonradiative decay rate

The nonradiative decay rate, W_{NR}, is due to multi-phonon emission and has been shown to depend, in glasses as well as in crystals, on the MVE, $h\nu_p^{max}$, as follows [Van Dijk_83]:

$$W_{NR} = B^* \, e^{-\alpha(\Delta E - 2h\nu_p^{max})} \qquad (2\text{-}3)$$

when the energy gap between the two levels of the transition, ΔE, is larger than twice the MVE, and where B^* and α are constants which vary only slightly from host to host, so that the host dependence is mainly contained in the MVE. The nonradiative decay rate contributes to the fluorescence decay rate of the excited rare-earth, W_F, governed by $W_F = W_R + W_{ET} + W_{NR}$, where the other contributions are W_R, the rate of radiative emission (spontaneous and stimulated), and W_{ET}, the rate of energy transfer to quenching centres.

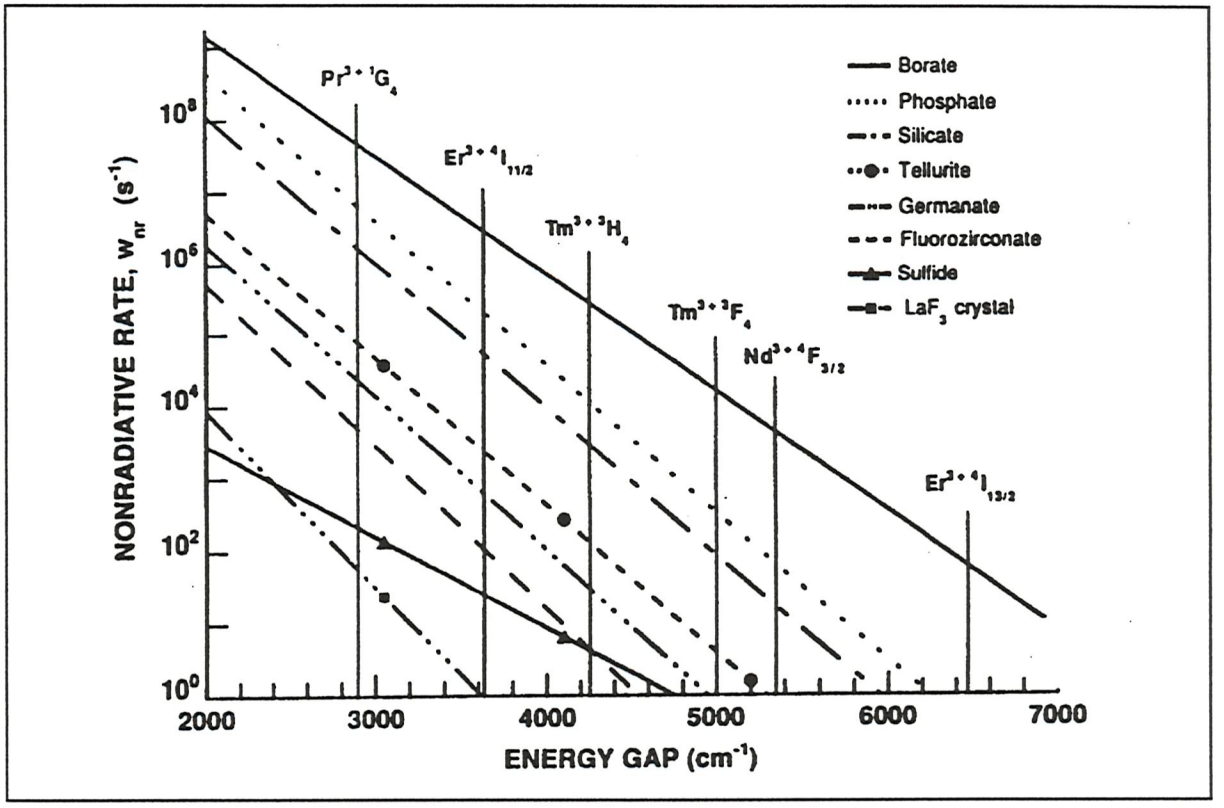

Fig. 2.3 Nonradiative relaxation rate as a function of the energy gap for the indicated glasses (after [Reisfeld_87])

Fig. 2.3 illustrates the host dependence of W_{NR}. As predicted from equation (2-3), W_{NR} increases with the maximum energy of the host given in Table 2.2, i.e. in the set germanate-silicate-phosphate-borate glasses. It should be noted that Table 2.2 gives only trends as the values presented here depend on the exact composition and on the glass preparation.

Glass	Parameters for eqn (2-3) [1]			Transitions in Er^{3+}		
	B^*	α	$h\nu_p^{max}$	$^4I_{11/2} \rightarrow {}^4I_{13/2}$		$^4I_{13/2} \rightarrow {}^4I_{15/2}$
	s^{-1}	10^{-3} cm	cm^{-1}	W_{NR} [2]	W_{NR} [1]	W_{NR} [1]
Germanate	$10^{6.74}$	4.9	900	$2\ 10^4$	810	$5.5\ 10^{-4}$
Silicate	$10^{7.89}$	4.7	1100	10^5	$1.1\ 10^5$	0.13
Phosphate	$10^{7.88}$	4.7	1200	10^6	$2.7\ 10^5$	0.32
Borate	$10^{7.89}$	3.8	1400	10^7	$3.7\ 10^6$	61

Table 2.2 Nonradiative relaxation rate in s^{-1} for the indicated glasses.
Energy gaps ΔE = 3600 cm^{-1} for $^4I_{11/2} \rightarrow {}^4I_{13/2}$ & 6500 cm^{-1} for $^4I_{13/2} \rightarrow {}^4I_{15/2}$,
[1] = [Reisfeld_87], [2] = [Gapontsev_82]

2.3.2 Role of the erbium $^4I_{11/2} \rightarrow {}^4I_{13/2}$ multiphonon decay rate

Artemev has experimentally shown that only phosphate and borate glasses have a high enough MVE to allow sufficient accumulation in the Er lasing level, whereas lithium silicate and germanate glasses are plagued by back-transfer [Artemev_81].

This can be explained by a model including the effect of the back transfer of energy (see appendix 1 and chapter 6 for the description of the model). Fig. 2.4 shows the results of a Nd : YAG pumped Er : Yb amplifier simulation. We plotted the excited ion populations as a function of length. Three different hosts with widely differing $^4I_{11/2} \rightarrow {}^4I_{13/2}$ nonradiative decay rates, W_{NR}, (taken from Table 2.2, reference [2]) are compared. All the other parameters are taken as identical. The launched pump power is chosen to be 20 mW and the small signal back transfer time is 15 µs.

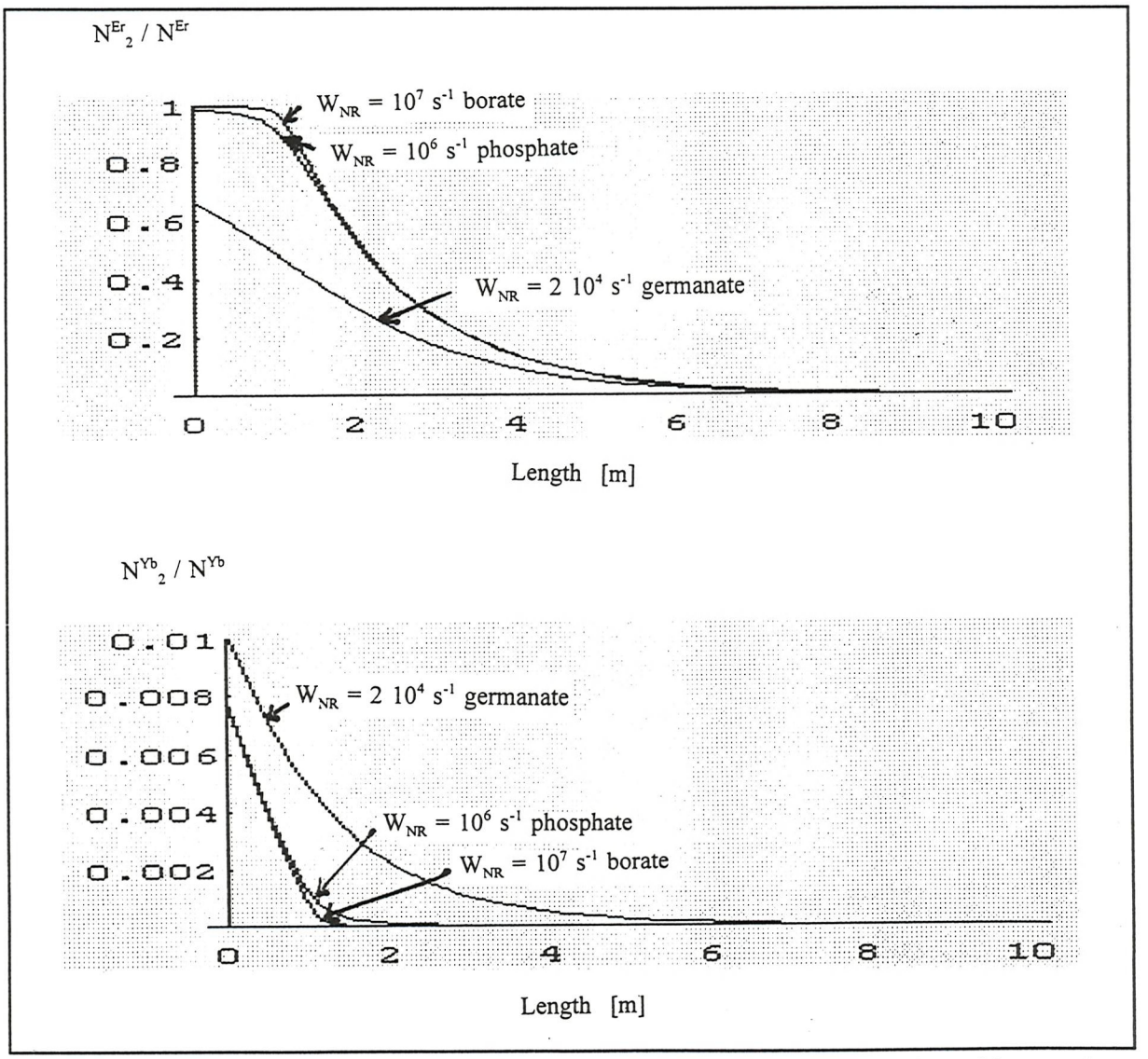

Fig. 2.4 Simulation of the role of the nonradiative decay rate. Proportion of inverted erbium and ytterbium ions vs length in germanate, phosphate and borate glasses.

We see that for the germanate glass the desired accumulation of ions in the erbium metastable state is reduced compared to the case of phosphate or borate glasses. Varying the back transfer rate, W_{BT} ,this 'impeded accumulation of energy' was symptomatic of the situation $W_{NR} < W_{BT}$. In Fig. 2.4 we also observe that the more significant effect of the back transfer in the germanate glass leads to a higher excited ytterbium ion population. This means that the ytterbium absorption will be more easily bleached. Eventually the Yb^{3+} ions will start lasing as a quasi 4-level system instead of transferring their energy nonradiatively to the erbium ions. In summary, the MVE of the host should be chosen sufficiently high to obtain a rapid depopulation of the $^4I_{11/2}$ level, to leave no time for the back transfer mechanism to occur.

At the same time, the MVE should not be so high as to reduce the lifetime of the erbium metastable level. Note that this effect is not accounted for in the simulation shown in Fig. 2.4 since this parameter has been chosen to be the same (10 ms) in all the glasses. Despite its high energy transfer, a borate glass did not produce efficient lasers [Gapontsev_82]. From table 2.2, we see that for a borate glass, the multiphonon emission reduces significantly the lifetime of the $^4I_{13/2}$ metastable level, and thus reduces the wanted accumulation of energy in this level.

In conclusion, energy transfer and radiative efficiency impose stringent conditions on the MVE, i.e., on the choice of the host glass. To date, only glasses containing phosphorus have been proven to satisfy these conditions.

2.4 Phosphosilicate glasses

Vitreous silica has exceptional suitability for optical waveguides. Its low thermal expansion, high intrinsic strength, exceptional durability, low absorption and scattering losses in the visible and near infrared make silica a material as ideally suited to photonics as its parent silicon is to electronics. To ensure compatibility with the existing fibre network it is necessary that our amplifying fibres be silica based. Another advantage of chosing a silica based fibre is that it can be produced by the well established Modified Chemical Vapour Deposition (MCVD) fabrication technique.

As stressed in the previous section, the presence of phosphorus in the active region is essential to the efficient energy transfer needed in our codoped fibres. Incorporation of phosphorus in the core of silica based fibres has been investigated since the beginning of the MCVD

technique [Payne_74], [Gambling_76]. The maximum concentration of phosphorus which is possible to combine with SiO_2 is limited by the maximum mismatch of temperature coefficient of expansion between the core and the silica supporting tube. However, this has been estimated to be at least 25 mol% [Payne_74]. A more critical factor which limits the phosphorus incorporation is its high volatility at the temperatures needed for collapsing the preform tube processed by MCVD. A study of the fusion temperature of SiO_2-P_2O_5 binary glasses also shows that the processing temperature of silica is much reduced by incorporation of phosphorus [Hammond_78].

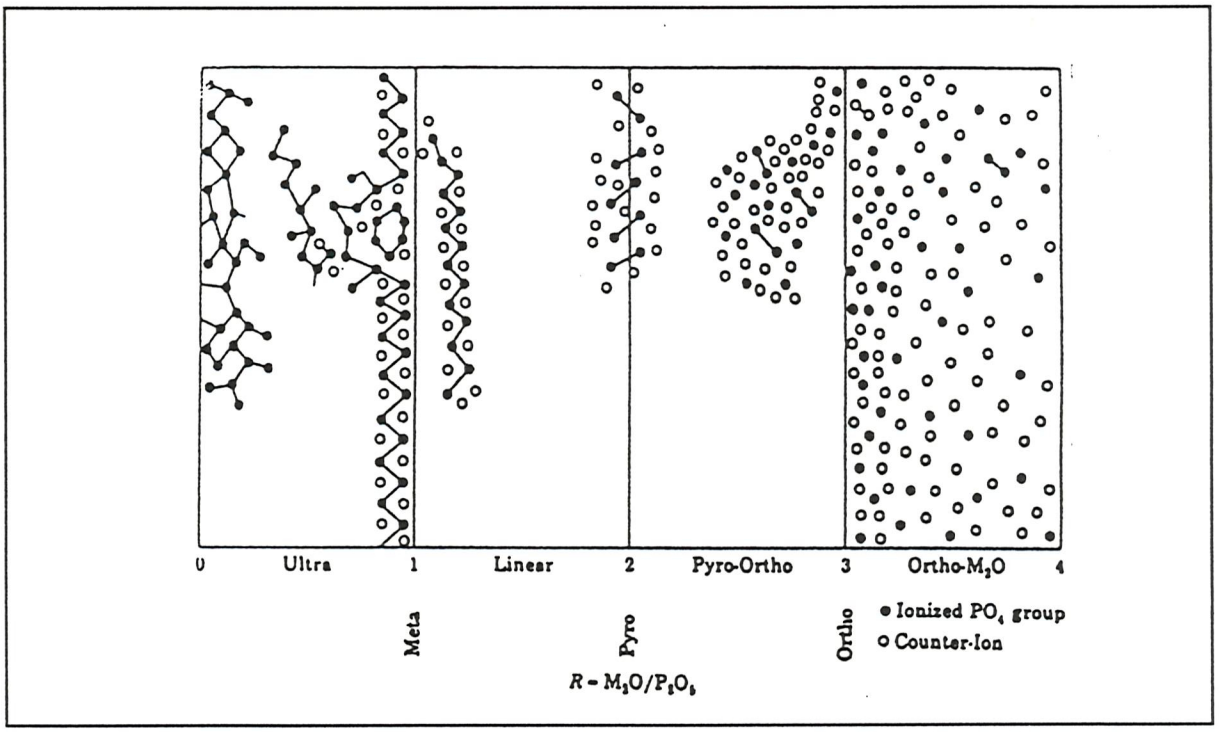

Fig 2.5 Depolymerisation of the phosphate glass network with addition of a modifier (after [Martin_91])

The very different properties of phosphate and silicate glasses can be explained by looking at the network structures. These differences are a consequence of the more open network of the phosphate glass. Phosphorus is four-coordinated in a phosphate glass and forms tetrahedral units as does silicon in a silica glass, but one of the four oxygens is non-bridging and is double-bonded to phosphorus. Furthermore, when modifiers are added the phosphate network depolymerises, creating even more non-bridging oxygens (NBOs) . This behaviour is illustrated in Fig.2.5. When the number of bridging oxygens in the PO_4 units decreases, the negative charge of the phosphate unit increases. In order of increasing negative charge, the phosphate units are:

- the neutral "branching unit", with three bridging oxygens, noted Q^3;
- the "middle unit" -O-PO^-_2-O-, or metaphosphate unit, noted Q^2;

- the "end unit" -O-PO^{2-}_3 or pyrophosphate unit, noted Q^1 ;
- the "monomer" PO^{3-}_4 or orthophosphate unit, noted Q^0.

Evidence of the depolymerisation can be given by paper chromatography, ^{31}P MAS-NMR or Raman spectroscopy.

EXAFS studies show that rare-earth cations require the coordination of a high number of oxygen ions for screening their electric charge (see for instance [Marcus_91], [Gurman_92]). From crystal field considerations the ytterbium ion has been revealed to be six-fold coordinated in a phosphate glass [Robinson_70]. In the highly rigid network of silica, oxygen ions from NBOs are scarce and the rare-earths are not easily accommodated. On the other hand the high concentration of NBOs in the all phosphate glass structures allows large amounts of rare-earths to be incorporated. Fig. 2.6 shows how the phosphate glass structure evolves with increasing rare-earth modifier concentration. At first only a small part of the double bonded oxygens from the Q^3 units can find an adjacent modifier cation (noted Me^{v+}). The position of MeO_n units approach each other with increasing modifier content. Finally, both NBOs from a Q^2 unit can attach different MeO_n sites (Fig. 2.6 middle schematic). When the number of NBOs available per modifier decreases below the coordination number of the modifier, the structure has a new way of forming. In this configuration modifiers cluster to share NBOs and satisfy their coordination number. MeO_n units come into contact by corners, edges, possibly faces. The network appears as two interpenetrating patterns, a structure well known in silica glasses and characterised as the modifier random network introduced by Greaves [Greaves_85].

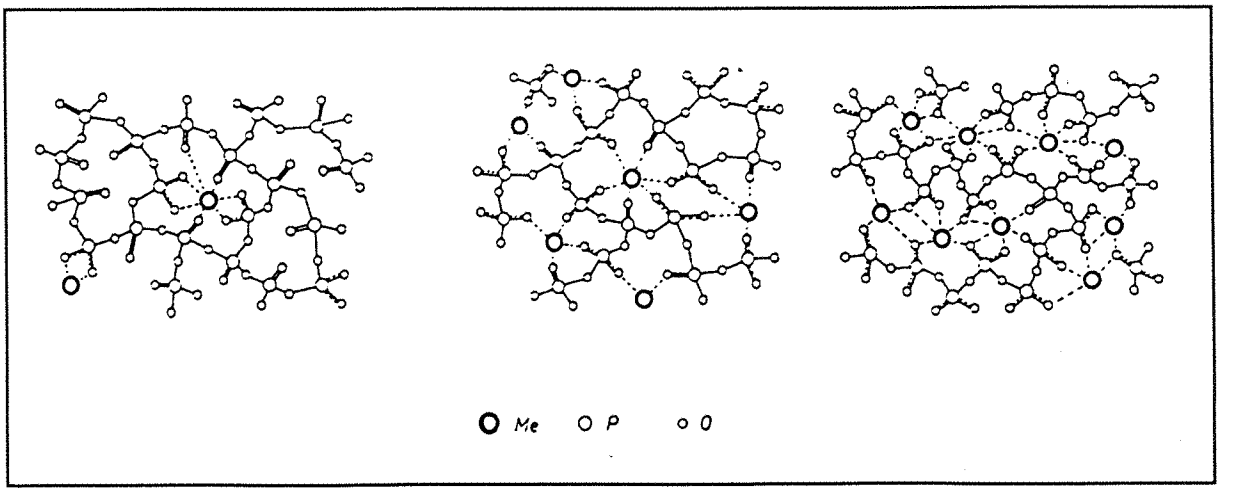

Fig. 2.6 Coordination of a rare-earth in a phosphate glass (after [Hoppe_96])

2.5 Doped fibres fabrication techniques

We used the MCVD technique to fabricate our fibres. We will assume that the reader is familiar with this technique (good reviews can be found in [Nagel_82] and [Meunier_88]). Unfortunately , rare-earth ions cannot be incorporated as easily as other codopants such as phosphorus, boron or germanium due to the absence of high vapour pressure precursors. Many MCVD compatible methods have been researched to incorporate rare-earths in silica based fibres. In [Vienne_94] we compared the merit of the dopant carrier chamber method [Poole_85], deposition of organo-metallic chelates [Tummineli_90], aerosols [Morse_91] and sol-gel dipcoating [Wu_93]. It is now clear that one method has emerged as the standard method for rare-earth doping. It is the solution doping technique, also known as the 'liquid phase technique'. A review of this method can be found in [Townsend_90] and necessary details will be given in chapter 3.

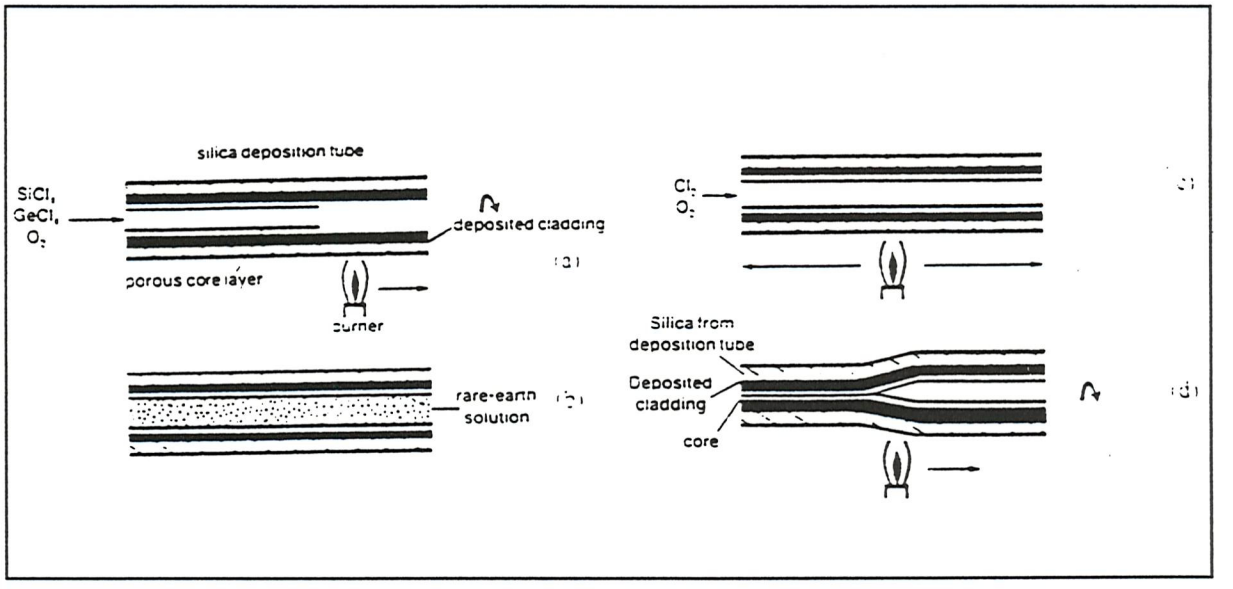

Fig 2.7 The solution doping technique (after [Ainslie_91])

Here we will just outline the method which is quite straightforward, as illustrated in Fig. 2.7. A cladding layer is deposited inside a substrate tube in the normal way, but the following core deposition is carried out at a lower temperature so that the layer is not fully sintered. The porous layer is then soaked in an aqueous or alchoholic solution of the rare-earth salts and allowed to impregnate the pores. This impregnated layer is dried and fused into a clear glassy layer and subsequently the tube is collapsed into a preform in the usual way.

Chapter 3

FABRICATION

3.0 Introduction

We saw in the previous chapter that phosphate glasses have a very low viscosity and a high volatility in the processing temperature range of silica. The fabrication process requires significant adaptation to cope with this mismatch. In fact we experienced in the past some difficulties in reproducing our own results. However, we have since progressed in our understanding of the process and are now able to show how major pitfalls can be avoided. In the first part of this chapter we will review each step of the process. Here we aim to give a sufficiently accurate description of the process to allow any interested fabricator to reproduce our results. So the emphasis is on practical guidelines. We also hope that the discussions will make this chapter interesting to anybody motivated by the study of glasses.

3.1 Fabrication technique

3.1.1 The choice of the fabrication technique

Three methods proved to be of interest for the fabrication of Er : Yb fibres. The first one is based on a soft glass approach. A mixture of powders containing more than 50 mol% of phosphate, the rare-earths dopants, and additional constituents are melted in a crucible to form a glass. It is then shaped into a rod and inserted in a cladding glass tube of slightly lower index and similar viscosity. This method allows for very high dopant concentrations which is particularly attractive for ultrashort lasers. Volatile components can also be incorporated in the glass. For example sodium has been incorporated in the batch to allow fabrication of planar waveguides by ion exchange. However, a major problem associated with this work was the imperfect dehydration of the glass. Moreover, the fact that the soft glass fibres cannot be spliced to the fibres deployed in networks represents a serious limitation.

In contrast, a technique based on the MCVD process produces network compatible fibres. The

phosphorus can be incorporated in the solution containing the rare-earths which is used to impregnate a silica frit. This is the phosphoric acid route which was extensively studied in [Carter_94]. It was concluded in this work that the technique lead to a poor mixing of the phosphate and silicate phases. This resulted background losses of at least 1 dB / m, a figure too high for many applications. We have produced four preforms by this technique which confirmed this result. The lowest loss that we obtained at 1200 nm was 0.62 dB / m.

The third technique, also based on the MCVD process, produces fibres with significantly lower background losses. It is this technique which will be presented in this chapter.

3.1.2 Preliminary stages

The availability of high quality tubing is crucial to the successful application of the MCVD process. We chose to use the Hereaus F300 synthetic silica tubes because they could be supplied with low impurities and tight geometrical tolerances. Synthetic silica is produced by the hydrolysis of silicon tetrachloride. The residual chlorine has the effect of slightly reducing the refractive index (compared to natural quartz), and to soften the glass [Glodis_94]. We indeed observed that synthetic silica tubes can be more rapidly collapsed than natural quartz tubes.

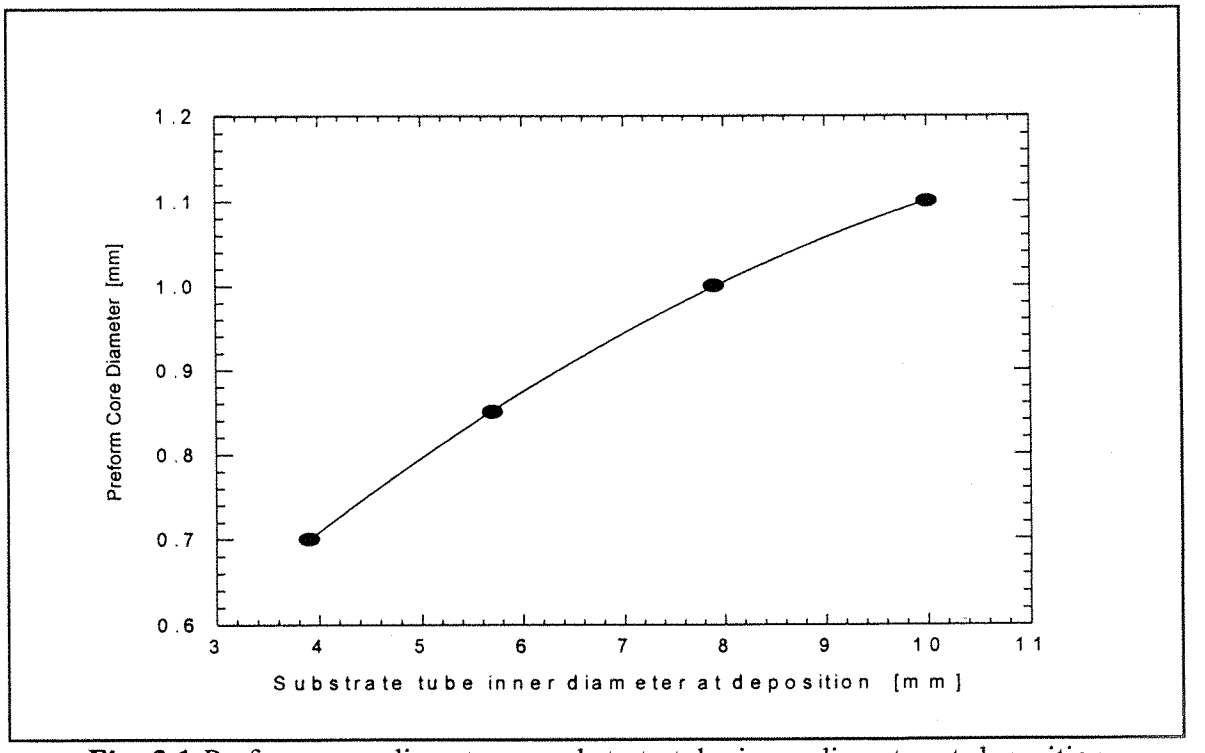

Fig. 3.1 Preform core diameter vs substrate tube inner diameter at deposition

Our standard tube has an inner diameter of 20 mm, an outside diameter of 25 mm, and is typically 50 cm long. It is joined as straight as possible on the glass lathe to avoid ellipticity developing during the process. We start by etching the inner surface of the tube with SF_6 to eliminate any surface impurity. We then deposit 5 to 10 silica buffer layers. The tube is subsequently heated to around 2000 °C so that its diameter decreases under the effect of surface tension and viscous flow. This is the so-called precollapse stage (the prefix 'pre' indicates that this operation takes place before the core deposition). Fig. 3.1 shows how the extent of the precollapse influences the core diameter. Other parameters which determine not only the core size but also the core composition are discussed below.

3.1.3 Core deposition

The core layer must remain porous after the deposition pass to allow for solution doping. For the deposition of silicate or germanosilicate porous layers the burner and the reactants are copropagating. It results in the burner passing over the soot which has accumulated downstream. The soot particles have a sufficiently high viscosity so that they do not fuse together and the porous layer 'survives' when the burner passes over.

On the other hand, we find that with a phosphorus content exceeding 5 mol% the phosphosilicate porous layer is sintered by the burner at the deposition pass. The problem is solved by translating the burner in the opposite direction to the reactants. With this backward deposition a porous layer with a high phosphorus content can be fabricated.

Fig. 3.2 shows the results of a study of the deposition position as a function of the deposition temperature. We checked that at low temperature the $POCl_3$ is much more efficiently oxidised than the $SiCl_4$. As the temperature increases the frit becomes thicker and appears whiter. The beginning of the deposition zone becomes more clearly defined and comes nearer to the burner. When the temperature increases further the beginning of the deposition zone is pushed further behind the burner because the temperature is high enough to sinter the frit near the burner. We chose to deposit at the temperature corresponding to the minimum in Fig. 3.2. This temperature is high enough so that both $POCl_3$ and $SiCl_4$ are oxidised and low enough to avoid significant sintering near the burner.

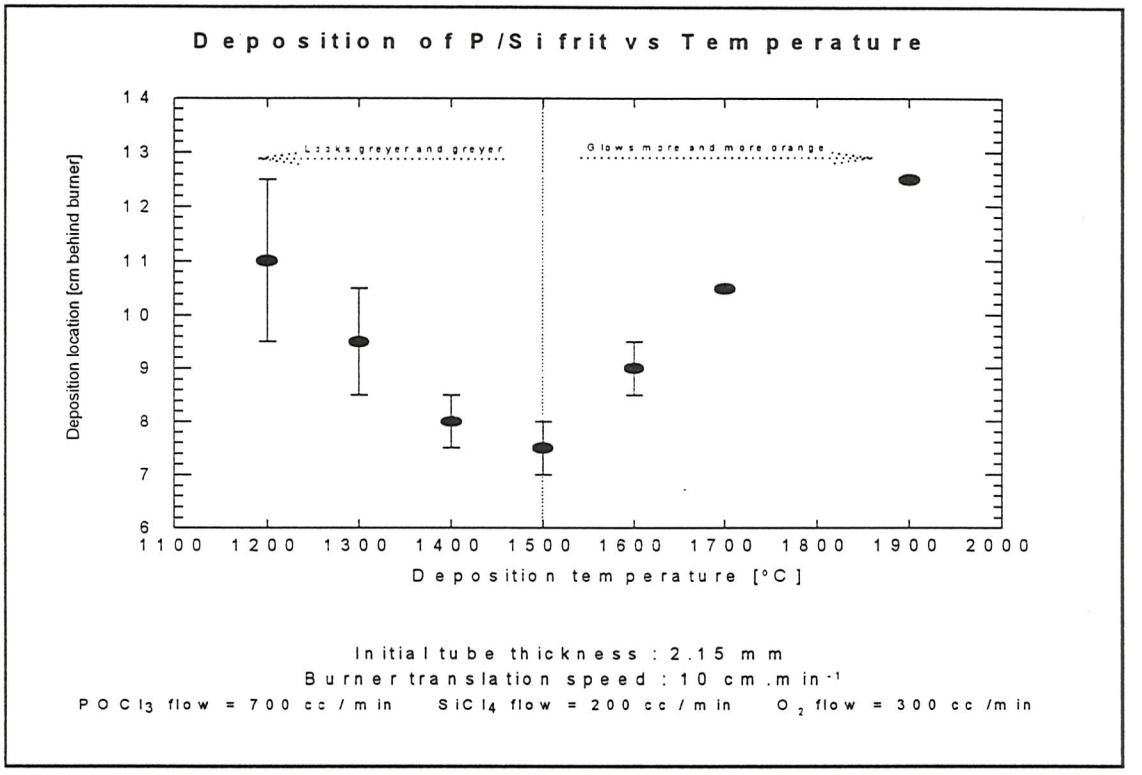

Fig. 3.2 Deposition position vs deposition temperature for a P/Si frit

The glass particles are mainly driven by their initial speed and the temperature gradient in the tube [Simpkins_79]. The thermophoretic force towards the tube wall is reduced if this wall is heated. The heating up of the wall behind the burner is much more significant in the backward than in the forward deposition. It explains why even at the minimum in Fig. 3.2 the deposition zone is located much further away from the burner than during forward deposition.

We now examine the role of the reactants flows on the refractive index and size of the core. We decide to fix the $POCl_3$ and O_2 flows to 1000 cc/min and 300 cc / min respectively and to vary the $SiCl_4$ flow. We see in Fig. 3.3 that when the silicon tetrachloride flow is very low (50 cc / min) the core diameter and the index difference between core and cladding are small. Indeed, the material deposited, being essentially a phosphate glass, is particularly prone to evaporation. The silica content must be increased to retain the phosphorus during the processing of the preform. With increasing silicon tetrachloride flow, the refractive index increases to a maximum of 6.5 10^{-3} and then decreases as the proportion of silica in the core increases. The core size increases with increasing silicon tetrachloride flow as more material, and a less volatile material, is deposited. From this study we chose to operate with a $SiCl_4$ flow of 200 cc / min to maximise the refractive index difference, and so as to maximise phosphorus content.

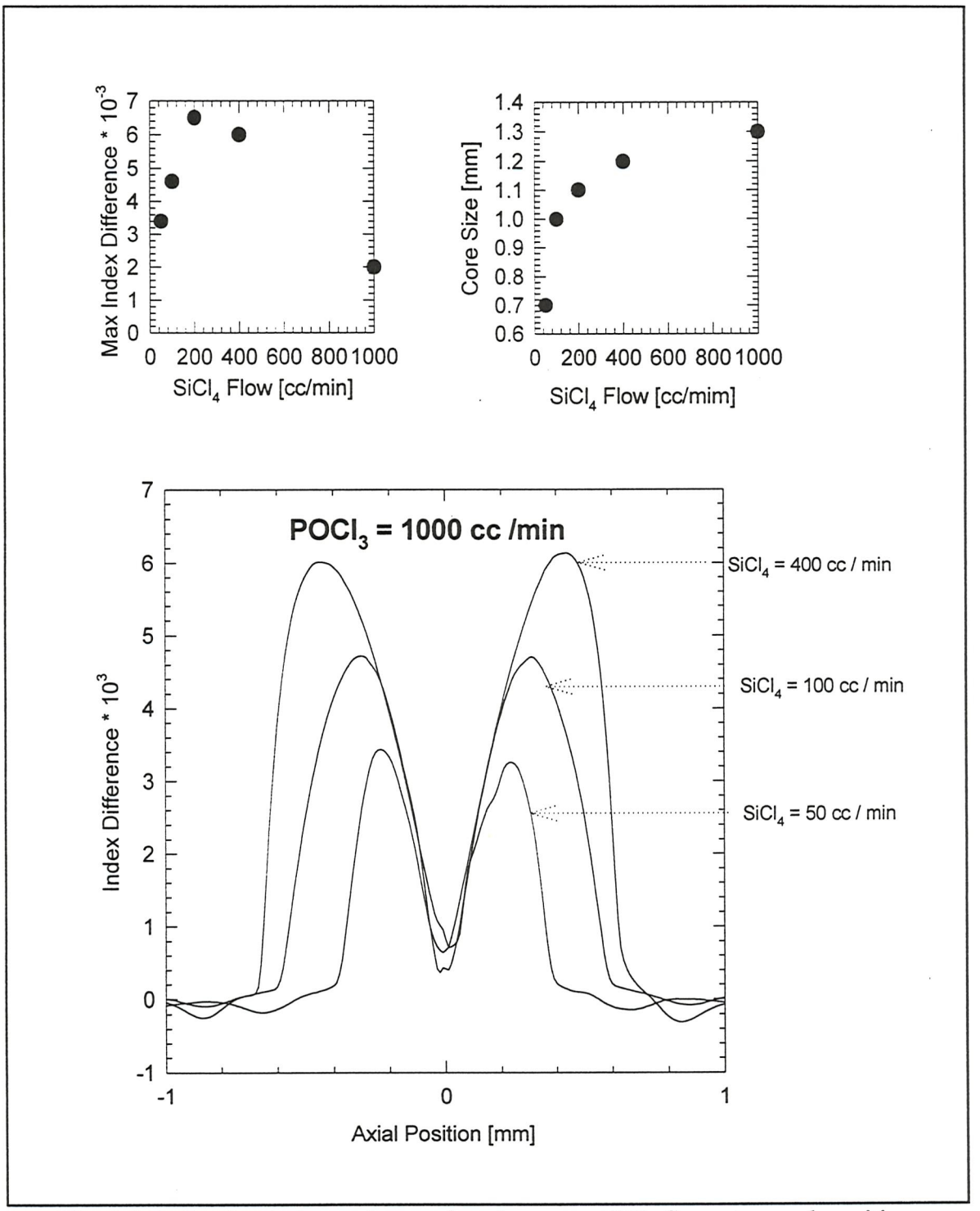

Fig. 3.3 Refractive index and core size change vs $SiCl_4$ flow at core deposition. Measurements were made with a York P104 refractive index profiler

3.1.4 The presintering pass

We explained above that the burner should not pass over the phosphosilicate frit at the deposition pass to avoid sintering it. But if we immerse the frit produced by backward deposition in the doping solution, it peels off rapidly. The glass particles float in the solution instead of sticking to the tube wall. In an attempt to minimise the damage to the frit we tried to immerse only a few centimeters of the frit and to let the solution diffuse upwards. The diffusion was very slow (12 hours / 40 cm) and more critically, the frit was again damaged at the end of the diffusion.

We found that the only way to preserve an homogeneous frit was to densify it prior to immersion. This is done by the so-called presintering pass. The burner is quickly passed over the preform tube after the deposition to partially sinter the frit. Fig. 3.4 shows the effect of the presintering temperature on the 'sponge' structure of the frit. With increasing temperatures the number of pores decreases as lumps of glass are fused together. The open network contracts under the effect of viscous flow and surface energy reduction (see [Scherrer_77] for a model of this behaviour). This decreases the surface area and increases the density of the frit.

Fig. 3.5 shows that the dopant incorporation decreases with increasing presintering temperature. This can be understood by the reduction of area at the glass - solution interface with increasing temperature that we have observed in Fig. 3.4. We also see that the detrimental hydroxyl contamination is associated with too low a presintering temperature. This is probably due to partial fusing when drying the preform with the burner. The fine porous network associated with low presintering temperatures is easily fused and water can be trapped at the first pass of the drying process.

During the test on the role of aluminium presented in chapter 5, we noticed some frit drop-off at immersion, except when the solution contained at least 3 g $AlCl_3$ / 200 ml H_2O. It was subsequently tested that the frit particles dissolved in HCl. We later produced aluminium free preforms and regulated the solution flow in an attempt to limit the damage to the frit when introducing or removing the solution. This approach was abandoned as it resulted in uneven redeposition of peeled off particles over the frit. We observed that when the presintering temperature was increased sufficiently to prevent frit particles from dropping off, the onset of devitrification had decreased from around 14 000 to 3000 ppm of rare-earths.

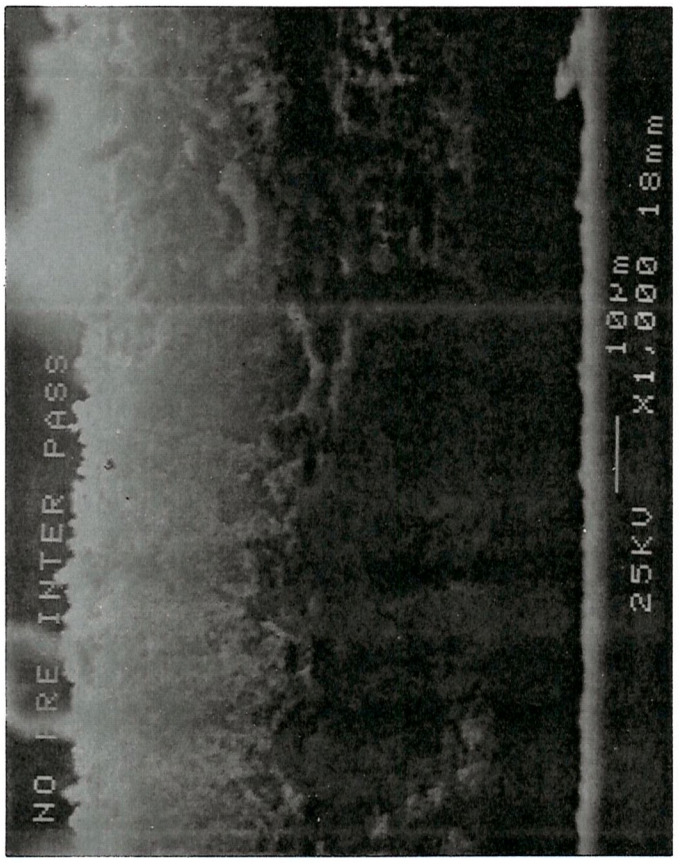

No presinter

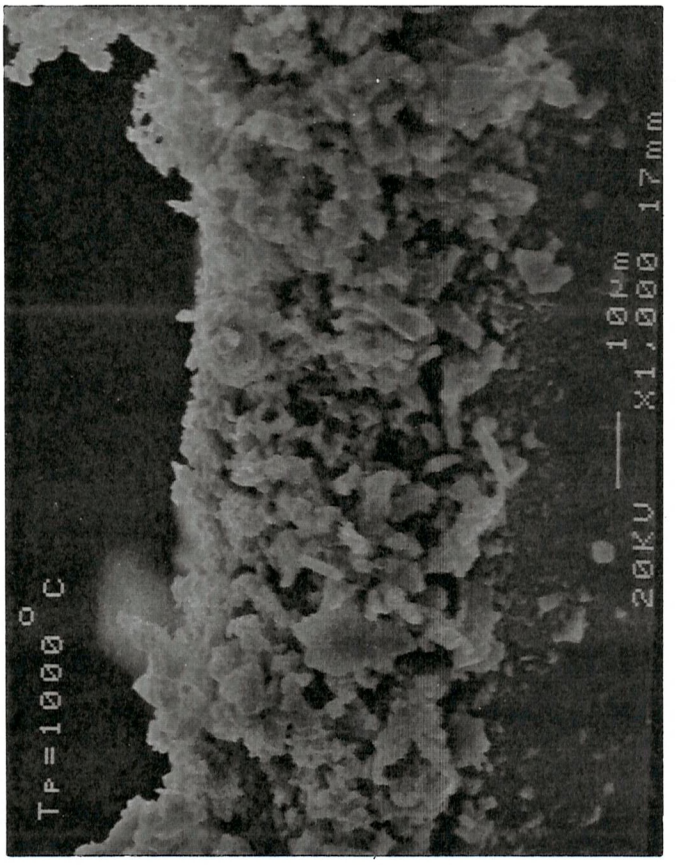

T_{pr} = 1000 °C

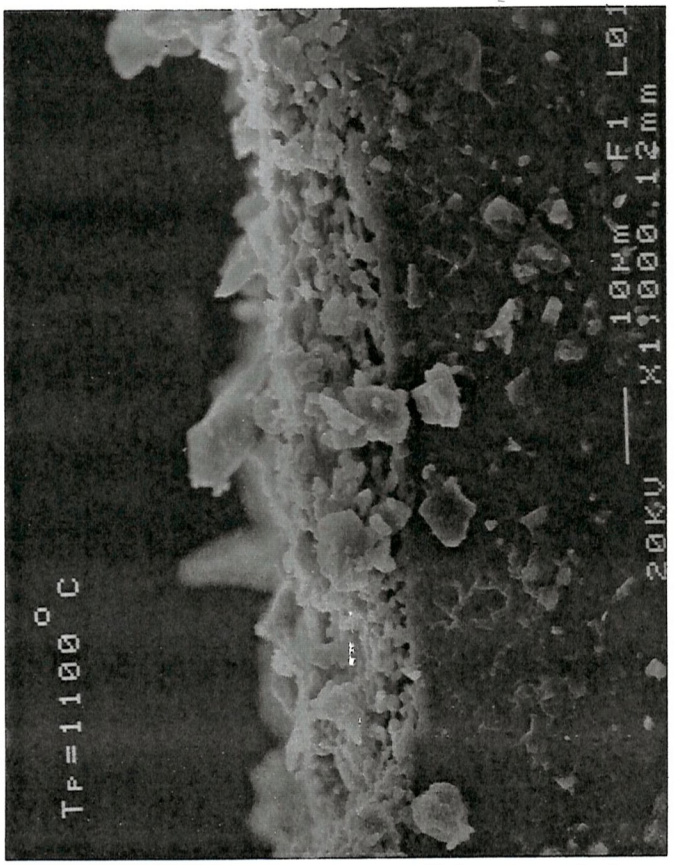

T_{pr} = 1100 °C

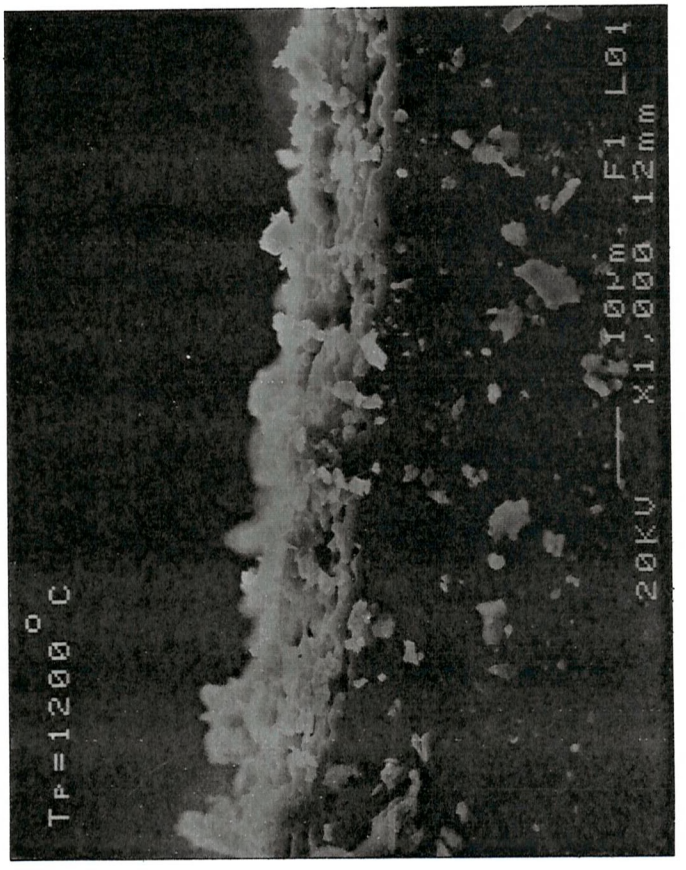

T_{pr} = 1200 °C

Fig 3.4a SEM picture of section of frits presintered at different temperatures

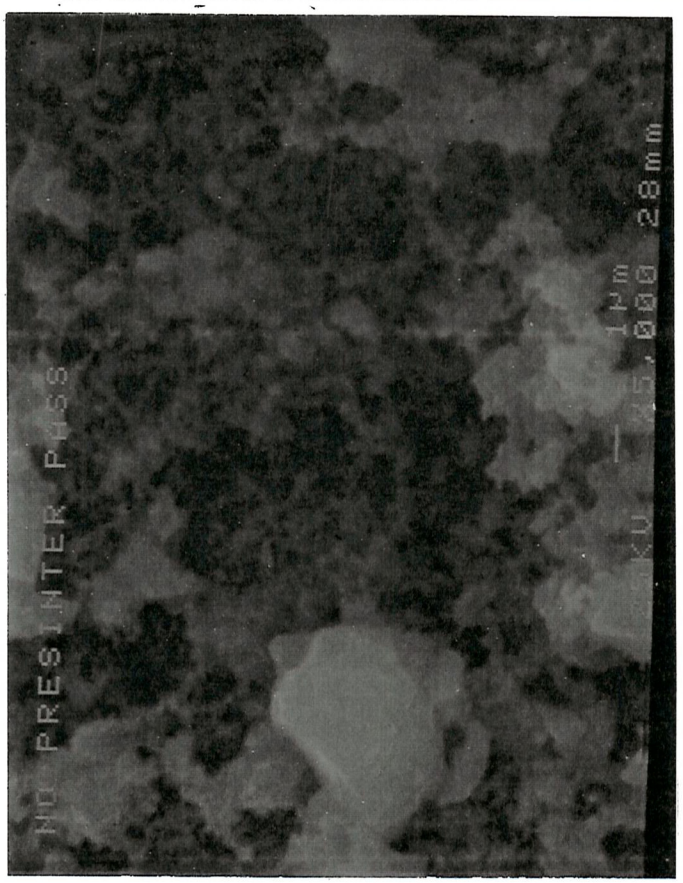

No presinter

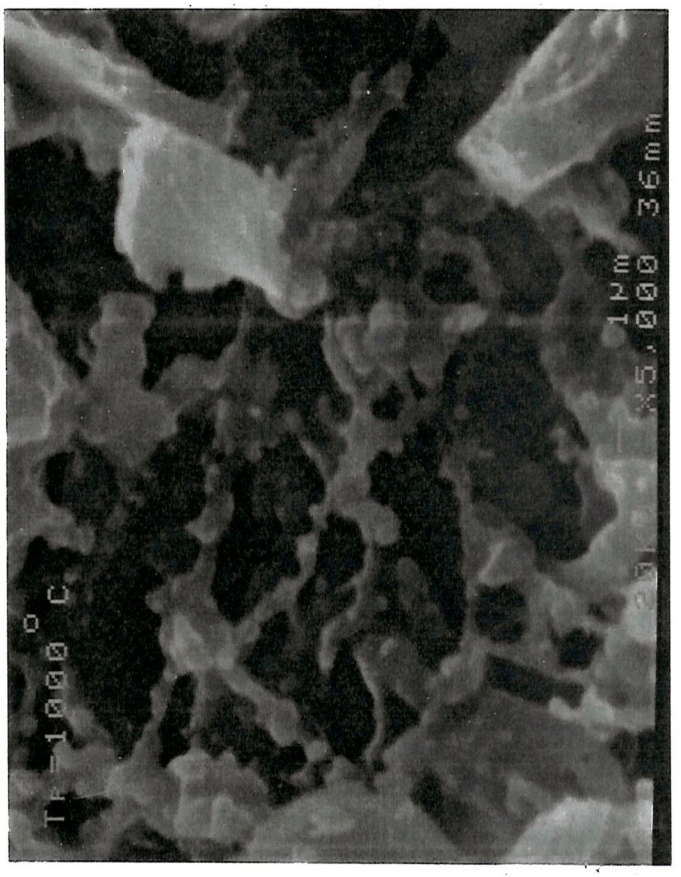

T_{pr} = 1000 °C

T_{pr} = 1100 °C

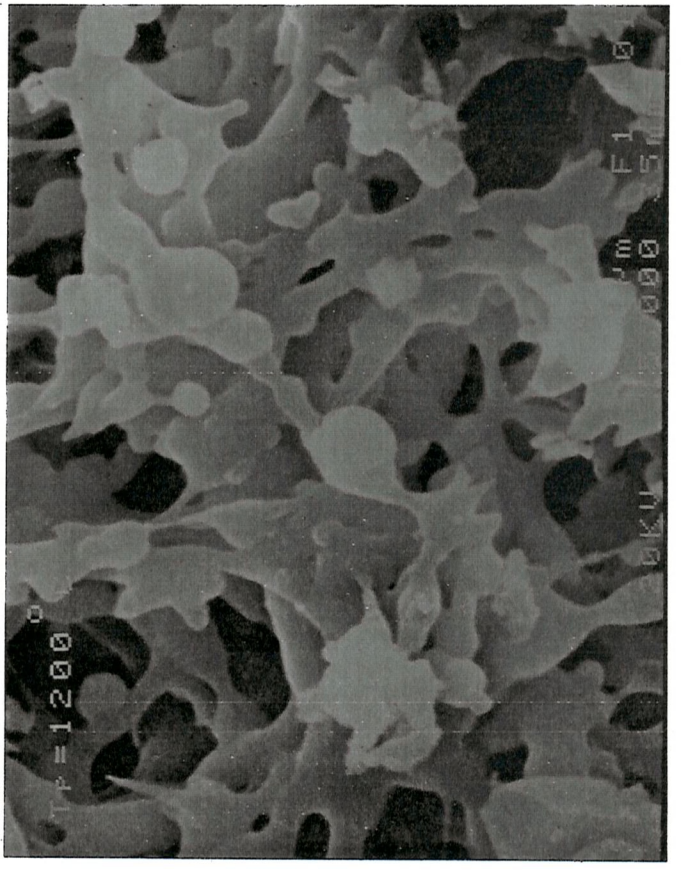

T_{pr} = 1200 °C

Fig 3.4b SEM picture of top of frits presintered at different temperatures

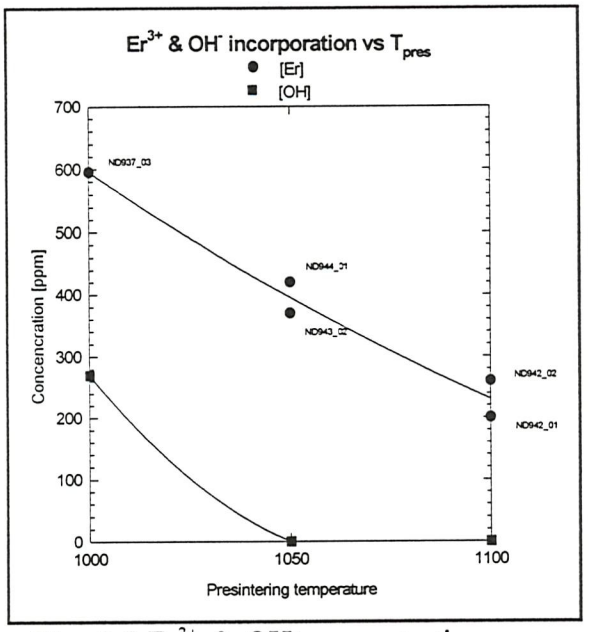

Fig. 3.5 Er^{3+} & OH^- concentrations vs presintering temperature

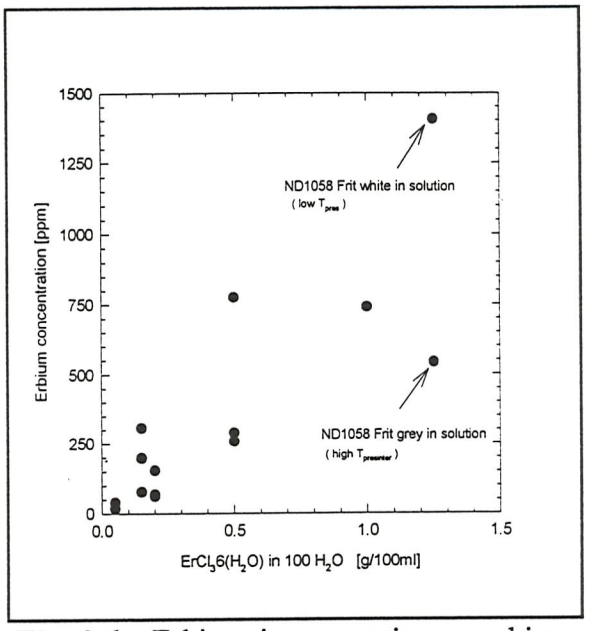

Fig. 3.6 Erbium incorporation vs erbium solution strength

3.1.5 Doping

After presintering, the tube was removed from the lathe and cut at the soot tube end. The porous layer was immersed for an hour in a tube containing 100 ml of de-ionised water with typically a few grams of $ErCl_36(H_2O)$ and $YbCl_36(H_2O)$. Fig. 3.6 shows that the rare-earth incorporation (see §4.3.3 for the concentration measurement method) increases with the rare-earth solution strength but the large variance is due to the influence of frit porosity variations. Fixing the presinter temperature at 1050 °C, we have studied how much erbium -or ytterbium as the two rare-earth ions have almost the same size and polarisability -could be incorporated in the core by making three preforms with increasing the erbium solution strength. The preform which produced the fibre containing 1.1 mol% rare-earths was partially devitrified. The onset of devitrification was typically 1.5 mol% RE. However, when the presintering temperature was increased so that the frit looked grey when immersed in the solution, the onset of devitrification was only a few thousand ppm due to the confinement of the dopants at the middle of the core.

Fig. 3.7 demonstrates that the rare-earth concentration can significantly influence the refractive index difference dn_{max}. The erbium concentrations were calculated using a beam-dopant overlap integral (see Fig. 4.17), taking into account the non-uniform spatial distribution of the dopants. The erbium molar refractivity of $5.4 \cdot 10^{-3}$ mol^{-1} deduced from this plot agrees

well with the value of 5.0 . 10^{-3} mol^{-1} determined in bulk silica glass [Shelby_90], [Gan_81]. Moreover, the extrapolated index difference of 6.5 10^{-3} when no dopant is incorporated corresponds to the value measured in Fig. 3.3.

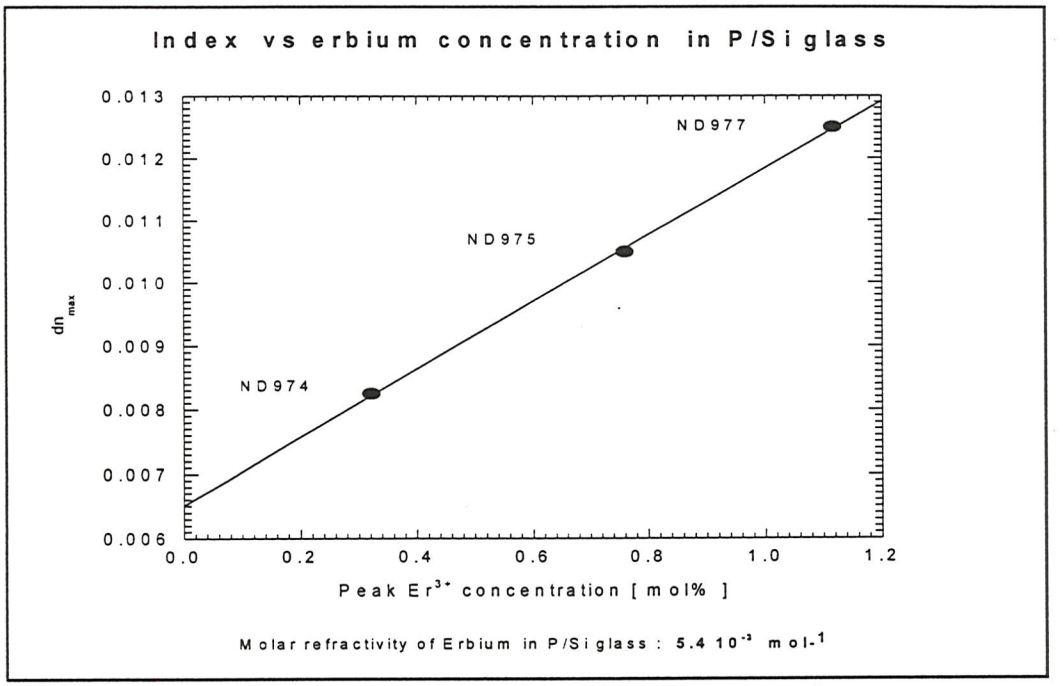

Fig. 3.7 Refractive index vs erbium concentration

3.1.6 Drying

We will justify in the second part of this chapter why we insist on drying the frit carefully. Here we only describe how to efficiently eliminate the water introduced at the doping stage. After the solution doping stage, we join the tube on the lathe and rotate during several hours while flowing nitrogen through. The rotation is essential to avoid accumulation of dopants on one side of the core. We then pass the burner on pilot at maximum speed to heat gently the tube for an hour with the gas still flowing through. Two precautions are also needed : the nitrogen and oxygen are passed through a drier and the gas delivery lines are continuously purged to avoid accumulation of water in the deposition system. With this drying process the hydroxyl content was around 1ppm, as in our undoped fibres.

3.1.7 Fusing

The fusing stage was seen to be of little influence on the rest of the process. Although the ideal fusing temperature is around 1600 °C, the control on the temperature is not so important.

Bubbles resulting from fusing at too high temperature are systematically seen to disappear at the collapse stage due to the low viscosity of the glass. In that regard, phosphosilicate frits are much easier to process than germanosilicate frits.

3.1.8 Collapsing and sealing

During the collapse stage the preform is heated to over 2000 °C. This high temperature causes the evaporation of the phosphorus, which results in a depressed index in the middle of the refractive index profiles. This 'evaporation dip' can be seen in Fig. 3.3. During the process this evaporation manifests itself by the orange glow illustrated in Fig. 3. 8.

For germanosilicate preforms, flowing $GeCl_4$ when collapsing is a well known technique to reduce the evaporation of germanium. This operation is called overdoping. We observed that the overdoping is inefficient when dealing with phosphosilicate preforms.

A more efficient way to limit the evaporation is to collapse the preform as quickly as possible. This can be done if the deposition diameter is small. When the inner diameter at deposition is below 6 mm we can in fact skip the collapse stage and seal the preform immediately after the fusing pass.

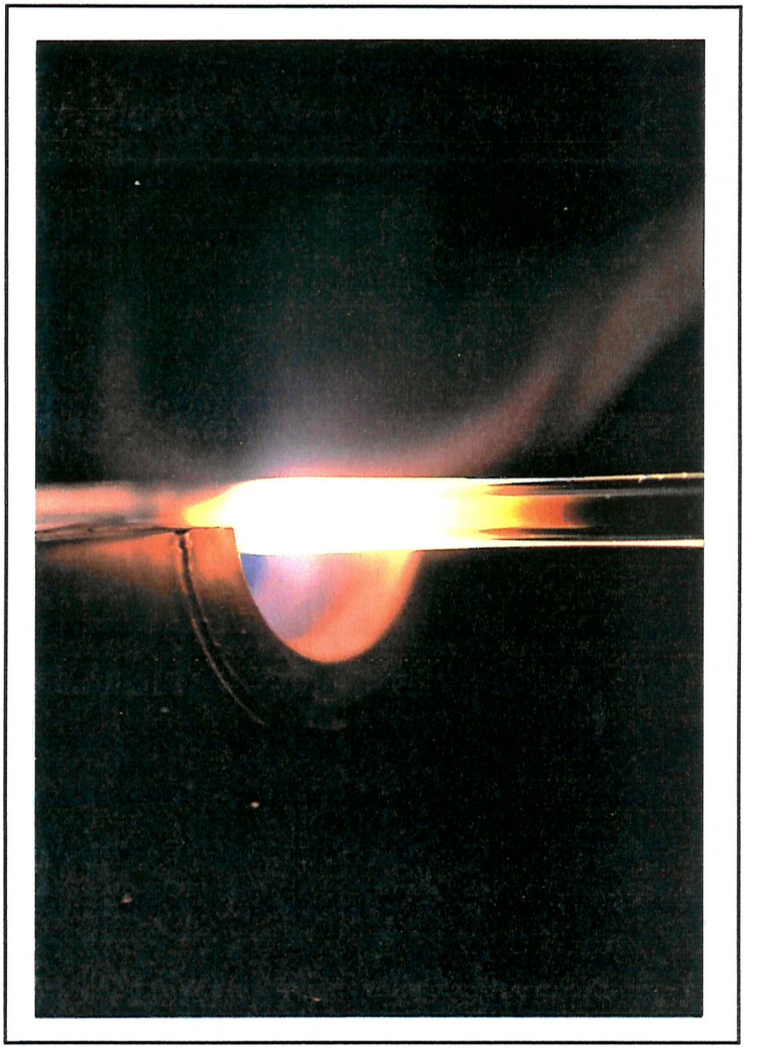

Fig. 3. 8 View of a phosphosilicate preform during the collapse stage

To seal the preform, the burner (at maximum temperature) is translated at a speed of around 1 cm / min along the preform and the core can be partially recircularised during this pass by applying pressure on the inside of the tube. The high temperature necessary for collapsing and sealing burns off some silica from the outside of the preform which make the outer of the preform opaque. The outer surface is fire polished at the end of the preform fabrication process, and the amount of green thermoluminescence generated during this operation can be used as an indication of the erbium incorporation.

3.1.9 Overcladding, fibre pulling, and cladding pumping structure

Overcladding -also called sleeving- is done by collapsing a silica tube over the finished preform. Its purpose is to increase the cladding to core diameter ratio. The optical quality of the sleeving tube is not important as it forms the outer part of the cladding where the optical field has almost vanished.

Overcladding can also be used to create the outer guiding structure needed for cladding pumped devices. To produce the structure shown in Fig. 3.9, we overclad a doped preform with a tube of synthetic silica coated with a layer of fluorine doped silica. This tube is obtained by drilling out the central part of a silica core multimode preform (NA = 0.23), supplied by Hereaus, with a drilling machine. The doped preform is stretched beforehand if the core size needs to be reduced. The interface between the doped preform and the fluorine coated silica tube is not apparent in Fig. 3.9.

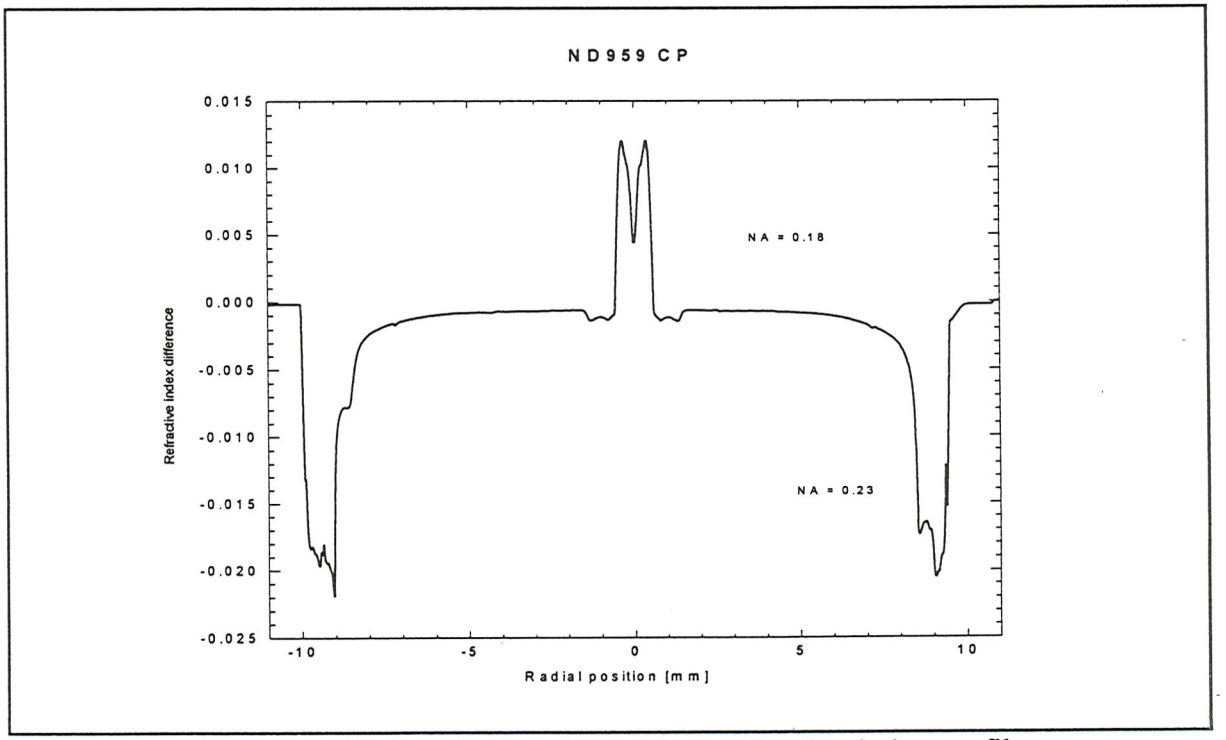

Fig. 3.9 All-glass double clad preform refractive index profile

Fig. 3.10 shows a microscope image of a fibre pulled from the preform whose refractive index profile is shown in Fig. 3.9. The outer fluorine doped layer thickness is still about 10 % of the total radius. Indeed, to avoid fluorine evaporation, which can lead to pump beam leakage, we pulled the preform at low temperature (while still retaining a workable fibre tension).

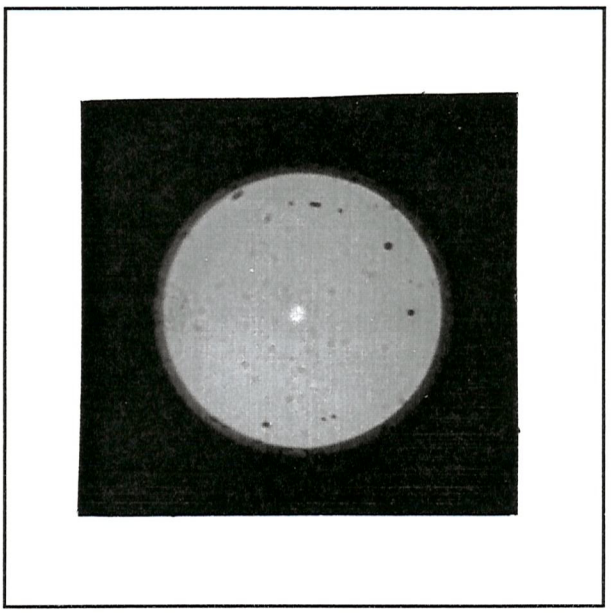

Fig. 3.10 Double clad fibre structure. The overall diameter in 250 μm.

Even with standard preforms, we avoid using unnecessarily high pulling temperatures. During the fibre drawing process specific components may be forced to occupy non-equilibrium states at low temperature due to the rapid quenching from high temperature. These states may give rise to so-called drawing-induced absorption bands. A UV loss advantage has been identified from drawing high NA germanosilicate fibres at low temperature [Ainslie_81]. In the case of phosphosilicate fibres, a drawing-induced absorption band at 0.55 μm has been observed [Imoto_78]. Another reason to keep the pulling temperature low will be explained in §3.2.3.

For mechanical protection the fibres are coated with an UV curable acrylate during the draw. Its high index suppresses cladding modes. However, to produce a cladding pumped fibre without having to overclad the preform with fluorine, we use a heat curable silicone rubber coating. Its index is lower than that of silica so that it can provide the outer guiding structure (NA=0.4). In general, the all glass approach is prefered for its superior stability and power handling.

3.2 Three fabricator's nightmares

3.2.1 Hydroxyl contamination

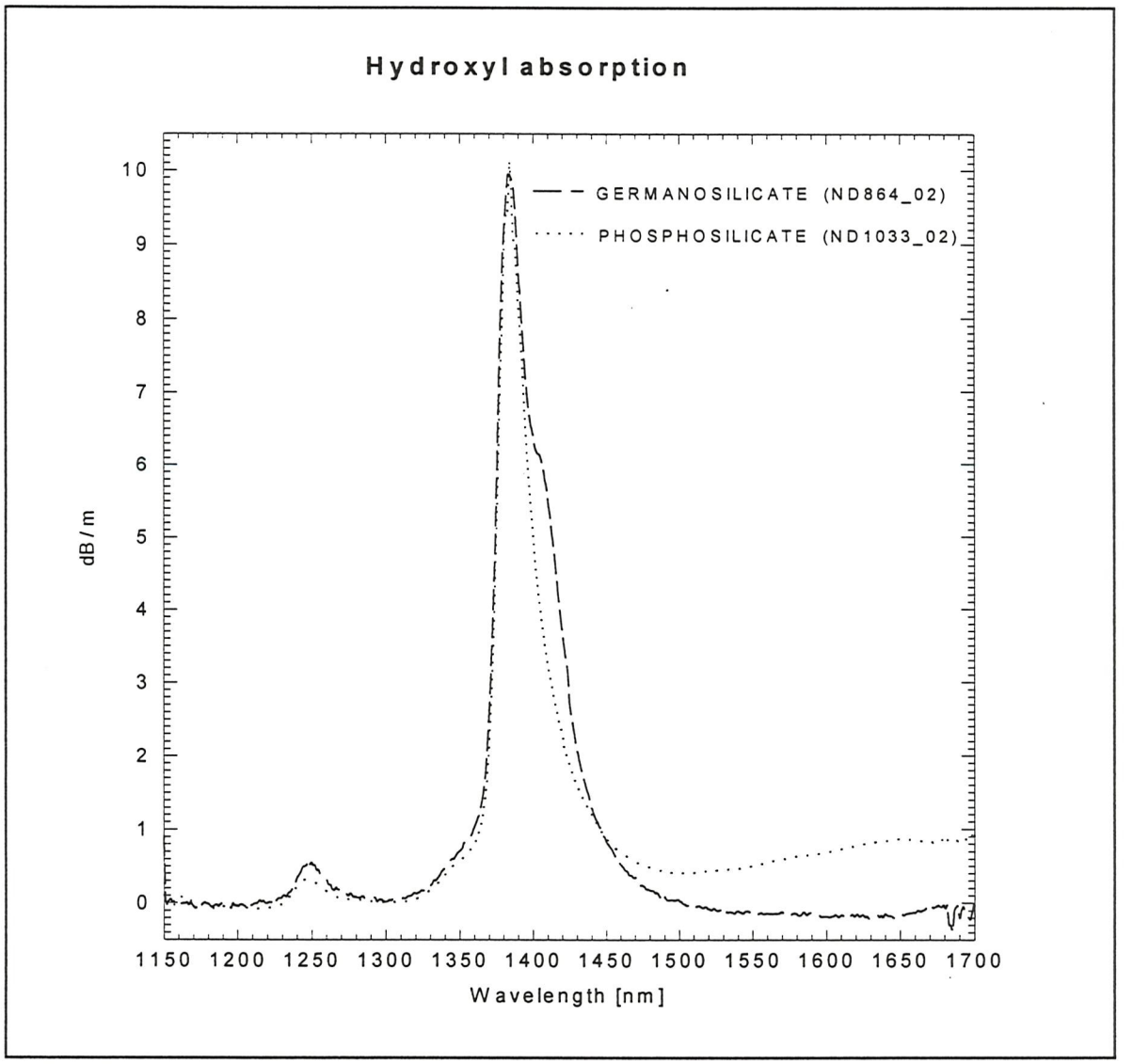

Fig. 3.11 Absorption overtones of hydroxyl in phospho- and germanosilicate fibres

OH absorption	950 nm	1250 nm	1383 nm	1550 nm
P / Si	0.013	0.04	1	0.06
Ge / Si	0.025	0.05	1	0.002

Table 3.1 Ratio of absorption contributed by hydroxyl absorption to the peak at 1383 nm in phosphosilicate and germanosilicate

The main vibration of hydroxyl in silica fibres is at around 2.75 μm. Overtones give rise to absorption at around 1380 nm, 1250 nm, and 950 nm. To estimate the hydroxyl concentration we used the value of 50 dB / km / ppm at 1383 nm reported by many authors [Nagel_82], [Garett_82], [Olschansky_79]. The erbium absorption at 1383 nm for phosphosilicate fibres is 0.25 dB / km / ppm (about two hundred times lower than at the 1535 nm absorption peak). In our Er : Yb fibres the 950 nm peak is masked by the ytterbium peak and the 1250 nm is often masked by the mode cutoff peak. In fibres doped with 1000 ppm of erbium only hydroxyl concentrations greater than 5 ppm can be measured from the 1383 nm absorption.

In Table 3.1, we have summarised the relative values of the hydroxyl absorption peaks in germanosilicate and phosphosilicate fibres. Fig. 3.11 shows the presence of an additional peak centered around 1650 nm in the phosphosilicate fibres. This peak has already been reported in [Edahiro_79] and it has been clearly identified as the first overtone of the broad P=O..H vibration peaking at around 3.4 μm [Itoh_86]. It represents a source of loss at the emission wavelength in an erbium doped phosphosilicate fibre.

Fig. 3. 12 shows the fluorescence decays at 1535 nm of five fibres with different erbium and hydroxyl concentrations. The decays were measured with an integrating sphere to avoid any distortion by reabsorption. All fibres were kept straight to eliminate any pump radiation leakage. We pumped directly into the metastable level of erbium using a 1480 nm diode. The pump falltime was measured to be 0.1 ms. The launched power was around 8 mW.

Despite the modest pump power used, the erbium upconversion (discussed in more details in chapter 4) seems to be significant. Indeed ND937_03, ND849_04 and ND845_01 exhibit an initial decay of around 7 ms, whereas the two lowest erbium concentration fibres exhibit a initial decay of 9 ms. However, 30 ms after the beginning of the decay, the effect of the hydroxyl contamination appears clearly different from the effect of the upconversion : the two high hydroxyl content fibres have a decay time of 9 ms, whereas the other fibres have resumed the intrinsic erbium decay time of 10.5 ms. In ND937_03 and ND849_04 the decay times are lower than in fibres which are hydroxyl free over the whole duration of the measurement. From these measurements it can be concluded that the OH^- contamination reduces the lifetime of the $^4I_{13/2}$ - $^4I_{15/2}$ transition.

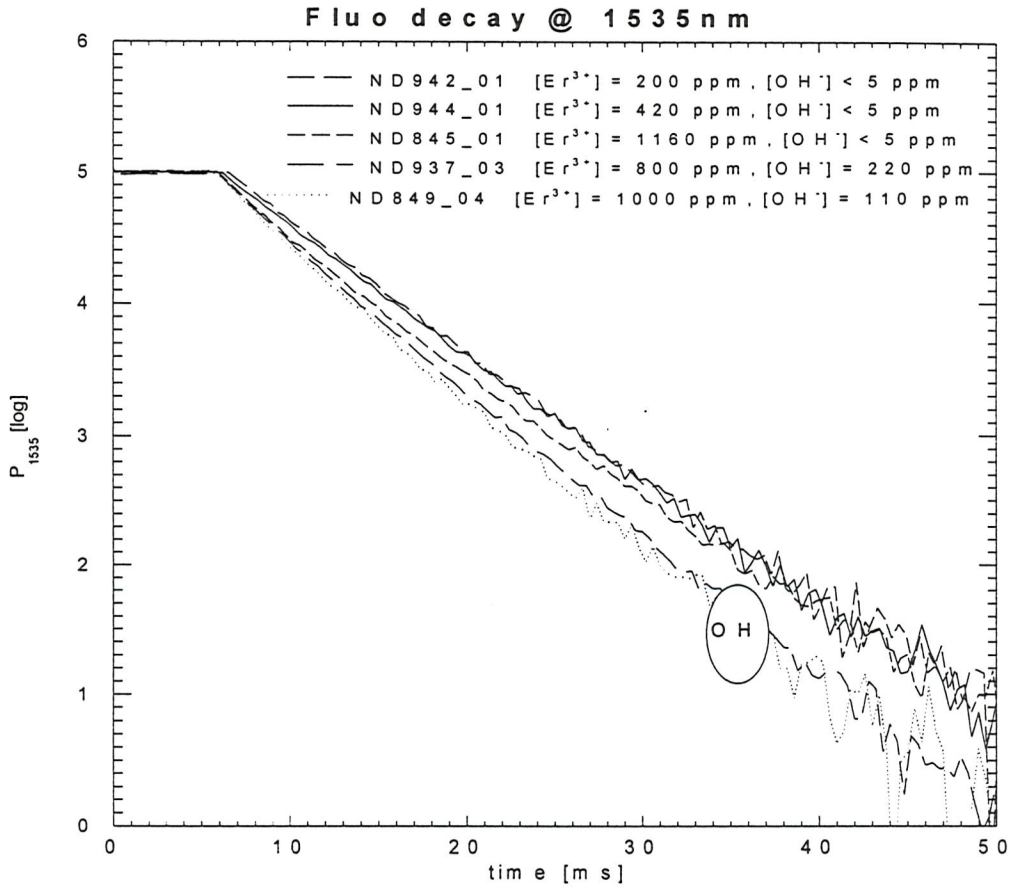

Fig. 3.12 Erbium 1.53μm fluorescence decays

Pump laser	Fibre	α_{1383}	α_{pump}	[Yb]:[Er]	P_{launch}	Laser slope 's' & minimum threshold power 'P_{th}' with corresponding fibre length
Mini Nd:YAG 1064 nm	844_02	0.5	2.2	15:1	190 mW	s = 24% @ 4.0 m, P_{th} = 25 mW @ 1.0 m
	849_04	5.4	2.4	15:1	190 mW	s = 12% @ 3.0 m, P_{th} = 90 mW @ 2.0 m
	855_03	2.9	0.71	15:1	180 mW	No lasing
	862_01	4.3	1.5	30:1	180 mW	s = 10% @ 8.0 m
	937_03	11	3.1	20:1	110 mW	No lasing
Nd:YLF 1047 nm	849_04	5.4	5.2	15:1	400 mW	s = 12% @ 2.2 m, P_{th} = 50 mW @ 1.0 m
	898_01	6.5	4.8	15:1	400 mW	s = 8% @ 2.5 m, P_{th} = 70 mW @ 1.4 m

Table 3.2 Laser performance of fibres with various OH^- contamination levels quantified by the absorption at 1383 nm 'α_{1383}'. The absorption coefficients 'α' are given in dB / m.

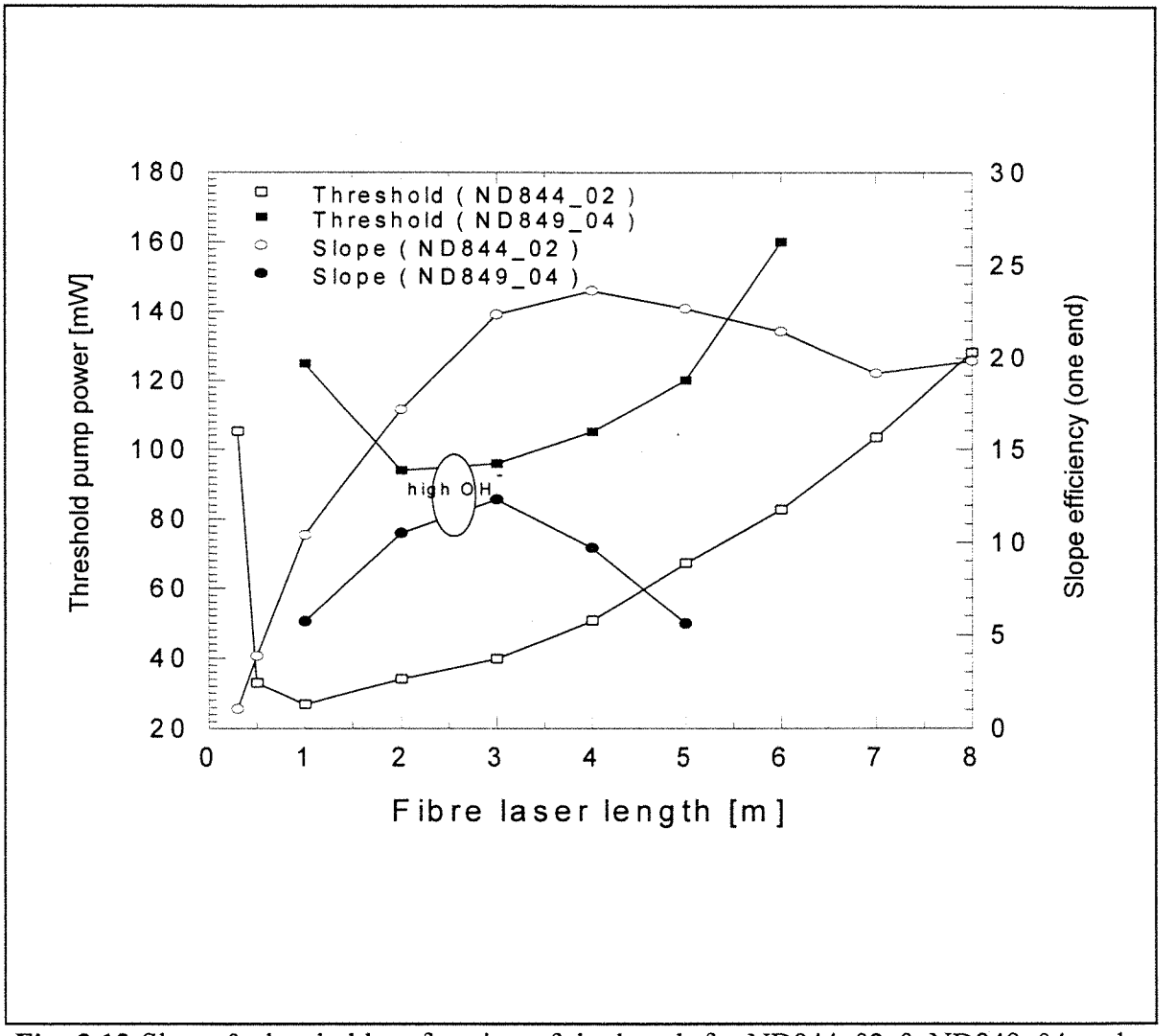

Fig. 3.13 Slope & threshold as function of the length for ND844_02 & ND849_04 under Nd : YAG pumping (1064 nm)

Fig. 3.13 shows a comparison of laser performances for the fibres with similar rare-earth content but different hydroxyl contents. The hydroxyl contamination both increases the threshold and decreases the slope of the fibre lasers. As expected from the additional signal loss the slope drops sharply for lengths greater than the optimum value. Table 3.2 shows the results of laser cutback measurements for fibres with various hydroxyl contents. The Si - OH^- concentration of 10 ppm for ND844_02 still allows to build an efficient laser (s > 20%). The results for ND849 and ND898 show that the performances deteriorate with increasing hydroxyl content. However, a comparison between ND855 and ND862 shows that the hydroxyl content is only one of several factors determining the laser efficiency.

3.2.2 Damaged frit

When pumping our Er/Yb fibres at 980 nm, we often measure much higher laser slope efficiencies than when pumping at 1064 nm. The main difference between the two pumping schemes is that pumping at 980 nm offers a pump rate two orders of magnitude higher than pumping at 1064 nm. In the latter, the background losses may approach the pump absorption.

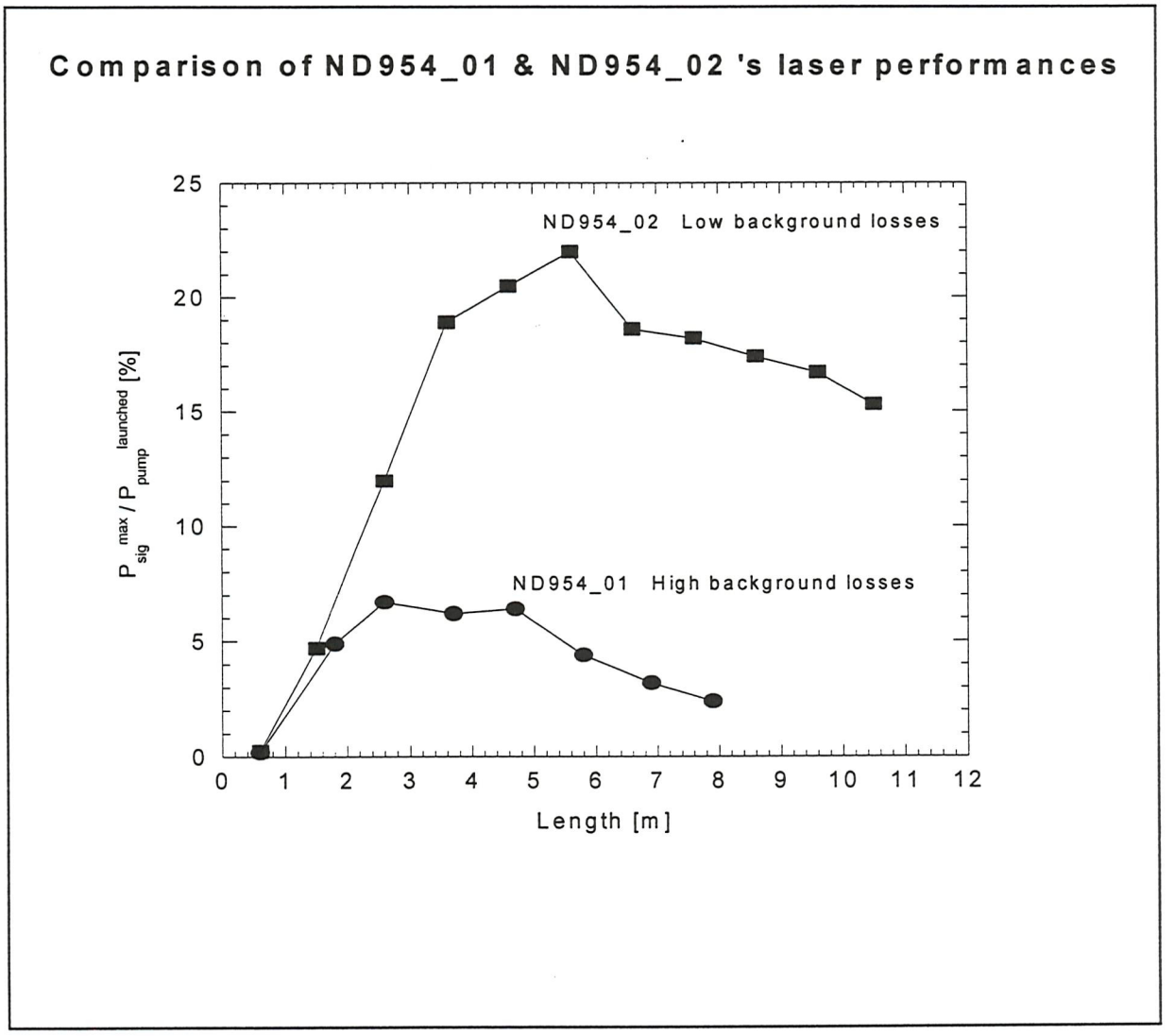

Fig. 3.14 Comparison of ND954_01 & ND954_02 laser performance expressed by the ratio of the maximum lasing power vs launched pump power at 1064 nm.

Pull	⊖	λ_{cutoff}	α_{1064}	α_{1492}	α_{1535}	λ_{min}	α_{min}	N_{Yb}	N_{Er}
01	80	1250	3.0	11	32	1150	0.75	1.09	545
02	80	1300	2.3	12	36	1150	0.17	1.19	595

Table 3.3 Summary of parameters for ND954_01 and ND954_02. Diameter given in μm, losses α in dB/m, wavelength λ in nm, and concentrations N in mol%.

Fig. 3.14 shows the laser performances of two fibres pulled from the same preform. We see in Table 3.3 that the two fibres are very similar and that the only significant variations are the value of the background losses and absorption at 1064 nm. In this table the subscript 'min' refers to the minimum losses in the region 1000-1500 nm. The values of α_{1064} is 0.7dB/m higher in ND954_01 than in ND954_02 despite the similar doping level. Indeed, this difference corresponds to the difference in minimum losses α_{min}, found at 1150 nm in both fibres.

These two fibres are ideal to test the role of the background losses. Fig. 3.14 demonstrates the intuitive results that, with extra background losses :

- the maximum signal power is lower;
- the maximum signal power is obtained at a shorter length;
- the maximum signal power drops more sharply with increasing length beyond the optimum length.

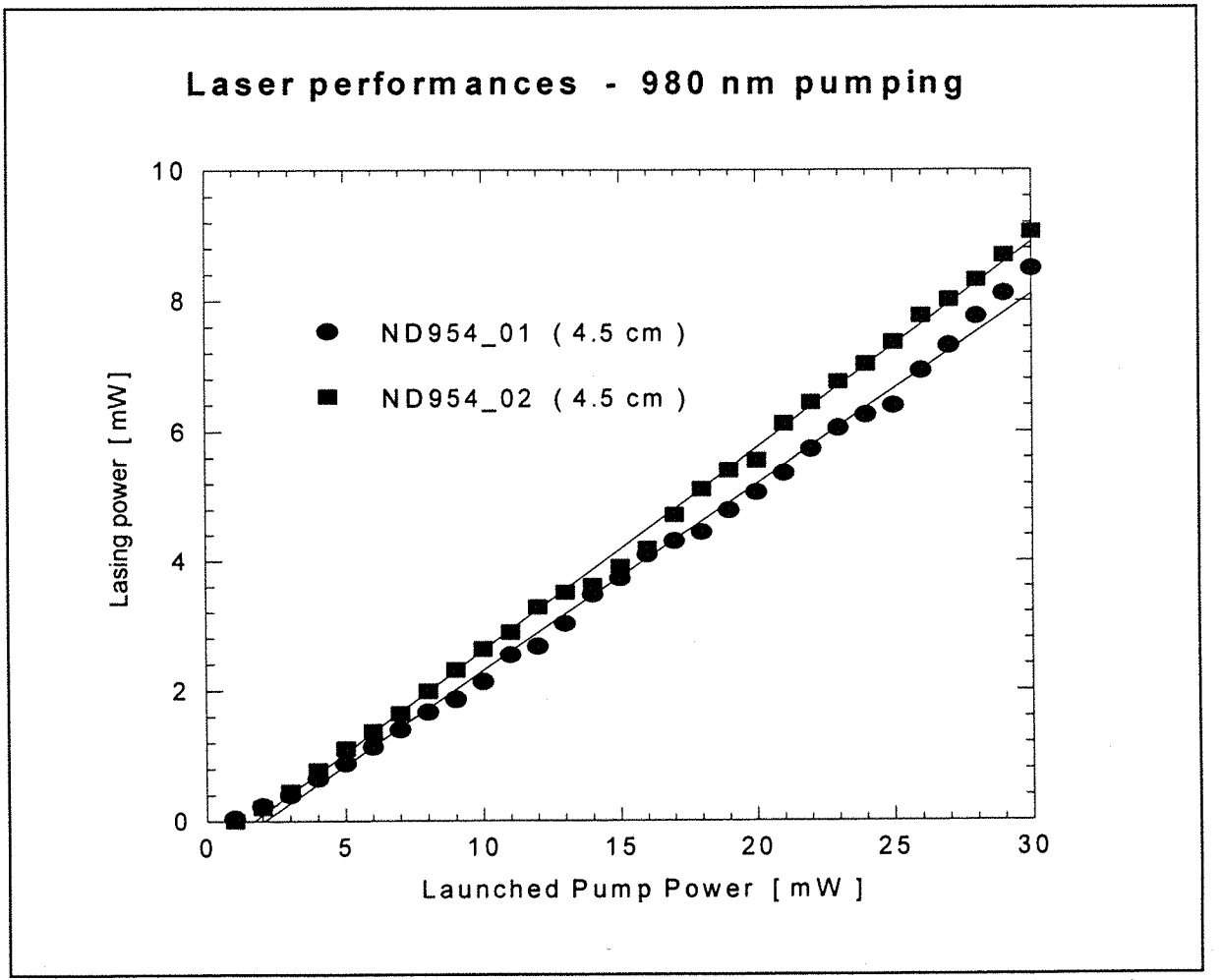

Fig. 3.15 Comparison of laser performance between ND954_01 and ND954_02 pumping at 980 nm

Fig. 3.15 shows that in contrast to the case of 1064 nm pumping, the laser performances of the two fibres when pumped at 980 nm are almost the same. This confirms that the background losses manifest themselves most severely at low pump rate.

Fig. 3.16 Frit with visible structures after immersion in doping solution (scaling bar : 1 mm)

It is essential to be able to relate the excess background losses to the fabrication process. The difference in background losses between the two fibres can be attributed to the variation in the structure of the frit along the preform. During the fabrication process we observed that 10 to 15 centimetres at the tail of the preform were inhomogeneous. ND954_01 was pulled from this region of the preform. The frit was fragile and after immersion the 'bark like structures' shown in Fig. 3.16 were visible. The fragile frit was a consequence of the temperature undershooting at the beginning of the presintering pass.

3.2.3 Phase separation

Phase separation was often observed during the fabrication process and produced a white core in the sealed preform. It was generally detected when the preform was heated up just after consolidation of the frit. At this stage we observed several 'blue dotted lines' all along the preform. The colour turned from blue to white as the size of the clusters increased during the collapse. Due to their dramatic effect on the performance of fibres, from scattering and rapid upconversion within clusters of rare-earth ions, we decided to have a closer look at the clusters.

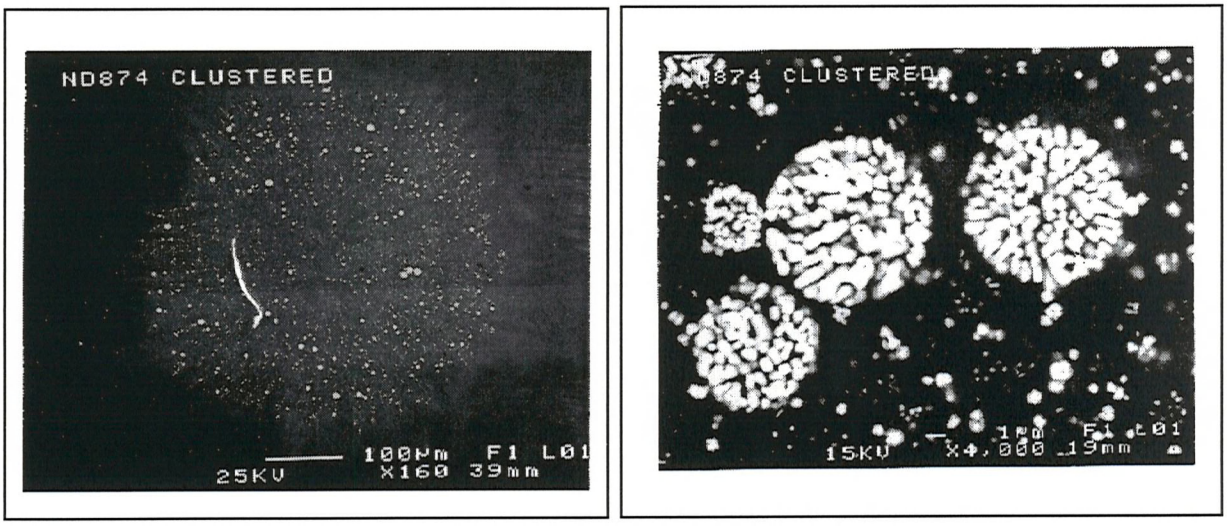

Fig. 3.17 Clusters observed at two magnifications (magnification bars : left 100 µm, right 1 µm) in a phase separated preform (ND874)

With a Scanning Electron Microscope (SEM) we invariably observed the presence of round and contrasted regions inside devitrified fibre or preform cores. This is illustrated in Fig. 3.17. The spherical shape shows that, in this low viscosity glass, clusters can minimise their surface tension before solidification occurs. The high contrast in the SEM is associated with the presence of high atomic number elements (see chapter 4). ND874 presented particularly large clusters and we carried out an analysis in the centre of one of the three large clusters shown on the left picture in Fig. 3.17. Results are shown in Table 3.4.

The measurement clearly shows :

- a very high concentration of rare-earths in the cluster;
- a very low concentration of SiO_2 in the cluster which demonstrates the small affinity of the rare-earth for silica.

Line	Yb -L	Si -K	P -K	Er -L
Formula	Yb_2O_3	SiO_2	P_2O_5	Er_2O_3
wt%	56	12.2	29.1	2.7

Table 3.4 EDS analysis on the largest cluster shown in Fig. 3.18

An important issue to be addressed is the influence of the fabrication process on the formation of the clusters. Clusters have been seen to dissolve when a undoped phosphosilicate inner core layer was deposited after consolidation of the doped layer. The additional phosphorus was effective at coordinating the rare-earths. This inner layer also served as a protection against the evaporation of phosphorus which led to the growth of the clusters during the collapse.

But the inner layer deposition cannot systematically eliminate the phase separation problem. In the first place, we need to control the incorporation of rare-earth ions in the frit. As we saw in the first part of this chapter, the good control of the dopant incorporation is most critically dependent on the control of the presintering temperature. But even when we control carefully the presintering temperature we often obtain some slightly devitrified regions in the preform when we try to push the rare-earth concentration to the limit, typically 1.5 mol% of rare-earths, in order to make devices as short as possible.

As the cooling rate is a critical factor in determining glass formation, the question also arises whether the rapid quenching occurring at the draw can be beneficial in reducing or dissolving the clusters. More precisely, simple nucleation theory (a good discussion of crystal nucleation and growth kinetics can be found in [Turnbull_56]) dictates that crystal nucleation is promoted by the change in free energy on crystallisation, and at the same time retarded by the work needed to form the crystal-liquid interface; the interplay between these two competing factors insures that only those crystals which contain more than some critical number of atoms exist as crystal nuclei; all others remelt. The associated energy barrier tends to infinity when we approach the melting temperature so that phase separation may disappear in the pulling tower furnace. It is well known from dynamical models of glass formation that an essential prerequisite for glass formation from the melt is that the cooling be sufficiently fast to preclude crystal nucleation and growth [Uhlmann_83]. Whether core revitrification or crystal growth occurs on reheating and quenching, can be tested experimentally.

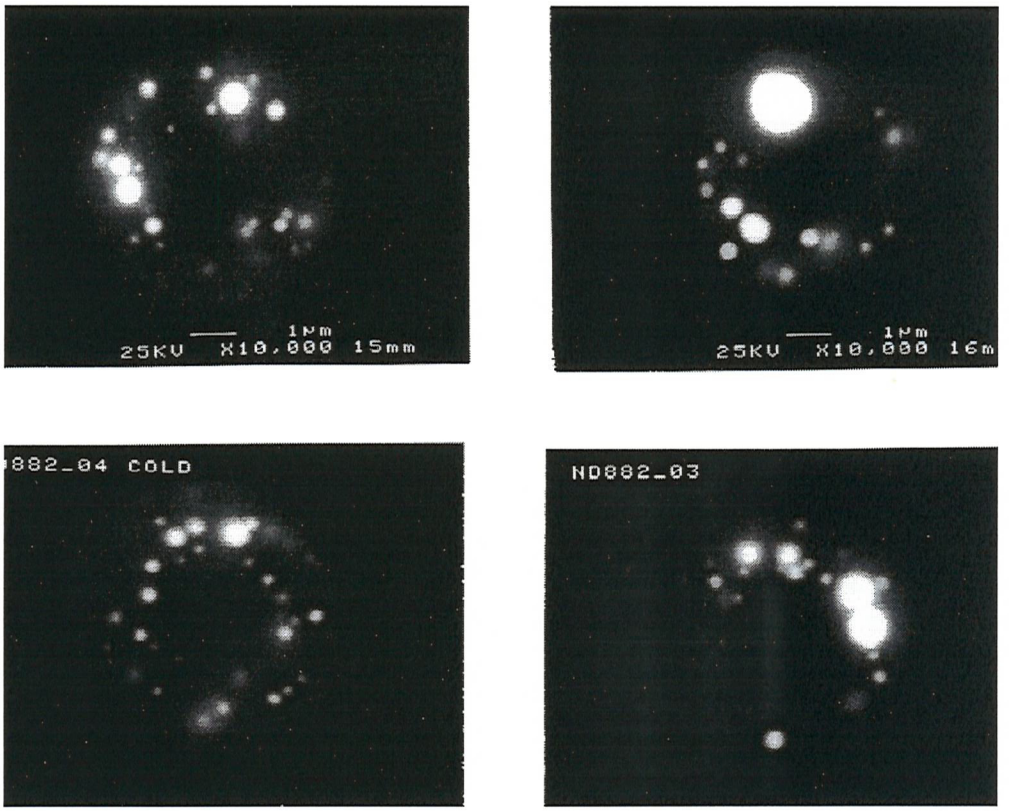

Fig. 3.18 Clusters in fibres pulled at different conditions (refer to Table 3.5)

	T = 2040 °C	T = 2140 °C
s = 2 mm/min	01 Weak	02 Strong
s = 4 mm/min	04 Weak	03 Strong

Table 3.5

Test on ND882: Pulling conditions - Phase separation (s is the preform feed-speed)

We tested the effect of the pulling conditions on the phase separation using ND882, a preform which was phase separated all along its length. We observed a section of each fibre (pulling conditions are summarised in Table 3.5) under an electron microscope. We used the image produced by the backscattered electrons, because they reflect the in-depth composition of the sample. Fig. 3.18 shows the four resulting pictures. In all cases, the clusters were not seen to remelt. A growth of the clusters with increasing temperature and increasing time spent in the hot zone is visible. We conclude that heat treatment only favours phase separation. There is other evidence to support this statement : cores which are highly doped but still transparent before pulling turn slightly blue just above the meniscus after pulling.

3.3 Conclusions

We have described the fabrication process step by step showing how phosphorus and the rare-earths could be efficiently incorporated into silica fibres. The dopants have been seen to contribute to up to half of the core-cladding index difference. The fabrication of new all-glass cladding pumped fibres based on a fluorine doped outside cladding has been presented.

We have shown that the 'presintering pass', the extra pass introduced to adapt the solution doping technique to low viscosity glasses, is a very critical pass of the process. Indeed, it influences the trapping of hydroxyl, the frit stability, and the dopant incorporation. This has been explained by examining the structure of the frit for different presintering temperatures. Hydroxyl contamination has been seen to increase the losses at the signal wavelength and to decrease the erbium metastable level lifetime. An unstable frit resulted in increased background losses, which were seen to seriously deteriorate the laser performances for low pumping rates. Finally, it was essential to control the presintering temperature to avoid phase separation, which could not be reduced by heat treatment.

Chapter 4

CHARACTERISATION

4.0 Introduction

Although the vapour composition and the doping solution strength can be accurately controlled in the fabrication of preforms, they are not related in a simple fashion to the chemical composition of the final preform. Hence, methods for the determination of the final composition in the preform are important for the fibre characterisation. We first compare the accuracy and practicality of two different chemical analysis methods. Our interest is not limited to the composition of the core glass but we also attempt to investigate the glass structure by Raman spectroscopy, and by optical spectroscopy. Finally we show how to estimate the suitability of our fibres to build efficient lasers and present some potential loss mechanisms.

4.1 Concentration measurements

Two methods have been used :
- Inductively Coupled Plasma Mass Spectrometry (ICP-MS);
- Energy Dispersive X-ray Spectrometry (EDS).

In the following we see how each method can be implemented and we compare the practicality and accuracy of the two methods.

4.1.1 Inductively Coupled Plasma Mass Spectrometry (ICP-MS) :

This method enables us to assess quantitatively elements present even at very low concentrations in the sample. There is also no particular difficulty in detecting low atomic number elements, a problem which plagues the X-ray analysis methods, and the ICP-MS offers a very high sensitivity for rare-earths. Two types of measurements have been carried out differing by the sample introduction method:
- sample dissolution;
- sample laser ablation.

4.1.1.1 Analysis by sample dissolution

The measurements are made on samples extracted from preforms. The measurements can also be performed in the fibres but then there is no possibility of extracting a sample containing the core in large proportion, which lowers considerably the accuracy of the measurements. The geometry of the sample analysed below is shown in Fig. 4.1.

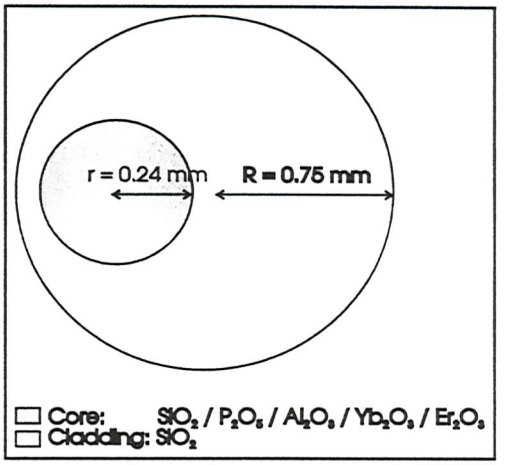

Fig. 4.1
Section of a sample extruded from ND844 (preform) for ICP-MS by dissolution measurement

The sample is dissolved twice. A reagent blank is prepared alongside and analyzed with the samples. Following calibration the resulting solutions are introduced into the plasma where the dissolved metals are vaporised, ionised and subsequently analysed by mass spectrometry.

The results are shown in Table 4.1. The molar masses used for the calculations are in g / mol M(Er) = 167.26, M(Yb) = 173.04, M(Al) = 26.98, M(P) = 30.97, M(Si) = 28.09, M(O) = 16.00, $M(Er_2O_3)$ = 382.52, $M(Yb_2O_3)$ = 394.08, $M(Al_2O_3)$ = 101.96, $M(P_2O_5)$ = 141.94, $M(SiO_2)$ = 60.09.

ND844	Er	Yb	Al	P	Si	O
ppmwt sample	263	3390	1070	8100	-	-
wt% ion	0.257	3.31	1.04	7.91	35.5	52.0
wt% oxide	0.294	3.77	1.97	18.1	75.9	-
mol% ion	0.0318	0.396	0.798	5.29	26.2	67.3
mol% oxide	0.0541	0.674	1.36	8.99	88.9	-

Table 4.1 ICP-MS results for ND844

The wt% in the core for Er, Yb, Al, P are calculated from the concentrations measured in the sample using $wt\%_{core} = (R/r)^2 \, wt\%_{sample}$.

To calculate the wt% of the oxides Er_2O_3, Yb_2O_3, Al_2O_3, P_2O_5 we use the formula

$$wt\%(A_xO_y) = M(A_xO_y) \cdot wt\%(A) / (x.M(A)) \quad (4-1)$$

The value of wt%(SiO_2) is calculated as the complement to 100%.
The mol%(ion, oxide) can be deduced from the wt%(ion, oxide) using

$$mol\%(ion, oxide) = 100\ wt\%(ion, oxide) / (M(ion, oxide) \sum_{all\ ions,\ oxides} \frac{wt\%(ion, oxide)}{M(ion, oxide)}) \quad (4-2)$$

The sum in the expression above is dominated by the silica. If we make the approximation that the core is essentially made of silica we can use mol%(ion, oxide) = wt%(ion, oxide).M(Si, SiO_2) / M(ion, oxide). This approximation gives for the erbium oxides mol%(Er_2O_3) = wt%(Er_2O_3) M(SiO_2) / M (Er_2O_3) = 0.157 wt%(Er_2O_3) = 462 ppm instead of 541 ppm. The error is 17% and is more significant than suggested in [Townsend_90]. The mol%(Er^{3+}) in oxide is given by

$$mol\%(Er^{3+}) = 2\ mol\%(Er_2O_3) \quad and \quad [Er^{3+}] = 10^4\ mol\%(Er^{3+}) \quad [ppm] \quad (4-3)$$

The concentration [Er^{3+}] is commonly quoted and we will favour this definition in this thesis. A common measure also used to define the rare-earth content of glasses is the ion density 'd'

$$d(Er^{3+}) = \frac{D \cdot N_A}{W} mol\%(Er^{3+})\ [ions / cm^3] \quad where\ W = \sum_{all\ oxides} mol\%(oxide)\ M(oxide) \quad (4-4)$$

where D is the density of the glass and $N_A = 6.02.10^{23}$ is the Avogadro number.
Assuming that the core is essentially composed of silica we have the relation

$$d(Er^{3+}) = \frac{D_{SiO_2} \cdot N_A}{M(SiO_2)} mol\%(Er^{3+}) / 100 \quad [ions / cm^3] \quad (4-5)$$

where $D_{SiO2} = 2.2$ g /cm^3 is the density of silica. Numerically this gives 1 ppm(Er^{3+}) = $2.2\ 10^{16}$ ions / cm^3. In our sample mol%(Er) = 0.1082%, [Er^{3+}] = 1082 ppm, and d(Er^{3+}) = $2.38\ 10^{19}$ ions / cm^3.

4.1.1.2 ICP-MS by laser ablation :

We use the PlasmaQuad system from Fisons Instruments VG Elemental [Fisons_92] in the Geology Department of the University of Southampton to carry out ICP-MS analysis. The machine is connected to a laser ablation system based on a Q-switched frequency quadrupled Nd:YAG laser emitting at 266 nm (repetition rate 6.5 Hz, pulse width 5 ns). The ablated material is carried to the analysis unit by an argon vector gas and subsequently partially ionised in an argon plasma with addition of nitrogen to increase the thermal conductivity. The plasma reaches a maximum temperature of approximately 8000 K. It is generated by a 1.35 kW RF field, enough to ionise 90% of the periodic table to more than 90% ionisation efficiency (if the power is further increased double ionisation may occur. Also, coatings used for the SEM are to be avoided, especially carbon coatings which may impede the ionisation). The ions are then focused, filtered in the DC plus AC driven quadrupole, and detected.

The technique of laser ablation offers two major advantages over the dissolution technique:

- the material can be analysed over a small region controlled by the beam focusing and the laser power;

- the sample preparation is simplified. We cut a few millimetres thick slice from the preform. Polishing is not necessary as we set up the machine to analyse only the material ablated well below the surface, by setting the pre-ablation time to three seconds (followed by 15 sec ablation).

On the other hand, the operator has to pay attention to the focusing to assure that the quantity of material ablated does not vary from point to point. The choice of the material standard is also of great importance. In fact, the availability of a suitable standard is a very serious limitation of this method. Indeed, the standard should show the same ablation properties as the sample to be analysed, and should also contain the trace elements at concentrations within maximum two orders of magnitude of the concentrations present in the sample. We use a standard [NIST] formed of a glass matrix 72 mol% SiO_2, 14 mol% Na_2O, 12 mol% CaO and 2 mol% Al_2O_3 containing 61 trace elements, among them Er and Yb were both present at a concentration of 450 ppmwt, corresponding to $wt\%(Er_2O_3) = 0.0515$. The blank is simply a sample of the carrier gas and should offer the minimum background for the elements to be analysed.

We filter in the quadrupole the main (or unique) isotopes of the elements: Al27, P31, Er166 and Yb174. The silicon is too abundant to be analysed with the other elements. The rare-earths are readily detected. Because of the space charge effect at the interface between the plasma and expansion chambers, we may have to lower the vacuum in the expansion chamber to achieve sufficient sensitivity for the aluminium and phosphorus. For each analysis it is necessary to record the operating conditions, described by the parameters below:

- the supply voltage of the laser which is usually 12.4 V. It is related to the flashlamp voltage and to the laser power which are not directly measured;

- the vacuum in the expansion chamber which influences the sensitivity as a function of the atomic number. A high vacuum will lead to a large flow of ions from the plasma to the expansion chamber, which are connected by a tiny hole in the sampling cone. The large flow induces a high charge density near the hole. This is the space charge effect mentioned above. As the lightest ions are more deviated than the heaviest ones, they have less chance of passing through the hole.

Fig. 4.4 shows the result of the linescan illustrated in Fig. 4.2 & 4.3 (upper pits' row). From point three onwards the pits are regularly spaced every 40 μm. They are about 20 μm in diameter. It is difficult to use this analysis method with pits smaller than about 10 μm, which means that this method is not suitable to analyse the core of a monomode fibre. The video camera associated with the laser probe offers a very poor depth of field which proves insufficient to evaluate the quantity of material ablated. Indeed, the pits of the two linescans on the SEM picture shown in Fig. 4.3 appear very similar using the video camera. To obtain accurate measurements it is crucial to check that the laser creates similar pits in the sample and the standard. The comparison is difficult because even with the SEM, it is difficult to measure the depth of the pits. Moreover, it is difficult to locate the core within the sample, which explains why the linescan does not pass exactly over the centre of the core (see Fig. 4.2).

To fabricate the preform which we analysed we used a doping solution with an ytterbium to erbium concentration ratio of 30. Fig. 4.4 shows that this ratio is conserved within 10% from the solution and that it remains constant all along the core. From attenuation measurements we estimated an average erbium content of 1000 ppmwt, which is in good agreement with the results presented in Fig. 4.4.

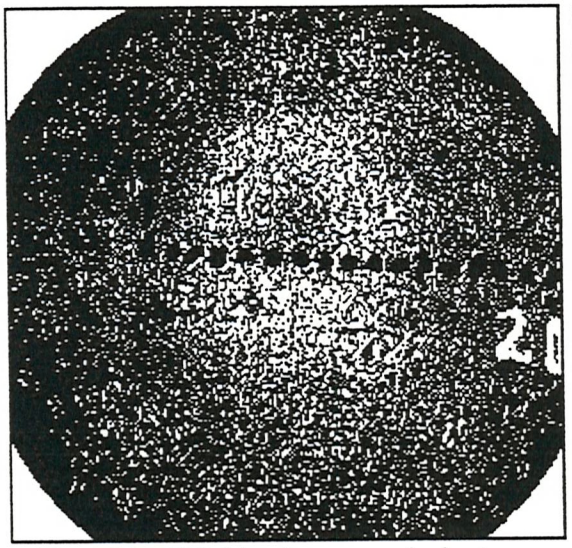

Fig. 4.2 SEM backscattered electrons image of a laser ablation linescan on preform ND862 (2 first points not apparent, core size 0.4 mm)

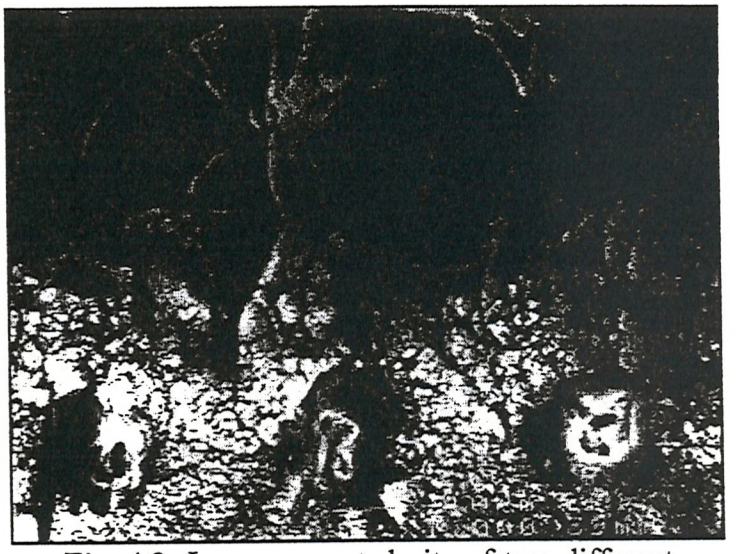

Fig. 4.3 Laser generated pits of two different linescans

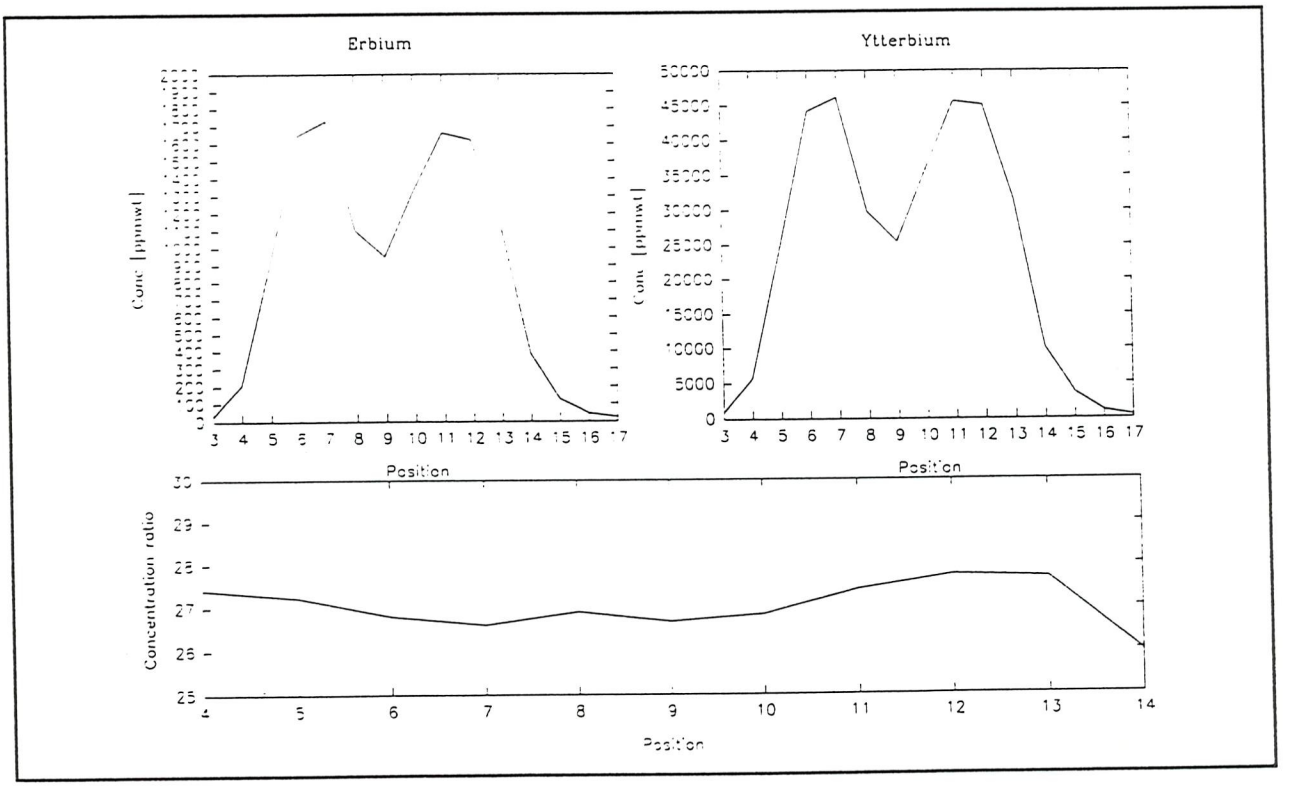

Fig. 4.4 Rare-earth concentrations across the linescan for the positions shown in Fig. 4.2 & Fig. 4.3

4.1.2 Energy Dispersive X-ray Spectrometry (EDS):

The EDS is an X-ray analysis method. An incident electron ejects a K, L or M electron of a collided atom which subsequently relaxes, emitting an Auger electron or an X-ray. Details on the line nomenclature and X-ray analysis can be found in [Goldstein_92]. The X-rays emitted by the bombarded sample are detected by a p-i-n diode and statistics are built up in 100 seconds or so. We list the main detectable lines emitted by the elements present in our fibres in Table 4.2.

Element/line	Al	Si	P	Er	Yb
K	1.487	1.740	2.015	ND	ND
L	NE	NE	NE	6.948	7.414
M	NE	NE	NE	1.406	1.521

Table 4.2 Main X-ray lines Energies (in keV)
ND: Non Detectable with our detector; NE: Non Existent

This table outlines the main problem we encounter with the EDS, namely the possible overlap of different X-ray emission peaks. Although the program we use for the analysis (Tracor SQ program) can deconvolute different overlapping peaks, a minimum peak spacing of 0.2 keV is required. In our case we are concerned that the Yb M - line and the Al K - line are very closely spaced. Fortunately, the Yb - L line, which does not present any overlap, can be used to analyse the ytterbium content. Only peaks which are statistically significant should be considered for the analysis. The minimum size of the peak after background subtraction should be at least three times the standard deviation of the background at the peak position (see [Goldstein_92']). In our Er :Yb fibres no erbium peak fulfils this condition and we discard it from the list of elements to be analyzed. Due to the small amount of erbium present in the sample, typically 10 to 30 times less than the amount of ytterbium, this should not introduce a significant error in the analysis of the other elements. The oxygen content is not measured from the O -K line, as this element is too light for reliable X-ray analysis. Instead it is calculated from the oxides formula, supposing the elements to be fully oxidised.

The fibres are inserted and glued in a capillary, mounted on a plastic block and polished with small grains of Al_2O_3 (around 50 nm in diameter). The block is coated in an evaporator with a layer of carbon around 30 nm thick to reduce charging of the sample. Gold coating is avoided when elemental analysis is needed because the Au M-line (2.12 keV) interferes strongly with the P K-line (see Table 4.2).

Imaging and chemical analysis are performed using the Scanning Electron Microscope JEOL-6400 from the Geology Department of the University of Southampton and a JEOL-840A. With a tungsten filament we typically use a probe current of 10^{-9} A and an accelerating voltage of 25 kV resulting in a probe diameter of approximately 0.2μm. However, it is essential to bear in mind the resolution limit of the X-ray analysis: even if the electron beam incident on the sample surface is very thin, the X-rays will be emitted from a volume below the surface of minimum radius 1 μm, the depth of emission depending on the type of X-ray lines excited and on the atomic number of the emitting element [Goldstein_92"]. The lighter the element, the bigger the excited volume. For Si an accelerating voltage of 25 kV leads to an excited volume 5 μm in diameter [Potts_87].

To image the sample we generally use the backscattered electron image because it emphasises the differences in atomic number of the constituents [Goodhew_88]. It offers a much higher core-cladding contrast than the secondary electron image, which is more suitable to reveal the topography of the sample. The distribution of the rare-earths is imaged as the light grey region in Fig. 4.5. The image is also used to position the probe for the X-ray analysis. Indeed, the incident electrons charge the sample, leaving a remnant image of the incident beam which is used to monitor the position of the successive analysis.

Fig. 4.6 shows clearly that the fibre linescans are unable to resolve the central dip in the rare-earth distributions observed in Fig. 4.5. The analysis is nevertheless suited to compare fibres. Fig. 4.6 shows that ND844_03 and ND849_04 have very similar compositions.

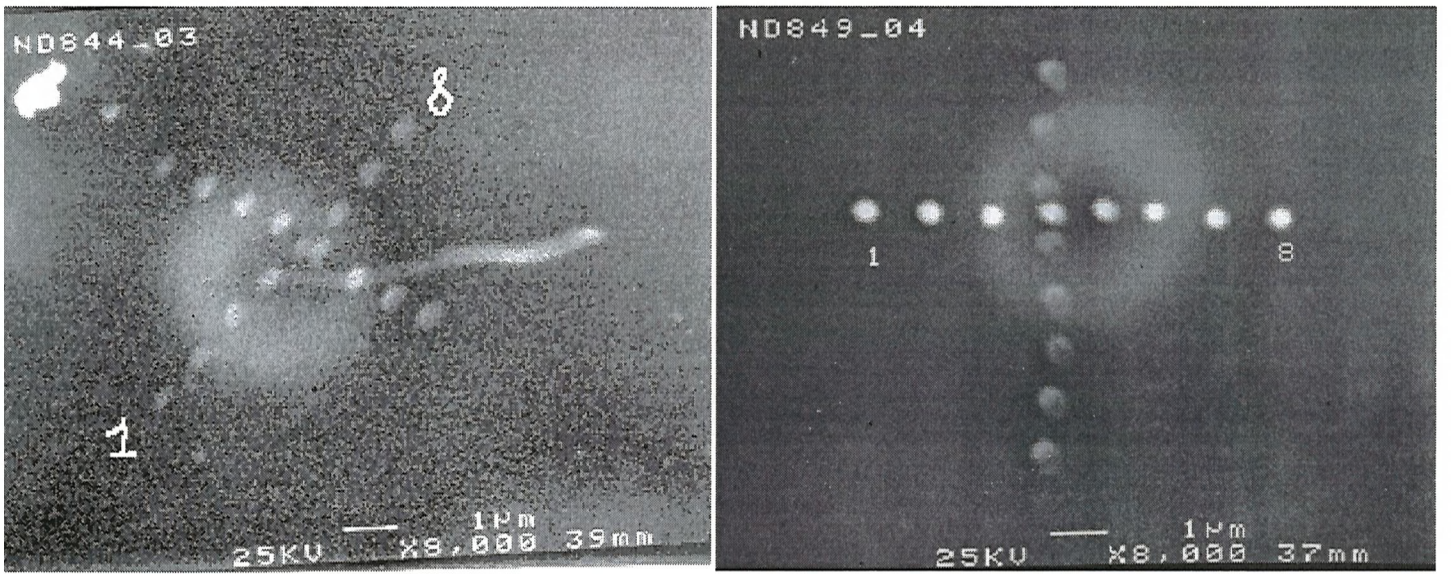

Fig. 4.5 Backscattered image of the core superimposed to secondary image showing the probe trajectory after ND844_03 & ND849_04's linescans

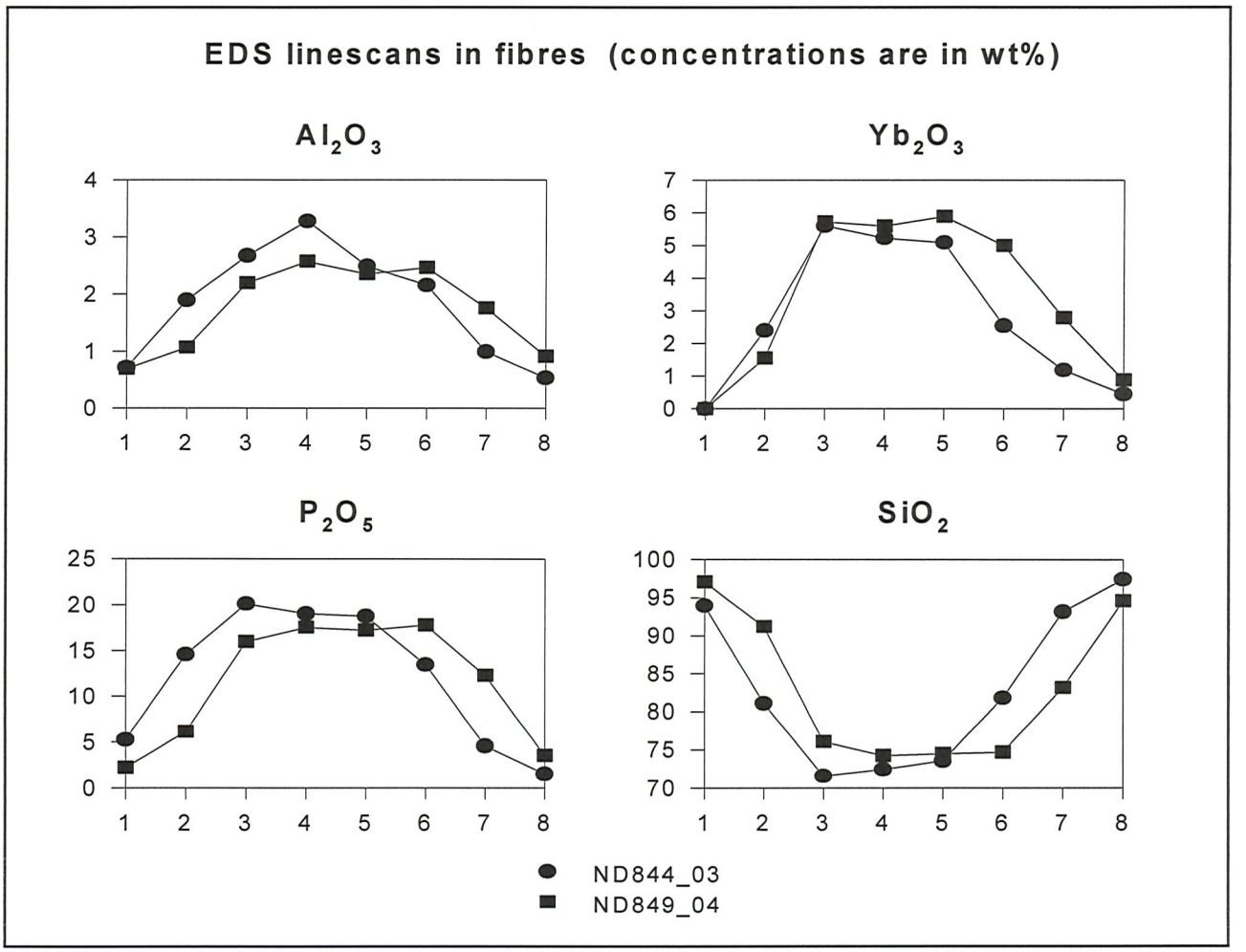

Fig. 4.6 Results of the linescans shown in Fig. 4.5 interval = 1 µm for ND844_03s linescan 1 interval = 1.1 µm for ND849_04s linescan

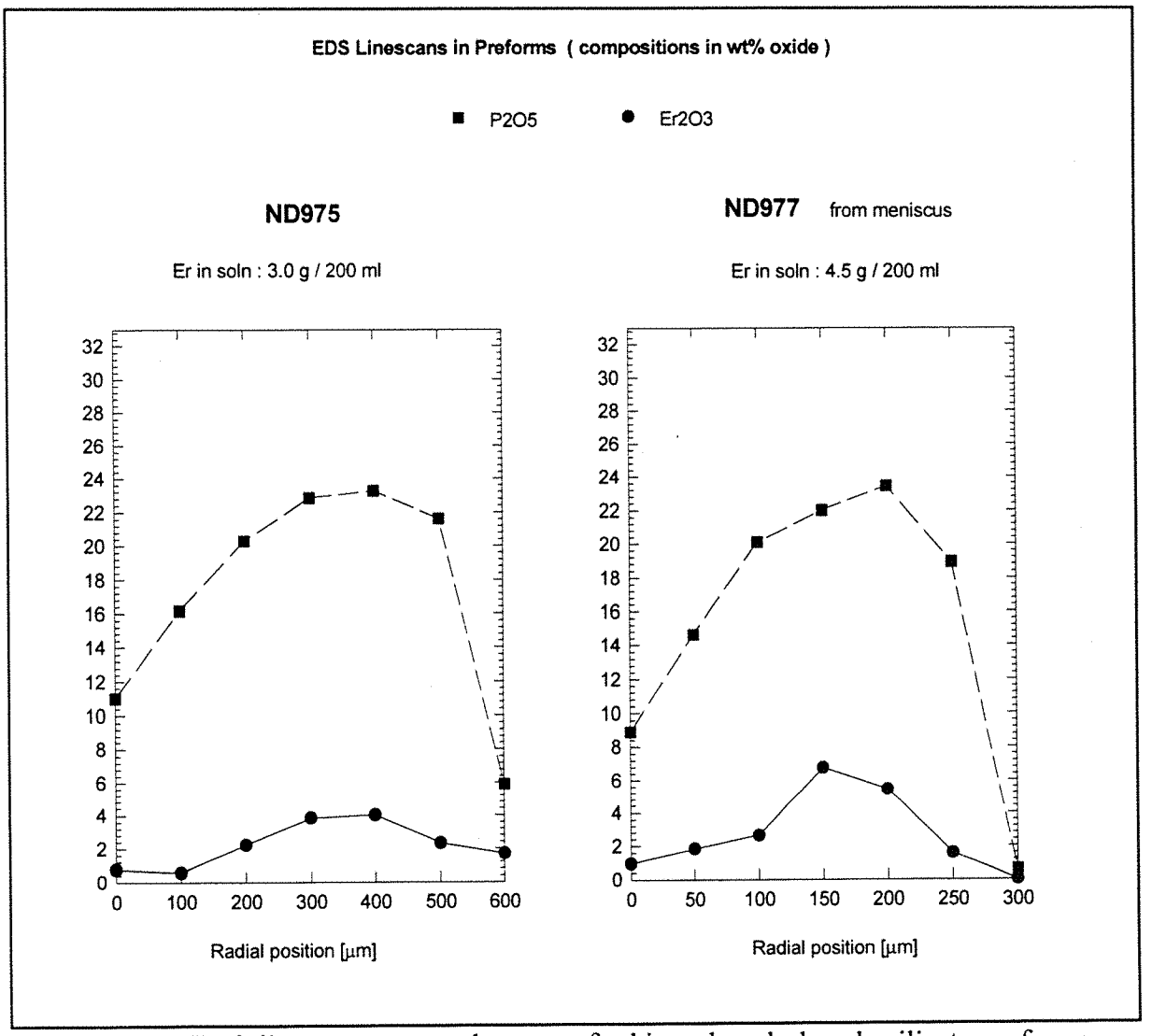

Fig. 4.7 EDS linescans across the core of erbium doped phosphosilicate preforms

In contrast to fibres, preform compositions can be mapped by an EDS analysis. Fig. 4.7 reveals clearly the evaporation dip in ND975 and ND977, which are aluminium free. The maximum P_2O_5 concentration is 23 wt% in both preforms, translating into 12 mol%. The molar refractivity of P_2O_5 is 5.5 10^{-4} mol^{-1} [Hammond_77]. This leads to an index difference of 6.6 10^{-3}, in very good agreement with the value of 6.5 10^{-3} measured in chapter 3 (see Fig. 3.3 & 3.6). This gives us confidence in the accuracy of this method to determine the P_2O_5 content. On the other hand, from comparison with optical attenuations, the erbium concentrations seem overestimated. Indeed, in Fig. 4.7 the maximum erbium oxide concentration of ND977 is 6.75 wt%, translating into 2.60 mol%(Er). This is more than twice the concentration shown in Fig. 3.7, which was obtained by attenuation measurements calibrated by ICP-MS in §4.3.3.

4.1.3 Comparison of the chemical analysis methods

To conclude this section we summarise the advantages and drawbacks of the different methods. Note that the evaluation is based on the machines available to us. It does not account for the state of the art of each technique.

	ICP-MS dissolution	ICP-MS laser ablation	EDS
Destructive	Yes	Partially	No
Sample preparation	Complex	Very Simple	Simple
Standard	Readily available	Not readily available	Readily available
Fibre analysis	No	No	Yes (comparison only)
Preform linescan	No	Yes	Yes
RE limit dtct. / accuracy	a few ppm / ++	a few ppm / ++	a few 1000ppm / -
P limit dtct. / accuracy	a few 10 ppm / +	a few 10 ppm / +	unknown / =

Table 4.3 Comparison of the chemical analysis methods

The mass spectrometry methods are much superior to the EDS method in terms of limit of detection and accuracy. This is why we will base our estimation of the erbium absorption cross-section on the measurement presented in §4.1.1. Nevertheless, the EDS provides accurate measurements of the P_2O_5 content. The ICP-MS by laser ablation seems attractive because it offers the same sensitivity as the ICP-MS by dissolution, but can also resolve the spatial distribution of the ions in preforms. It also requires minimal sample preparation. But in practice, it is difficult to position the laser beam accurately on the core. More importantly it is difficult to check whether the sample and the standard are ablated similarly.

The EDS method is suited for comparison of composition in preforms and also in fibres. It is much simpler to implement than the mass spectrometry methods and the image from the SEM provides us with the rare-earth distribution. This makes the EDS the method of choice when absolute measurements are not needed.

4.2 Raman spectroscopy

The methods presented in §4.1 allow us to determine the composition of our glass but give no information on their structure. Raman and infra-red spectroscopies are perhaps the tools most widely applied to structural studies. We measure Raman spectra to determine the vibrational characteristics of our host glass. Of particular interest is the maximum phonon energy of our host, which is critical to ensure that energy transfer is efficient (see chapter 2). We investigate whether the vibrational characteristics in our phosphosilicate fibres are modified upon addition of rare-earths.

4.2.1 Apparatus

Raman scattering is a non-linear effect and thus a high intensity light source is required. The scattered light intensity can be shown to be proportional to the fourth power of the frequency of the exciting beam [Loudon_83]. Thus a short wavelength source is preferred and the most appropriate source available to us is an argon laser (Coherent Innova 70). We select the 476.5 nm line to excite the samples. This excitation wavelength is chosen to avoid any absorption by the erbium and to put the 900-1500 cm^{-1} Raman shifted light in a wavelength range as free of fluorescence as possible.

The spectra are taken on a commercial triple grating micro-Raman spectrometer (Jobin-Yvon S3000). The excitation laser and back-scattered Raman signal are guided to and from the fibre through a microscope to enable a spatial resolution sufficient to probe small areas such as the core of the fibre.

To detect the Raman signal a 578 * 385 pixel CCD array is used. It is cooled to 144 K by a weak thermal link to a liquid nitrogen bath (Astromed CCD 3200 from Jobin Yvon). For the configuration of our spectrometer a spectral region of around 230 cm^{-1} can be acquired in one CCD image, a technique called multichannel detection. The signal to noise ratio depends on the exposure time of each CCD (we use 10 sec) and on the number of images averaged, or 'shots' (typically from 1 to 10).

4.2.2 Spectra

Raman spectra of crystals show sharp lines corresponding to the well defined phonon modes of the crystal. In glasses, the observed Raman peaks are not normally sharp and well defined, instead broad bands are observed, which is to be expected since there are no well defined discrete vibrational modes in a glass due to the absence of long range order. However, many authors have assigned Raman peaks in glasses to certain motions of the constituent ions through polarisation and isotope exchange studies.

Fig. 4.8 shows the spectra measured in an undoped phosphosilicate fibre containing 8 mol% P_2O_5 and three erbium doped phosphosilicate fibres containing 12 mol% P_2O_5. As we are interested in comparing intensities, our results are normalised with respect to a reference band at 800 cm^{-1} which is due to the Si - O - Si bond stretching vibration. Other bands due to silica are present at 600 cm^{-1}, 1050 cm^{-1} and 1180 cm^{-1}. The sharp features are spurious lasing plasma lines.

Introduction of phosphorus provides the high energy phonons required. Indeed, we see in Fig. 4.8 that the phosphosilicate fibres present a high phonon energy peak at 1330 cm^{-1}. This peak has been assigned to the vibration mode of the P = O double bond [Galeener_79]. The presence of P = O double bond implies that phosphate Q^3 groups are present in our glass. The spectrum of the undoped phosphosilicate fibre is similar to the spectrum reported for an undoped phosphosilicate fibre fabricated by the VAD technique containing 14 mol% P_2O_5 [Shibata_81]. However, Shibata could clearly observe a scattering peak at 1145 cm^{-1}, which we do not observe on Fig. 4.8. He assigned this peak to the Si - O - P bond stretching vibration, and concluded that the fibre core was made up of a random network of SiO_2 and P_2O_5 tetrahedra. It is interesting to note that with a concentration of 30 mol% P_2O_5 the peak at 1145 cm^{-1} was no longer visible, and a new peak around 1200 cm^{-1} had appeared. This peak was assigned to the O - P - O stretching vibration and its emergence suggested that a phase of interconnected phosphate chains had been formed. The spectrum of the undoped phosphosilicate fibre shown in Fig. 4.8 does not show any well defined peaks at 1145 cm^{-1} or 1200 cm^{-1}, so that it is not possible to find out from this measurement whether or not the phosphate groups are randomly dispersed within the silica.

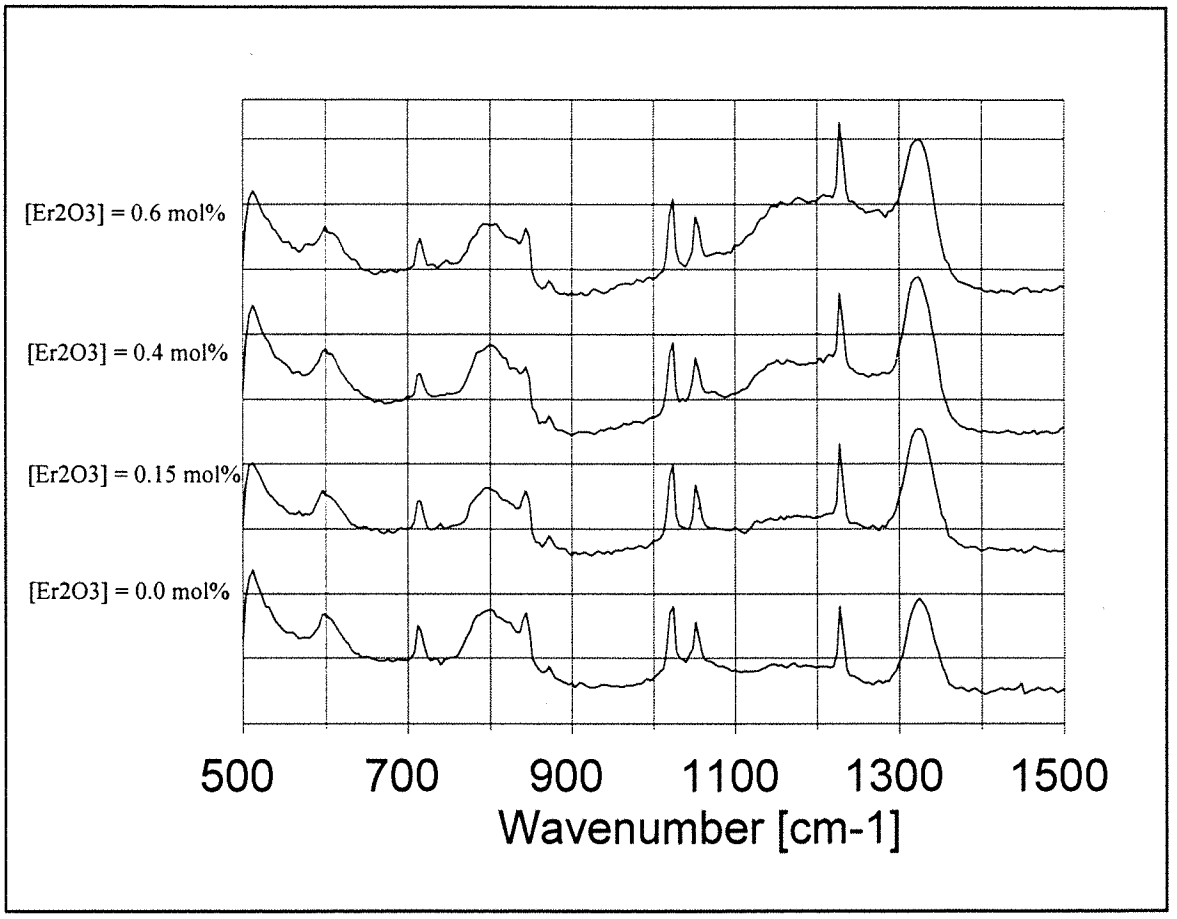

Fig. 4.8 Raman spectra of phosphosilicate fibres doped with different amounts of erbium

Fig . 4.8 shows that the spectrum is not dramatically altered by the introduction of the erbium ions. In particular no Si - O^- vibration peak appears. Similarly, no peak at 550 cm^{-1}, 850 cm^{-1} or 950 cm^{-1} associated with Si - O^- vibrations appeared upon addition of sodium to a phosphosilicate glass [Nelson_85]. This excludes the association of non-bridging oxygens with SiO_2 so that the rare-earths have to be coordinated by phosphate groups. We see in Fig. 4.8 that the only noticeable effect of the increasing rare-earth content is an increase in scattering around 1200 cm^{-1}. A similar trend has been observed when Na^+ was added to an equimolar SiO_2 - P_2O_5 glass [Chakraborty_85]. Chakraborty concluded that the sodium combined with P_2O_5 to form metaphosphate chains while residual P_2O_5 combined with SiO_2. We propose that the same structural change occurs upon addition of rare-earths.

4.3 Attenuation, cutoff and cross-section measurements

The attenuation, cutoff and cross section measurements are essential to the fibre characterisation. The background loss measurements may reveal the presence of impurities, scattering centres or colour centres. The absorption spectra are less dependent on the host glass for the rare-earth ions than for other ions, such as the transition metal ions, but their shape is nevertheless characteristic of the host glass. The cutoff wavelength is needed to work out the mode-dopant overlaps and we will show that the cutoff wavelength can be optimised to obtain a maximum lasing output power. We will calculate the dependence of the beam-dopants overlap factor on the cutoff wavelength for two fibres having different refractive index profiles and dopant distributions. This calculation, combined with results from §4.1, will enable us to work out erbium and ytterbium absorption cross sections. Knowledge of the absorption cross sections will in turn prove very useful to estimate the rare-earth concentrations from the optical measurements presented in this section, without systematically having to resort to chemical analysis.

4.3.1 Attenuations

The measurements are carried out by the cutback technique, thereby eliminating detector and system responses. For the background loss measurement we usually need at least 100 m of fibres to obtain an accurate measurement.

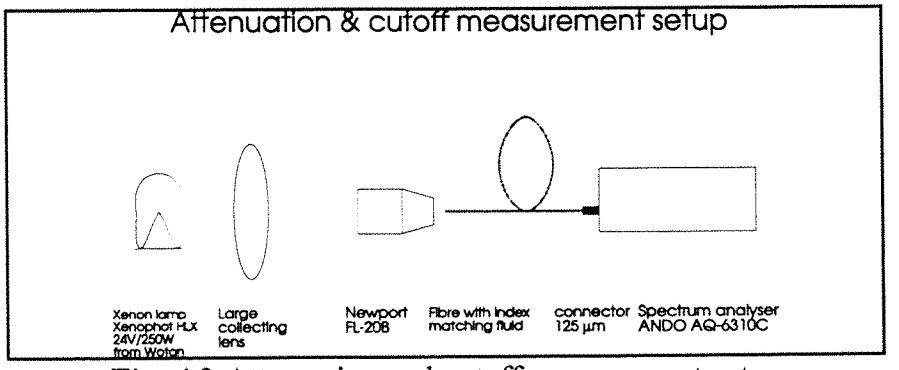

Fig. 4.9 Attenuation and cutoff measurement setup

We use the setup shown in Fig. 4.9 for the attenuation and cutoff measurements. The spectrum analyser is sometimes replaced by a grating monochromator and a Si detector for the 400 - 1100 nm wavelength range or a N_2-cooled Ge detector for the 800 - 1800 nm range. To resolve the 1535 nm absorption peak of Er^{3+} it was often necessary to replace the white light source by an ELED emitting in the 1400 - 1600 nm region.

4.3.1.1 Background loss

Fig. 4.10 shows a typical Er/Yb phosphosilicate fibre background loss spectrum. The measurement is done in a codoped fibre and the absorptions of the ytterbium and erbium contribute to the spectrum. The peak at 1300 nm is a feature which, to the author's knowledge, has not been reported before. The magnitude of this peak increases with the erbium concentration, but is independent of the ytterbium concentration. We quantify the peak absorption at 1300 nm to 0.5 dB / m / mol%(Er^{3+}).

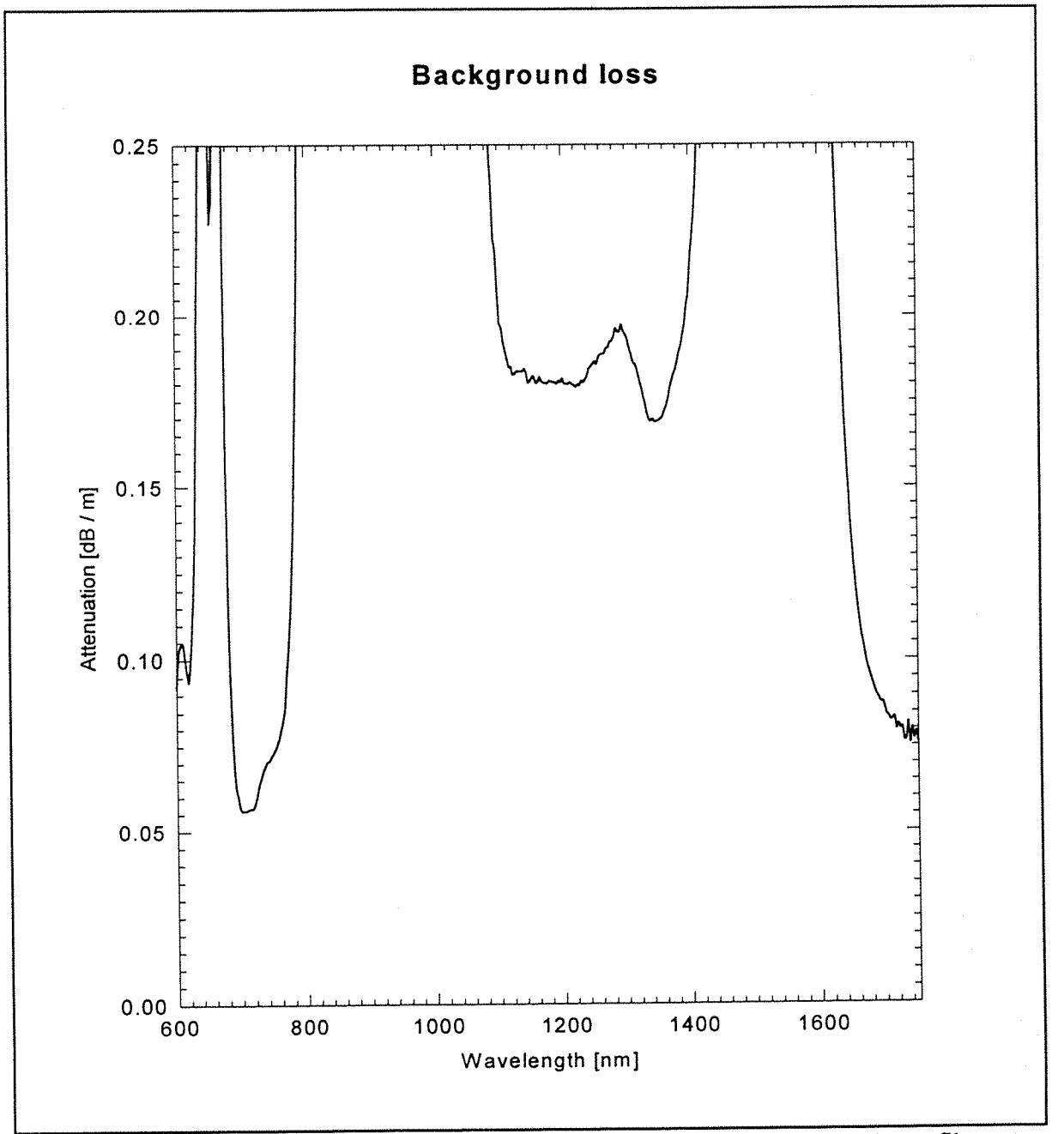

Fig. 4.10 Background loss in an erbium ytterbium codoped phosphosilicate fibre

Interpolating in the regions of rare-earth absorption, the overall shape of the background loss spectrum is known from Fig. 4.10. It is significantly different from the shape observed in erbium doped germanosilicate fibres, but similar to the shape observed in erbium doped aluminosilicate fibres [Craig-Ryan_89]. Craig-Ryan proposed that the excess loss around 1200 nm was caused by Fe^{2+} contamination. This was not an unreasonable assumption since Fe^{2+} has a broad absorption band centred at 1100 nm [Dong_92]. Craig-Ryan suggested that the aluminium precursor was the source of contamination. However, no aluminium was introduced in our fibres. Another possible source of contamination is the rare-earth chloride introduced in the doping solution. But one fact contradicts this assumption : in Er/Yb codoped germanosilicate fibres no large absorption peak centred near 1100 nm can be seen.

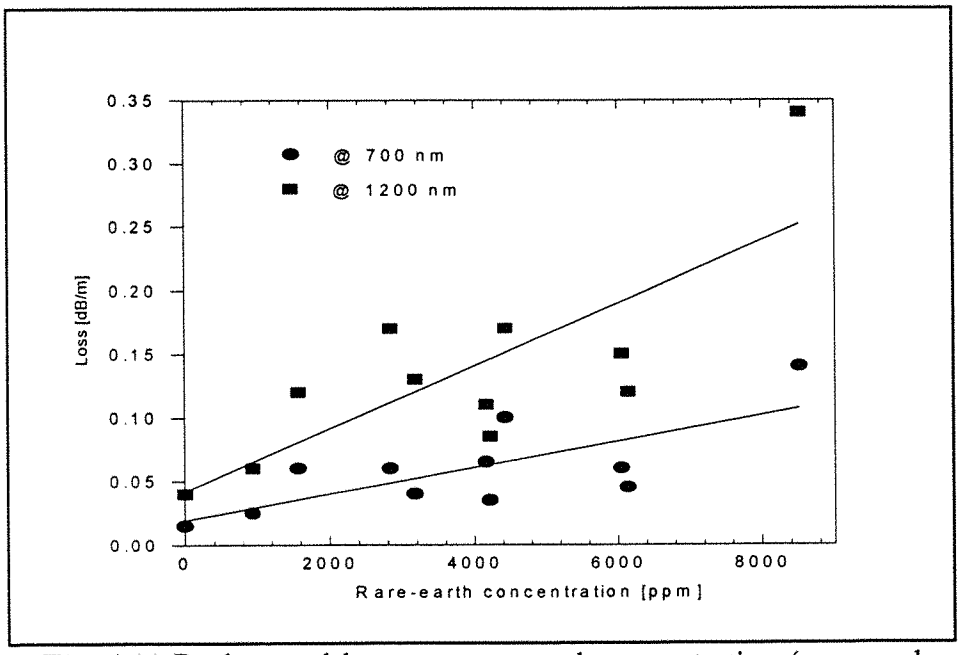

Fig. 4.11 Background losses vs rare-earth concentration (measured using the technique described in §4.3.3)

Fig. 4. 11 shows that the minimum losses increase with the rare-earth concentration, but with large variations. We associate these variations to changes in the presintering of the frit, which occurred as the tube diameter at the deposition stage was varied. The presintering temperature was lower in the preforms from which the two fibres containing 6000 ppm of rare-earths were pulled. When part of the frit is fused at the presintering stage, the sites available to the rare-earths are reduced, and clustering is more likely. In a fibre pulled from a preform whose frit was very presintered and appeared very thin, scattering by clusters was seen although the total rare-earth concentration was only 3000 ppm. Note however that the losses at 700 nm remain lower than the losses around 1200 nm for the whole range of concentrations tested in Fig. 4.11. So here the origin of the loss cannot be attributed to scattering, which predicts a loss increase with decreasing wavelength [France_90].

Measurements in two undoped phosphosilicate fibres showed the same shape as observed in Fig. 4.10, and the broad peak absorption at 1100 nm was only 40 dB / km. Carter also observed the same broad absorption in undoped phosphosilicate fibres fabricated by flash condensation of phosphoric acid [Carter_94]. From Electron Spin Resonance (ESR) measurements he attributed the broad absorption peak to the presence of a defect centre, but could not identify it. When irradiating a phosphosilicate fibre, Griscom had previously observed that a broad absorption centred at 1100 nm could be induced [Griscom_83].

Many researchers showed that phosphosilicate fibres exhibiting less than 1 dB / km loss at 1 μm could be produced, and the addition of phosphorus was even seen to reduce the loss of optical fibres [Gambling_76'], [Horiguchi_76], [Tajima_92]. In contrast, fibres produced by the phosphoric acid route exhibited a peak absorption of 1000 dB / km or more. This is a good indication that the structure of phosphosilicate fibres is strongly dependent on the preparation technique. In the low loss fibres, the phosphate units are probably well dispersed in the silica network, whereas Carter could show from atomic force microscope measurements that fibres produced by the phosphoric acid route contain spherical phases of P_2O_5 around 50 nm in diameter [Carter_94]. These phases are expected to be larger than when vapour deposition techniques are used, because of the poor initial intermixing of phosphorus with the silica frit, which is inherent to the phosphoric acid fabrication technique. Our fibres have intermediate background loss. This gives us reason to believe that they contain phosphorus rich phases, but that they are smaller than in fibres produced by the phosphoric acid route. The increase in background loss with rare-earth concentration must be due to the growth of phosphate rich regions to accommodate the modifiers. The large proportion of phosphorus in the rare-earth clusters (see §3.2.3) corroborates this interpretation. Furthermore, we have observed in aluminophosphosilicate fibres that the visible phase separation resulting from structures in the frit (see Fig. 3.16) can lead to losses of up to 1 dB/m at 1200 nm. The ratio of the losses at 1200 and 700 nm was 2-3, suggesting that in that case also, the main effect of the phase separation on the background loss was not scattering, but rather generation of defects.

In conclusion, the origin of the background loss is not yet clearly identified, but comparison with the literature suggest that it is related to the formation of defect centres due to phase separation. The addition of rare-earths favours the growth of phosphorus rich phases, and results in an increase in background loss with rare-earth concentration.

4.3.1.2 Ytterbium absorption :

The peak absorption due to ytterbium is usually too high to be measured in our fibres. However, we could resolve the entire spectrum in a fibre doped with 500 ppm. In Fig. 4.12 we see that even at room temperature we can observe three absorption peaks corresponding to the three Stark levels of the $^4F_{5/2}$ multiplet of ytterbium at 913, 940 and 975 nm. The three Stark levels within this multiplet can be better resolved by lowering the temperature with liquid helium [Carter_94]. The inset in Fig. 4.12 shows the particularly large peak absorption at 975 nm. The absorption cross-section at the peak is around 10 times greater than the absorption of erbium at 980 nm (see Fig. 1.3). However, this peak is particularly narrow, making it difficult to fully exploit this very high peak cross-section when pumping with semiconductor laser diodes. The Full Width Half Maximum is 5 nm, compared to 18 nm for the erbium absorption peak at 980 nm. The narrowness may be caused by the small degree of directionality of the P = O double bond and the subsequent low inhomogeneous broadening.

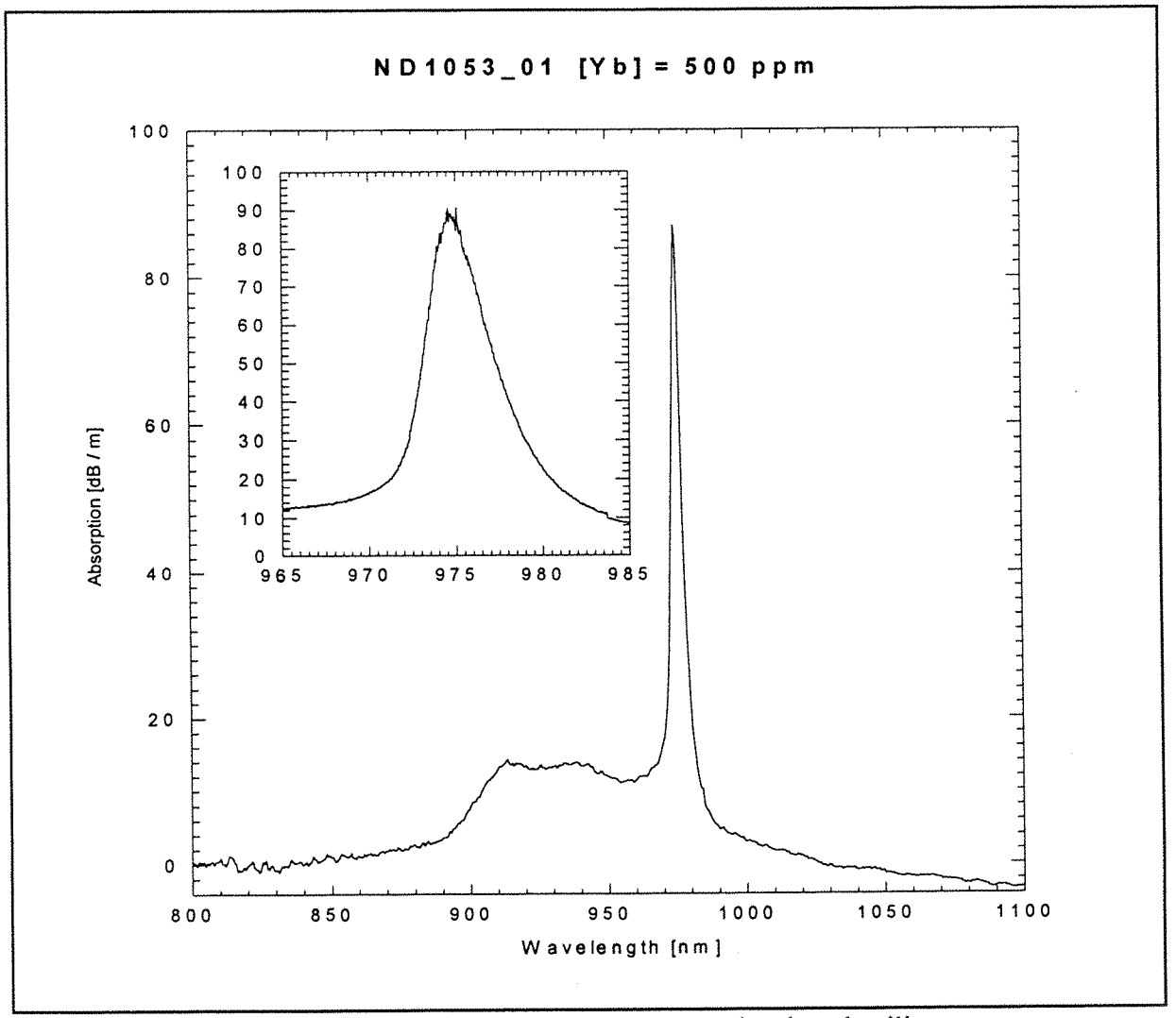

Fig. 4.12 Ytterbium absorption spectrum in phosphosilicate

4.3.1.3 Erbium absorption and emission spectra

Fig. 4.13 shows the absorption spectrum of Er^{3+} around 1500 nm in different silica based hosts. The secondary peak at 1493 nm is typical of phosphate hosts. The ratio of the 1535 nm absorption cross-section to the 1493 nm absorption in our fibres is 2.7. In metaphosphates this ratio is nearer 2 [Roman_95]. The absorption and emission peaks are narrower in germanosilicate and phosphosilicate than in aluminogermanosilicate. In Wavelength Division Multiplexing, equal amplification over a wide spectral range is sought after, making the aluminogermanosilicate the preferred host.

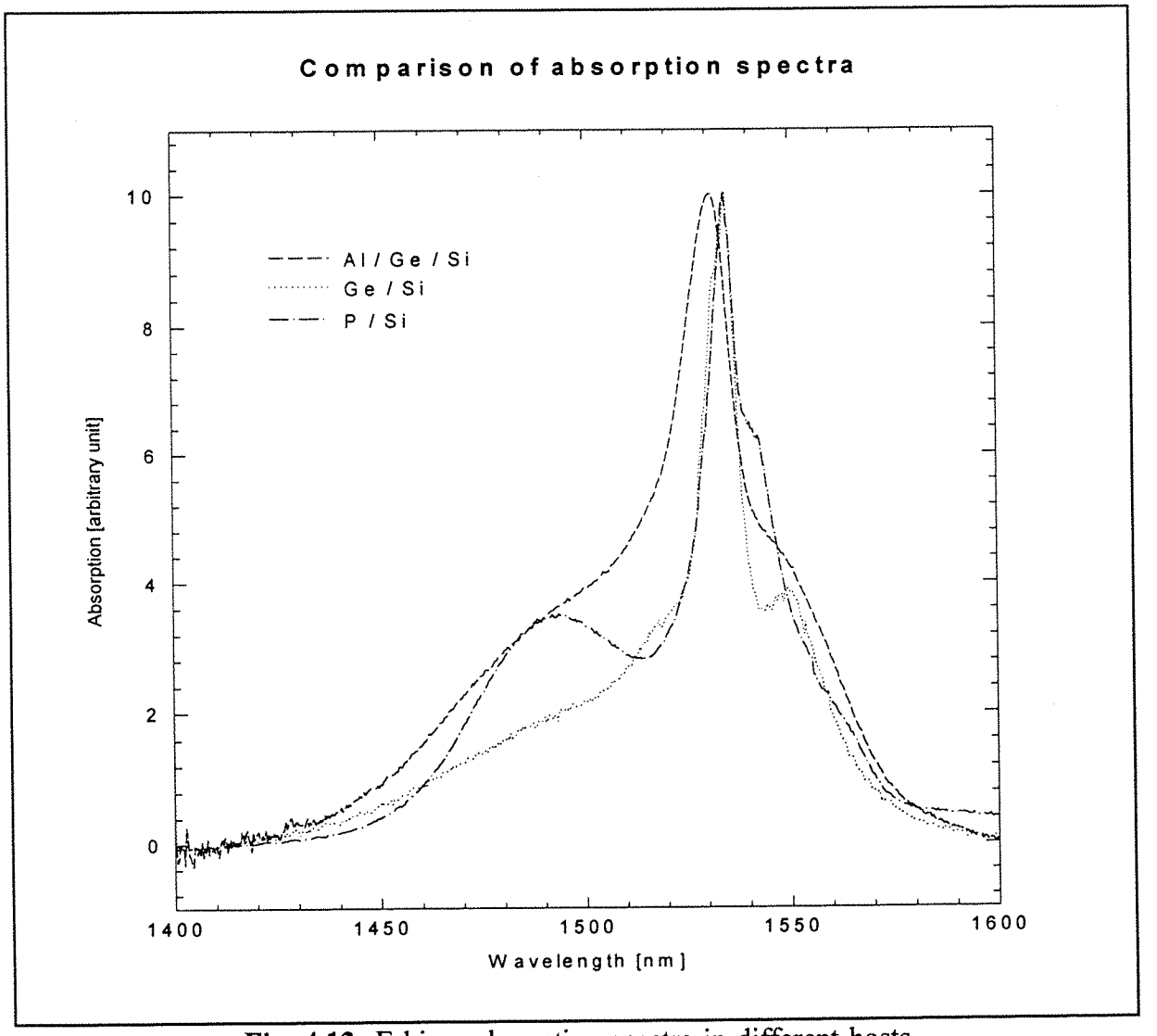

Fig. 4.13 Erbium absorption spectra in different hosts

We use the McCumber analysis to deduce the emission spectra from the absorption spectra. The only assumption of the McCumber analysis, which is verified here, is that the time to establish a thermal distribution within each manifold is short compared with the lifetime of that manifold.

The McCumber analysis [McCumber_64] relates emission and absorption cross-sections by

$$\sigma_e(\nu) = \sigma_a(\nu)\, e^{[(\varepsilon - h\upsilon)/kT]} \quad with \quad \exp(\varepsilon/kT) = \frac{1+\sum_{j=2}^{8}\exp(-E_{1j}/kT)}{\exp(-E_0/kT)[1+\sum_{j=2}^{7}\exp(-E_{2j}/kT)]} \qquad (4-6)$$

where T is the temperature, k is the Boltzmann constant, E_0 is the separation between the lowest component of each manifold and E_{ij} is the difference in energy between the jth and the lowest component of level i. We see here that the major drawback of this analysis is that the knowledge of the positions of all Stark levels in both manifolds is required. However, Miniscalco has shown in [Miniscalco_91] that a full knowledge of the Stark levels is not necessary. He observed that at room temperature the peaks of the absorption and the emission spectra of erbium are almost always within 1 nm. Fig. 4.14 shows the calculated emission spectra considering that the absorption and emission peaks coincide.

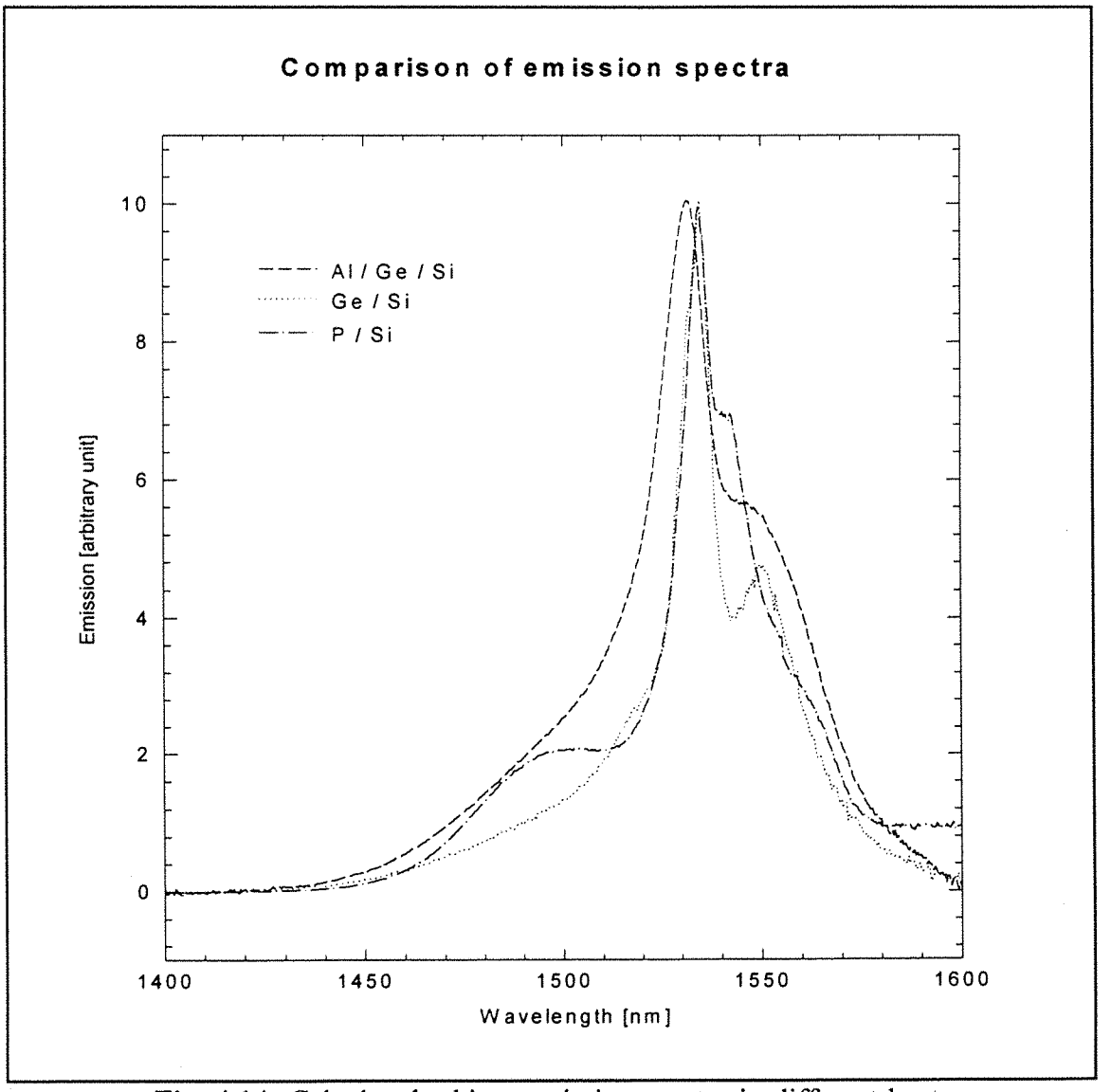

Fig. 4.14 Calculated erbium emission spectra in different hosts

4.3.2 Optimal cutoff wavelength

Cutoff wavelength measurements on single-mode fibres probably cause more difficulty in interpretation than any other measurement. This is not because the measurement itself is ambiguous or difficult, but because the end users are often unfamiliar with the meaning of 'cutoff wavelength'. Theoretically, the LP_{11}-mode cutoff is defined as the wavelength above which the mode begins radiating due to a nonzero imaginary part in its propagation constant. But the practical issue is the effective cutoff, or the wavelength where the high-order modes cannot propagate significant distances. The measured cutoff depends on the length and configuration of the measured fibre and is chosen for convenience and reproducibility of the measurement, not to represent any typical system configuration.

To measure the cutoff wavelength we subtract the transmitted powers when the fibre is held as straight as possible and when a loop is introduced. To make sure that we distinguish the higher mode attenuation peak from an impurity or dopant absorption peak the size of the loop is varied. The attenuation peak extends to shorter wavelengths when the loop diameter is reduced, but the long wavelength edge of the peak remains constant. This long wavelength edge is taken as the cutoff wavelength and used for mode overlap calculations.

Fig. 4.15 shows results, which allow us to optimise the cutoff wavelength in terms of signal output power. It consists of two series of measurements, one from a 4 cm fibre laser, diode pumped around 980 nm, and one from a fibre laser several meters in length, pumped at 1053 nm by a multiwatt Nd:YLF laser. The feedback is provided by two butted mirrors in the first case, and two spliced gratings in the second case. The signal reflectivities are 100% in both cases at the input reflector, and 92.5% & 40% respectively at the output reflector.

For the purpose of the test summarised in Fig. 4.15, an Er/Yb preform doped with 600 ppm(Er3+) and 12000 ppm (Yb3+) was pulled to six different diameters ranging from 140 μm to 80 μm. The most abrupt change in laser efficiency is observed when the measured cutoff wavelength is increased to 1350 nm for the short laser and 1510 nm for the long one. This transition is due to the same effect in both cases but the different measured cutoff values at which it occurs illustrates the importance of the effective cutoff value explained above. We attribute this transition to the presence of the LP_{11} mode which is amplified, but is near its cutoff wavelength so that it is very weakly guided. It partially depletes the gain at the expense of the fundamental mode, and is dissipated in the cladding. In fact we expect that when the cutoff wavelength is further increased the laser efficiency increases, because the LP_{11} becomes

more strongly guided and can then contribute to the lasing output power.

On the shorter cutoff wavelength region, the trend is similar for both lasers, but of different amplitude. We cannot attribute the decrease in laser efficiency with shorter wavelengths to the bending losses because the effect would be much more significant in the long laser than in the short one. In the short laser the length of the fibre is fixed, but the level of inversion varies. Indeed, the gain per unit length decreases with decreasing cutoff wavelength [Digonnet_90] so that the inversion needs to be higher in the shorter cutoff wavelength laser to compensate for the losses. The higher level of inversion with shorter cutoff wavelength is confirmed by the saturation of the 80 μm fibre observed in Fig. 4.16. For larger diameters, no saturation is observed and the increase in output power with increasing cutoff wavelength is probably caused by the increase in launch efficiency.

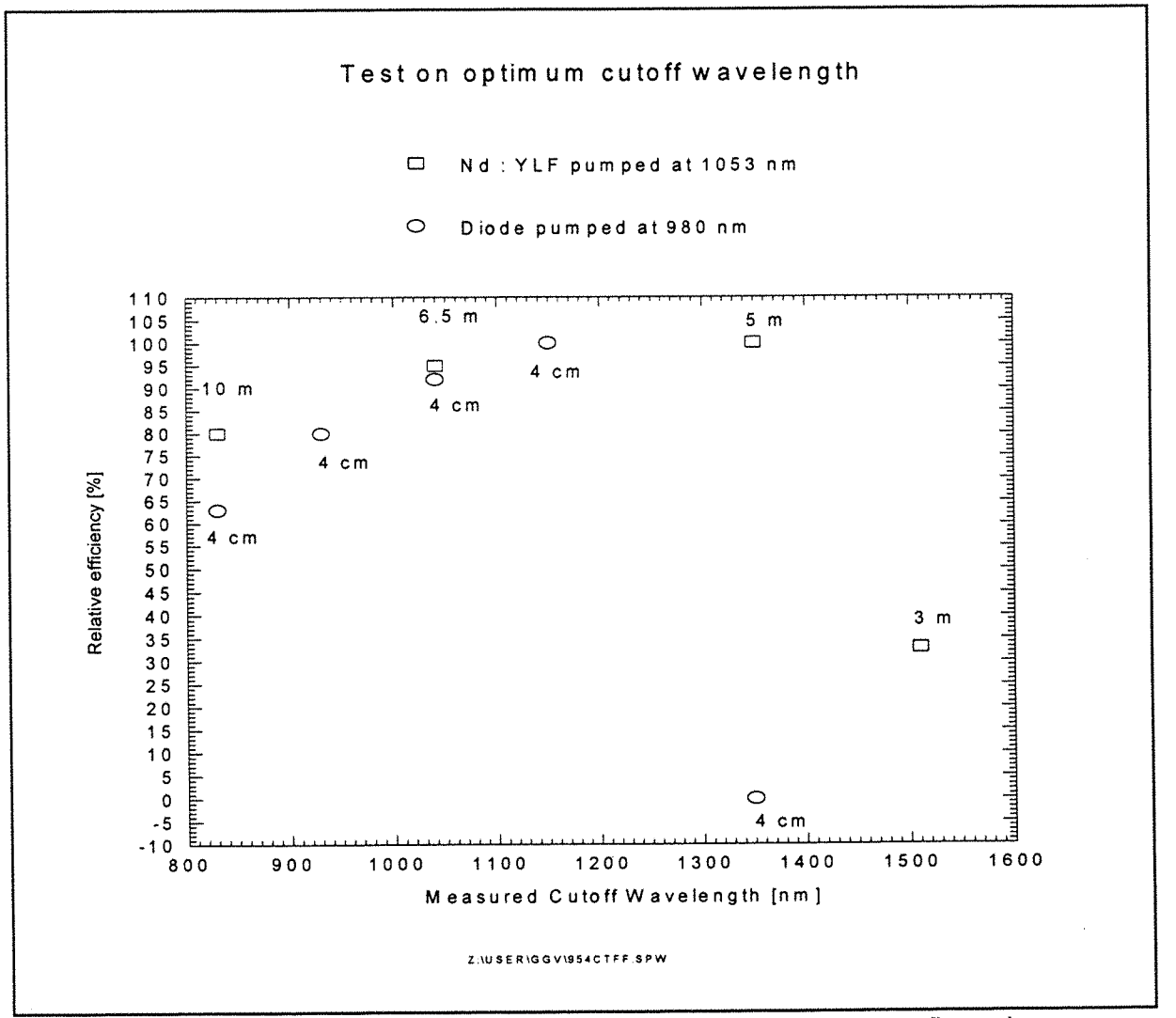

Fig. 4.15 Laser efficiency vs cutoff wavelength for two laser configurations

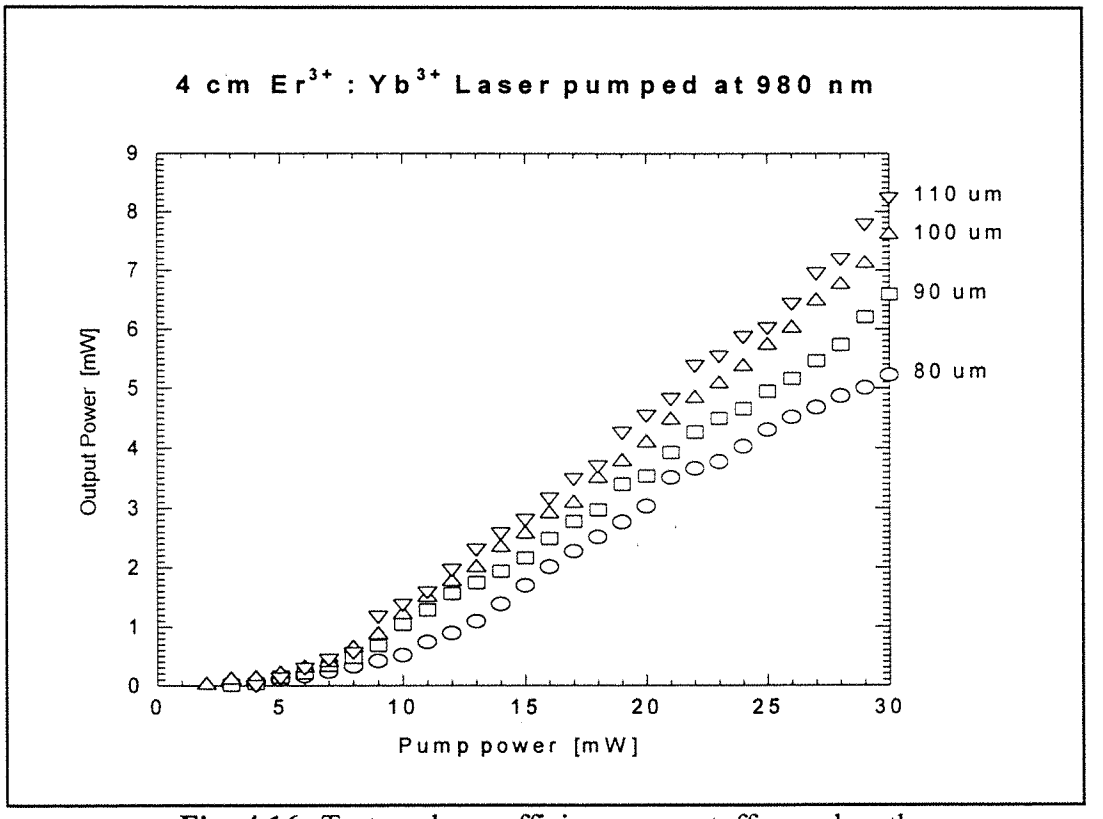

Fig. 4.16 Test on laser efficiency vs cutoff wavelength

For the long laser, the length is optimised at each cutoff wavelength so as to obtain the maximum possible output power. The optimum length increases with decreasing cutoff wavelength. As the length is increased the contribution of the background losses become more significant and the laser maximum output power is reduced.

In conclusion, we found that the optimum cutoff wavelength, i.e the measured cutoff wavelength which provides the maximum signal power, is the longest cutoff wavelength which does not allow the LP_{11} mode to deplete the gain significantly. In practice, this value varies slightly with the laser configuration, but the measured cutoff wavelength should be lower than 1500 nm in any case. A value of 1250 nm appears to be a safe choice. This is different from the case of a 980 nm pumped erbium-doped amplifier where the measured cutoff wavelength is usually chosen at around 800 nm to maintain a uniform intensity across the core [Bjarklev_94].

4.3.3 Erbium and Ytterbium cross-sections

The measurement of absorption cross-sections is more critical in fibres than in bulk samples because the dopants are not evenly distributed across the fibre core and the beam profile needs to be evaluated numerically to work out the mode-dopant overlap factor.

To simplify the problem as much as possible, we will operate at $\lambda < \lambda_{cutoff}$ to support only the fundamental mode. With the knowledge of the refractive index profile, the mode profile at the given wavelength can be calculated from the propagation equation. The index profile is often assumed to be 'top hat'. This is not a good approximation for our phosphosilicate fibres where the index profile departs strongly from this simple profile. The refractive index profiles for a typical phosphosilicate fibre and for a step index fibre are illustrated in Fig. 4.17 together with the corresponding fundamental mode intensity distributions at 1535 nm. The index difference of the step index is calculated to give the same cutoff wavelength as for the phosphosilicate profile. Note that the mode intensities are given in arbitrary units but are normalised so that both beams carry the same power.

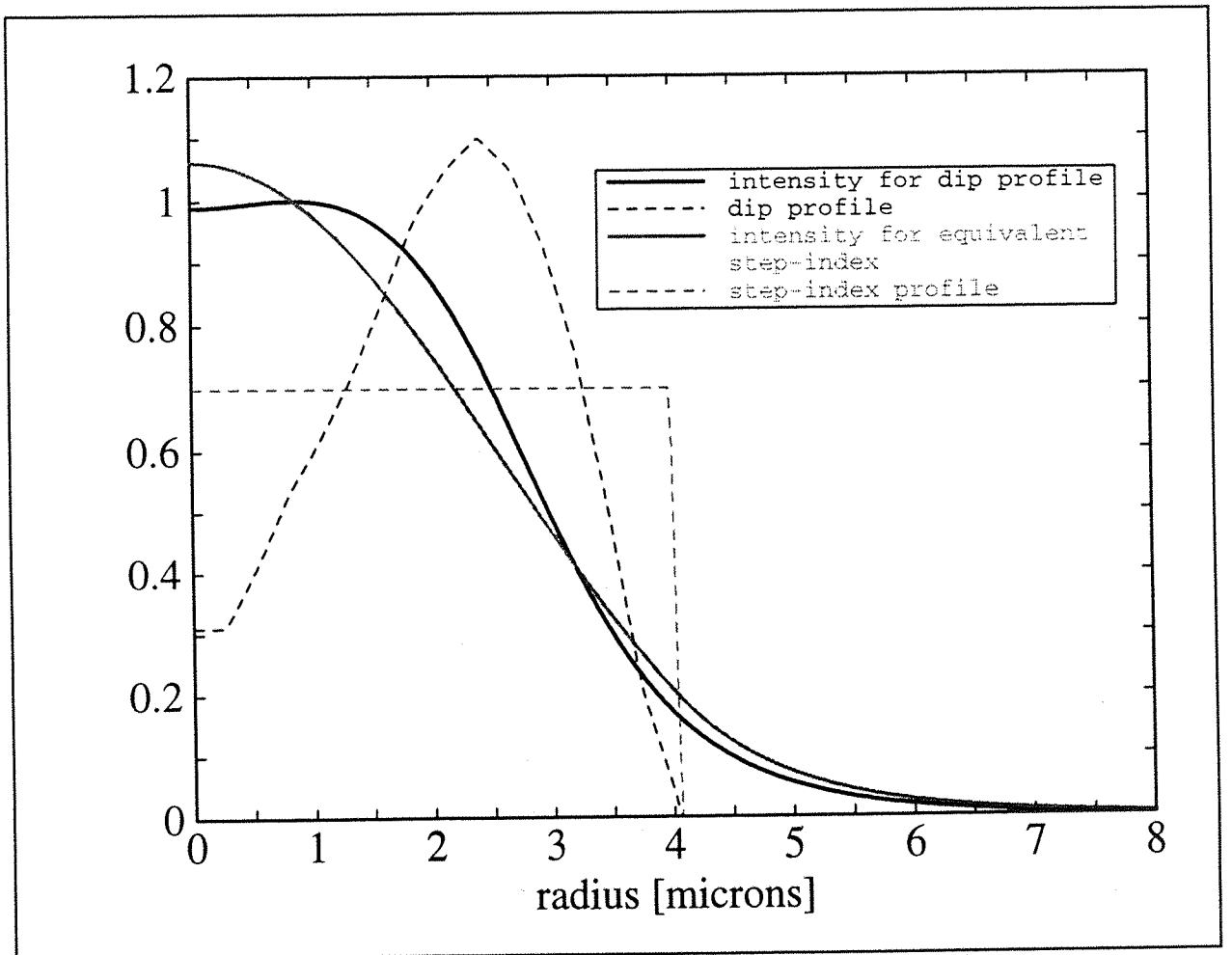

Fig. 4. 17 LP_{01} mode intensities at V = 2.35 for a typical refractive index profile and its equivalent step index profile. The scale for the refractive index difference has been multiplied by a factor of 100.

The fundamental mode-dopant overlap at the wavelength λ is given by :

$$\Gamma_\lambda = \frac{\int_0^\infty I_\lambda(r)\, n(r)\, r\, dr}{N_{RE} \int_0^\infty I_\lambda(r)\, r\, dr} \quad where \quad N_{RE} = \frac{2\int_0^\infty n(r)\, r\, dr}{R^2} \qquad (4-7)$$

$I_\lambda(r)$ is the fundamental mode intensity distribution, n(r) is the dopant density profile, N_{RE} is the rare-earth concentration, and R is the core radius. As we saw in §4.1, n(r) cannot be measured in the fibre but it is reasonable to assume that it follows the index profile. For the 'dip-profile' shown in Fig. 4.17 the average dopant concentration is 1.65 lower than the maximum concentration. Note that only the dopant density profile, not the absolute dopant concentration is needed to evaluate the overlap factor. Fig. 4.18 shows the overlap factors computed for the measured profile and for a 'top hat' profile. Also included are the values calculated using the Gaussian beam approximation [Marcuse_77] :

$$\Gamma_\lambda = \frac{P_{core}}{P_{total}} = 1 - \exp\left(-\frac{d^2}{2w^2}\right) \quad where \quad \frac{2w}{d} = 0.65 + 1.619\, V^{-3/2} + 2.879\, V^{-6} \qquad (4-8)$$

where d is the fibre diameter, w is the spot size, and $V = 2.4\, \lambda_{cutoff} / \lambda$ is the V-value. The overlap factor for the measured and 'top hat' profiles differ by maximum 15% over the whole range of wavelengths studied. The Gaussian approximation leads to the lowest overlap factor. The Gaussian approximation is indeed known to overestimate the fraction of power travelling in the cladding, particularly at low V values [Jeunhomme_83]. In this thesis we use the overlap factors calculated for the measured profile. With the additional knowledge of the optical absorption α_{1535} and the average rare-earth concentration N_{RE} defined above, we can finally calculate the absorption cross-section :

$$\sigma_\lambda^{RE} = \frac{\alpha_\lambda}{\Gamma_\lambda\, N_{RE}} \qquad (4-9)$$

We apply this procedure to ND844, whose average concentration is measured in §4.1 to be $2.38\ 10^{25}\ m^{-3}$. The absorption at 1535 nm is measured as 60 dB/m or 13.8 m^{-1} ($\alpha[m^{-1}] = \alpha[dB/m] / 4.34$). The cutoff wavelength of 1250 nm leads to $\Gamma_{1535} = 0.86$ (see Fig. 4.18). This results in $\sigma^{Er}_{1535} = 6.8\ 10^{-25}\ m^2$. This is in good agreement with the results of Alekseev *et al.* who provide peak absorption cross-sections for a number of phosphate glasses, all of which fall into the range $6 - 8\ 10^{-25}\ m^{-3}$ [Miniscalco_91].

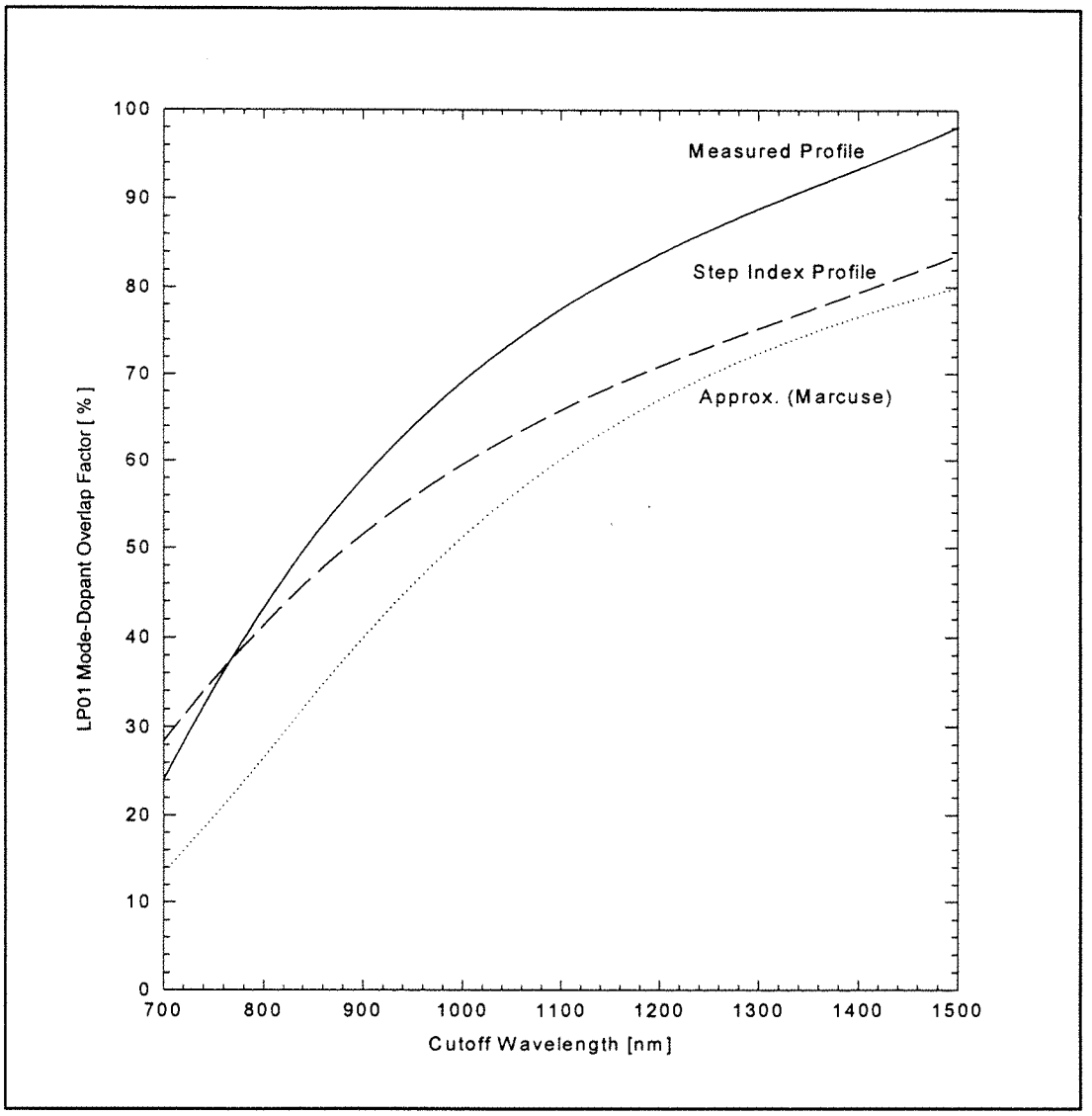

Fig. 4.18 Fundamental mode - dopant overlap factor at 1535 nm vs cutoff wavelength for the measured profile and a step index profile.

Now that the erbium absorption cross-section is known, the erbium concentrations in fibres can be deduced from absorption measurements and overlap calculations. Having verified in §4.1 that the ytterbium : erbium concentration ratio in the doping solution is conserved in the glass, we can obtain the ytterbium concentration from the erbium concentration. We used fibres with cutoff wavelengths below 900 nm to measure the ytterbium absorption cross-sections. We measured $\sigma^{Yb}_{975} = 2.1\ 10^{-24}\ m^2$. The cross-section off the peak wavelength can be scaled using Fig. 4.12, except at the tails of the spectrum. Using multiple cutbacks we obtained $\sigma^{Yb}_{1064} = 2.0\ 10^{-27}\ m^2$. Thus the ytterbium absorption cross-section at the operating wavelength of the Nd:YAG laser is a thousandth of the peak ytterbium absorption cross-section.

To deduce the emission cross-section from the absorption cross-section the following relationship, the so-called Fuchbauer- Ladenburg relationship is often used :

$$g_1 \int_0^\infty \nu^2 \sigma_a(\nu)\, d\nu = g_2 \int_0^\infty \nu^2 \sigma_e(\nu)\, d\nu \quad (4-10)$$

where g_i is the degeneracy of level i, ν is the photon frequency, σ_a and σ_e are the absorption and stimulated emission cross-sections respectively. This relationship applies only when either all components of the two levels are equally populated or all the transitions have the same strength regardless of the components involved. Neither of these two conditions are generally fulfilled.

Instead, we use a method proposed in [Barnes_91] based on the gain-loss measurement of an amplifier to determine the ratio of the peak absorption to peak emission cross section. We used a short length of fibre (4 cm) to be able to saturate the gain with the available pump power from a $Ti^{3+} : Al_2O_3$. The result of the measurement is shown in Fig 4.19.

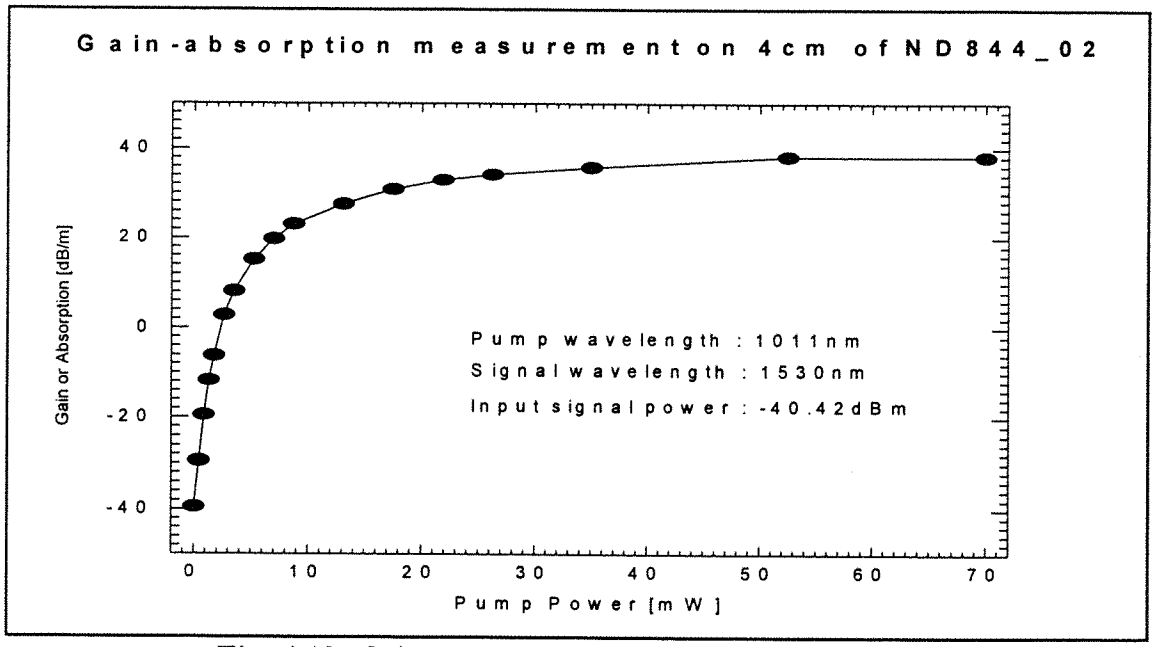

Fig. 4.19 Gain saturation measurement on ND844_02

From this measurement we can deduce the ratio of the cross sections at 1530nm:

$$\frac{\sigma_a}{\sigma_e}(1530) = \frac{Loss_{max}}{Gain_{max}}(1530) = 1.04 \quad (4-11)$$

The corresponding ratio of emission to absorption cross section at 1535nm is 1.03. The emission cross section is slightly larger than the absorption cross section at 1535nm.

4.4 Device performance

It is important rapidly to determine if a fibre shows potential for efficient devices. Two techniques used for this purpose are described below.

4.4.1 Backward Amplified Spontaneous Emission

This measurement has been proposed to evaluate the amplifier efficiency [Lee_93]. The setup is simple as it comprises only a WDM coupler spliced to a pump source, a long enough piece of the doped fibre so that all the pump is absorbed, an isolator and a detector.

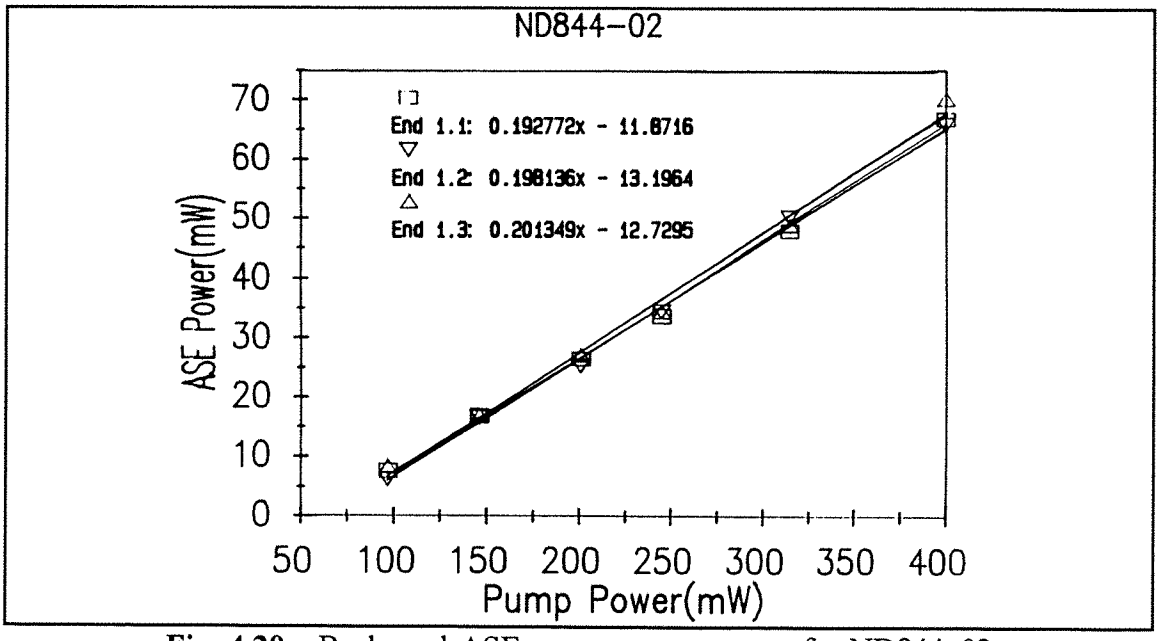

Fig. 4.20 Backward ASE power measurement for ND844_02

Measurements of backward ASE power as a function of pump power were made using a Nd-doped solid state laser as a pump source. Fig. 4.20 shows a slope of 20% for ND844_02. This value is uncorrected for the 1 dB isolator and WDM losses, so that the effective backward ASE slope is 25%. Measurements can be interpreted with a model of Er/Yb amplifiers assuming no input signal.

4.4.2 Bare-ends fibre laser

This Backward ASE method is particularly quick because the fibre length does not need to be varied. But this method does not give any information on the reabsorption which is important for the design of three level devices, and in practice we prefer to build a laser.

A fibre laser can readily be obtained by carefully cleaving both fibre ends of the doped fibre and pumping one end with a few tens of mW. The silica (2) - air (1) interface provides the coupling necessary for lasing so that no mirror butting or grating splicing are necessary. The Fresnel reflection at the interface is $r_{fresnel} = 1 - t_{fresnel} = [(n_2-n_1) / (n_2+n_1)]^2$, which gives, with $n_1=1$ and $n_2=1.46$, $r_{fresnel} = 3.5\%$.

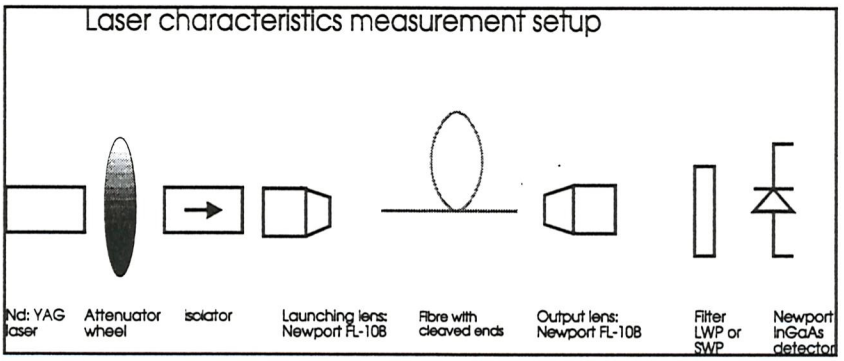

Fig. 4.21 Laser characteristics measurement setup

Fig 4.21 shows the measurement setup used. The pump source is a Nd: YAG, or a Nd:YLF laser, which allows a few hundreds of milliwatts to be launched in the fibre. The fibre length is typically a few meters to allow sufficient gain to build up. For a given length of fibre, lasing can occur only if the gain available from the bleached section equals, or exceeds, the loss of the remaining length of fibre (and of course, any other losses present). From the foregoing, it is clear that for a given amount of pump power an optimum fibre length will exist. This length will be long enough to absorb a significant fraction of the pump power but short enough to minimise reabsorption in the unbleached section. In the following, we will show an example of laser cutback measurement and comment on the information offered by this measurement.

Fig. 4.22 shows the result of a laser cutback measurement on an efficient phosphosilicate fibre with average doping concentrations of 9000 ppm(Yb^{3+}) and 600 ppm (Er^{3+}). The slope stabilises to around 25% once sufficient power has been absorbed. This value has to be compared to $s_{max} = h\nu_s / 2h\nu_p = \lambda_p / 2\lambda_s \approx 33\%$, corresponding to the maximum possible slope from one end, assuming maximum quantum efficiency. The threshold first decreases with increasing fibre length due to the reducing level of erbium inversion required to reach threshold and then increases because of increasing reabsorption.

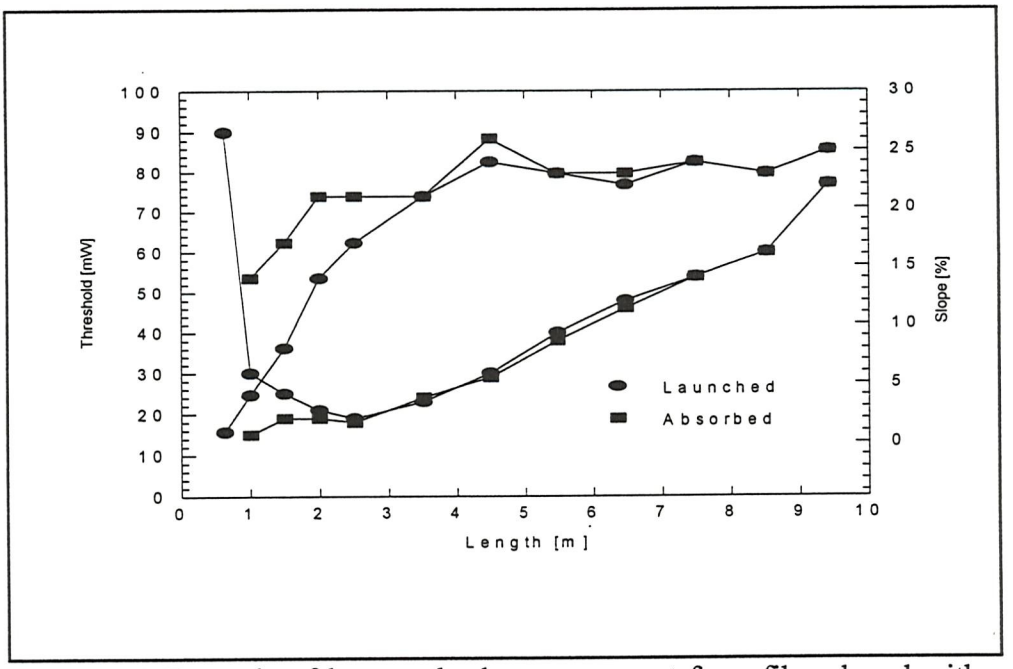

Fig. 4.22 Example of laser cutback measurement for a fibre doped with 600 ppm(Er^{3+}), 9000 ppm(Yb^{3+}), and a pump wavelength of 1047 nm.

Fig. 4.23 shows another effect of reabsorption, which was first simulated by Desurvire [Desurvire_89]. For long fibre lengths an unbleached region remains at the output end of the fibre laser which reabsorbs light preferentially over the short wavelength part of the fluorescence band. The ratio of gain to loss is thus greatest for such a system at long wavelengths and so lasing occurs around 1.56 μm. Reducing the fibre length decreases the gain so that the lasing wavelength shifts nearer to the fluorescence peak. In practice a wavelength of operation can be favoured by using wavelength selective output couplers such as gratings.

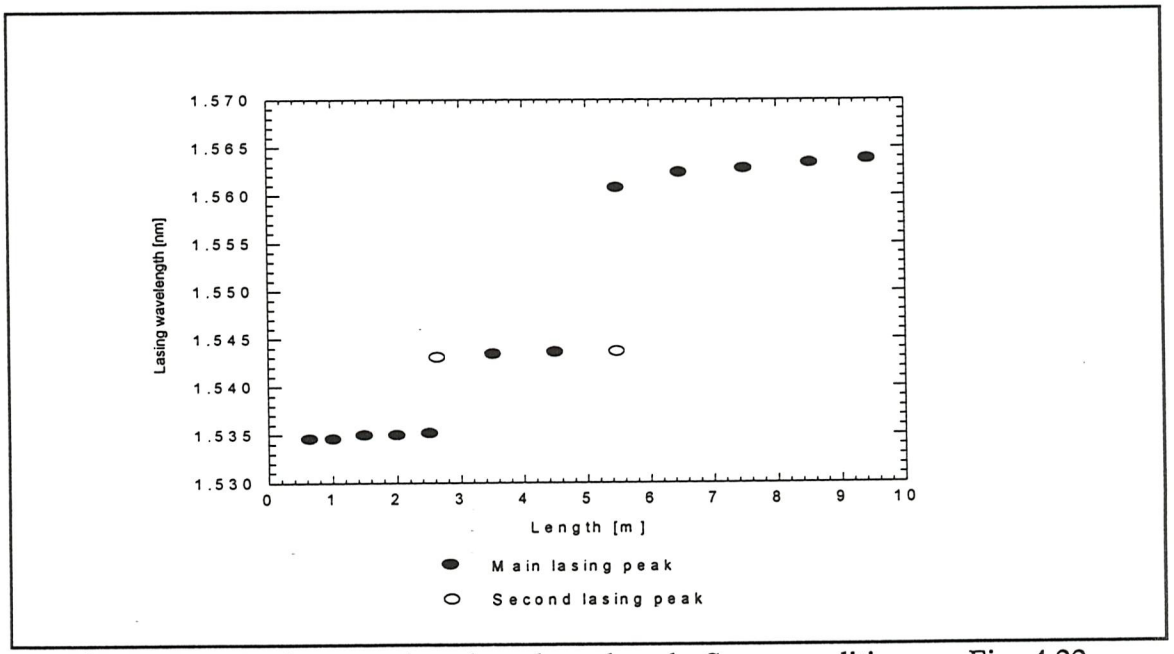

Fig. 4.23 Lasing wavelength vs laser length. Same conditions as Fig. 4.22.

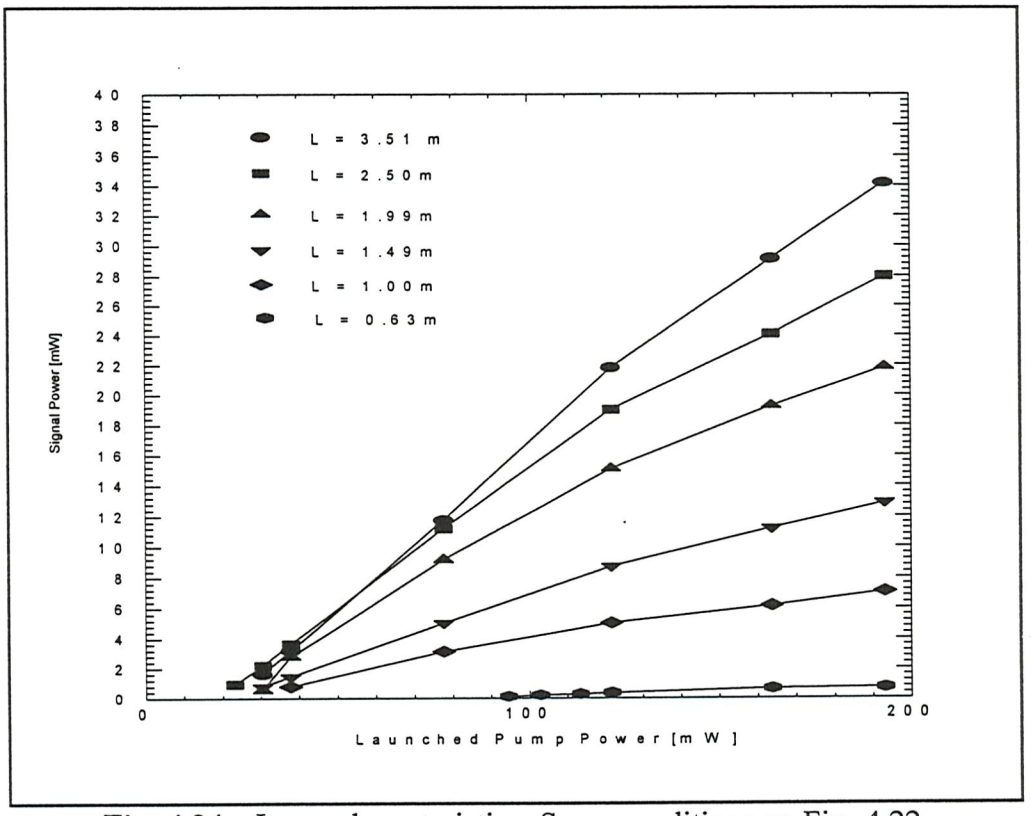

Fig. 4.24 Laser characteristics. Same conditions as Fig. 4.22.

Fig. 4.24 shows that the laser characteristics at short lengths are not linear. In this regime the laser slope is in fact power dependent. At high pump powers the erbium ions near the pump end are fully inverted and no energy transfer from ytterbium to erbium can occur. The ytterbium ions can then be considered as decoupled from the erbium ions. They are in turn highly inverted and the pump power is no longer efficiently absorbed. This bleaching of the ytterbium absorption is illustrated in Fig. 4.25. This is the so called saturation regime.

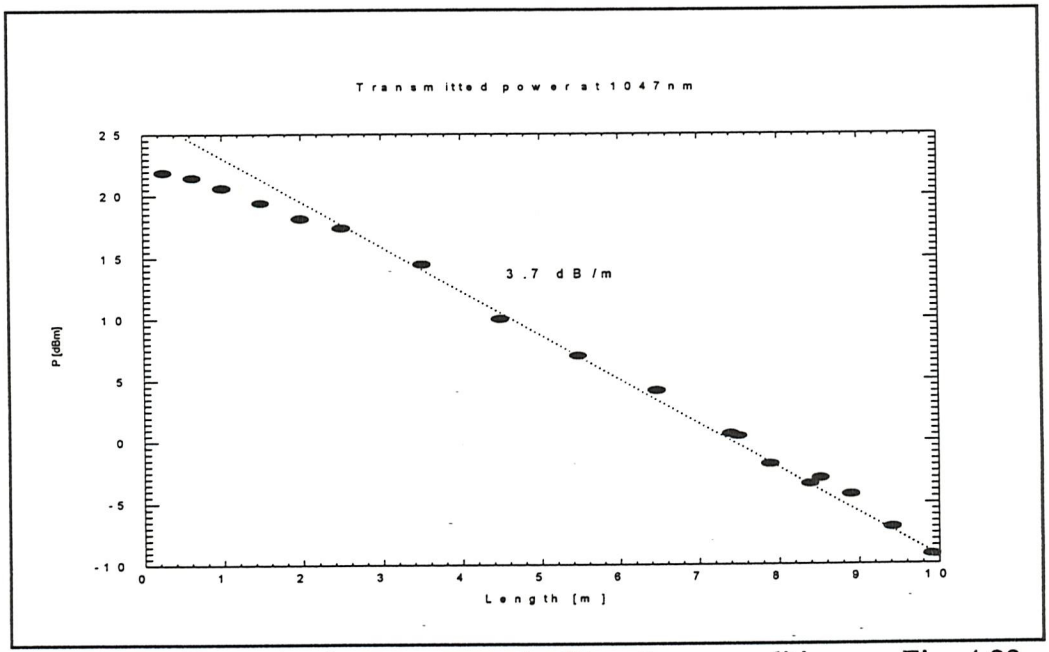

Fig. 4.25 Transmitted pump power in dBm. Same conditions as Fig. 4.22.

In Fig. 4.26 we summarise the efficiencies of fibres pumped at 1064 nm. The fibres had a pump absorption of 2.5 ± 0.5 dB/m at 1064 nm and no significant hydroxyl contamination was observed. A trend can clearly be seen in Fig. 4.26. High slope efficiencies (> 15 % for the backward ASE, > 20 % for the lasers) can be obtained until the background loss exceeds 0.3 - 0.4 dB/m. However, when the background loss becomes larger than 0.5 dB/m, the efficiency drops. This dependence of the efficiency on the background loss is due to the low pump rate at 1064 nm.

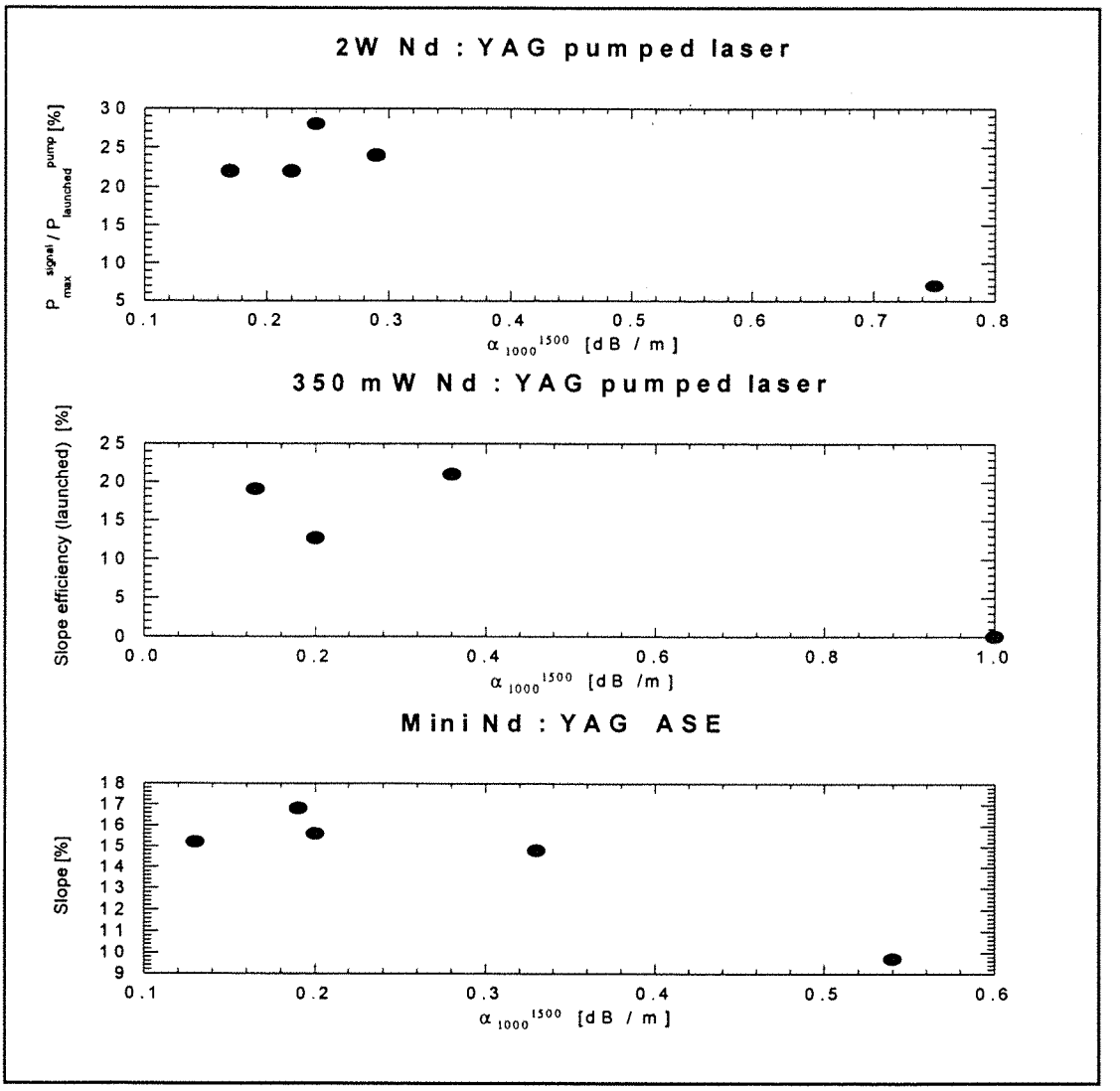

Fig. 4.26 Device efficiencies vs minimum losses between 1000 and 1500 nm. The pump absorption is 2.5 ± 0.5 dB/m in all fibres

Our interest has now shifted to 980 nm pumped devices (see §6.2). We propose that in the future, we pull our preforms with low silicone rubber coating for evaluation as cladding pumped fibres. With the high pump rate associated with 980 nm pumping, we expect the efficiency to be much less affected by the background loss. In cladding pumped fibres the pump background loss in the core has little effect as it is reduced by the first cladding to core area ratio.

4.5 Green fluorescence and upconversion

4.5.1 Green fluorescence

Green fluorescence is a well-known phenomenon in 800 nm pumped erbium doped fibre amplifiers [Miniscalco_91]. This emission results from pump Excited State Absorption (ESA) from the erbium metastable level. When pumping Er/Yb codoped fibres at 975 nm, the peak of the ytterbium absorption, we also observe some green fluorescence. This observation motivates this preliminary study.

We use a 50 mW cw laser diode emitting at 975 nm to excite the ions, a monochromator to filter the fluorescence (side-collected), and a GaAs photomultiplier (flat response 300-900 nm) to detect the signal. No attempt to measure the fluorescence power is made. Three fibres are tested : ND844_02, an efficient Er/Yb phosphosilicate fibre doped with around 13000 ppm(Yb) and 1100 ppm (Er), ND545_05, an aluminosilicate fibre doped with 19000 ppm(Yb) and 700 ppm(Er), which showed strong saturation behaviour [Fermann_88], and HD212, an inefficient codoped germanosilicate fibre.

Fig.4.27 shows the lower-lying energy levels of the ytterbium and erbium ions. Three mechanisms can populate the $^4F_{7/2}$ and thus give rise to green fluorescence from the erbium ions. This level can be excited by pump ESA from the $^4I_{11/2}$ level, by energy transfer from an ytterbium ion excited in the $^2F_{5/2}$ level to an erbium ion excited in the $^4I_{11/2}$ level, or by energy transfer between two ions excited in the $^4I_{11/2}$ level. Note that this latter mechanism is very unlikely, as it involves two ions excited simultaneously in the weakly populated $^4I_{11/2}$ level.

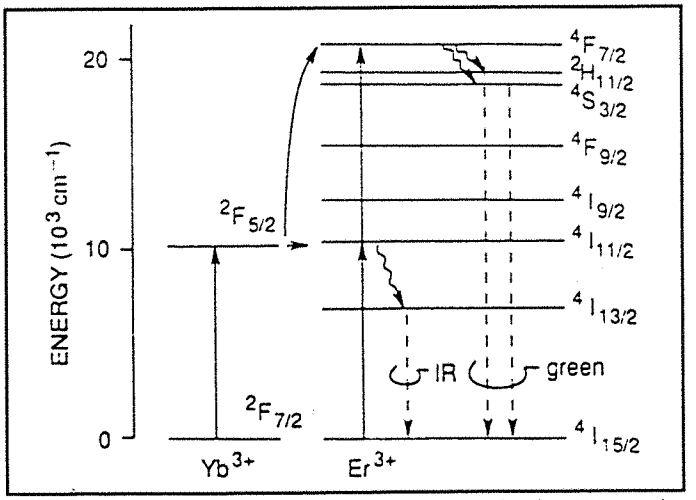

Fig. 4.27 Lower-lying energy levels for Er and Yb with excitation paths

An erbium ion excited in the $^4F_{7/2}$ relaxes quasi-instantaneously onto the $^2H_{11/2}$ and $^4S_{3/2}$ where further relaxation occurs by multiphonon decay, and to a lesser extent, by radiative transition to the ground state. The $^2H_{11/2}$ level is thermally populated from the $^4S_{3/2}$ level. The emissions from the $^2H_{11/2}$ and the $^4S_{3/2}$ levels are responsible for the two bands at 525 nm and 550 nm

respectively, observed in Fig. 4.28. At the blue edge of the spectrum of ND545 the spectral shape corresponds to the convolution of the infra-red fluorescence of Yb^{3+} with itself, implying the presence of cooperative luminescence in Yb^{3+} [Magne_93]. A peak at 480 nm is present in the spectrum of ND844. A similar peak, implying the occurrence of an upconversion process involving more than two photons, has been reported in [Jackel_92]. However, these two processes appear marginal compared to the green fluorescence.

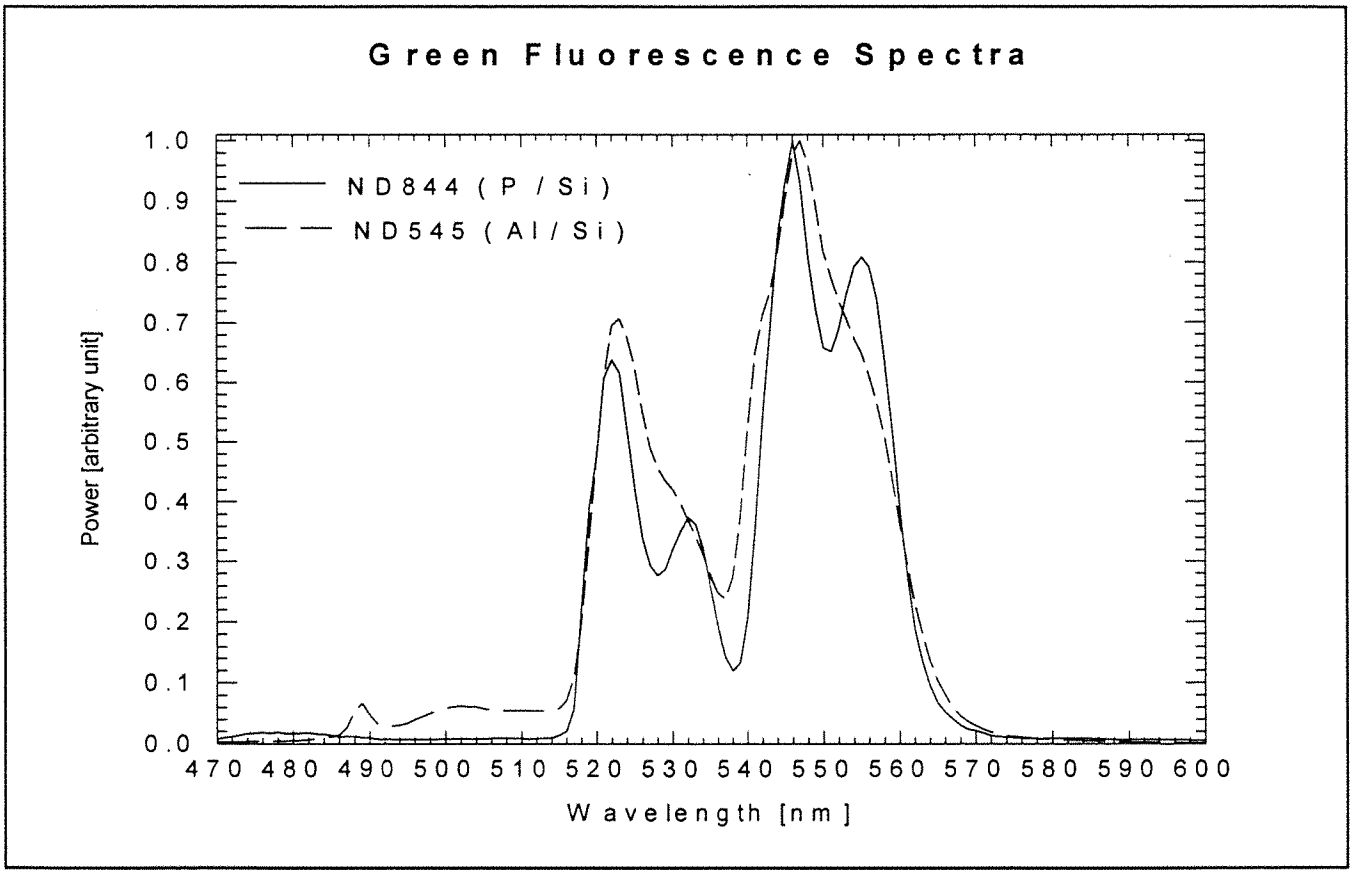

Fig. 4.28 470 - 600nm fluorescence spectra of a phosphosilicate and an aluminosilicate Er/Yb fibre

The decay times are measured at 545nm. An acousto-optic modulator is used. The 90% to 10% fall time of the modulated beam was measured to be 60ns. The resolution is either 20µs or, for HD212_01, 50µs. The temporal evolution of the $^4S_{3/2}$ population N_g , of intrinsic decay time t_g , can be modelled by :

$$\frac{dN_g}{dt} = k_f\, e^{-\frac{t}{t_f}} - \frac{N_g}{t_g} \qquad (4-12)$$

where k_f and t_f describe the exponential decay of the feeding mechanism after the pulse. This gives :

$$N_g(t) = \frac{k_f}{\frac{1}{t_g} - \frac{1}{t_f}} \left(e^{-\frac{t}{t_f}} - \frac{t_g}{t_f}\, e^{-\frac{t}{t_g}} \right) \qquad (4-13)$$

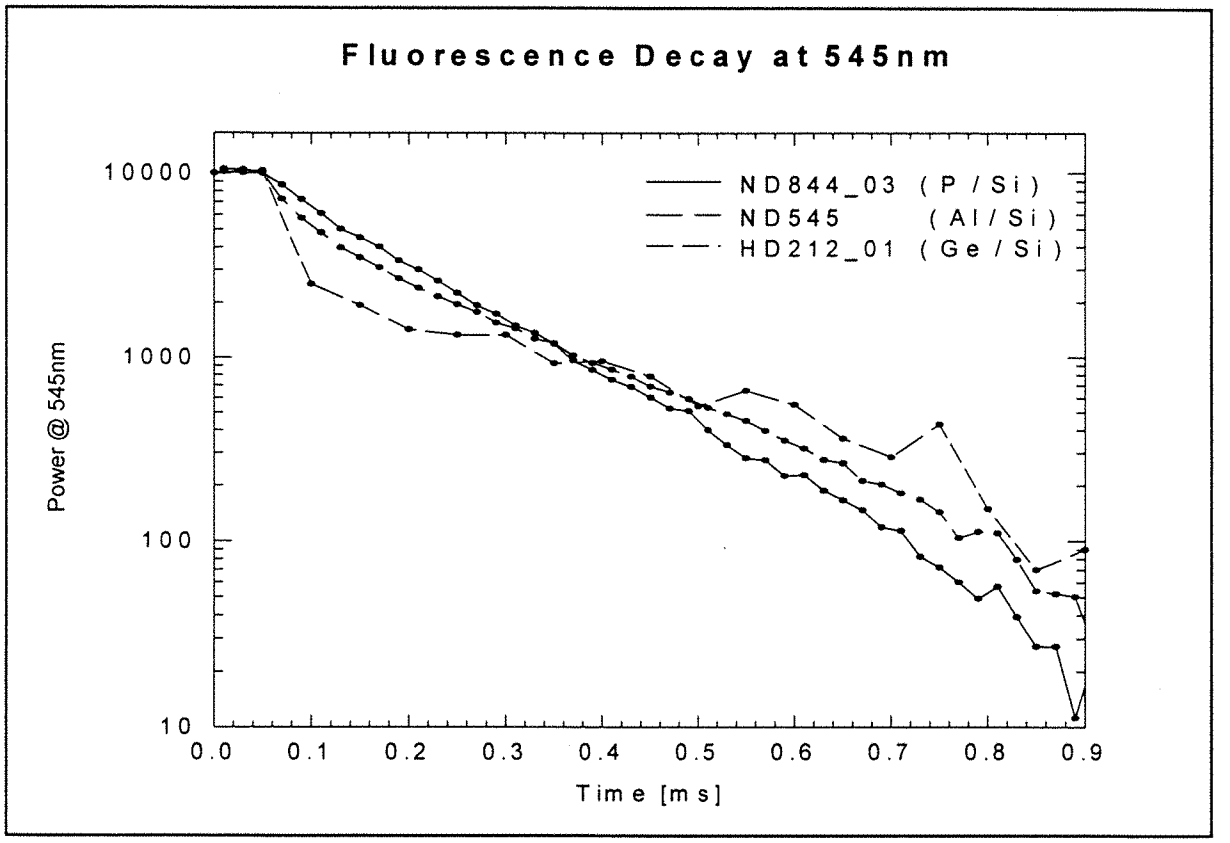

Fig. 4.29 Fluorescence decays at 545nm for Er/Yb fibres ND545, ND844_03, HD212_01

The feeding mechanism dies immediately after the pulse when the pump ESA is solely involved. So $t_f = 0$ and the green level population is expected to decay at its intrinsic lifetime t_g (of 0.4 μs in phosphosilicate fibres, see chapter 5). No initial decay is observed in the fluorescence of the phosphosilicate fibre, showing that the pump ESA plays no part in the green fluorescence of this fibre. It can be shown that when the feeding mechanism is the double energy transfer from ytterbium ions, the feeding mechanism is expected to decay at twice the ytterbium decay rate [Maurice_96]. The decay time of the feeding mechanism is then much larger than the intrinsic decay, and the green fluorescence decay time is of the order of a few 100 μs, as observed in Fig. 4.29.

An increase in the first transfer coefficient will always be accompanied by a similar increase in the second transfer coefficient, as both depend in the same fashion on interionic distances. However, the first transfer rate is proportional to the ground state population of the erbium ions, whereas the second transfer rate is proportional to the much lower $^4I_{11/2}$ population of erbium, making the second transfer negligible compared to first energy transfer except perhaps at very high erbium inversion.

4.5.2 Erbium fluorescence quenching

The mechanism of energy transfer upconversion from the metastable level of erbium is illustrated in Fig. 4.30. When two neighbouring Er^{3+} ions are in the excited $^4I_{13/2}$ state, one of them (the donor) transfers its energy to the other (the acceptor), thus promoting the acceptor to the high energy level $^4I_{9/2}$, while the donor relaxes to the ground state. From this higher energy level, the acceptor relaxes rapidly mostly down to the metastable state via phonon coupling. The process adds a nonradiative relaxation path to the ground state with a time constant that can be orders of magnitude smaller than the metastable radiative lifetime. Since an excited electron can decay at a much faster rate, a higher power pump source is required to achieve a given excited state population.

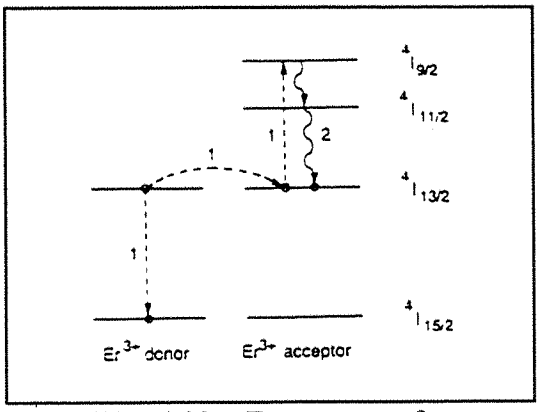

Fig. 4.30 Energy transfer upconversion between two erbium ions

We excite the fibre with a Nd : YAG laser beam chopped mechanically at a low enough frequency to allow nearly full relaxation of the Er ions between two excitation cycle. The output beam is filtered with a long wavelength pass filter, and detected with an InGaAs diode. The signal is amplified with a transimpedance amplifier, and monitored on a digital oscilloscope. The decays measured for different pump powers are presented in Fig. 4.31.

We see that the decay is exponential only at low power. The reduction of lifetime with increasing pumping level can be attributed to upconversion to the $^4I_{9/2}$ level of erbium (a requirement for this mechanism to be effective is that a high proportion of the ions be in the metastable level). The uniform upconversion can be described by the following equation for the metastable level population N_2^{Er} :

$$\frac{dN_2^{Er}(t)}{dt} = -\frac{N_2^{Er}(t)}{\tau_f^{Er}} - C_{up}\, N_2^{Er}(t)^2 \qquad (4-14)$$

The initial population $N_2^{Er}(0)$ increases with the pump rate of the exciting beam and then saturates. The solution of the equation is

$$N_2^{Er}(t) = \frac{N_2^{Er}(0)}{1 + C_{up}\, N_2^{Er}(0)\, \tau_f^{Er}} \frac{e^{\frac{t}{\tau_f^{Er}}}}{1 - \frac{C_{up}\, N_2^{Er}(0)\, \tau_f^{Er}}{1 + C_{up}\, N_2^{Er}(0)\, \tau_f^{Er}} e^{-\frac{t}{\tau_f^{Er}}}} \qquad (4 - 15)$$

We observe in Fig. 4.31 that with increasing pump power, the analytical solution deviates more and more from an exponential. The initial decay rate is $1/\tau_f^{Er} + C_{up}N_2^{Er}(0)$. Above 100 mW of pump power the erbium fluorescence saturates. The upconversion factor is found by fitting curve 1 to the analytical solution using the fibre parameters τ_f^{Er} = 10.2 ms, $N_2^{Er}(0)$ = 1.32 10^{25} m^{-1}. We obtain C_{up} = 5.86 10^{-24} m^3/s.

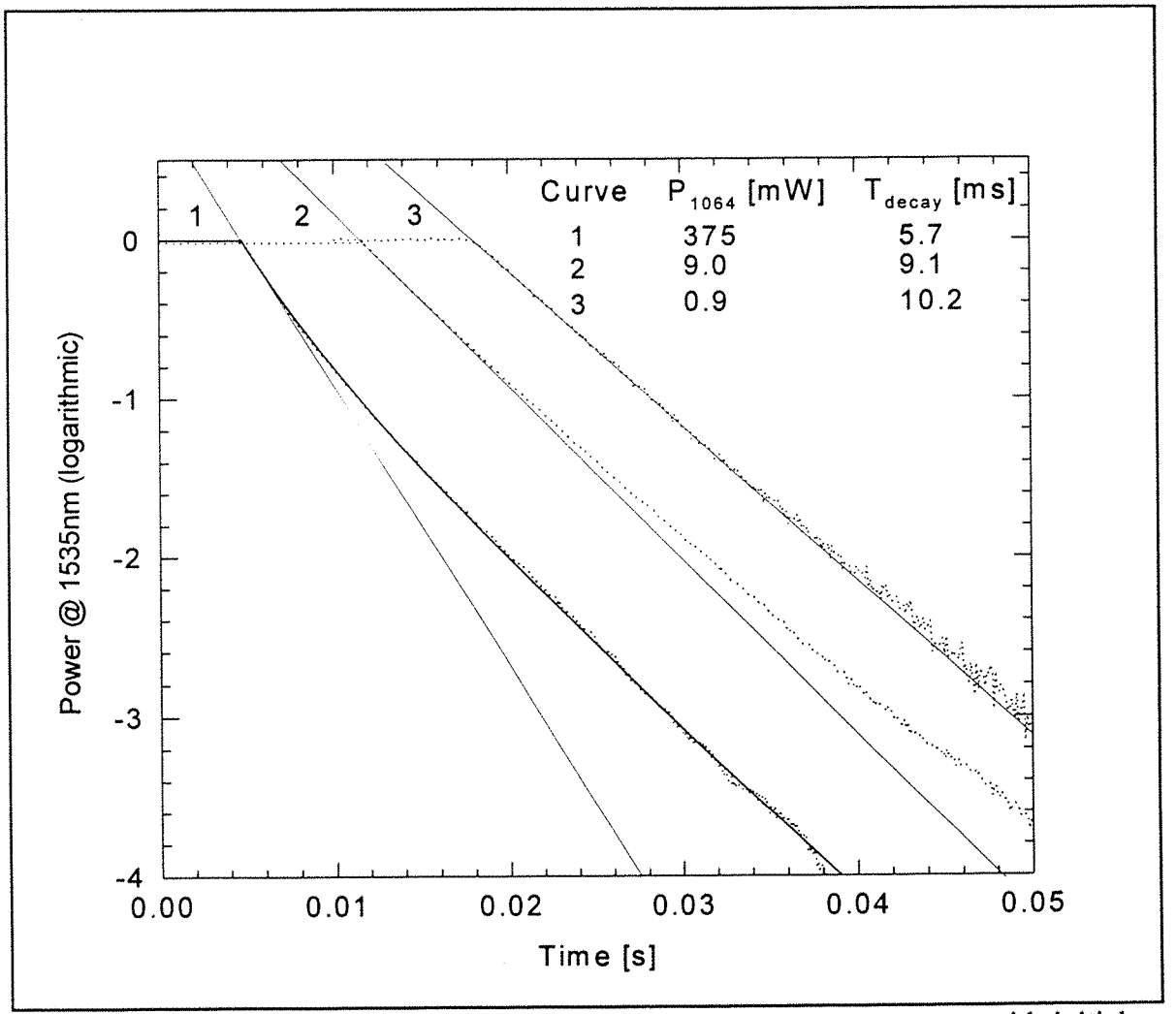

Fig. 4.31 Fluorescence decay of ND815_01 for different pump powers with initial decay times & fit to the uniform upconversion model for curve 1.

The Er^{3+} ion pair lifetime is maximum a few μs [Ye_95]. This explains why ion-pair upconversion has little effect on the decay of the metastable population. To measure the effect of clustering Delavaque et al. proposed an alternative method based on the measurement of

unbleachable losses [Delevaque_93]. We carried out this measurement in highly doped erbium fibres fabricated in our laboratory. Using a MOPA emitting at 980 nm, we typically launched 100 mW of pump power, which in all fibres exceeded the saturation power of unclustered ions. The results are summarised in table 4.4.

Fibre	Host	α_{980} in dB / m	α_{unsat} / α_{sat} in %
HD202	Ge / Si	15	45
HD322	Ge / Si	20	67
HD339	Al / Ge / Si	40	37
ND190_02	Al / Ge / Si	26	17
ND191_02	Al / Ge / Si	43	20
ND974_01	P / Si	40	62
ND975_01	P / Si	85	78
ND977_01	P / Si	120	73

Table 4.4 Fraction of unsaturable loss for erbium fibres in different hosts

We fabricated the highly erbium-doped phosphosilicate fibres by the same process as for the erbium: ytterbium codoped fibres. The average rare-earth concentrations in ND974/75/77 were 2200, 5200, and 8000 ppm. From the results shown in table 4.4, we see that erbium clustering is higher in phosphosilicate than in aluminogermanosilicate fibres. Clustering, rather than the host phonon energy, may explain why phosphosilicate is a particularly suitable glass for Er/Yb devices. Phosphosilicate fibres with lower erbium concentrations will be needed for comparison with germanosilicate fibres.

4.6 Conclusions

The composition of our fibres was measured by two different methods : inductively coupled plasma mass spectrometry and energy dispersive X-ray spectrometry. The first method was the most accurate and the results, in combination with absorption measurements, were used to determine the erbium and ytterbium absorption cross-section. On the other hand, the second method was much simpler to implement, and sufficient for comparison between fibres. Our fibres contain up to 12 mol% (P_2O_5) and 1.5 mol% of rare-earth ions. We checked that the ytterbium to erbium ratio in the glass was conserved from the doping solution.

We found evidence that the rare-earths are not randomly distributed in the glass but are associated with phosphate units : by introduction of rare-earths the Raman spectra showed no appearance of new Si related vibration modes whereas a new scattering peak attributed to metaphosphate chains appeared around 1200 cm^{-1} ; increasing the rare-earth content increased the background loss which is probably due to defects in the phosphate phase ; the absorption spectrum of the erbium ion in our fibres was typical of a phosphate host.

We saw that the preforms should be pulled to obtain a core size corresponding to a cutoff wavelength of around 1200 nm to maximise the output power of our 1064 nm and 980 pumped fibre lasers. We compared the signal-dopant overlap factor for a measured profile and a step index profile and found that the difference did not exceed 15% over the 700 - 1500 nm range of cutoff wavelengths.

Backward ASE and laser cutback measurements have been described as methods to evaluate the device performances of the erbium : ytterbium fibres. Using a Nd:YAG laser as a pump source, the performance of fibres doped with 1.0 - 1.5 mol%(Yb^{3+}) was reduced by a background loss in excess of 0.5 dB / m.

The main mechanism responsible for the green fluorescence in our efficient fibres was identified as the energy transfer $[(Yb, {}^2F_{5/2});(Er, {}^4I_{11/2})] \rightarrow [(Yb, {}^2F_{7/2});(Er, {}^4F_{7/2})]$. The uniform upconversion constant in erbium was estimated from lifetime measurements and measurement of unbleachable losses showed that the erbium ions cluster less in aluminogermanosilicate than in phosphosilicate fibres.

Chapter 5

ALUMINIUM CODOPING

5.0 Introduction

All efficient Yb - Er fibres reported to date contain phosphorus. However, phosphorus is highly volatile so that numerical apertures (NA) higher than 0.20 ($\Delta n = 1.4\ 10^{-2}$) are not easily achieved by the MCVD process. Our phosphosilicate fibres also show a particularly narrow emission spectrum around 1535 nm. In this work we attempt to change the host glass composition to increase the NA and broaden the emission spectrum of the fibre.

In aluminogermanosilicate fibres, aluminium is well known to broaden the emission spectrum of the rare-earths and to allow a high rare-earth incorporation without clustering [Ainslie_91]. Alumina also has a high molar refractivity in silica ($2.3\ 10^{-3}$ index change / mol%) [Walker_87] and is not prone to evaporation [Ainslie_91]. In phosphate glasses, addition of aluminium is known to toughen the glass and to reduce its hygroscopicity [Elder_91]. But, although addition of aluminium has been well studied in silica for applications in active optical fibres, there is to our knowledge little information on the role of aluminium in phosphosilicate rare-earth doped fibres.

In this study we investigate whether some of the attractive features of aluminium doping of silica, also appear in a phosphosilicate host. Our approach is to start with a phosphosilicate host because it is a suitable glass for efficient Yb : Er doped fibres and to modify the fibre core by addition of aluminium in order to alter its refractive index and the fluorescence spectrum of the erbium ions. As this modification can also have consequences on the energy transfer, we measure the efficiencies of lasers with different aluminium contents. In the last part of this chapter we present lifetime and Raman scattering measurements in an attempt to relate the device efficiency results to the structure of the glass.

5.1 Results and discussion

We fabricated a series of preforms by depositing a phosphosilicate frit and doping it in an aqueous solution containing the rare-earths, using the fabrication process described in chapter 3. We preferred to introduce the aluminium by the liquid phase but it is also possible to deposit it by the vapour phase. However, heated delivery lines are needed in this case. We gradually increased the aluminium solution strength of the doping solution from 0 to 24 g $AlCl_36(H_2O)$ / 200 ml H_2O and paid attention to keeping all the other fabrication parameters identical. Special care was also taken to dry the frits before sintering. The refractive index profiles of preforms and fibres were calculated from deflection measurements performed by York P101 and S14 profilers.

Table 5.1 shows the concentrations in three fibres measured by EDS, following the guidelines of §4.1.2. Note that the nonzero aluminium concentration for the first fibre is an artefact of the EDS method. The ratio of ytterbium to erbium is 20. The OH^- concentration is lower than 5 ppm in all the fibres.

$AlCl_36(H_2O)$	Al_2O_3	P_2O_5	Yb_2O_3	SiO_2
0	1.76 (2.53)	8.85 (17.72)	0.85 (4.74)	88.5 (75.01)
12	6.12 (8.36)	9.59 (18.25)	1.22 (6.46)	83.07 (66.93)
24	7.14 (9.78)	9.99 (19.03)	0.97 (5.11)	81.90 (66.08)

Table. 5.1 Concentrations in fibres measured by EDS in mol% (and wt% in brackets). $AlCl_36(H_2O)$ is given in g / 200 ml H_2O. The $[Er_2O_3]$ is too low to be measured.

Fig. 5.1 shows that the Numerical Aperture (NA) decreases significantly with addition of aluminium. A preform fabricated in the same way as the ones of this series but doped with erbium only and 48 g $AlCl_36(H_2O)$ / 200 ml H_2O exhibited an NA of 0.06, confirming the trend observed in Fig. 5.1. This low NA was impractical because of the weak guidance making the fibre very prone to bending losses.

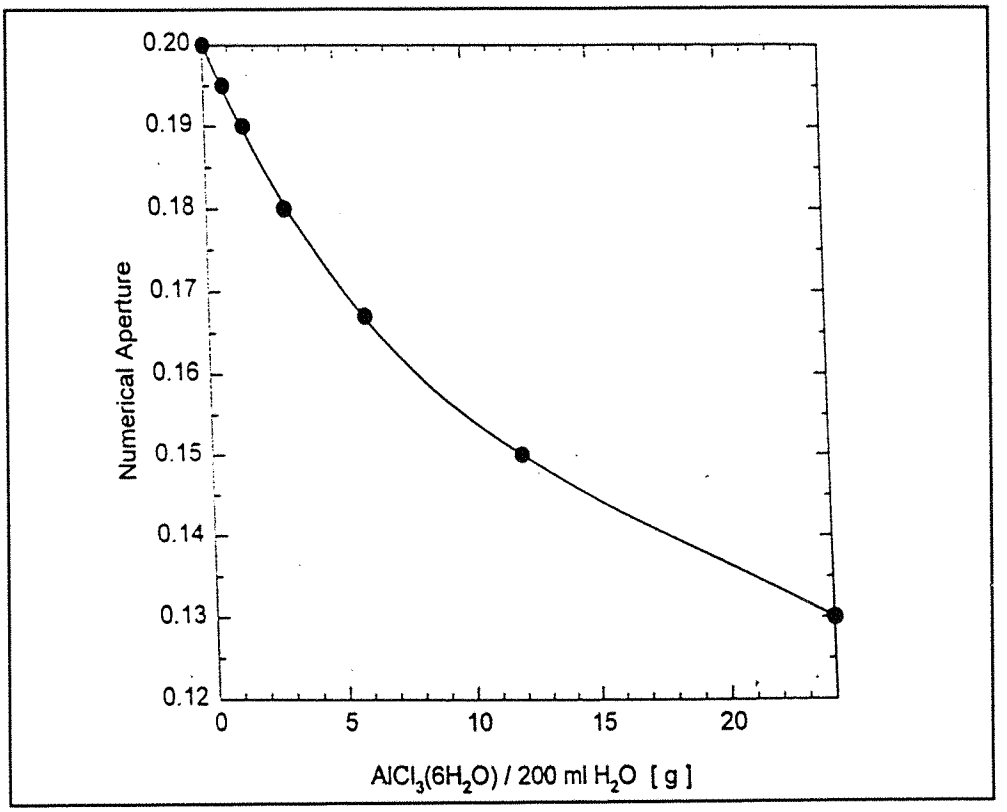

Fig. 5.1 Numerical Aperture vs $AlCl_3(6H_2O)$ solution strength in the aluminophosphosilicate fibres

Fig. 5.2 illustrates the role of the addition of aluminium on the Refractive Index Profile (RIP). Not only does the aluminium reduce the maximum refractive index but it also reduces the central dip. Indeed, the aluminium prevents the phosphorus from evaporating during the collapse of the preform just as it prevents germanium from evaporating in germanoaluminosilicate preforms [Ainslie_91]. There is however an important difference with the case of germanoaluminosilicate preforms : although the RIP is flattened, a ripple is present all across the core. It is due to the inhomogeneity of the glass and can also be observed by eye.

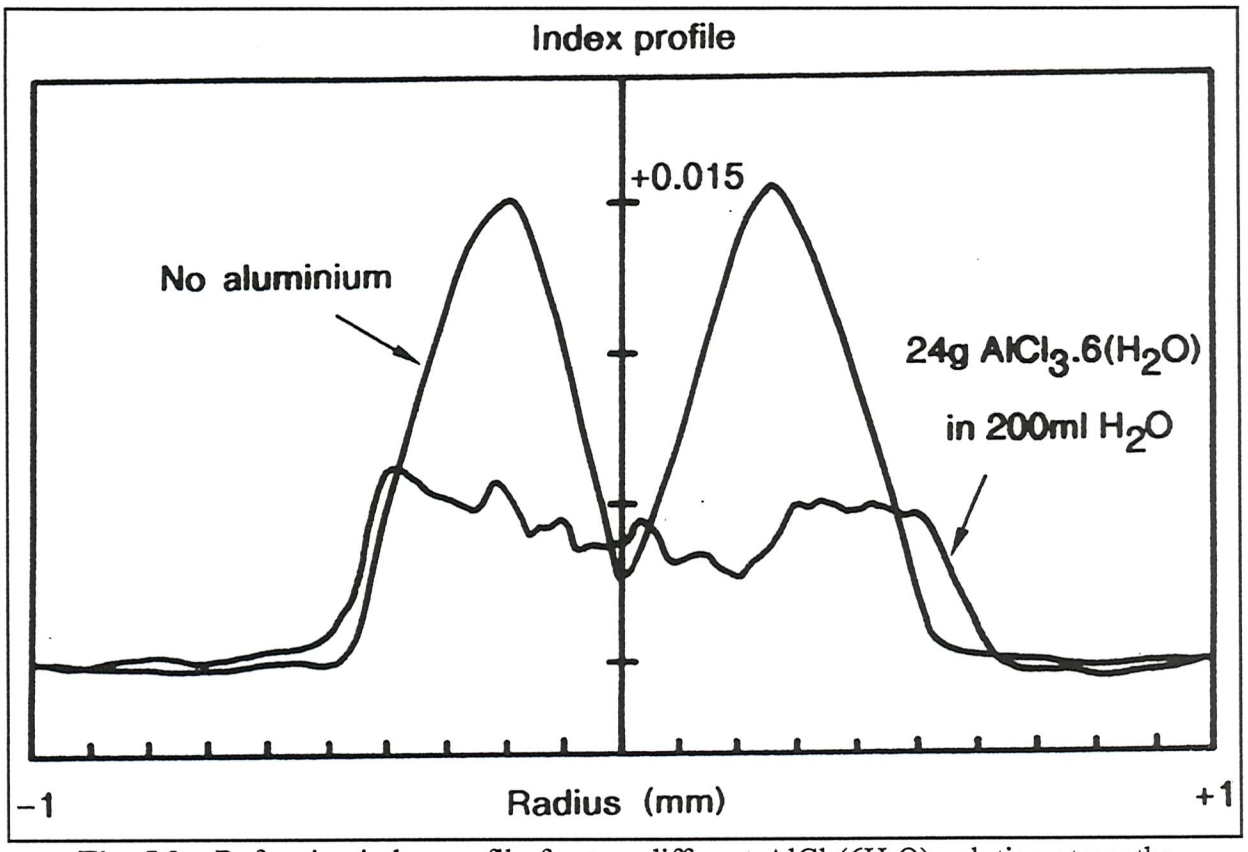

Fig. 5.2 Refractive index profile for two different $AlCl_3(6H_2O)$ solution strengths

The minimum loss (measured around 1.2 μm) increases with increasing aluminium content as can be seen in Fig. 5.3. The preforms also showed an increasing tendency to shatter when heated or sawed with increasing aluminium content.

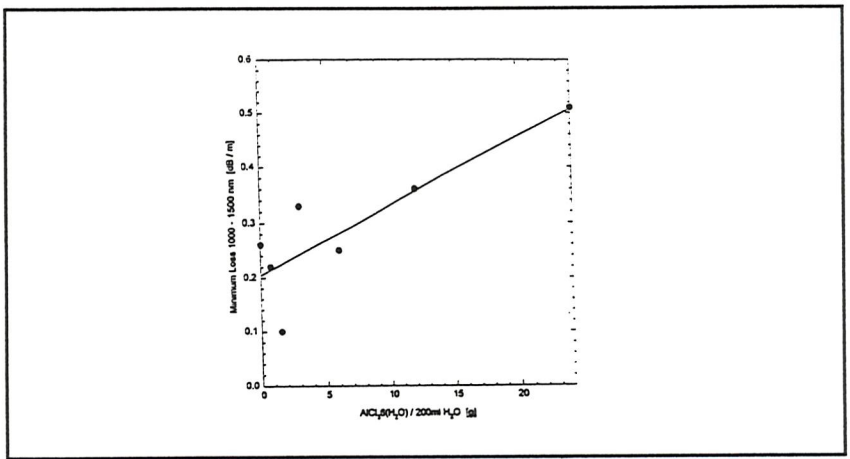

Fig. 5.3 Background loss vs $AlCl_3(6H_2O)$ solution strength

Backscattered electron images (see §4.1.2 for discussion of the technique) for four aluminium concentrations are shown in Fig. 5.4. The aluminium clearly reduces the evaporation of the rare-earths. The distribution of the rare-earths explains why the phase separation appears as a thin line in the middle of the core for aluminium rich preforms, whereas it appears as two lines at the edge of the core for low aluminium preforms.

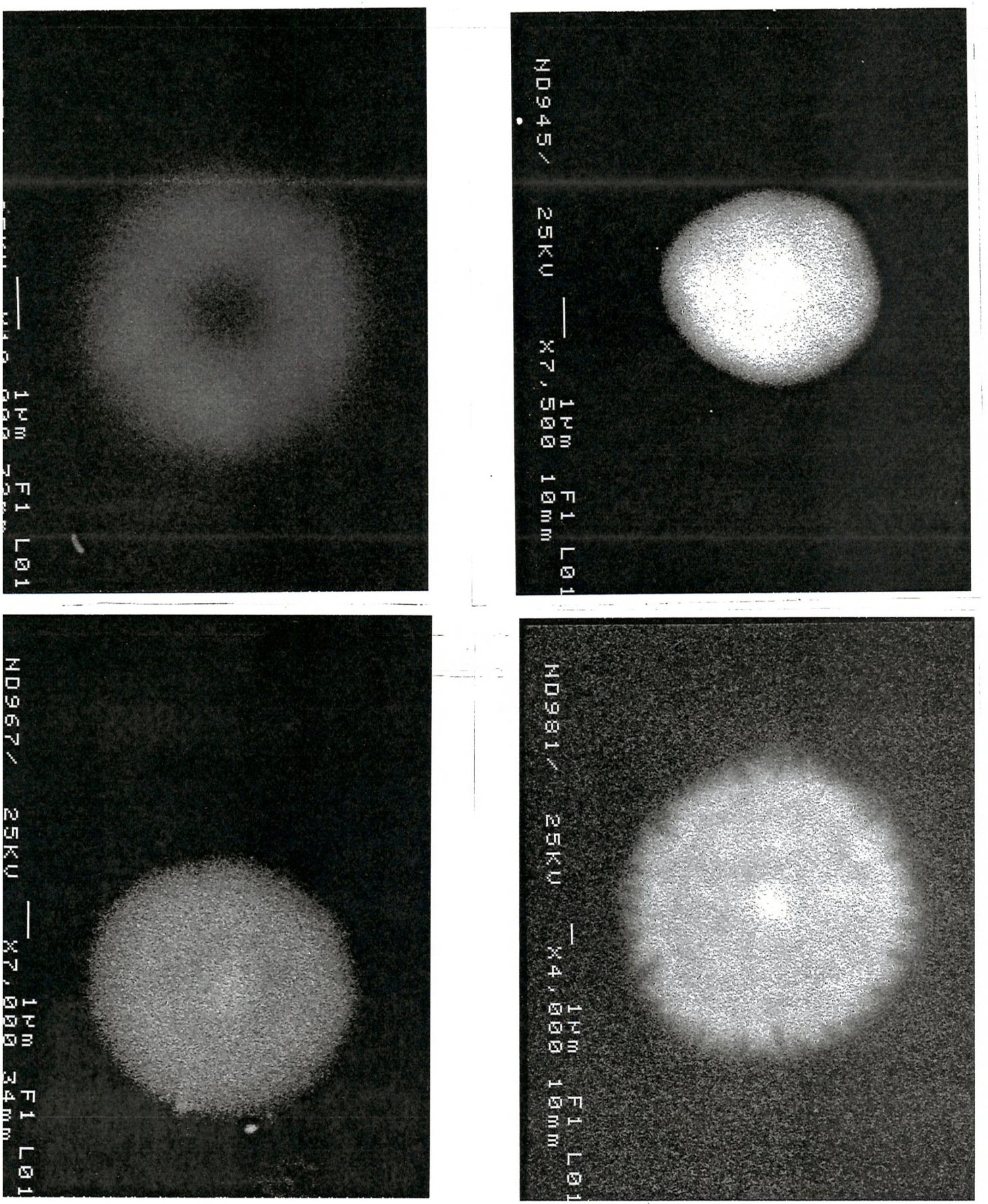

Fig. 5.4 Backscattered electron images of fibrecores for $AlCl_3 6(H_2O)$ = 0 (ND951), 12 (ND945), 24 (ND967), 48 (ND981) g / 200 ml (H_2O)

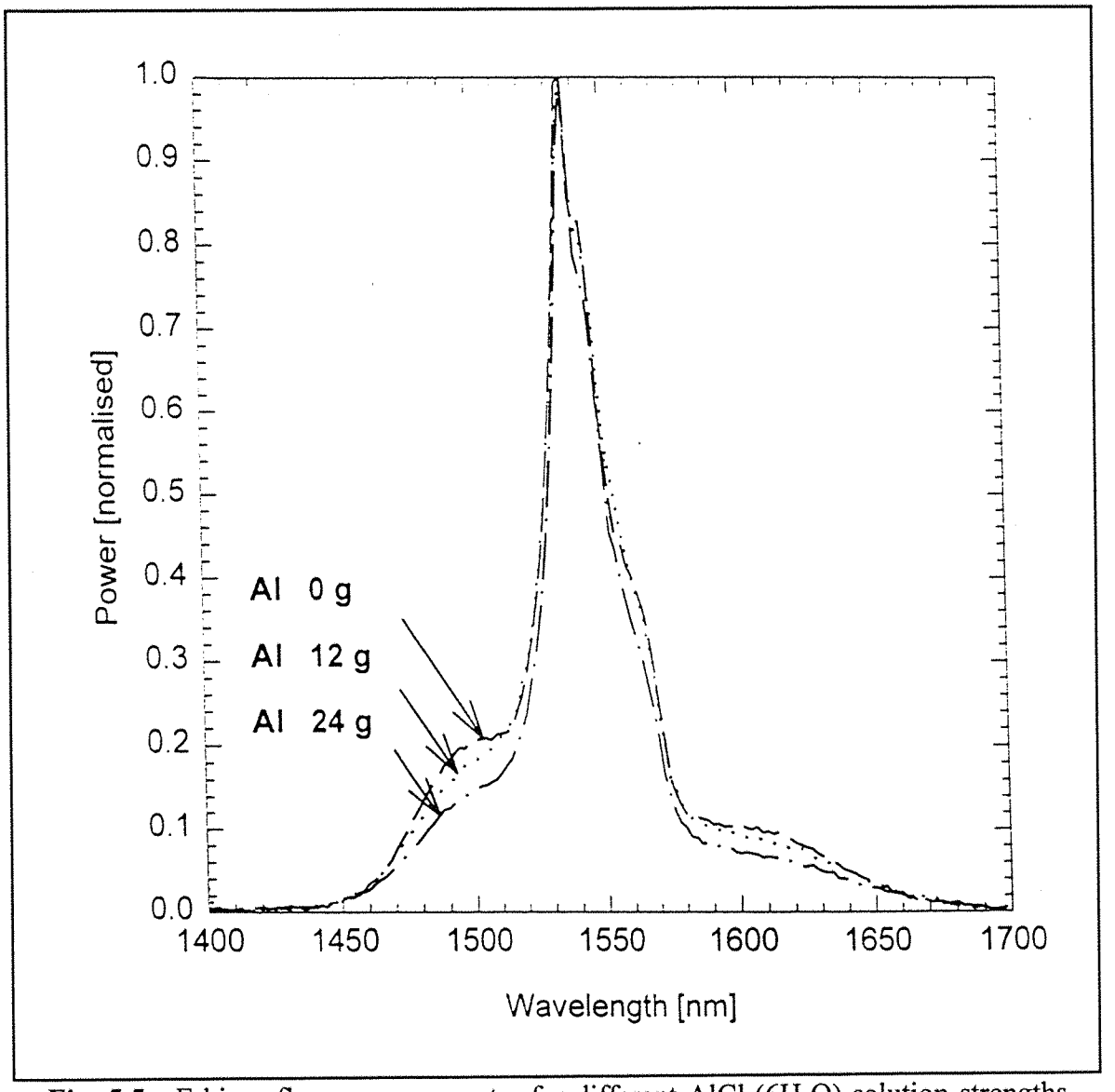

Fig. 5.5 Erbium fluorescence spectra for different $AlCl_3(6H_2O)$ solution strengths

To perform the 1.5 μm fluorescence spectra measurements we used very short lengths of fibres, typically 4 cm, to avoid distortion due to reabsorption. We also reduced progressively the excitation power at 980 nm to check that the spectra were not affected by stimulated emission. Fig. 5.5 shows that the fluorescence spectrum is not significantly affected by the aluminium content around the peak at 1535 nm. All fibres had a Full Width Half Maximum (FWHM) of 20 - 22 nm. We note no broadening of the spectrum when the aluminium content is increased. In fact, further from the peak at 1535 nm, the fluorescence decreases with increasing aluminium content. On the other hand, we measured that an Yb - Er codoped aluminophosphosilicate fibre where [P] < [Al] (2 mol% P_2O_5 and 11 mol% Al_2O_3) had a FWHM of 52 nm [Townsend_91']. However, this fibre showed a very poor efficiency and most of the lasing from the bare ends originated from the ytterbium rather than the erbium.

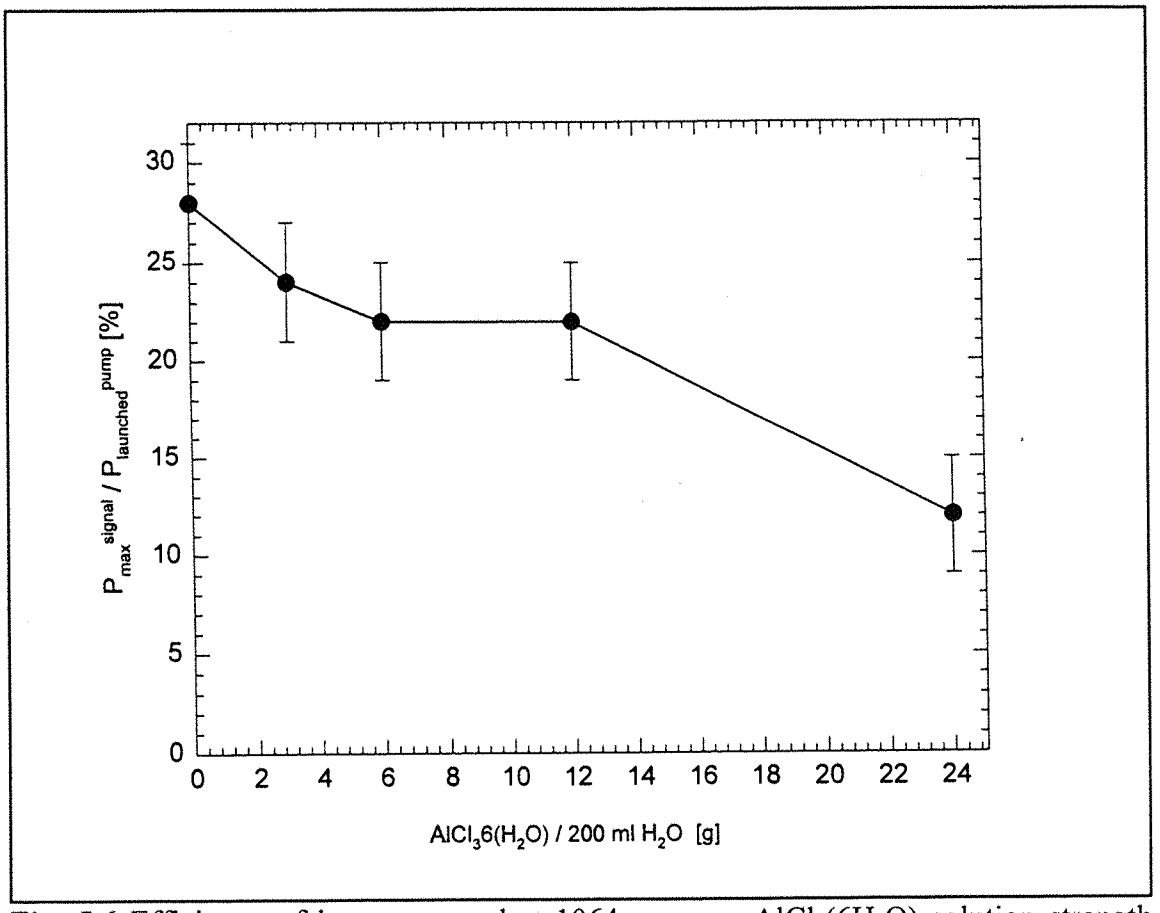

Fig. 5.6 Efficiency of lasers pumped at 1064 nm vs $AlCl_3(6H_2O)$ solution strength

We can also observe in Fig. 5.5 that the ratio of emission at 1480 and 1535 nm is reduced when aluminium is added. Kringlebotn *et al.* recently proposed to use an Yb:Er codoped fibre as a laser source for remote pumping of amplifiers around 1480 nm [Kringlebotn_96]. For this device the amplified stimulated emission at 1535 nm competes strongly with the emission at the laser wavelength. To obtain a ratio of stimulated emission at 1480 and 1535 nm as high as possible the phosphosilicate host should be aluminium free.

To measure the laser efficiencies we launched 1 W of pump power at 1064 nm into the fibres, a value far exceeding the laser threshold of typically 30 mW. We performed a fibre cutback to obtain the maximum output power. The deterioration of device efficiency with addition of aluminium already occurs in the region [P] > [Al], as evidenced in Fig. 5.6. There can be several causes to the reduction in slope efficiency : hydroxyl quenching of the erbium metastable level; a high background loss; or finally a deterioration of the energy transfer efficiency. The first reason can be ruled out as we have checked that the concentration of hydroxyl was below 5 ppm in all fibres.

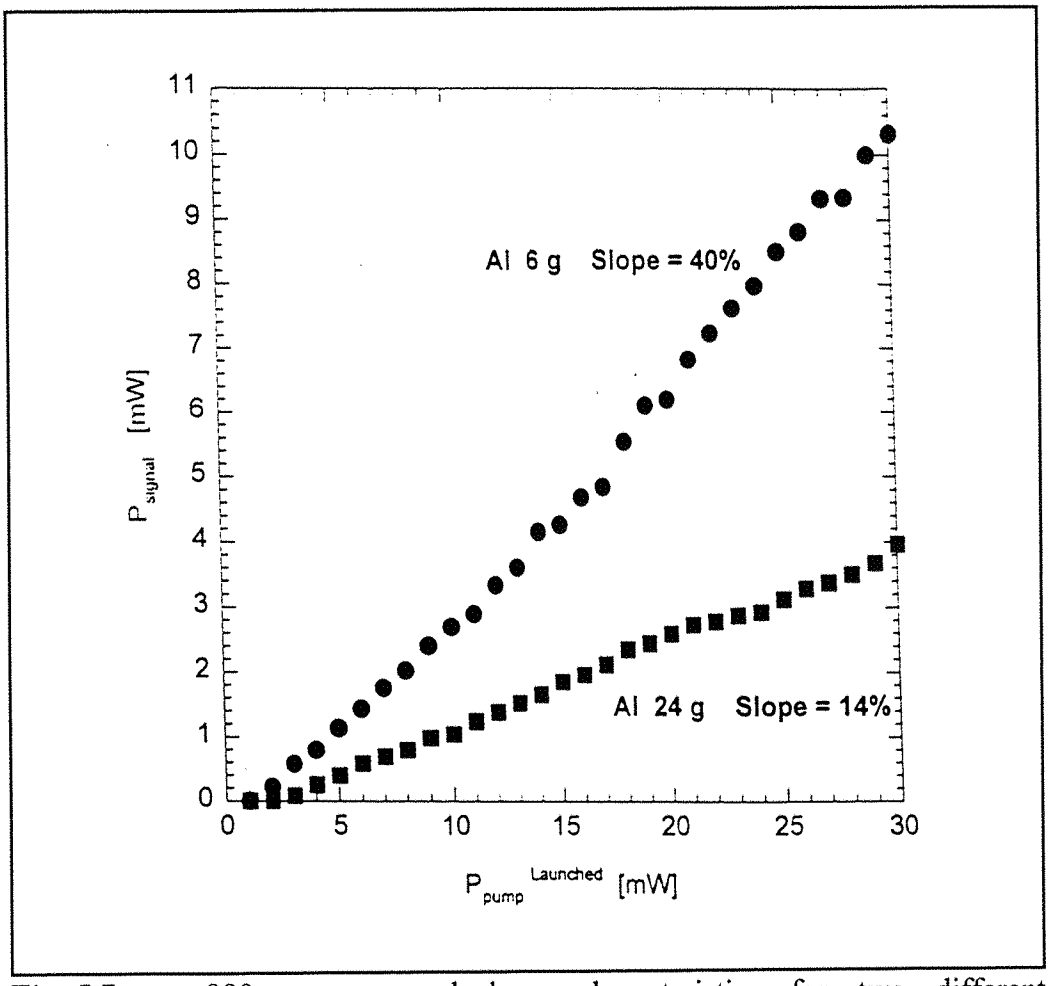

Fig. 5.7 980 nm pumped laser characteristics for two different $AlCl_3(6H_2O)$ solution strengths

However, as the pump absorption at 1064 nm is low (2 - 3 dB /m) the increased background loss with increasing aluminium solution strength already observed in Figure 5.3 may correlate with the reduction in slope efficiency. Indeed, we have already shown in Fig. 3.13 that the slope efficiency could be severely reduced with an increase in background loss when pumping at 1064 nm. We have also shown in Fig. 3.14 that on the other hand, the slope efficiency was not significantly affected by the increase in minimum loss when pumping at 980 nm. Fig. 5.7 shows that in this case, however, even when pumping at 980 nm the slope efficiency is significantly reduced for the fibre doped with 24 g $AlCl_36(H_2O)$ / 200 ml H_2O. This gives us reason to believe that the reduced efficiency is related to the role of the aluminium in the energy transfer rather than the increase in minimum loss.

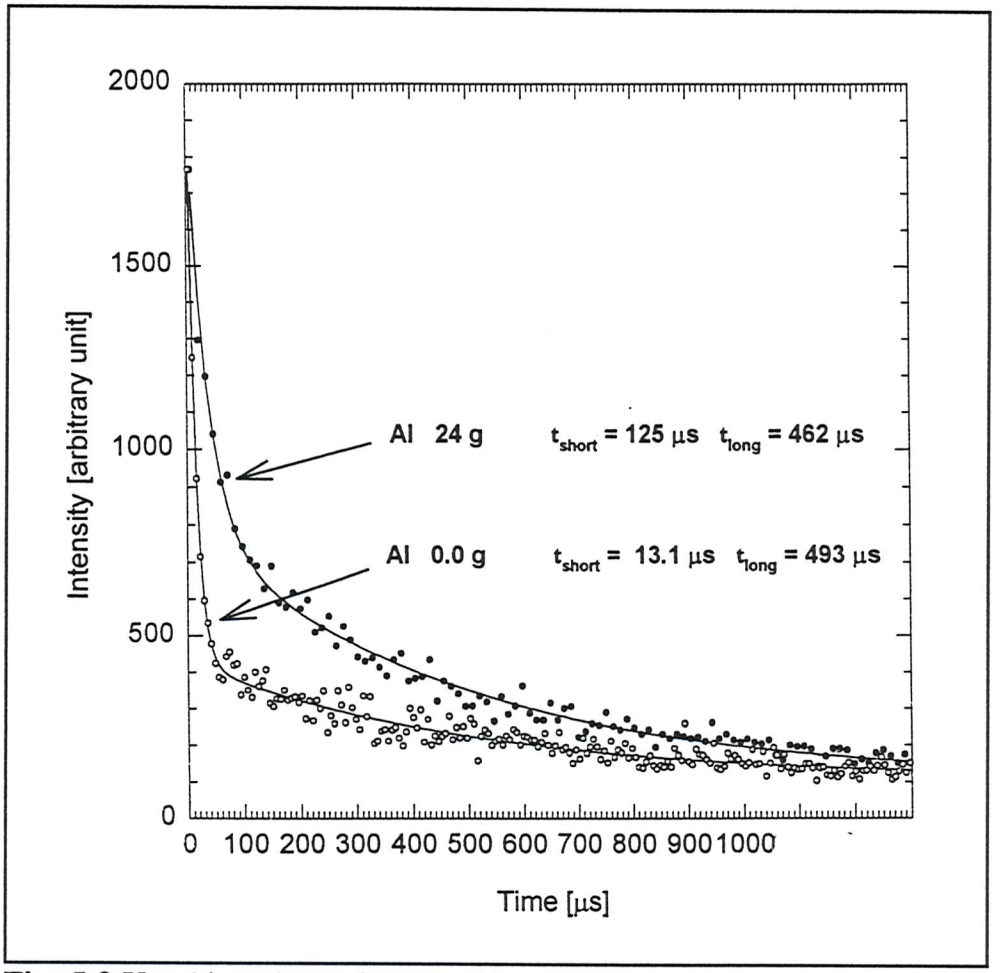

Fig. 5.8 Ytterbium decay for two different $AlCl_3(6H_2O)$ solution strengths with biexponential fit

To investigate the energy transfer between ytterbium and erbium we measured the decay of the excited ytterbium ions. Ytterbium decays were detected with a photomultiplier. The fibres were pumped with a Q-switched Nd:YAG laser. The repetition rate was 30 Hz allowing 95% of the excited erbium ions to relax to the ground state between each pulse. The resolution of the measurement was 100 ns. Fig. 5.8 shows the decay of a fibre with high aluminium content and the aluminium-free fibre, together with the double exponential fits. The two phases of the decay can be explained as follows : the closest donor - acceptor pairs rapidly undergo energy transfer initially and their population becomes depleted early in the decay because the slow erbium de-excitation prevents any more transfer from occurring within the ytterbium intrinsic excitation lifetime. The depletion continues radially outwards from the donor ions as time progresses until the only unexcited erbium ions remaining are sufficiently separated from the donor so that energy transfer does not occur.

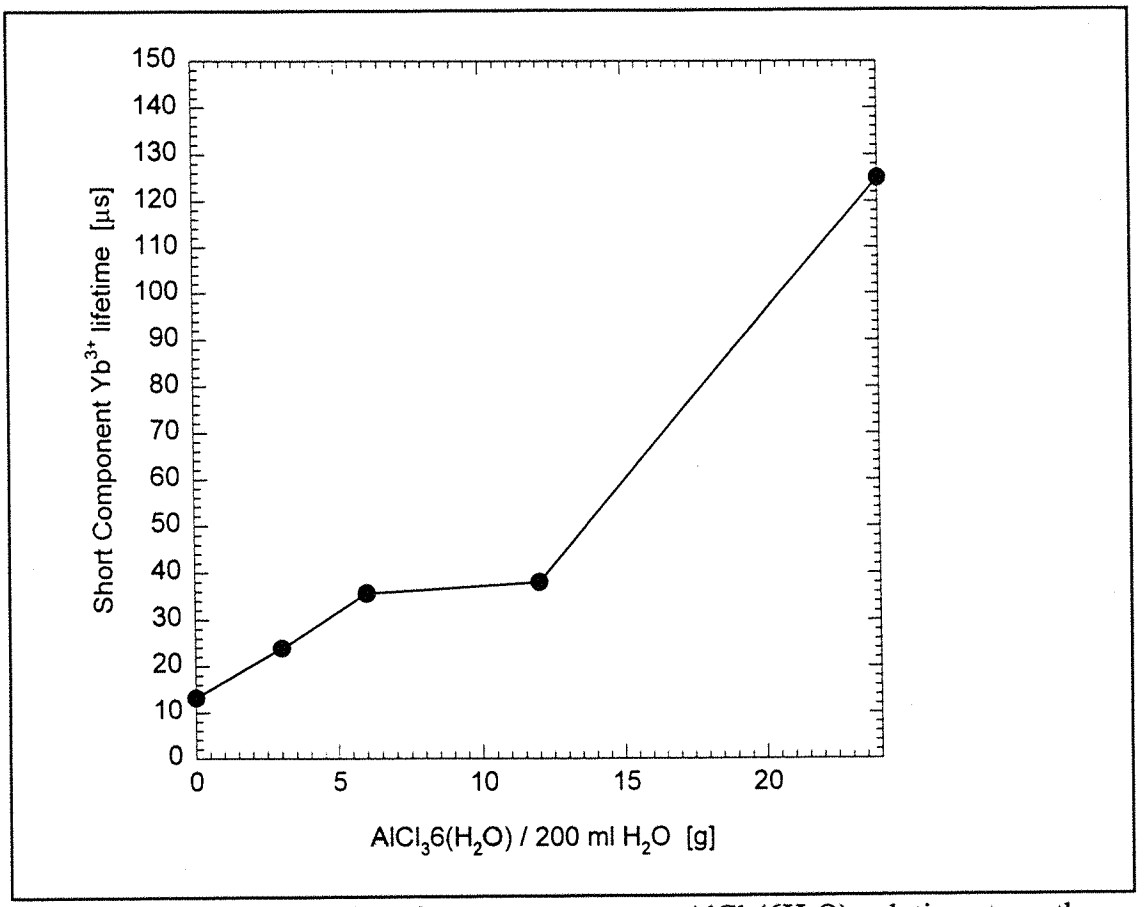

Fig. 5.9 Ytterbium lifetime fast component vs $AlCl_3(6H_2O)$ solution strength

The slow decay component shows little variation with the aluminium content. The time constant is 500 +- 100 μs over the whole range of concentrations. On the other hand, Fig. 5.9 shows that the fast component increases with increasing aluminium concentration and the fibre doped with 24 g $AlCl_3 6(H_2O)$ / 200 ml H_2O exhibits a much slower initial decay than all the other fibres. We conclude that the reduction in slope efficiency is linked to the slower energy transfer when aluminium is added.

The measurements performed so far can provide some insight into the structure of the glass. In silica, addition of aluminium alone or phosphorus alone is well known and widely used to increase the refractive index [Walker_87]. Here, we saw that combination of the two codopants leads to much lower refractive indices than would be expected from the superposition of the two binaries Al_2O_3 - SiO_2 and P_2O_5 - SiO_2. DiGiovanni also observed this behaviour in the [Al] < [P] region of undoped phosphoaluminosilicate prepared by MCVD [DiGiovanni_89]. This is a clear evidence that the mixture of these two codopants in silica results in a ternary glass significantly different from the individual binary systems. A

structural modification must take place when the two binary glasses are mixed together. The reduced evaporation of phosphorus when aluminium is added to the glass suggests that an unpaired aluminium ion presents a favourable site for phosphorus bonding. Finally, the fluorescence spectra provide information on the environment of the rare-earths. The shape of the fluorescence spectra is almost unchanged until 12 g $AlCl_3 6(H_2O)$ and is characteristic of a phosphate host. The narrowing at 24 g $AlCl_3 6(H_2O)$ maybe due to the reduction of available P = O bonds after pairing with aluminium. In any case no broadening is observed suggesting that no rare-earth is coordinated by $[AlO_4]$ or $[AlO_6]$ groups and the rare-earths remain coupled to phosphate sites.

Finally, an interesting question still remains to be answered : What is the cause of the increase in transfer time? In particular, we want to address whether the back transfer of energy or the reduced clustering is responsible for the deterioration in transfer efficiency.

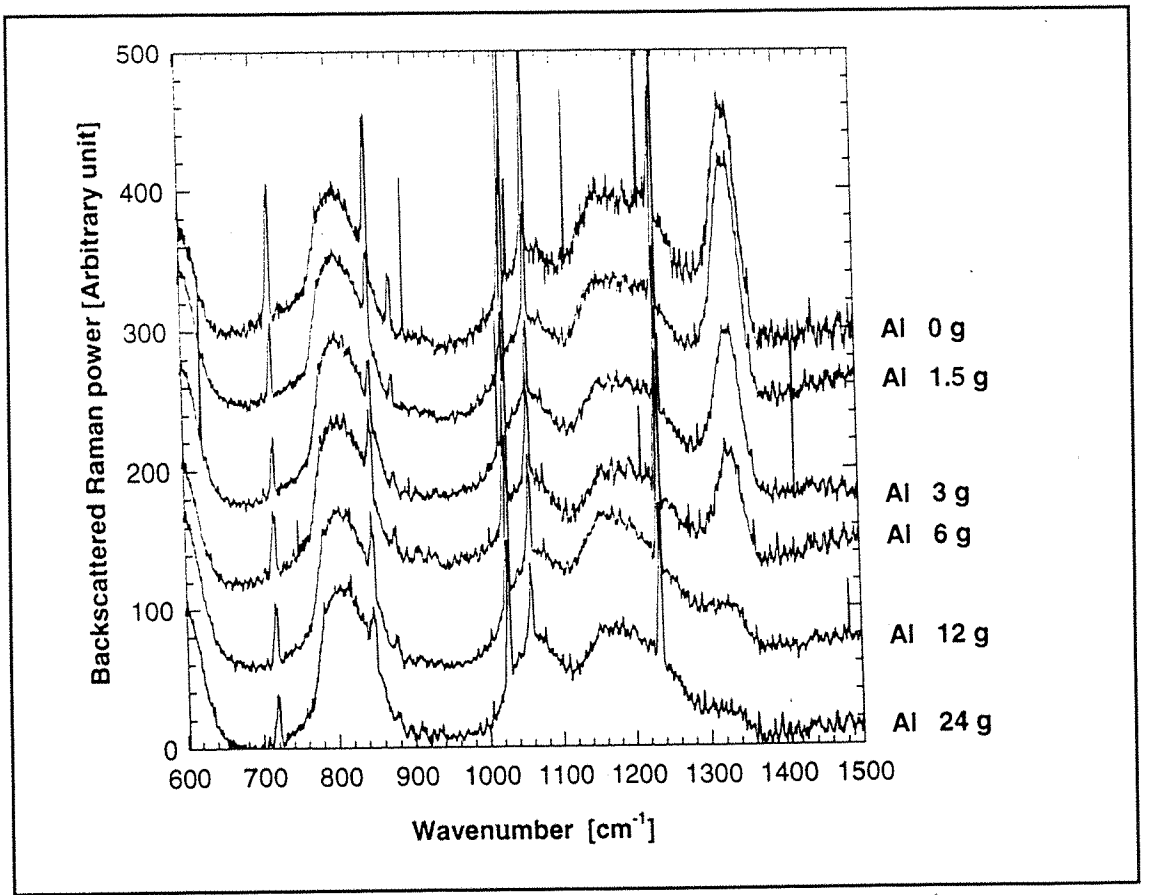

Fig. 5.10 Raman spectra for different $AlCl_3(6H_2O)$ solution strengths

Fig. 5.10 shows the Raman spectra for the different aluminium concentrations. We normalised the peak at 1330 cm^{-1}, due to P = O vibration (see §4.2), to the peak at 800 cm^{-1},

which is associated with the silica network. In Fig. 5.11 we show the ratio of these two peaks for the different aluminium solution strengths. We observe that the high phonon energy peak decreases with increasing aluminium content. The reduction of the 1330 cm^{-1} Raman peak with increasing aluminium doping can be attributed to the scavenging of P = O double bonds by the aluminium.

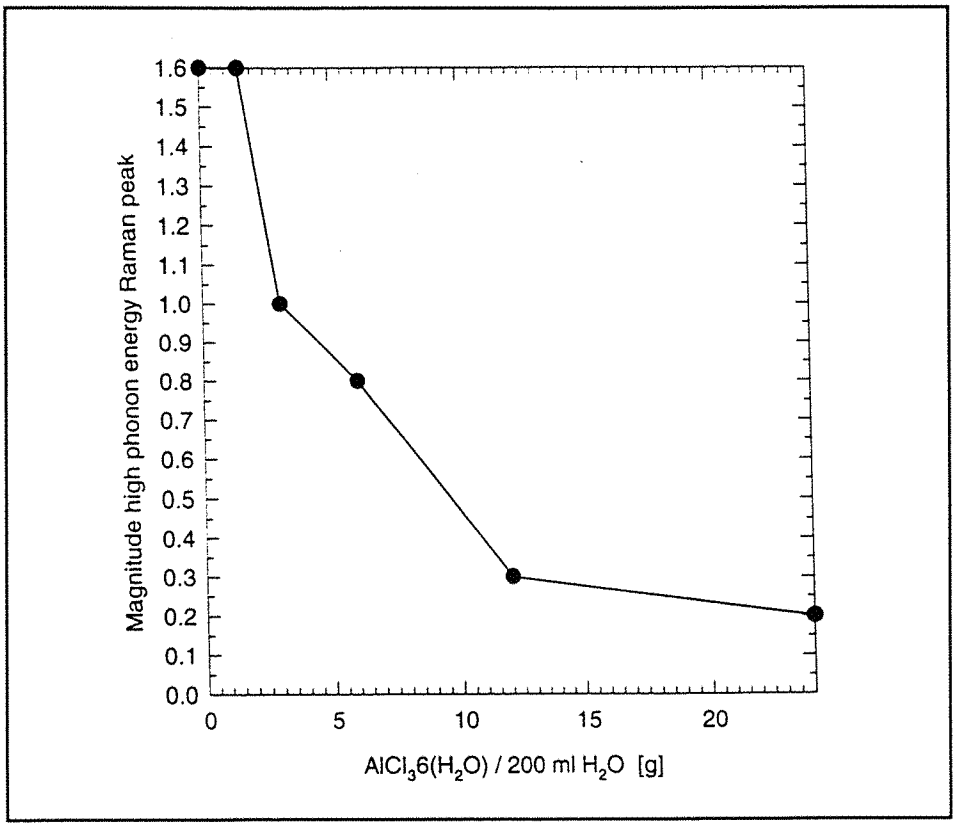

Fig. 5.11 Magnitude of the high phonon peak vs $AlCl_3(6H_2O)$ solution strength. The magnitude of the high phonon energy peak at 1330 cm^{-1} is normalised to the 800 cm^{-1} peak associated with SiO_2.

Fig. 5.12 shows the Al - O - P bonds resulting from the pairing of Al and P. Since phosphorus is electron-rich when incorporated in a silica host, a PO_4 unit can serve as a Lewis base by offering its double bonded oxygen as an electron pair donor. Similarly, aluminium may be considered a Lewis acid when coordinated tetrahedrally. In the SiO_2 - P_2O_5 - Al_2O_3 ternary glass the phosphorus serves to preserve the tetrahedral coordination of the aluminium. It is important to note that the almost complete disappearance of the high phonon energy peak in the fibre doped with 24 g $AlCl_3(6H_2O)$ cannot be attributed to pairing of aluminium and phosphorus only. Indeed, the concentration of aluminium is two thirds that of the phosphorus in this fibre and even if $AlPO_4$ units are formed with complete efficiency, as observed in [Kosinski_88], the P = O population should not be reduced by more than two thirds. The almost complete disappearance of the high phonon energy peak may result from

the partial depolymerisation of the phosphate structure with introduction of the aluminium centre (this phenomenon was illustrated in Fig. 2.5). It also casts some doubt on the assumption that the rare-earths are coordinated by P = O.

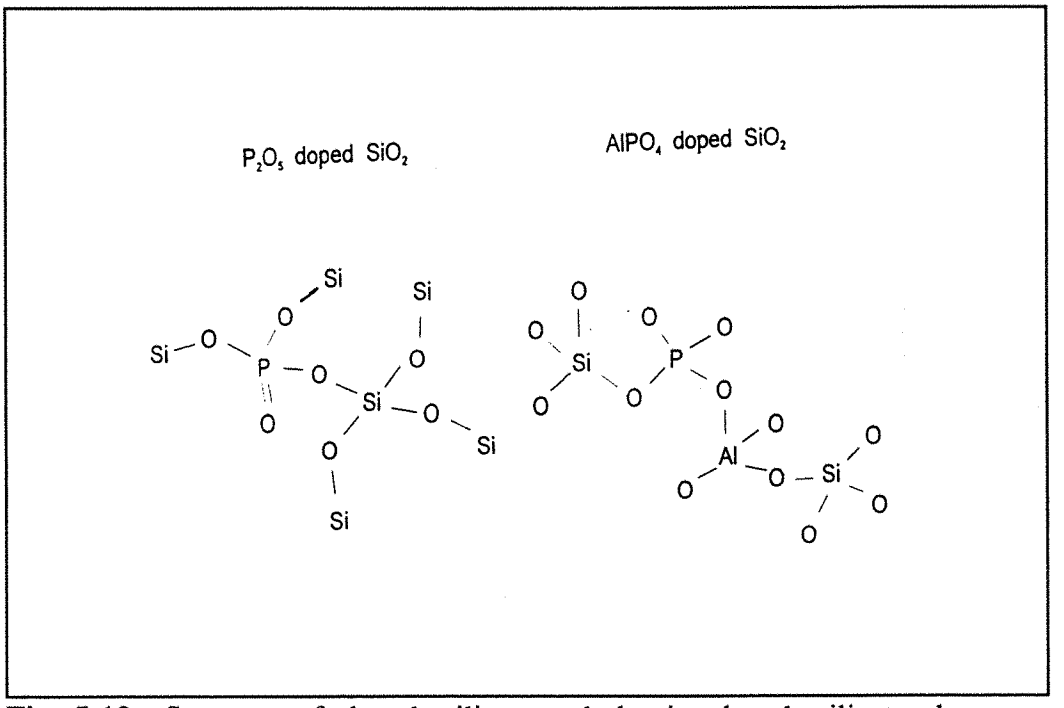

Fig. 5.12 Structure of phosphosilicate and aluminophosphosilicate glass

To probe the environment of the rare-earths we decided to measure the lifetime of the fluorescence of the erbium at 545 nm. Fluorescence from the $^4S_{3/2}$ level at 545 nm was generated by pumping with an argon ion laser at 488 nm. The ion laser was modulated acousto-optically, resulting in a turnoff time of less than 100 ns. Fluorescence was detected from the side of the fibre, filtered using a Jobin-Yvon HR640 monochromator, and detected using a GaAs photocathode photomultiplier. The system time resolution was better than 100 ns. The fluorescence originates from the $^4S_{3/2}$ level and the decay is dominated by non-radiative relaxation to the $^4F_{9/2}$ level, which is directly related to the maximum host phonon energy. Fig. 5.13 shows that the $^4S_{3/2}$ lifetime remains unchanged over the whole range of aluminium concentrations tested. The lifetime is 0.42 μs, which is in good agreement with measurements in phosphosilicate fibres from Lincoln (see §1.4). The very small variation of the green lifetime with the aluminium content suggests that the rare-earths remain coupled to phosphate units over the whole range of aluminium doping tested, as was inferred from the fluorescence spectra. We can conclude that the deterioration of energy transfer with increasing aluminium content is not due to an increase in back transfer of energy. The forward energy transfer must be affected.

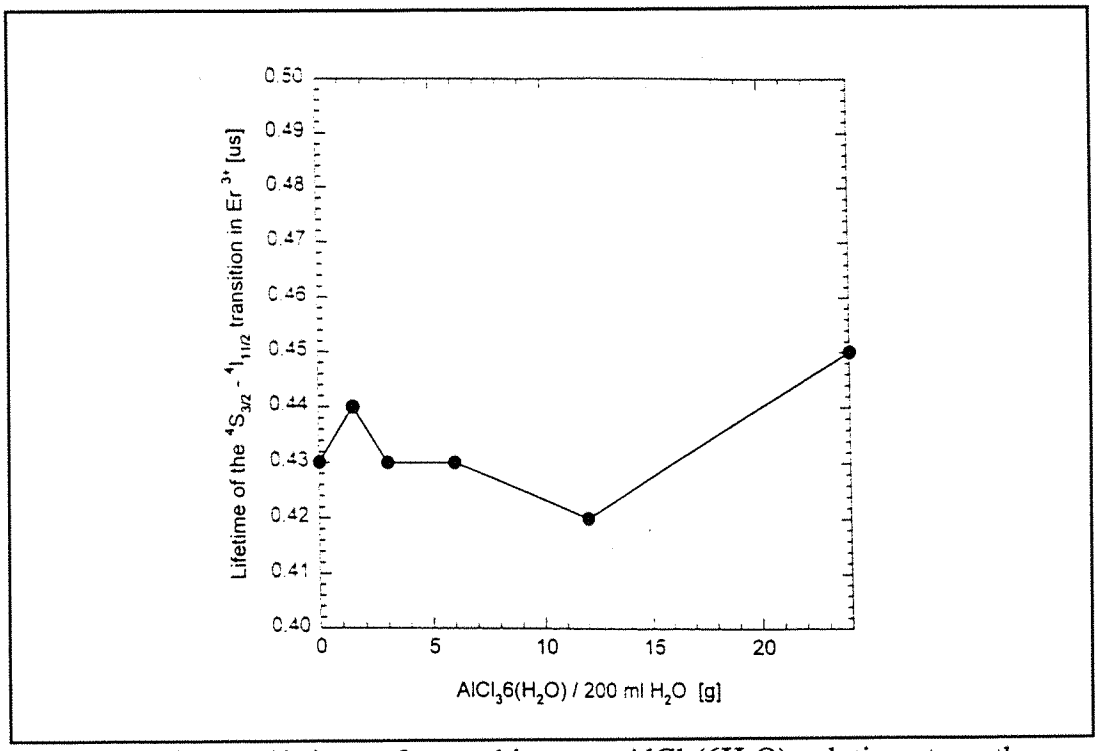

Fig. 5.13 Green lifetimes from erbium vs $AlCl_3(6H_2O)$ solution strength

Higher rare-earth concentration leads to shorter interionic distances if the ions are uniformly dispersed in the glass. So it is possible that the rare-earth concentration variation may be responsible for the variation in laser efficiency. We estimated the erbium concentrations from absorption and cutoff measurements using the method outlined in §3.3. It is clear from Fig. 5.14 that the variation in laser efficiencies is not simply correlated to the rare-earth content.

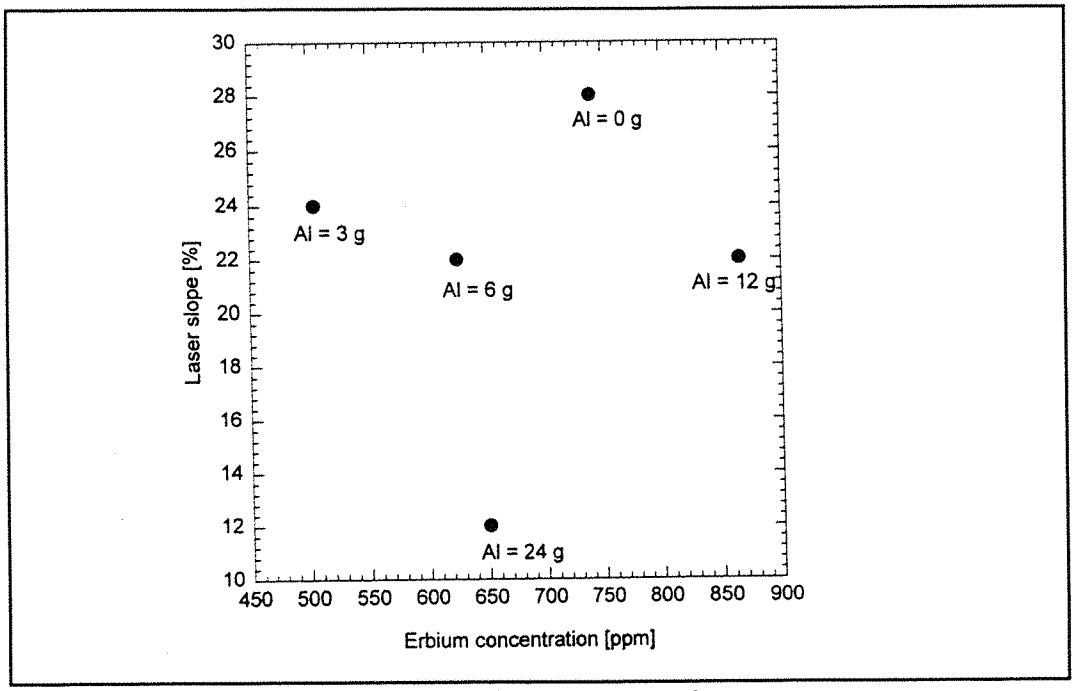

Fig. 5.14 Laser efficiencies vs erbium concentrations

To confirm that addition of aluminium to the phosphosilicate glass reduces the clustering of rare-earth ions we compared the 1535 nm fluorescence decay of erbium doped fibres. The pump power was chosen to be high enough to saturate the fluorescence. Fig. 5.15 shows that the decay is less exponential in the two aluminium free fibres, although the aluminium containing fibre has an intermediate erbium concentration.

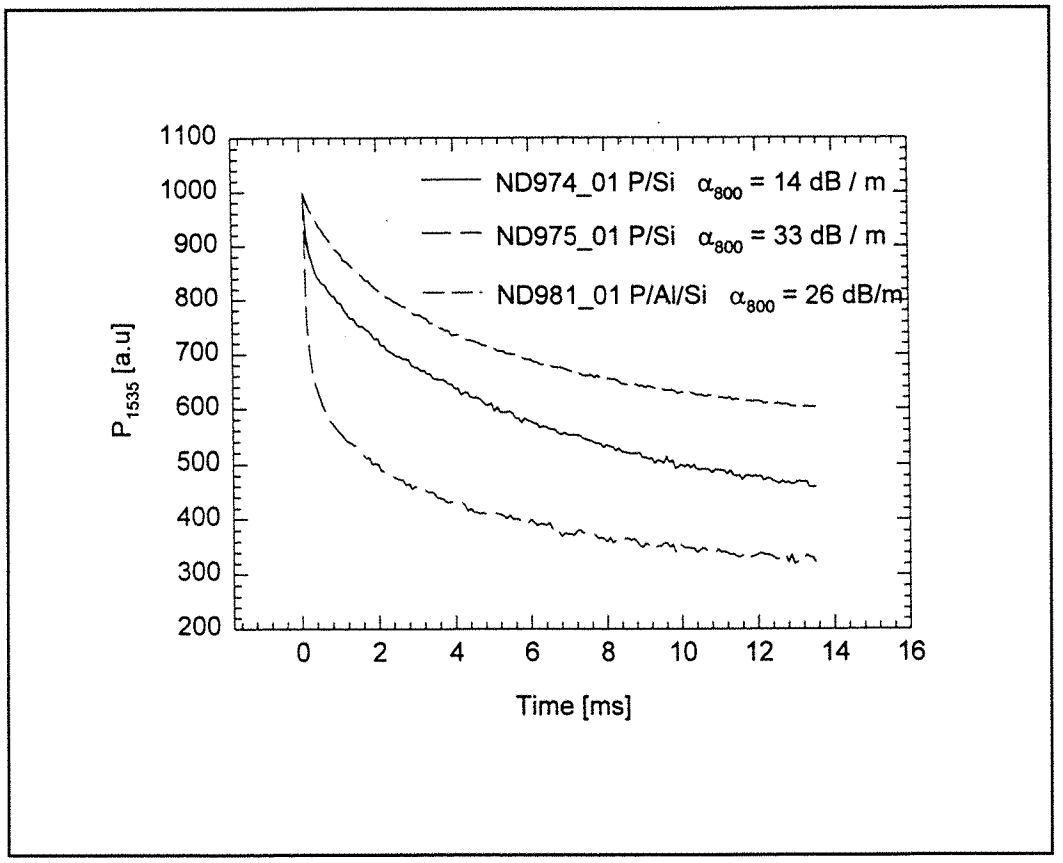

Fig. 5.15 1535 nm fluorescence decay in P/Si and Al/P/Si fibres

We conclude from this study that the competition of the aluminium with the rare-earths for the available non-bridging oxygens disrupts the phosphate network and reduces the rare-earth clustering. The aluminium may increase the average distance between the rare-earth ions or create phase separation on a nanometre scale resulting in pockets of ytterbium ions too far apart from any erbium ion to transfer their energy.

The laser performance was significantly reduced only when we introduced 24 g $AlCl_3 6(H_2O)$ in the solution. In the fabrication process we have observed that aluminium free phosphosilicate preforms are prone to phase separation in patches. Addition of a few grams of aluminium was found to reduce this problem. This is not surprising as we have shown that the aluminium tends to reduce rare-earth clustering. We now typically use a doping solution

containing 6 g $AlCl_3 6(H_2O)$ / 200 ml(H_2O).

5.2 Conclusions

We have shown that addition of aluminium in the region [Al] < [P] decreases the refractive index of the glass, produces striae, and does not lead to spectral broadening around 1.5μm. The reduction in laser efficiency with increasing aluminium content was seen to be related to an increase in energy transfer time. Evidence from fluorescence lifetimes and fluorescence spectra, showed that in this series of fibres where [Al] < [P], the rare-earths preferably couple to phosphate units rather than Al-O, probably because all aluminium ions bond to phosphorus to create $AlPO_4$ units. This made clear that the back transfer of energy could not be responsible for the reduction in laser efficiency. The reduction in laser efficiency was related to a reduction in forward transfer. This was caused by the reduction of rare-earth clustering when aluminium was introduced in the phosphosilicate host. On the other hand, introduction of a few grams of aluminium in the doping solution was efficient at reducing the phase separation in patches which plagues the fabrication of phosphosilicate rare-earth doped fibres, without severely deteriorating the device performances.

Chapter 6

MODELLING AND DEVICES

6.0 Introduction

The aim of the model presented in this chapter is to gain some insight into the effect of the fibre design on the device performances. The results from the fibre characterisation summarised in appendix A.3 provide the parameters for the simulations. We study the dependence of the slope and the threshold on the laser length. We consider a low pump rate scheme which enable us to test the limitations of the model by confronting it to a laser cutback measurement. The codoped fibres which we developed led to the demonstration of a number of devices emitting around 1.5 μm with superior performances to devices based on fibres doped with erbium only. We describe these devices in the second part of this chapter and we point out how they benefit from ytterbium codoping.

6.1 Modelling of Er/Yb devices

In this model we use a term containing the product of erbium and ytterbium populations to describe the energy transfer by a system of rate equations. This assumes that energy migration within the ytterbium population 'moves' an excited ion around, bringing it close to and allowing it to interact with a larger number of erbium ions than its direct neighbours.

6.1.1 Presentation of the Model

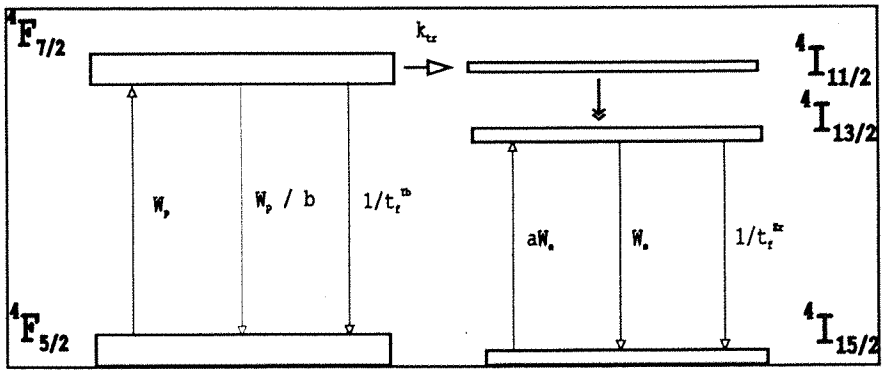

Fig. 6.1 Yb/Er Energy Diagram with model parameters (only lowest levels for Er)

The description of the Er/Yb system, proposed in [Morkel_92], is illustrated in Fig. 6.1. It translates into the system of rate equations which provides the starting point of the model

$$\begin{cases} \dfrac{dN_2^{Yb}(z)}{dt} = W_p(z)\, N_1^{Yb}(z) - \left(\dfrac{W_p(z)}{\beta} + \dfrac{1}{\tau_f^{Yb}} + k_{tr}\, N_1^{Er}(z)\right) N_2^{Yb}(z) & (6-1a) \\ \dfrac{dN_2^{Er}(z)}{dt} = \left(\alpha W_e(z) + k_{tr}\, N_2^{Yb}(z)\right) N_1^{Er}(z) - \left(W_e(z) + \dfrac{1}{\tau_f^{Er}}\right) N_2^{Er}(z) & (6-1b) \\ N^{Yb}(z) = N_1^{Yb}(z) + N_2^{Yb}(z) & (6-1c) \\ N^{Er}(z) = N_1^{Er}(z) + N_2^{Er}(z) & (6-1d) \end{cases}$$

where

- N^{RE}, N_1^{RE}, N_2^{RE}, are respectively the average density of rare-earths (RE is Er or Yb), the average density of excited RE, and the average density of RE in the ground state.

- τ_f^{Er} is the erbium fluorescence lifetime and τ_f^{Yb} is the ytterbium fluorescence lifetime when all Er ions are inverted (or no Er is present).

- k_{tr} accounts for the energy transfer from Yb to Er and relates to the small signal (all Er ions in the ground-state) quenching rate W_{tr} by:

$$k_{tr} = \frac{W_{tr}}{N^{Er}} \qquad (6-2)$$

The quenching rate is taken as the inverse of the fast component of the ytterbium decay.

- α and β are the ratios of the absorption cross-section σ_{12} to the emission cross-section σ_{21} for the Er and the Yb transitions respectively. They are dependant on the signal and pump wavelength.

$$\alpha(\lambda) = \frac{\sigma_{12}^{Er}(\lambda)}{\sigma_{21}^{Er}(\lambda)}, \quad \beta(\lambda) = \frac{\sigma_{12}^{Yb}(\lambda)}{\sigma_{21}^{Yb}(\lambda)} \qquad (6-3)$$

- W_p and W_e are the pump absorption rate from the Yb and the stimulated-emission rate from the Er, respectively. They express the interaction between the rare-earths and the optical powers:

$$W_p(z) = \frac{\sigma_{12}^{Yb}\ \lambda_p\ \Gamma_p}{Ahc}\ P_p(z)\ ,$$

$$W_e(z) = \frac{\sigma_{21}^{Er}\ \lambda_s\ \Gamma_s}{Ahc}\ (\ P_s^+(z) + P_s^-(z) + P_{ase}^+(z) + P_{ase}^-(z)\ ) \qquad (6-4)$$

A is the core area of the fibre, λ_p and λ_s are the pump and signal wavelength, Γ_p and Γ_s are the overlap of the pump and signal modes with the fibre core, as defined in §4.3.3. P_p, P_s and P_{ase} are the pump, signal and Amplified Spontaneous Emission (ASE) powers. By convention the pump is taken to propagate in the forward direction and the symbols '+' and '-' account for the co- and counterpropagating directions of the signal and ASE powers.

We operate in steady state so that the time varying terms in system (6-1) are equal to zero. This leads to :

$$\begin{cases} \dfrac{N_2^{Yb}(z)}{N^{Yb}} = \dfrac{W_p(z)}{(1 + \frac{1}{\beta})\ W_p(z) + \frac{1}{\tau_f^{Yb}} + k_{tr}\ (N^{Er}(z) - N_2^{Er}(z))} & (6-5a) \\ \dfrac{N_2^{Er}(z)}{N^{Er}} = \dfrac{\alpha\ W_e(z) + k_{tr}\ N_2^{Yb}(z)}{(1 + \alpha)\ W_e(z) + \frac{1}{\tau_f^{Er}} + k_{tr}\ N_2^{Yb}(z)} & (6-5b) \end{cases}$$

By substituting (6-5b) in (6-5a) we obtain a quadratic equation for N_2^{Yb} in function of the propagation powers.

The second building block of this model is provided by the power propagation equations:

$$\begin{cases} \dfrac{dP_p(z)}{dz} = -\left[\alpha_p \left[1-(1+\dfrac{1}{\beta}) \dfrac{N_2^{Yb}(z)}{N_T^{Yb}} \right] + \alpha_{b,p} \right] P_p(z) & (6-6a) \\ \dfrac{dP_s^{+,-}(z)}{dz} = \pm (\gamma(z) - \alpha_{b,s}) P_s^{+,-}(z) & (6-6b) \\ \dfrac{dP_{ase}^{+,-}(z)}{dz} = \pm 2 \mu(z) \gamma(z) h\nu \Delta\nu \pm (\gamma(z) - \alpha_{b,s}) P_{ase}^{+,-}(z) & (6-6c) \end{cases}$$

with

$$\alpha_p = \sigma_{12}^{Yb} \Gamma_p N^{Yb} \qquad (6-7)$$

$$\gamma(z) = \sigma_{21}^{Er} \Gamma_s [(1+\alpha)N_2^{Er}(z) - \alpha N^{Er}], \qquad (6-8)$$

$$\mu(z) = \frac{N_2^{Er}(z)}{[(1+\alpha)N_2^{Er}(z) - \alpha N^{Er}]} \qquad (6-9)$$

$h\nu.\Delta\nu$ is the equivalent input noise power corresponding to one photon per mode in bandwidth $\Delta\nu$ and $\mu(z)$ is the local inversion coefficient. $\alpha_{b,p}$ and $\alpha_{b,s}$ are the background losses at the pump and signal wavelength, respectively.

Closed-form expressions for these powers cannot be obtained but we can now outline how solutions can be obtained using numerical analysis. In the following we treat the cases of an amplifier and a laser.

The amplifier:

For an amplifier extending from z = 0 to z = L, the initial conditions are $P_s(0) = P_s^{in}$ for co-propagating pump and signal or $P_s(L) = P_s^{in}$ for the counterpropagation case, combined with $P_p(0) = P_p^{in}$, $P_{ase}^{+}(0) = P_{ase}^{-}(L) = 0$. The difficulty arises from the fact that in both cases, at either ends of the fibre, not all powers are known.

The equations are then solved by a shooting method: initial guesses are made on the excited population densities and $P_{ase}^{-}(0)$, $P_{ase}^{+}(L)$ (and also $P_s(0)$ in the counterpropagation case), the equations in (6-5) & (6-6) are propagated forwards and backwards, and the initial guesses are refined; This procedure is repeated until convergence to a solution verifying all the initial conditions.

The laser:

We note 'loss' the round-trip cavity loss, and R1, R2 the input and output mirror reflectivities for the signal. The reflectivities for the pump are neglected.

The threshold is reached when the round-trip gain compensates for the losses:

$$2 \int_0^L \gamma(z)\, dz = -(1-loss)\ln(R_1 R_2) \qquad (6-10)$$

The threshold pump power P_p^{th} is obtained by solving equation (6-6a) for increasing pump values using a secant method, until the threshold condition is satisfied. The calculation is simplified by the fact that $P_s^+(z) = P_s^-(z) = 0$ below threshold.

The (maximum) slope efficiency, S, of the laser can be expressed as [Guitart_92]:

$$S = \frac{P_{out}}{P_p(0) - P_p^{th}(0)} = \eta_{abs} \frac{\lambda_p}{\lambda_s} \frac{\ln(R_2)}{\ln(R_1 R_2)\,(1-loss)} \qquad (6-11)$$

where the output power and the absorption efficiency are given as:

$$P_{out} = (1-R_2)\, P_s(L), \quad \eta_{abs} = 1 - \frac{P_p(L)}{P_p(0)} = 1 - \frac{P_p^{th}(L)}{P_p^{th}(0)} \qquad (6-12)$$

Here we assumed the slope efficiency to be constant above threshold.

6.1.2 Varying the rare-earth ratio

We first study the case where the erbium ion concentration is fixed to 500 ppm and the ytterbium concentration is 2500, 7500, and 15000 ppm. Fig. 6.2 shows the results of the simulation. When the ytterbium concentration is increased the pump power is absorbed in a shorter length so that the optimum length is reduced. We also see that the minimum threshold decreases with increasing ytterbium concentration. The erbium ions are more easily inverted because the pump rate is increased. Indeed, we see from eqns (6-5) that the energy transfer pump rate, which is responsible for the erbium inversion, increases with the ytterbium ion population.

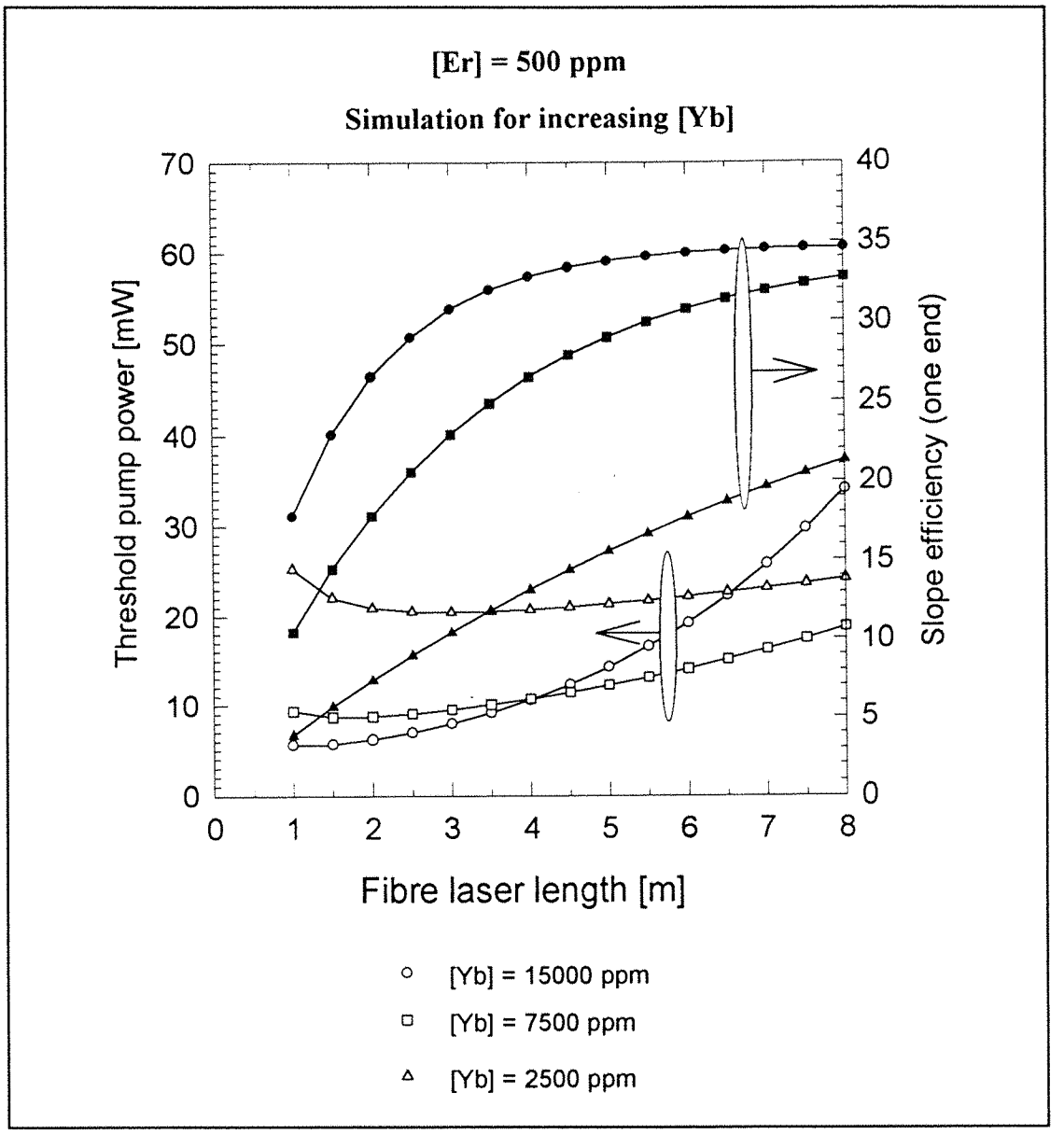

Fig. 6.2 Laser simulation of the effect of increasing ytterbium population

To design short lasers with low threshold the ytterbium population should be kept as high as possible while still avoiding devitrification. There is another reason to incorporate large amounts of ytterbium: in a study on bulk phosphate glasses, Gapontsev has shown that W_{tr} is nearly proportional to $(N^{Yb})^{1.6}$ in a phosphate glass [Gapontsev_82] (whereas it varies linearly with N^{Er}). It is indeed expected that at low rare-earth concentration the ions become too far apart to transfer energy.

We typically can incorporate a maximum rare-earth concentration of 15000 ppm before the onset of devitrification. The question now arises of how to choose the concentration ratio 'r' once the overall concentration is fixed. Fig. 6.3 shows the results of the simulation. The slope is only slightly increasing with increasing ratio r because the ytterbium concentration does not vary significantly. On the other hand the threshold decreases with increasing ratio because

the energy transfer pump rate of the erbium ions is N_2^{Yb} / N^{Er} W_{tr}.

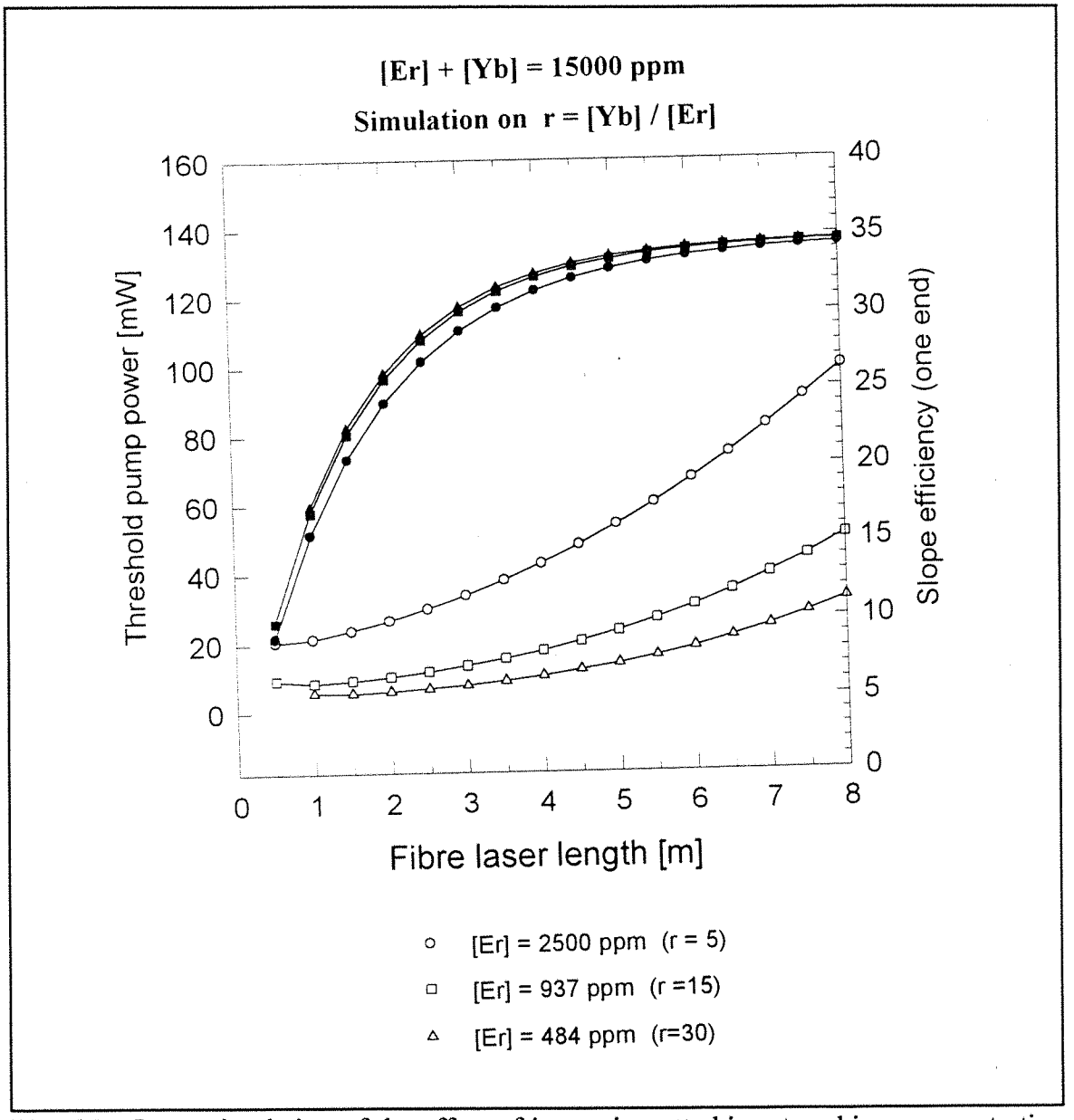

Fig. 6.3 Laser simulation of the effect of increasing ytterbium to erbium concentration ratio for a fixed rare-earths concentration.

At very high power

$$\frac{N_2^{Yb}}{N^{Yb}} \rightarrow \frac{1}{1 + \frac{1}{\beta}} \quad \textit{and} \quad \frac{N_2^{Er}}{N^{Er}} \rightarrow \frac{k_{tr}\,\tau_f^{Er}\,N^{Yb}}{(1 + \frac{1}{\beta}) + k_{tr}\,\tau_f^{Er}\,N^{Yb}} \qquad (6-13)$$

Numerically this gives N_2^{Yb} / N^{Yb} -> 0.0909 and N_2^{Er} / N^{Er} -> 0.997. So almost full erbium inversion can be obtained.

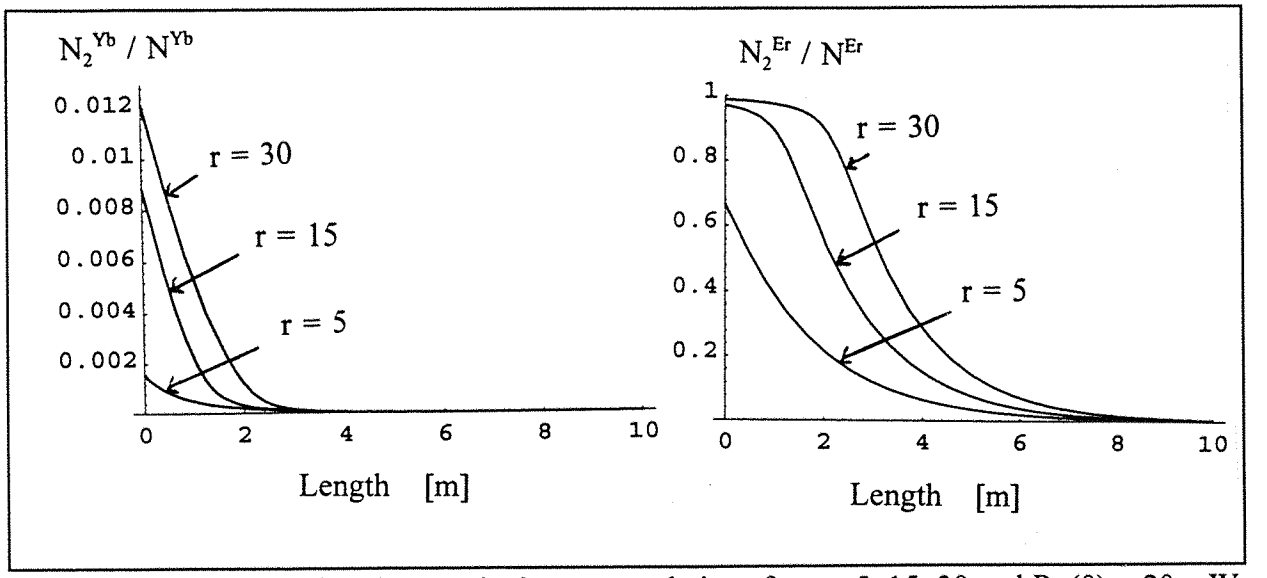

Fig. 6.4 Ytterbium and erbium excited state populations for r = 5, 15, 30 and P_p (0) = 20 mW.

We see in Fig. 6.4 that even at low power the smallest erbium population can be almost fully inverted. In fact erbium clustering may reduce the inversion. This detrimental effect will affect most the low ratio fibre, where the erbium population is a few thousands of ppm. On the other hand we also see from Fig. 6.4 that the ytterbium population is more inverted for the high ratio fibre. Thus the high ratio fibre will be more affected by laser saturation.

6.1.3 Critical discussion

For a very short length the fractional absorbed pump power becomes negligible and the threshold cannot be reached. In fact, we can calculate the minimum length required for lasing (assuming total Er population inversion in the threshold condition):

$$L_{min} = -\frac{1}{2\,\sigma_{21}^{Er}\,\Gamma_s\,N^{Er}}\ln(R_1R_2)\,(1-loss) \qquad (6-14)$$

For our set of parameters L_{min} = 24.1cm. This is in good agreement with the measurement shown in Fig. 6.5. For very long lengths the threshold grows infinitely as the re-absorption (characteristic of 3-levels systems) becomes large. As expected, there is an intermediate length which minimises threshold. Both theoretical and experimental curves show that this length is around 100 cm. The predicted value of this minimum threshold is however smaller than the measured value.

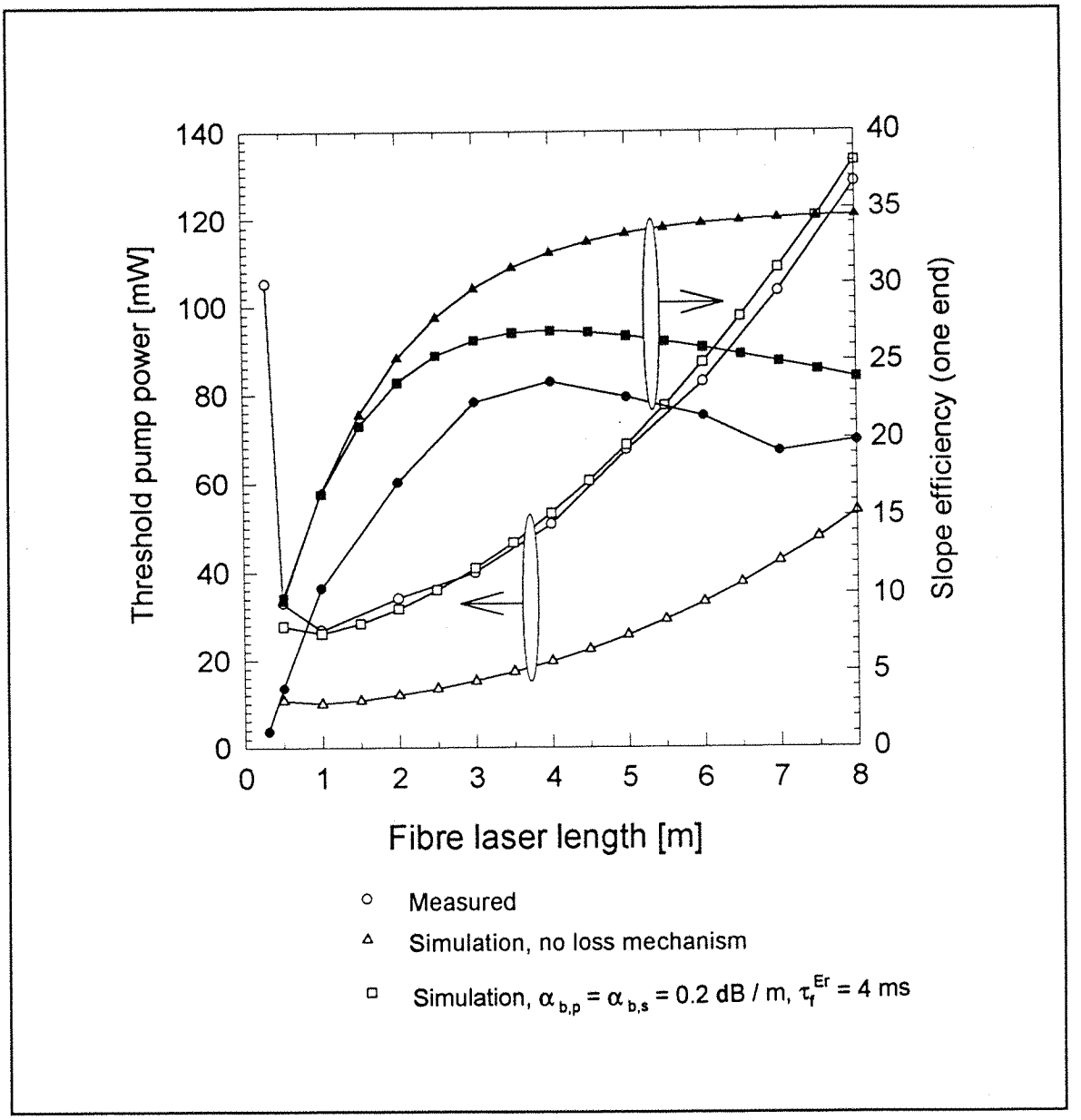

Fig. 6.5 Comparison of laser simulation and measurement

Including the background losses and the reduction of the erbium metastable lifetime (this is a first approximation of the effect of uniform upconversion) leads to a better agreement between prediction and measurement, although the slope remains overestimated. This clearly indicates that loss mechanisms need to be further studied to model this system accurately.

6.2 Devices

Initially fibre lasers were considered to be low power devices, because the low NA and small spotsize of the single-mode fibres are incompatible with the beam parameters of available high power diode lasers. Scaling up the power requires increasing the launch efficiency. A possibility is to use a larger fibre core which is adapted to the emitter dimension of the high power source. But the laser threshold increases quadratically with the core diameter and an increase in fibre diameter results in multimode operation with a reduced beam quality. Two efficient ways to scale up the output power while retaining the single mode operation are presented below. Both ways require ytterbium codoping. Ytterbium codoping is also beneficial in Q-switched and single frequency lasers.

The author gratefully acknowledges the work of Stuart Gray on the Nd: YAG pumped high power laser, John Minelly and Zhi-Jie Chen on the cladding pumped devices, Gareth Lees on the Q-switched laser, and Thomas Kringlebotn & Wei Loh on the single-frequency lasers. All the experimental results presented here make use of the Er:Yb fibres developed in this work.

6.2.1 High power amplifiers and lasers pumped around 1.05 μm

The first approach pursued at Southampton to scale up the power of Er-doped monomode fibres was to pump the fibre with a Nd:YAG or a Nd:YLF laser. Low brightness AlGaAs diodes emitting around 800 nm are used to side pump a Nd-doped crystal rod which lases in the TEM_{00} mode. This technique allows up to several watts of pump power to be launched into a monomode fibre. The pump laser operates around 1.05 μm where the erbium ions do not absorb. It is therefore necessary to incorporate ytterbium ions in the core. This approach has now reached the marketplace: ATx Telecom System Inc. commercialises a Nd:YLF pumped Er:Yb fibre amplifier capable of delivering an output power in excess of 27 dBm (see appendix A.4).

This pumping scheme was also chosen to demonstrate a laser delivering up to 950 mW at 1535 nm. This high power was needed to generate sufficient Raman gain at 1560 nm to assure lossless transmission of subpicosecond soliton pulses over 22 km of dispersion shifted fibre [10]. Fig. 6.6 shows the setup of the experiment. Note that the soliton source also makes use of an Er:Yb fibre with Nd:YLF pumping. The high pump power offered by this pumping scheme results in a high repetition rate.

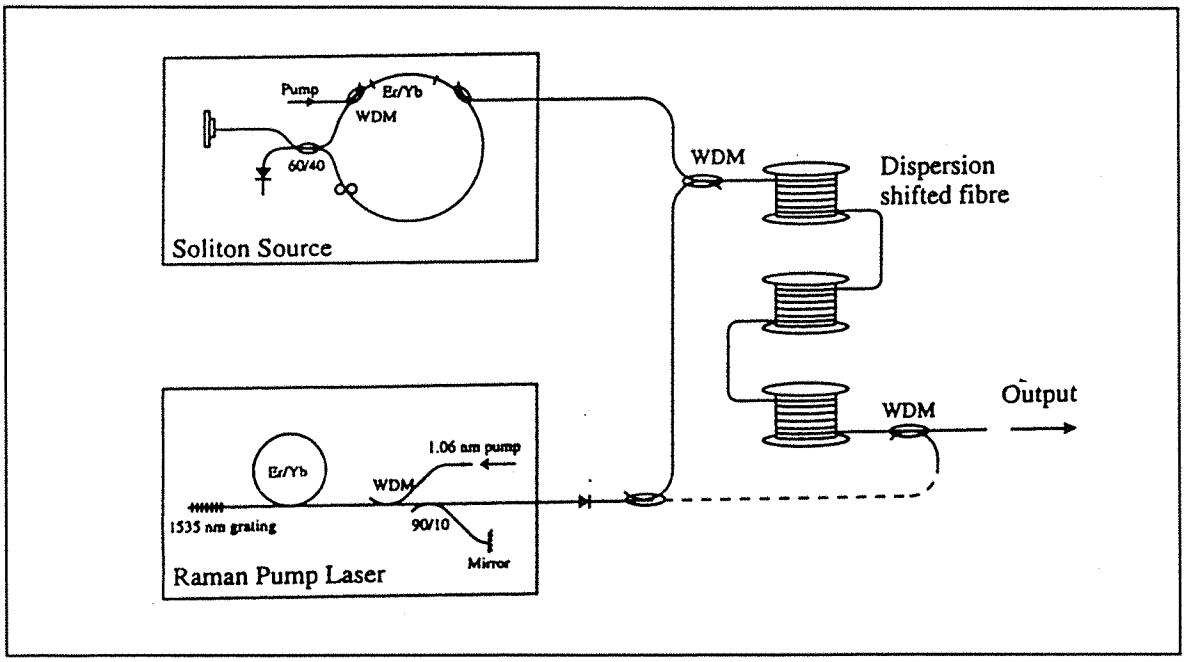

Fig. 6.6 Soliton propagation experiment with soliton source and Raman pump laser based on Er:Yb fibres.

6.2.2 Cladding pumped fibre devices

An intermediate pumping laser operating at around 1.05 μm reduces the device compactness and optical efficiency. There is no need for this intermediate laser if the brightness conversion can be achieved in the fibre. The structure of the double clad fibre illustrated in Fig. 6.7 allows such a conversion. The double-clad fibre is designed so that the pump beam is not directly launched into the doped fibre core, but rather into a surrounding multimode first cladding waveguide with large diameter and NA, which allows efficient coupling of pump power into the fibre. Then the pump light is intercepted and absorbed by the rare-earth doped core. The absorbed pump power scales with the first cladding to core area ratio [Bedo_93], and ytterbium is needed to reduce the threshold in large area ratio fibres.

We reported the performance of ND959CP, our most efficient all glass cladding pumped fibre in [11]. The fibre had the same geometry as ND950CP shown in Fig. 6.7, and was doped with 10 000 ppm (Yb) and 500 ppm (Er). The double clad fibre was first set up in the laser form pumped by two 1 W laser diodes operating at 977 nm and butted with a dichroic mirror at the input end to measure the efficiency. The laser characteristics at optimum length of 3.2 m indicated a threshold power of 20 mW, maximum lasing power of 330 mW and a slope efficiency of 41% with respect to absorbed power. Then we set up a power amplifier using

a fibre coupled circulator to isolate the signal source and separate the input and output signals. The gain and output signal of an optimised 3.2 m amplifier measured at 1535 nm indicates that small signal gain of 33 dB and saturation output power in excess of 23 dBm were achieved (Fig. 6.8).

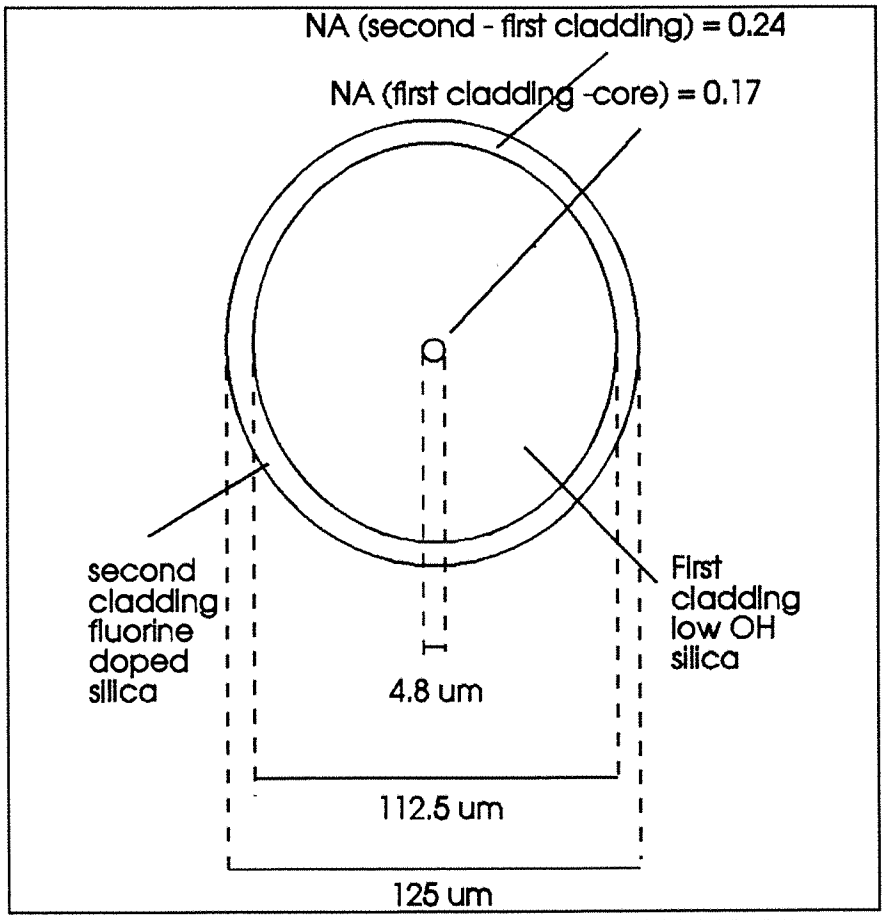

Fig. 6.7 All glass double clad fibre geometry (ND950_04)

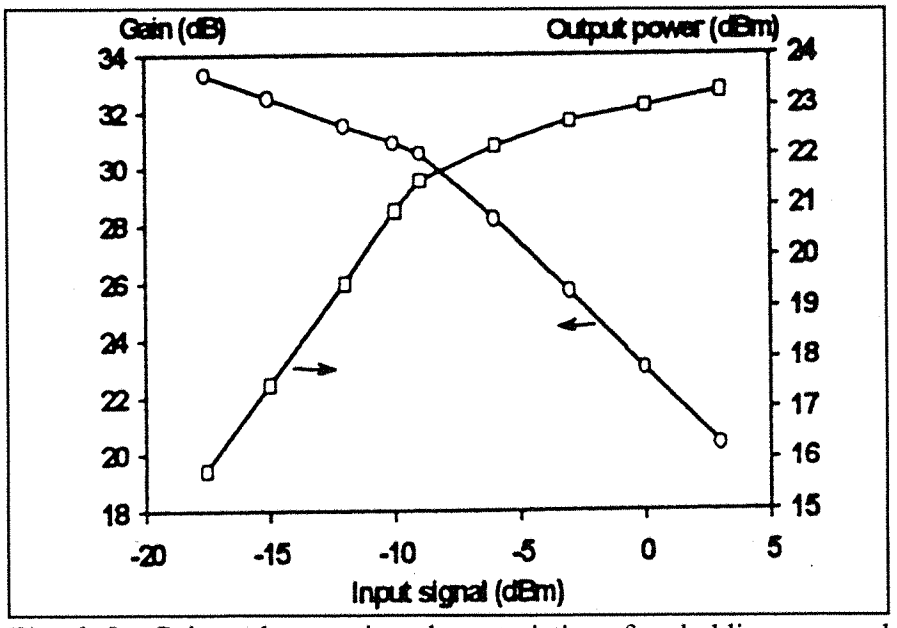

Fig. 6. 8 Gain and saturation characteristics of a cladding pumped fibre amplifier

We saw in §4.3 that the ytterbium ion offers a wide absorption band. It is important to know how much deviation in the emission wavelength of the pump laser diode peak is acceptable. A Ti:sapphire laser tunable from 930 nm to 990 nm was used to measure the pump wavelength dependence of the CW lasing performance of the cladding pumped fibre ND959. A simple laser cavity comprising two 4% reflections was employed with the output measured at the fibre end remote from the pump. The measured output was doubled to obtain the overall conversion efficiency. The launched pump power was approximately 1 W over the measuring range. Fig. 6.9 shows the conversion efficiency at the optimum length for each pump wavelength. The optimum length was 2.5 m at 976 nm and 5 -7 m at all other wavelengths. Efficiency in excess of 30% was obtained over a 50 nm band from 950 nm to 990 nm. However at wavelength outside the narrow 976 nm absorption peak the lasing occurred at a wavelength of 1544 nm and 1556 nm rather than the peak of 1536 nm indicating incomplete inversion over the pump absorption length. While this is not an issue for the CW laser, it would reduce the efficiency of a 1536 nm pulse amplifier. A longer length could also lead to performance degradation from stimulated Raman scattering. The inset in Fig. 6.9 shows the wavelength dependent performance when the optimum length for 976 nm pumping is chosen. In this case the high efficiency window is only ±3 nm. A broader wavelength tolerance on the pump diode and longer signal wavelength is preferable.

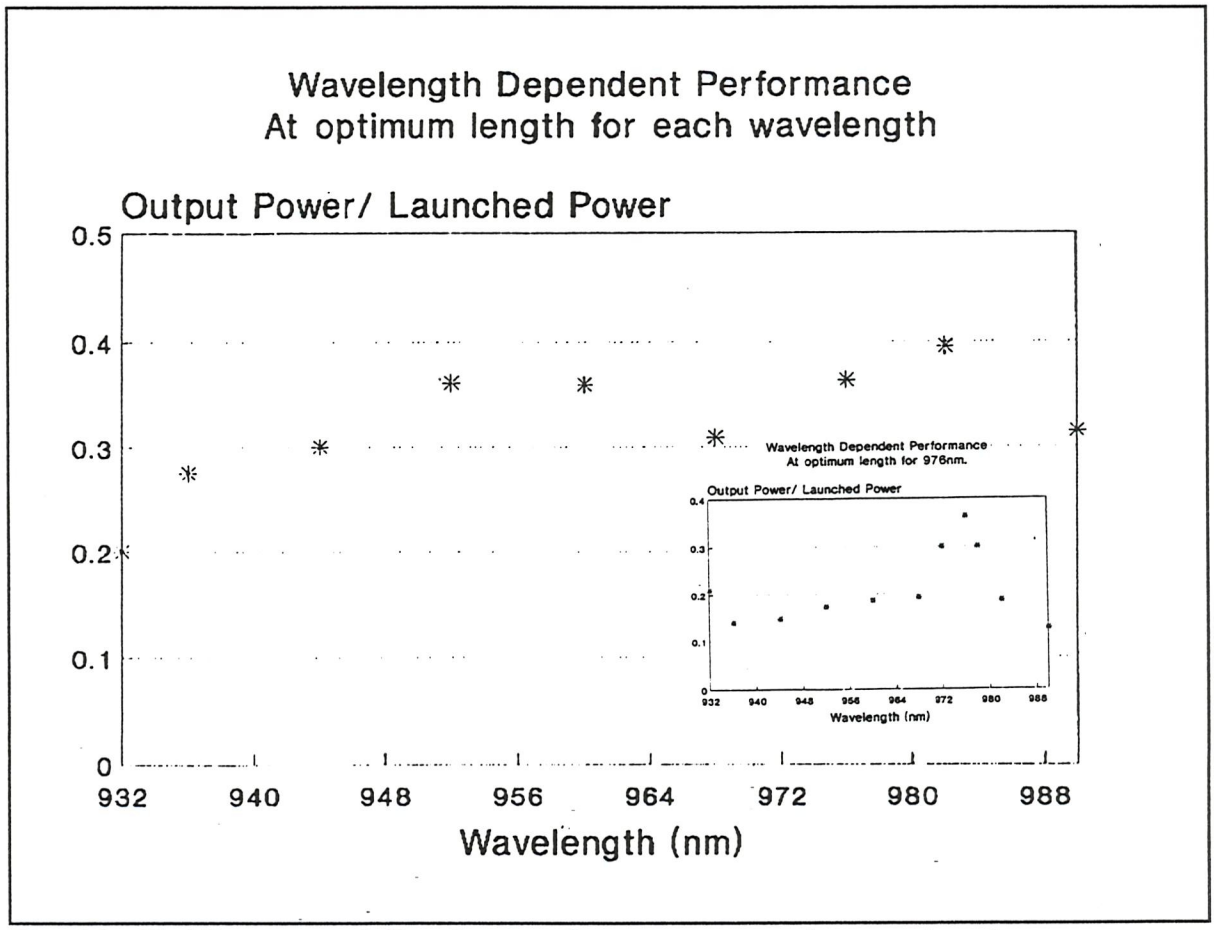

Fig. 6.9 Cladding pumped fibre laser performance vs pumping wavelength

6.2.3 Q-switched fibre laser

High power short pulses at 1.55 μm have many uses in areas such as long range optical time domain reflectometry (OTDR) [Lees_96], laser marking, and laser range finding [Minelly_96]. Lees carried out a comparison of Q-switched lasers based on Er-doped and Er-Yb codoped fibres [Lees_95]. The experimental apparatus used is shown in Fig. 6.10.

The phosphosilicate Er:Yb-doped fibre used had an average rare-earth concentration of 12000 ppm, an ytterbium to erbium concentration ratio of 20, and an NA of 0.17. For the estimated 45 mW of launched pump power, a length between 5 and 10 cm produced the best results. The length used for this test was 8.7 cm. The aluminosilicate Er- doped fibre was 80 cm long, had a rare-earth concentration of 800 ppm, and an NA of 0.15. Fig. 6.10 illustrates the peak power and pulse width against the repetition rate for both Er and Er:Yb Q-switched fibre lasers.

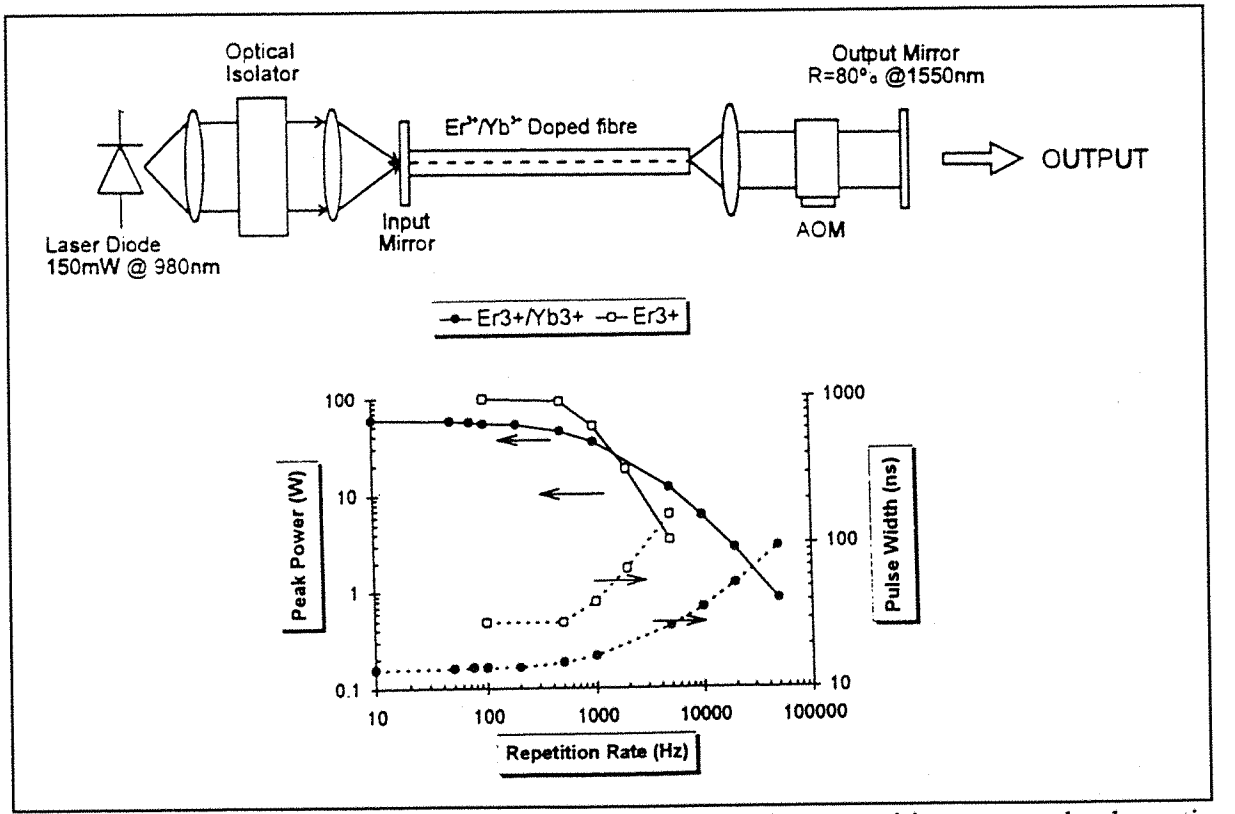

Fig. 6.10 Q-switched peak power and pulse width against repetition rate and schematic diagram of diode pumped Q-switched Er:Yb fibre laser

Fig. 6.10 shows that the addition of ytterbium allows high peak powers to be produced at higher repetition rates. The same effect was observed when the pumping power of a Q-switched Er fibre laser was increased [Myslinski_92]. The higher pump rate offered by ytterbium codoping allows the population inversion to recover at a faster rate. As a result, the Er:Yb fibre can operate at higher repetition rates. The short length of the codoped fibre also results in the generation of shorter pulses. Finally, as higher and higher pump powers become available from diode lasers, the short length offered by ytterbium codoping will be important to reduce detrimental nonlinear effects such as self phase modulation and Raman scattering.

6.2.4 Grating-feedback single frequency lasers

Distributed Bragg Reflector (DBR) fibre lasers are only single -frequency provided that the grating bandwidth is kept below about 0.2 nm and the laser length is reduced to a few cm to increase the axial mode spacing. The single-frequency stability increases with decreasing cavity length and decreasing grating bandwidth. With Er^{3+}-doping the pump absorption (both at 980 & 1480 nm, two practical pump wavelength of Er^{3+}) in such short laser lengths is normally only a few percent, and hence the slope efficiency of these lasers is very low (<1%) even with high Er^{3+} concentration. A solution is to co-dope the Er^{3+}-doped fibre with Yb^{3+} which increases the absorption at the pump wavelength by more than two orders of magnitude and enables highly efficient operation of cm-long lasers.

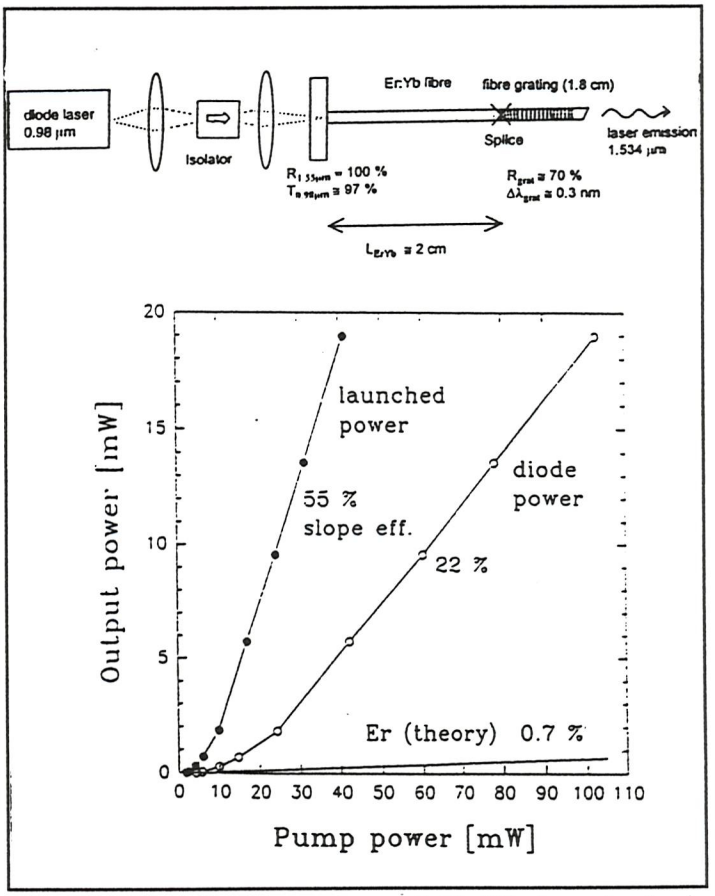

Fig. 6. 11 Configuration of Er:Yb-doped single frequency fibre laser with laser output and output power of an ideal lossless fibre laser doped with Er alone for comparison

The main difficulty which we faced with grating-feedback lasers was that grating are not easily written in the phosphosilicate host used in Er:Yb

fibres [Dong_94]. Fig. 6.11 illustrates the setup and the performance of the first efficient DBR Er:Yb single frequency laser reported [1,2]. In this case we chose to splice a grating to the Er:Yb fibre. Kringlebotn *et al.* later reported a Distributed FeedBack (DFB) Er: Yb laser [Kinglebotn_94]. Although we obtained >99% reflectivity, the writing process took four hours and hydrogen loading was needed. Hydrogen loading dramatically increases the loss at the pump wavelength. It induces a loss of 0.5 dB / cm at 980 nm [Loh_96]. Therefore the slope efficiency was 5% only.

Recently Dong *et al.* showed that tin-codoping is an efficient way to write gratings in phosphosilicate fibres, without the need for hydrogenation [Dong_95]. Using a tin codoped phosphosilicate fibre of 0.17 NA and 1270 nm cutoff containing 600 ppm of erbium and 2000 ppm of ytterbium, Loh et al. succeeded in improving the efficiency of 1.5 μm fibre DFB lasers [Loh_96]. To achieve single-sided output operation, a 1.5 cm strong (»99% reflectivity, 1 nm bandwidth) grating fabricated in a B/Ge fibre was directly spliced to the 8.5 cm Er/Yb fibre, in which a 80% reflectivity, 0.10 nm bandwidth grating had been written (Fig. 6.12 Inset). The laser performance obtained is shown in Fig. 6.12. Other approaches are currently studied to scale up the power of 1.5 μm fibre DFB lasers to 100 mW.

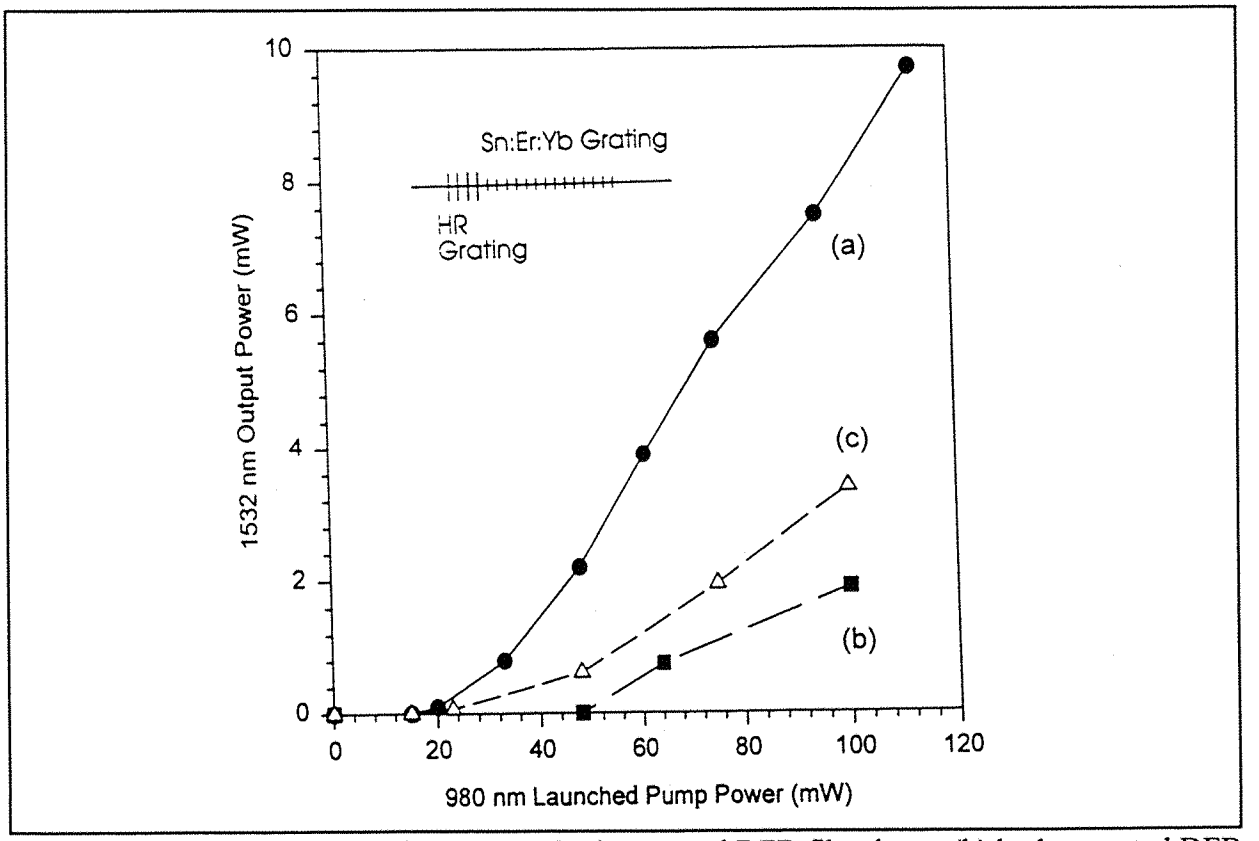

Fig. 6.12 Lasing characteristics of (a) unhydrogenated DFB fiber laser, (b) hydrogenated DFB fiber laser, (c) 5 cm long hydrogenated DFB fibre laser. Inset: schematic of DFB laser.

6.3 Conclusions

A model of Er/Yb fibre devices was presented and applied to predict the effect of varying Yb to Er concentration ratios on the laser threshold and slope. It was seen that the ytterbium concentration should be kept as high as possible to minimise the device length. In practice the maximum rare-earth concentration is fixed. A high ytterbium to erbium concentration ratio 'r' results in a low threshold as the erbium ions are easily inverted. It also reduces the effect of erbium clustering. However, a high ratio r makes the laser more prone to saturation. Confrontation with a laser cutback measurement shows that the model can be used to predict the length dependence of the laser threshold and slope, but it also indicates that the loss mechanisms will need to be studied in detail to accurately predict the laser performances. In the second part of this chapter we described the devices based on our Er/Yb fibres. In particular, performance of the cladding pumped laser based on the new all-glass design described in chapter 3 led to significant improvement over the previous work at Southampton [Minelly_93].

Chapter 7

CONCLUSIONS & FUTURE WORK

7.1 Summary & Conclusions

In chapter 1 we presented the context in which this work was initiated. We saw that erbium:ytterbium fibres are not only needed to fulfil new requirements in modern optical telecommunication networks, but that they are also expected to open new markets to fibre lasers.

In chapter 2 we reviewed the interactions between a rare-earth ion and its environment and we outlined the mechanism of energy transfer. Background knowledge on phosphate glasses and the solution doping technique were also presented.

In Chapter 3 we described the fabrication process step by step showing how the phosphorus and the rare-earths can be incorporated in the core of silica based fibres. We saw that to retain a maximum of phosphorus in the core an optimum $SiCl_4$ flow should be used at the deposition stage. To prevent the core layer from being sintered during the deposition the burner needed to be translated in opposite direction to the precursor gases. The layer deposited could not be immersed in the doping solution directly after deposition, and an extra pass, the presintering pass, was necessary to consolidate the frit beforehand. The structure of the frit presintered at different temperatures was observed, and was seen to influence the dopant incorporation. The evaporation of phosphorus resulted in a large 'evaporation dip' in the middle of the preform, but it could be reduced by increasing the precollapse and sealing the preform directly after fusing the core layer. We saw that the hydroxyl contamination could severely affect the lasing performance of our fibres. The hydroxyl contamination was seen to decrease the erbium metastable lifetime and to increase the loss at the signal wavelength. It was attributed to the P..OH first overtone, whose absorption overlaps with the erbium emission around 1.55 μm. A damaged frit, due to insufficient presintering of the frit before immersion in the doping solution, resulted in anomalously high background loss, which lowered the efficiency of Nd:YAG pumped lasers. Finally, we saw that it is important to control the presintering temperature accurately to avoid phase separation, which could not be

reduced when pulling the preform into a fibre.

In chapter 4 two techniques were used, ICP-MS and EDS, to analyse the composition of our preforms and fibres. The first method was the most accurate and the results, in combination with absorption measurements, were used to determine the erbium and ytterbium absorption cross-section. On the other hand, the second method was much simpler to implement, and sufficient for comparison between fibres. Our fibres contain up to 12 mol% (P_2O_5) and 1.5 mol% of rare-earths. We checked that the ytterbium to erbium ratio in the glass was conserved from the doping solution. We found evidence that the rare-earths are not randomly distributed in the glass but are associated with phosphate units : by introduction of rare-earths the Raman spectra showed no appearance of new Si-related vibration modes whereas a new scattering peak attributed to metaphosphate chains appeared around 1200 cm^{-1} ; increasing the rare-earth content increased the background loss which is probably due to defects in the phosphate phase ; the absorption spectrum of the erbium ion in our fibres was typical of a phosphate host. We saw that the preforms should be pulled to obtain a core size corresponding to a cutoff wavelength of around 1200 nm to maximise the output power of our 1064 and 980 nm pumped fibre lasers. We compared the signal-dopant overlap factor for a measured profile and a step index profile and found that the difference did not exceed 15% over the 700 - 1500 nm range of cutoff wavelengths. Backward ASE and laser cutback measurements were described as methods to evaluate the device performances of the erbium:ytterbium fibres. Using a Nd:YAG laser as a pump source, the performance of fibres doped with 1.0 - 1.5 mol%(Yb^{3+}) was reduced by a background loss in excess of 0.5 dB / m. The main mechanism responsible for the green fluorescence in our efficient fibres was identified as the energy transfer $[(Yb, {}^2F_{5/2});(Er,{}^4I_{11/2})] \rightarrow [(Yb, {}^2F_{7/2});(Er,{}^4F_{7/2})]$. The uniform upconversion constant in erbium was estimated from lifetime measurements and measurement of unbleachable losses showed that the erbium ions cluster less in aluminogermanosilicate than in phosphosilicate fibres.

In chapter 5, we showed that addition of aluminium in the region [Al] < [P] decreases the refractive index of the glass, produces striae, and does not lead to spectral broadening around 1.5 μm. The reduction in laser efficiency with increasing aluminium content was seen to be related to an increase in energy transfer time. Evidence from fluorescence lifetimes and fluorescence spectra, showed that in this series of fibres where [Al] < [P], the rare-earths preferably couple to phosphate units rather than Al-O, probably because all aluminium ions bond to phosphorus to create $AlPO_4$ units. This made clear that the back- transfer of energy could not be responsible for the reduction in laser efficiency. The reduction in laser efficiency

was related to a reduction in forward transfer. This was caused by the reduction of rare-earth clustering when aluminium was introduced in the phosphosilicate host. On the other hand, introduction of a few grams of aluminium in the doping solution was efficient at reducing the phase separation in patches which plagues the fabrication of phosphosilicate rare-earth doped fibres, without severely deteriorating the device performances.

In chapter 6, a model of Er/Yb fibre devices was presented and applied to predict the effect of varying Yb to Er concentration ratio on the laser threshold and slope. It was seen that the ytterbium concentration should be kept as high as possible to minimise the device length. In practice the maximum rare-earth concentration is fixed. A high ytterbium to erbium concentration ratio 'r' results in a low threshold as the erbium ions are easily inverted. It also reduces the effect of erbium clustering. However, a high ratio r is expected to make the laser more prone to saturation. Confrontation with a laser cutback measurement showed that the model can be used to predict the length dependence of the laser threshold and slope, but it also indicates that the loss mechanisms will need to be studied in detail to accurately predict the laser performances. In the second part of this chapter we described the devices based on our Er/Yb fibres. In particular, the performance of the cladding pumped laser based on the new all-glass design described in chapter 3 led to significant improvement over the previous work at Southampton [Minelly_93].

7.2 Future work

The main issue which remains to be studied in the erbium : ytterbium fibres is the effect of clustering on energy tranfers (between Er-Er, Yb-Yb, and Yb-Er). Enough fibres have already been fabricated to carry out a detailed study, and the understanding gained should allow us to optimise the efficiency of our devices. New designs and codopants for our cladding pumped fibres will also be investigated.

7.2.1 Improved laser efficiencies

Although the process is now sufficiently well understood to fabricate fibres with good reproducibility, the efficiency of the fibres needs to be improved. Our cladding pumped fibre lasers show a maximum slope efficiency of 40% and grating feedback lasers do not seem to perform as well as reported in [1,2]. An important task will be to identify and quantify the loss mechanisms.

Concentration quenching in erbium doped fibres is a well known phenomenon and we have seen in §4.5.2 that the resulting unsaturable losses can be easily measured. However, the source used for this measurement emitted around 980 nm where the ytterbium ions also absorb. To carry out a similar measurement in the codoped fibres we need to change the pump source wavelength, while still having at least a few tens of mW available to clearly observe the saturation of the unclustured ions. We are performing the measurement pumping around 1530 nm using a cladding pumped Er/Yb fibre laser.

Unsaturable losses in ytterbium doped fibres have recently been observed and it was reported that they can significantly affect the laser performance when pumping around 980 nm [Paschotta_97]. Their origin has not been identified and we do not yet know if they are present in our codoped fibres. To distinguish the effect of ytterbium quenching from the effect of erbium quenching the measurement will require that the Er:Yb fibre be free of erbium clustering so that the erbium ions can be fully inverted.

Clustering of ytterbium and erbium ions, which is essential for the energy transfer mechanism, remains to be investigated. We will need to quantify the effect of the ytterbium and erbium concentrations, and core composition & preparation (in particular porous layer presintering) on the transfer rate and on the efficiencies of lasers pumped at different wavelengths, particularly around 980 nm. A 'too slow' Yb → Er transfer is expected to deteriorate the laser efficiency and to increase the ytterbium fluorescence, which will need to be quantified. On the other hand, a 'too fast' Yb → Er transfer is expected to be linked to an increase in deleterious energy transfer, i.e. transfer to an excited erbium ion and erbium upconversion.

7.2.2 Cladding pumped fibre design

We have verified in [11] that offsetting the core of a cladding pumped fibre increases the pump absorption and makes it less sensitive to bends. The test was based on the comparison of silicone coated fibres pulled from a round section and a D-shaped section obtained from the same preform. The dependence of this effect on the position of the core would need to be further investigated. It is also possible to change the geometry of the first cladding to adapt it to the shape of the pump spot. The optimisation of the first cladding geometry will be carried out once the pump source will be delivered by our partners in the HIRAFS project.

We agreed with our partners on a first cladding diameter of 250 μm, to optimise the launch efficiency in our cladding pumped fibres. This large cladding results in a low pump rate and the optimum length currently exceeds 10 m. To increase the pump rate in our cladding pumped fibres we will need to increase the core size which requires to decrease the NA in order to maintain single-mode operation. The increase in core size will also increase the energy storage for pulse operation, and shift the onset of detrimental nonlinear effects to higher powers. The NA will be decreased from the present value of 0.17 - 0.20 to around 0.10. There are two ways to decrease the NA : the refractive index of the first cladding can be increased or the core refractive index can be decreased. The first approach has the advantage that the core material need not be altered. Tens of phosphosilicate or germanosilicate layers can be deposited on the silica substrate tube before the core deposition. However, the small tolerance in the index difference between core and cladding makes the process particularly critical. The second approach would result in a quicker and more reproducible process. Fluorine is extensively used to form P/F cladding layers as it reduces the index of phosphosilicate glass [Morrow_86]. It can be deposited with the phosphorus and silica at the deposition stage. To limit its evaporation the preform can be sealed after the fusing pass or a protective layer can be deposited over the doped material.

An alternative to fluorine codoping is aluminium codoping. We have shown in chapter 5 that aluminium codoping can be used to reduce the refractive index of aluminophosphosilicate fibres. The laser efficiency was only severely reduced for the fibre containing the highest aluminium concentration. We will need to test more fibres and it may be possible to increase the efficiency at high aluminium concentration. The prospect of high rare-earth concentration in a low index material is attractive for cladding pumped lasers and pulse amplification, and the role of aluminium codoping should be further checked.

References

[Ainslie_81] *Interplay of design parameters and fabrication conditions on the performance of monomode fibers made by MCVD*
B. J. Ainslie, K. J. Beales, C. R. Day, J. Rush
IEEE J. of Quantum Electronics Vol. QE-17, No. 6 (June 1981)

[Ainslie_91] *A review of the fabrication and properties of erbium-doped fibers for optical amplifiers*
B. J. Ainslie
J. Lightwave Tech. Vol. 9, No. 2 (February 1991)

[Arai_86] *Aluminium or phosphorus co-doping effects on the fluorescence and structural properties of neodynium-doped silica glass*
K. Arai, H. Namikawa, K. Kumata, T. Honda, Y. Ishii, T. Handa
J. Applied Physics Vol. 59, No. 10 (15 May 1986)

[Artemev_81] *Some characteristics of population inversion of the $^4I_{13/2}$ level of erbium ions in ytterbium-erbium glasses*
E. F. Artem'ev, A. G. Murzin, Y. K. Fedorov, V. A. Fromzel
Sov. J. Quantum Electron., Vol. 11, No. 9 (September 1981)

[Auzel_73] *Materials and devices using double-pumped phosphors with energy transfer*
F. E. Auzel
Proc. IEEE, Vol.61, No. 6, pp. 758-786 (June 1973)

[Bjarklev_94] *Rare-earth doped fibre amplifiers for optical communication systems*
A. Bjarklev
Doctor Technices Thesis, Technical University of Denmark, Chap. 6, p. 199 (April 1994)

[Barnes_89] *Er^{3+} - Yb^{3+} and Er^{3+}-doped fibre lasers*
W. L. Barnes, S. B. Poole, J. E. Townsend, L. Reekie, D. J. Taylor,
D. N. Payne
J. Light. Tech., Vol. 7, No. 10, pp. 1461-1465 (september 1989) #420

[Barnes_91] *Absorption and Emission Cross of Er^{3+} Doped Silica Fibers*
W.L. Barnes, R. I. Laming, E. J. Tarbox, P. R. Morkel
IEEE Journal of Quantum Electronics Vol.27, No.4 (April 1991)

[Bedo_93] *The effective absorption coefficient in double-clad fibres*
S. Bedo, W. Luthy, H. P. Weber
Optics Communications, Vol. 99 (5,6), pp. 331-335 (1993)

[Carter_94] *High phosphate content silicate optical fibres fabricated via flash-condensation*
A. L. G. Carter
Ph.D Thesis, Dept of Physical and Theoretical Chemistry, University of Sydney, Australia (September 1994)

[Chakraborty_85] *The vibrational spectra of glasses in the Na_2O-SiO_2-P_2O_5 system with a 1:1 SiO_2:P_2O_5 molar ratio*
I. N. Chakraborty, R. A. Condrate
Physics and Chemistry of glasses Vol. 26, No. 3 (June 1885)

[Craig-Ryan_89] *Fabrication of long lengths of low excess loss erbium-doped optical fibre*
S. P. Craig-Ryan, B. J. Ainslie, C. A. Millar
Electronics Letters Vol. 26, No. 3 (February 1990)

[Delevaque_93] *Modeling of pair-induced quenching in erbium-doped silicate fibres*
E. Delevaque, T. Georges, M. Monerie, P. Lamouler, J.-F. Bayon
IEEE Photonics Technology Letters Vol. 5, No. 1 (January 1993)

[Desurvire_89] *Amplification of spontaneous emission in erbium-doped single-mode fibers*
E. Desurvire, J. R. Simpson
J. Lighwave Technol. Vol. 7, No. 5 (May 1989)

[DiGiovanni_89] *Structure and properties of silica containing aluminium and phosphorus near the $AlPO_4$ join*
D. J. DiGiovanni, J. B. MacChesney, T. Y. Kometani
J. Non-Crystalline Solids Vol. 113, pp. 58-64, 1989

[Digonnet_85] *Theoritical analysis of optical fiber laser amplifiers and oscillators*
M. J. F. Digonnet, C. J. Gaeta
Applied Optics Vol. 24, No. 3, pp. 333-342 (February 1985)

[Dong_92] *Novel optical fibre devices based on the MCVD method*
L. Dong
Ph.D Thesis, University of Southampton (1992)

[Dong_94] *A study of UV absorption in MCVD preforms*
L. Dong, J. Pinkstone, P. St. J. Russell, D. N. Payne
J. Optical Society America B Vol. 11, No. 10, pp. 2106-2111 (1994)

[Dong_95] *Strong photosensitive gratings in tin-doped phosphosilicate optical fibres*
L. Dong, J. L. Cruz, J. A. Tucknott, L. Reekie, D. N. Payne
Opt. Lett. Vol. 20, No. 19, pp. 1982-4 (October 1995)

[Edahiro_79] *Spectral loss characteristics of GeO2-P2O5-doped silica graded-index fibres in long-wavelength band*
T. Edahiro, M. Horiguchi, K. Chida, Y. Ohmori
Electronics Letters No. 15, pp. 274-275 (April 1979)

[Elder_91] *Thermal-mechanical and physical-chemical properties of phosphate laser glasses*
M. L. Elder, Y. T. Hayden, J. H. Campbell, S. A. Payne, G. D. Wilke
American Ceramic Society Annual Meeting, Cincinnati, Ohio, April 28-May 2 1991

[Edwards_74] *A theoretical study of the Nd: Yb: Er glass laser*
J. G. Edwards, J. N. Sandoe
J. Phys. D: Appl. phys., Vol. 7, pp. 1078-1095 (1974)

[Fermann_88] *Characterisation techniques for special optical fibres*
M. E. Fermann
Ph.D Thesis, Dept of Electronics & Computer Science, University of Southampton, Chap. 4, pp. 32-80 (1988)

[Fisons_92] *Plasmaquad System Manual*
VG Elemental Fisons Instruments (1992)

[France_90] *Fluoride glass optical fibres*
P.W. Fance, M. G. Drexhage, J. M. Parker, M. W. Moore, S. F. Carter, J. V. Wright
Published by Blackie & Son Ltd, Chapter 7 pp. 187-204 (1990)

[Galeener_79] *The Raman spectra and structure of pure vitreous P_2O_5*
F. L. Galeener, J. C. Mikkelsen
Solid State Comm. Vol. 30, pp. 505-510 (1979)

[Gambling_76] *Optical fibres based on phosphosilicate glass*
W. A. Gambling, D. N. Payne, C. R. Hammond, S. R. Norman
Proc. IEE, Vol. 123, No. 6 (1976)

[Gambling_76'] *Optical fibres based on phosphosilicate glass*
W. A. Gambling, D. N. Payne, C. R. Hammond, S. R. Norman
Proc. IEE Vol. 123, No. 6, pp. 570-576 (1976)

[Gan_81] *Calculation of physical properties and composition design of inorganic glasses*
F. Gan
Shangai Sei Technology Press (1981)

[Gandy_67] *Stimulated emission of Tm^{3+} radiation in silicate glasses*
H. W. Gandy, R. J. Ginther, J. F. Weber
J. Appl. Phys., 38, pp. 3030-3031 (1967)

[Gapontsev_82] *Erbium glass lasers and their applications*
V. P. Gapontsev, S. M. Matitsin, A. A. Isineev, V. B. Kravchenko
Optics & Laser Tech.(August 1982)

[Gapontsev_89] *Migration-accelerated quenching of luminescence in glasses activated by rare-earth ions*
V. P. Gaptontsev, N. S. Platonov
Materials Science Forum Vol. 50, pp. 165-222, Trans Tech Publications (1989)

[Garrett_82] *Components and systems for long-wavelength monomode fibre transmission*
I. Garrett, C. J. Todd
Optical and Quantum Electronics Vol. 14, pp. 95-143 (1982)

[Glodis_94] *The application of synthetic silica tubing for large preform manufacture using MCVD*
P. F. Glodis, C. F. Gridley, W. M. Flegal, A. A. Klein, D. P. Jablonowsski, D. Kalish, A. Sorby, H. Damsgaard, G. Knudsen, H. Scharper, N. Treber, H. Fabian, P. C. Schultz
International wire and cable symposium, Atlanta (November 94)

[Goldstein_92] *Scanning Electron Microscopy and X-ray Microanalysis*
Goldstein, Newbury, Echlin, Joy, Romig, Lyman, Fiori
2cnd Edition, Lifshin Plenum Press (1992)

[Goldstein_92'] Chap. 6, p. 357 in [Goldstein_92]

[Goldstein_92"] Chap. 8 p. 404 in [Goldstein_92]

[Goodhew_88] *Electron Microscopy and Analysis*
P.J. Goodhew and F.J. Humphreys
2cnd Edition Taylor & Francis (1988)

[Greaves_85] G. N. Greaves
J. Non-Cryst. Solids No. 71, p. 203 (1985)

[Griscom_83] *Fundamental defect centers in glass: electron spin resonance and optical absorption studies of irradiated phosphorus-doped silica glass and optical fibres*
D. L. Griscom, E. J. Friebele, K. J. Long, J. W. Fleming
J. Appl. Phys. Vol. 54, No. 7, pp. 3743-3762 (1983)

[Grubb_91] *High power sensitized erbium optical fiber amplifier*
S. G. Grubb, R. S. Cannon, T. W. Windhorn, S. W. Vendetta,
P. A. Leilabady, D.W. Anthon, K. L. Sweeney,
W. L. Barnes, E. R. Taylor, J. E. Townsend
OFC' 91, San Diego, Posdeadline paper (18-22 February 1991)

[Grubb_91'] *+20 dBm erbium power amplifier pumped by a diode-pumped Nd:YAG laser*
S. G. Grubb, T. H. Windhorn, J. E. Townsend, K. P. Jedrzejewski, W. L. Barnes
Proc. Topical Meeting on Optical Amplifiers and their Applications, Snowmass, pp. 12-1 - 12-4 (24-26 July 1991)

[Gurman_92] *An extended x-ray absorption fine structure study of the rare earth sites in a neodynium doped glass*
S. J. Gurman, R. J. Newport, M. Overluizen, E. J. Tarbox
Phys. Chem. of Glasses, Vol.33, No.1(1992)

[Guitart_92] *Cavity length dependence of erbium-doped fiber laser performances*
J. Guitart, S. R. Moreno
SPIE Vol. 1789 Fiber Laser Sources and Amplifiers IV (1992)

[Hammond_77] *Silica based binary glass systems - Refractive index behaviour and composition in optical fibres*
C. R. Hammond, S. R. Norman
Optical and Quantum Electronics, Vol. 9, pp. 399 - 409 (1977)

[Hammond_78] *Fusion temperatures of SiO_2-P_2O_5 binary glasses*
C.R. Hammond
Phys. Chem. Glasses, Vol.19, No. 3 (1978)

[Hoppe_96] *A structural model for phosphate glasses*
U. Hoppe
J. Non-Cryst. Solids No. 195, pp. 138-147 (1996)

[Horiguchi_76] M. Horiguchi, H. Osanai
Electron. Lett. Vol. 12, 310 (1976)

[Imoto_78] K. Imoto, M. Sumi
Electron. Lett. Vol. 14, pp. 749-750 (1978)

[Itoh_86] *Phosphorus-dopant effect on hydroxyl absorption increases in silica glasses and fibres*
H. Itoh, Y. Ohmori, M. Horiguchi
J. of Non-Cryst. Solids Vol. 88, pp. 83-93 (1986)

[Inokuti_65] *Influence of energy transfer by the exchange mechanism on donor luminescence*
M. Inokuti, F. Hirayama
J. Chemical Physics Vol.43, No. 6 (September 1965)

[Jackel_92] *Guided blue and green upconversion fluorescence in an erbium-ytterbium-containing silicate glass*
J. L. Jackel, A. Yi-Yan, E. M. Vogel, A Von Lehmen, J. J. Johnson, E. Snitzer
Applied Optics Vol. 31, No. 18 (June 1992)

[Jeunhomme_83] *Single-mode fibre optics*
L. B. Jeunhomme
Editor Marcel Dekker, Inc., ISBN 0-8247-7020-X (1983)

[Kao_66] *Dielectric fiber surface waveguide for optical frequencies*
K.C. Kao, G. A. Hockham
Proc. IEE Vol. 113, No. 7, pp. 1151-8 (July 1966)

[Kosinski_88] *Raman and NMR spectroscopy of SiO_2 glasses co-doped with Al_2O_3 and P_2O_5*
S. G. Kosinski, D. M. Krol, T. M. Duncan, D. C. Douglass, J. B. MacChesay, J. R. Simpson
J. Non-Crystalline Solids Vol. 105, pp. 45-52 (1988)

[Kapron_70] *Radiation losses in optical waveguides*
F. P. Kapron, D. B. Keck, R. D. Maurer
Appl. Phys. Lett. Vol. 10, pp. 423-425 (1970)

[Lee_93] *Backward amplified spontaneous emission from erbium-doped fibers as a measure of amplifier efficiency*
D. Lee, D. J. DiGiovanni, J. R. Simpson, A. M. Vengsarkar, K. L. Walker
OFC/IOOC'93 ThF2, pp. 179-180 (1993)

[Lees_95] *980 nm diode pumped erbium/ytterbium doped Q-switched fibre laser*
G. P. Lees, A. Hartog, A. Leach, T. P. Newson
Electron. Lett. Vol.31, No. 21 (12th October 1995)

[Lees_96] *Diode pumped high power simultaneously Q-switched and self mode-locked erbium doped fibre laser*
G. P. Lees, T. P. Newson
Electron. Lett. Vol. 32, No. 4 (15th February 1996)

[Lincoln_93] *Spectroscopy of rare-earths in glass*
J. Lincoln
Ph.D Thesis, Dept of Physics, U. of Southampton, Chap. 8 (1993)

[Loh_96] *Single-sided output Sn/Er/Yb distributed feedback fiber laser*
W. H. Loh, L. Dong, J. E. Caplan
Submitted to Appl. Phys. Lett.

[Loudon_83] *The Quantum Theory of Light - 2nd Ed.*
R. Loudon
Section 1.5, p.13, Oxford University Press (1983)

[Macfarlane_87] *Spectroscopy of solids containing rare earth ions*
A. A. Kaplyanskii, R. M. Macfarlane
Chap. 3, Fig. 1, p. 56, North-Holland Physics Publishing (1987)

[Magne_93] *Cooperative luminescence in an Ytterbium doped silica fiber*
S. Magne, M. Druetta, J. P. Goure, J. C. Thevenin, P. Ferdinand,
G. Monnom
ICL'93, Th2C-3, Boston (1993)

[McCumber_64] D.E. McCumber
Phys. Rev. 134 , A299 (1964)

[Marcus_91] *Local structure around Er in silica and sodium silicate glasses*
M. A.Marcus, A. Polman
J. Non-Cryst. Solids 136, pp. 260-265 (1991)

[Marcuse_77] *Loss analysis of single-mode fiber splices*
D. Marcuse
Bell Systems Technical Journal, pp. 703-718 (1977)

[Martin_91] *Review of the structures of phosphate glasses*
S. W. Martin
Eur. J. Solid State Inorg. Chem. t. 28, pp. 163-205 (1991)

[Maurice_96] *Clustering effects on double energy transfer in heavily ytterbium-erbium-codoped silica fibers*
E. Maurice, G. Monnom, B. Dussardier, D. B. Ostrowsky
J. Opt. Soc. Am. B Vol. 13, No. 4, pp. 693-701 (April 1996)

[Mears_87] *High-gain rare-earth-doped fiber amplifier at 1.54 um*
R. J. Mears, L. Reekie, I. M. Jauncey, D. N. Payne
Proceedings Conference on Optical Fiber Communications and Conference on Integrated Optics and Optical Communications OFC/IOOC'87, paper WI2, p.167
Low-noise erbium-doped fiber amplifier operating at 1.54 um
R. J. Mears, L. Reekie, I. M. Jauncey, D. N. Payne
Electron. Lett. Vol.23, No. 19, 1026 (1987)

[Meunier_88] *Contribution a la creation d'un centre de fabrication de preformes pour fibres optiques hors normes, premieres realisations*
C. Meunier
These de Docteur en Physique, Partie C, Universite de Nice, Dept IMSP (1988)

[Myslinski_92] *High power Q-switched erbium doped fiber laser*
P. Myslinski, J. Chrostowski, J. A. Koningstein, J. R. Simpson
IEEE J. Quantum Electronics Vol. 28, No. 1 (January 1992)

[Minelly_92] *High-gain fibre power amplifier tandem-pumped by a 3W multi-stripe diode*
J. D. Minelly, R. I. Laming, J .E. Townsend, W. L. Barnes,
E. R. Taylor, K. P. Jedrzejewski, D. N. Payne
OFC' 92, San Jose, Paper TuG2, pp. 32-33 (3-7 February 1992)

[Minelly_92'] *High-power Er3+ / Yb3+ fibre laser pumped by a 962nm diode-array*
J. D. Minelly, W. L. Barnes, P. R. Morkel, J. E. Townsend,
S. G. Grubb, D. N. Payne
CLEO' 92, Paper CPD17, pp. 33-34, Anaheim (may 1992)

[Miniscalco_91] *Erbium-doped glasses for fiber amplifiers at 1500 nm*
W. L. Miniscalco
J. Light. Tech. Vol.9, No.2 (February 1991)

[Morgan_90] *Raman spectra of molybdenum phosphate glasses and some crystalline analogues*
S. H. Morgan
J. Am. Ceram. Soc, Vol. 73, pp. 753-56 (1990)

[Morkel_92] *Modelling erbium/ytterbium-doped fibre amplifiers*
P. R. Morkel
ECOC'92, paper FD2, PP. 206-209 (1992)

[Morse_91] *Aerosol techniques for glass formation*
T.F. Morse, A. Kilian, L. Reinhart, W. Risen, J. W. Cipolla
J. Non-Cryst. Solids. 129, pp. 93-100 (1991)

[Murzin_85] *Some features of laser excitation of ytterbium-erbium glasses*
A. G. Murzin, D. S. Prilezhaev, V. A. Fromzel
Soviet Journal of Quantum Electronics Vol.15, No.3 (March 1985)

[Nagel_82] *An overview of the Modified Chemical Vapour Deposition (MCVD) process and performance*
S. R. Nagel, J. B. MacChesney, K. L. Walker
I.E.E.E J. Of Quantum Electron. Vol. QE-18, No. 4. Pp. 459-476 (1982)

[Nelson_85] *Raman studies of sodium phosphates with low silica contents*
C. Nelson, D. R. Tallant
Physics and Chemistry of Glasses Vol. 26, No. 4 (August 1985)

[NIST] *Standart Reference Materials 610 'Trace Elements in a Glass Matrix' Certificate of analysis*
National Institute of Standards & Technology (USA)

[Olshansky_79] *Propagation in glass optical waveguides*
R. Olshansky
Rev. Mod. Phys Vol.51, No. 2 (April 1979)

[Pafcheck_90] *Optical absorption and emission in rare earth heavy metal fluoride glasses*
R. Pafcheck, J. Aniano, E. Snitzer, G. H. Siger Jr.
Proc. Symposium Optical Fiber Materials, Vol. 172

[Paschotta_97] *Lifetime quenching in Yb doped fibres*
R. Paschotta, J. Nillson, P. R. Barber, J. E. Caplen, A. C. Tropper, D. C. Hanna
Optics Commun. Vol. 136, No. 5-6, pp. 375-378 (1997)

[Payne_74] *Preparation of water-free silica-based optical fibre waveguide*
D. N. Payne. W. A. Gambling
Electron. Lett., Vol. 10, No. 16 (1974)

[Poole_85] *Fabrication of low-loss optical fibres containing rare-earth ions*
S.B. Poole, D. N. Payne, M. E. Payne
Electron. Lett., No. 21, pp. 737-738 (1985)

[Potts_87]] *Energy Dispersive X-ray Spectrometry* in *A Handbook of Silicate Rock Analysis*
P J Potts
p.337, Blackie (1987)

[Rausch_96] *Get Ready for the Crunch in Telecom*
H. Rausch
Photonics Spectra Vol. 30, No. 1, p. 23 (January 1996)

[Reisfeld_87] *Excited state phenomena in vitreous materials*
R. Reisfeld, K. Jørgensen
Handbook on the physics and chemistry of rare-earths, Elsevier Science,
Chap. 58, pp.1-90 (1987)

[Robinson_70] *Co-ordination of Yb3+ in phosphate, silicate, and germanate glasses*
C. C. Robinson, J. T. Fournier
J. Phys. Chem. Solids Vol. 31, pp. 895-904 (1970)

[Roman_95] *Er/Yb phosphosilicate and silicate glasses for ion-exchanged waveguide lasers and amplifiers*
J. Roman, J. Wang, M. Hempstead, J. S. Wilkinson
Internal Report, University of Southampton (December 1995)

[Ross_92] *Telecommunications in the Era of Photonics*
I. M. Ross
Solid State Technology, pp. 36 - 43 (April 1992)

[Rotman_96] *Practical models for enegy transfer between ions in solids*
S. R. Rotman, E. Luria, N. Yitzhaki, A. Eyal
Optical materials Vol. 5, pp. 1-33 (January 1996)

[Scherer_77] *Sintering of low-density glasses: I, Theory*
G. W. Sherer
J. Am. Ceram. Soc. Vol. 60, No. 5-6 (1977)

[Scott_84] *Optimization of composition for Al_2O_3 / P_2O_5 - doped optical fiber*
C. J. Scott
OFC' 84, Paper TUM4, New Orleans

[Shelby_90] *Rare-earth aluminosilicate glasses*
J. E. Shelby, J. T. Kohli
J. Am. Ceram. Soc. Vol.73, pp.39-42 (1990)

[Shibata_81] *Raman spectra of binary high-silica glasses and fibres containing GeO_2, P_2O_5, and B_2O_3*
N. Shibata, M. Horigudhi, T. Edahiro
J. Non Cryst. Solids Vol. 45, pp. 115-126 (1981)

[Simpkins_79] *Thermophoresis: the mass transfer mechanism in modified chemical vapor deposition*
P. G. Simpkins, S. Greenberg-Kosinski, J. B. MacChesnay
J. Appl. Phys. Vol. 50, No. 9 (Semptember 1979)

[Snitzer_61] *Optical maser action of Nd3+ in a barium crown glass*
E. Snitzer
Phys. Rev. Lett. Vol. 7, P. 444 (1961)

[Spirit_95] *High Capacity Optical Transmission Explained*
D. M. Spirit, M. J. O'Mahony
John Wiley & Sons - BT Series, p. 20 (1995)

[Tajima_92] *Low Rayleigh scattering P_2O_5-F-SiO_2 glasses*
K. Tajima, M. Ohashi, K. Shiraki, M. Tateda, S. Shibata
J. Lighwave Technology Vol. 10, No. 11 (November 1992)

[Tonooka_91] *A non-linear analysis of energy transfer in highly Tb3+-doped glasses*
K. Tonooka, N. Kamata, K. Yamada, K. Matsumoto, F. Maruyama
J. of Luminescence Vol. 50, p. 139-151 (1991)

[Townsend_90] *The development of optical fibres doped with rare-earth ions*
J. E. Townsend
Ph.D Thesis, University of Southampton (1990)

[Townsend_91] *Yb3+ sensitised Er3+ doped, silica-based optical fibre with ultra-high efficiency and gain*
J. E. Townsend, W. L. Barnes. S. G. Grubb
Materials Research Society Conference "Optical Waveguide Materials"
Vol. 244, pp. 143-146 (December 1991)

[Townsend_91'] *Yb3+ sensitised Er3+ doped silica optical fibre with ultra high transfer efficiency and gain*
J. E. Townsend, W. L. Barnes, K. P. Jedrzejewski, S. G. Grubb
Electronics Letters Vol. 27, No. 21, pp. 1958-1959 (October 1991)

[Tummineli_93] *Fabrication of high-concentration rare-earth doped optical fibers using chelates*
R. P. Tumminelli, B. C. McCollum, E. Snitzer
J. Light. Tech., Vol. 8, No. 11 (November 1990)

[Turnbull_56] D. Turnbull
Solid State Phys. Vol. 3, pp. 225-306 (1956)

[Uhlmann_83] *Glass: Science and Technology, Vol. 1 Glass-Forming Systems*
D. R. Uhlmann, N. J. Kreidl
Chap. 1 The Formation of Glasses, Academic Press (1983)

[Van Dijk_83] J. M. F. Van Dijk, M. F. H. Schuurmans
J. Chem. Phys., 78, pp. 5317-5323 (1983)

[Vienne_94] *Fabrication and characterisation of erbium : ytterbium phosphosilicate fibres*
G. G. Vienne
M. Phil. Thesis, University of Southampton (August 1994)

[Walker_87] *Optical fibre fabrication and characteristics*
K.L Walker
OFC' 87

[Wright_76] *Up-conversion and excited state energy transfer in rare-earth-doped materials*
J. C. Wright
Topics in Apllied Physics Vol. 15, Ed. F. K. Fong (1976)

[Wu_93] *Low-loss rare earth doped single-mode fiber by sol-gel method*
F. Wu, G. Puc, P. Foy, E. Snitzer, G. H. Sigel
Mat. Res. Bull., Vol. 28, pp. 637-644 (1993)

[Yokota_67] *Effects of diffusion on energy transfer by resonance*
M. Yokota, O. Tanimoto
J. Phys. Soc. Japan Vol. 22, No. 3 (March 1967)

Publications and talks arising from this work

1. *Efficient, low noise grating-feedback fibre laser doped with Er^{3+} : Yb^{3+}*
J. T. Kringlebotn, J. -L. Archambault, L. Reekie, J. E. Townsend, G. G. Vienne, D. N. Payne
Conference on Optical Communications (OFC'94), Vol. 4, Paper Tu G5, San-Jose, 20-25 February 1994

2. *Highly-efficient, low noise grating-feedback Er^{3+} : Yb^{3+} codoped fibre laser*
J. T. Kringlebotn, J. -L. Archambault, L. Reekie, J. E. Townsend, G. G. Vienne, D. N. Payne
Electronics Letters, Vol. 30, No.12, pp. 972-973, 9th June 1994

3. *Fabrication and characterisation of Er^{3+} : Yb^{3+} codoped phosphosilicate optical fibres for amplifiers and lasers*
G. G Vienne
Invited talk, Bell Northern Research (BNR Europe), Harlow, 27th April 1995

4. *Fibres optiques dopees*
G. G. Vienne
Euro-engineers tutorials, University of Southampton, 12th May 1995

5. *Progress towards an efficient all-glass erbium : ytterbium cladding pumped fibre*
G. G. Vienne
High Radiance Fibres Sources pre-project meeting, GEC Marconi Material Technologies, 17th July 1995

6. *Fabrication and characterisation of Er^{3+} : Yb^{3+} codoped phosphosilicate optical fibres for amplifiers and lasers*
G. G. Vienne, J. E. Caplen, Z. J. Chen, L. Dong, J. D. Minelly, J. E. Townsend
12th Quantum Electronics Conference, Southampton 4-8th September 1995

7. *Advances in cladding pumped fibre lasers*
J. D. Minelly, L. Dong, G. G. Vienne, J. E. Caplen, Z. J. Chen
12th Quantum Electronics Conference, Southampton 4-8th September 1995

8. *Broad-area diode-pumped 1 W femtosecond fiber system*
A. Galvanaukas, M. E. Fermann, D. Harter, J. D. Minelly, G.G. Vienne, J. E. Caplen
CLEO'96, CFD4, Anaheim, 2 - 7 June 1996

9. *Cladding pumped passively modelocked femtosecond fibre lasers*
M. E. Fermann, D. Harter, J. D. Minelly, G. G. Vienne
CLEO'96, CFD1, Anaheim, 2 - 7 June 1996

10. *Subpicosecond soliton transmission over 22 km of dipersion-shifted fibre with loss compensated by Raman gain*
A. B. Grudinin, S. Gray, G. G. Vienne
Electronics Letters, Vol. 32, No. 6, pp. 573-5, 1996

11. *Efficient cladding pumped Er3+/Yb3+-doped fibre amplifier and bending effect in cladding pumping scheme*
CLEO Europe' 96, Hamburg

12. *Role of aluminum in Er^{3+} : Yb^{3+} codoped aluminiphosphosilicate optical fibres*
G G Vienne, W. S. Brocklesby, R. S. Brown, J. E. Caplen, Z. J. Chen, Z. E. Harutjunian, J. D. Minelly, J. E. Roman, D. N. Payne
Optical Fibre Technology Vol. 2, pp. 387-393 (January 1997)

13. Saturable-absorber fiber Fabry-Perot tunable filters
K. Hsu, C. M. Miller, G. G. Vienne, D. N. Payne
To be submitted to Optics Letters

14. *Comparison of erbium clusturing in optical fibre hosts*
J.-P De Sandro, J. E. Caplen, B. N. Samson, G. G. Vienne
In preparation

Appendices

A.1 Model including the back-transfer of energy

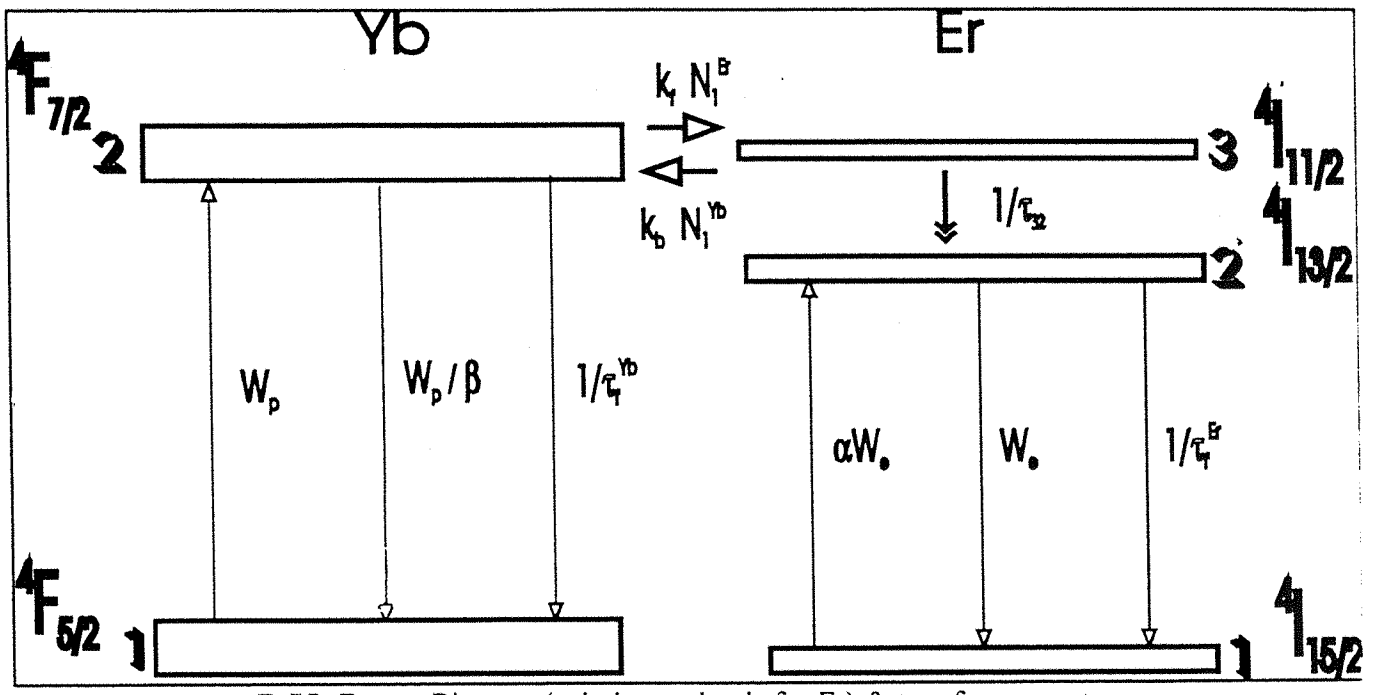

Er/Yb Energy Diagram (only lowest levels for Er) & transfer parameters

$$
\begin{cases}
\dfrac{dN_2^{Yb}(z)}{dt} = (W_p(z) + k_b N_3^{Er}(z)) N_1^{Yb}(z) - (\dfrac{W_p(z)}{\beta} + \dfrac{1}{\tau_f^{Yb}} + k_f N_1^{Er}(z)) N_2^{Yb}(z) \\
\dfrac{dN_3^{Er}(z)}{dt} = k_f N_1^{Er}(z) N_2^{Yb}(z) - (k_b N_1^{Yb}(z) + \dfrac{1}{t_{32}}) N_3^{Er}(z) \\
\dfrac{dN_2^{Er}(z)}{dt} = \alpha W_e(z) N_1^{Er}(z) - (W_e(z) + \dfrac{1}{\tau_f^{Er}}) N_2^{Er}(z) + \dfrac{N_3^{Er}(z)}{t_{32}} \\
N_T^{Yb}(z) = N_1^{Yb}(z) + N_2^{Yb}(z) \\
N_T^{Er}(z) = N_1^{Er}(z) + N_2^{Er}(z) + N_3^{Er}(z)
\end{cases}
$$

A.2 Fabrication logs - Test on the presintering temperature

Before deposition

F300 tube from Heraeus OD_{AV} = 25 mm, CSA = 170 mm^2, L = 50 cm

1 (10,1950;O = 600)	Warming-up
3 (10,2000; F/O = 190/600)	Etching
1 (10,2025; Si/O = 100/600)	T check
5 (10,2025;Si/O = 300/600)	Cladding
1 (10,2025;O = 600)	Fusing
1(10,2150;O = 100)	Pre-collapsing
1 (10,2200;O = 100)	Pre-collapsing (Tset = 2250)
1 (10,2025;Si/O = 100/600)	T check
1(10,2050;Si/O = 300/600)	Cladding
1 (10,2050;O = 600)	Fusing

Deposition

Set Pyrometer to reverse	
1R (10,1550;O = 300)	Set for core
1R (10,1550;Si/P/O = 200/1000/300)	Deposition (1 cm interface 9-10 cm from burner centre)
Set pyrometer to forward	

PRESINTERING

1R(15,T;O = 300)	**T = 1000 (ND937), 1050 (ND943, ND944), 1100 (ND942)**

Doping

60 min	$ErCl_3(6H2O)$	0.2 g	
	$YbCl_3(6H2O)$	4.0 g	in 200 ml H_2O
	$AlCl_3(6H2O)$	13.1 g	

Drying

30 min	N/O = 1000/500
30 min	(20,900; N/O = 1000/500)

Fusing

1 (10,1675; P/O = 200/300)

Collapsing & Sealing

1 (10,2100;P/O = 200/100)
2 (4,2275; P/O = 400/50)
1 (3,2275; P/O = 400/30)
1 (3,2275; P/O = 300/30)
1R (1.3,'2275'; O = 30)

Preforms fabricated

ND937	27.09.94	Increase Tpres compared to ND936 where frit peeled off in soln & reproduce ND921.
ND942	04.10.94	Increase Tpres to avoid 'snake skin' patterns in the frit.
ND943	05.10.94	Reduce Tpres because ND942 showed reduced dopant incorporation.
ND944	06.10.94	Reproduce ND943 because of reduced evaporation. Wait for cooling before deposition to supress lines at tail half.

Notation

'1 (10,1950;O = 600)' stands for 1 pass with a burner speed of 10 $cm.min^{-1}$, a burner temperature of 1950 °C, and an oxygen flow of 600 $cc.min^{-1}$. O, F, Si, P, and N are abbreviations of O_2, SF_6, $SICl_4$, $POCl_3$, and N_2. The suffixe 'R' after the number of passes indicates that the burner direction has been reversed to be counterpropagating with the gas flow.

A.3 Parameters for laser modelling (ND844 02)

Parameter	Reference	Value
σ_{12}^{Yb}	§4.3.3	$2.0\ 10^{-27}\ m^2$
$\beta = \sigma_{12}^{Yb} / \sigma_{21}^{Yb}$	[Morkel_92]	0.1
τ_f^{Yb}	[Barnes_92](1)	1.3 ms
$\tau_{tr} = 1 / W_{tr}$	[Brown_96] (2)	40 µs
σ_{12}^{Er}	§4.3.3	$6.8.10^{-25}\ m^2$
$\alpha = \sigma_{12}^{Er} / \sigma_{21}^{Er}$	§4.3.3	1.0
τ_f^{Er}	§4.5.1	10.2 ms
N^{Yb}	§4.1.1.1	$2.97\ 10^{26}\ m^{-3}$ (13480ppm)
N^{Er}	§4.1.1.1	$2.38\ 10^{25}\ m^{-3}$ (1080ppm)
λ_p	-	1064 nm
λ_s	-	1540 nm
Γ_p	§4.3.3 (3)	0.86
Γ_s	§4.3.3	0.86
loss	-	0.0
A	-	$1.6\ 10^{-11}\ m^2$
R1	§4.4.2	0.035
R2	§4.4.2	0.035

(1) [Barnes_92]: measurement on ND728 (Si/P as ND8xx but no Al), confirmed by measurement in saturated Er/Yb fibre

(2) corresponding to $k_{tr} = 1 / (\tau_{tr}.N_T^{Er}) = 1.05\ .\ 10^{-21}\ m^3 / s$

(3) corresponding to $\alpha_{1064} = 2.2$ dB / m

A.4 Amoco's fibre booster amplifier advertisement

It took an act of God to demonstrate the power of our new fiber amplifier.

At the height of the Flood of '93, rising water levels threatened a key fiber optic regenerator site on the Missouri River, endangering service for thousands of customers of a major telecommunications company. The solution: find a fiber amplifier powerful enough to boost signal levels and bypass the site entirely. The choice: ALC's new, advanced co-doped Er/Yb fiber amplifier with saturated power levels up to +24 dBm, the highest output power available.

For major players in the telecommunications and cable industries, integrating this powerful light source into their networks has proven invaluable. Eliminating expensive repeaters. Spanning greater distances. Adding more cable subscribers per transmitter.

Find out how far our new fiber amplifier can take you. Contact ALC Telecommunications Group today at (708) 961-8400 or fax us at (708) 369-4299. We've got the power to help you down the line. **ALC Telecommunications Group. The light of tomorrow.**

AMOCO

ALC Telecommunications Group

Circle No. 39